A radio view on the structural evolution of massive star-forming galaxies across cosmic time

Dissertation
zur
Erlangung des Doktorgrades (Dr. rer. nat.)
der
Mathematisch-Naturwissenschaftlichen Fakultät
der
Rheinischen Friedrich-Wilhelms-Universität Bonn

von
Eric Faustino Jiménez-Andrade
aus
Tecamachalco, Mexiko

Bonn, July 2019

Angefertigt mit Genehmigung der Mathematisch-Naturwissenschaftlichen Fakultät der Rheinischen Friedrich-Wilhelms-Universität Bonn.

1. Gutachter:	Prof. Dr. Frank Bertoldi
2. Gutachter:	Prof. Dr. Cristiano Porciani
Tag der Promotion:	17.01.2020
Erscheinungsjahr:	2020

A mis padres –Carmen y Faustino– y hermanos

Abstract

It is not well understood what processes regulate the global formation of stars in galaxies throughout cosmic history. My work aims to measure the structural evolution of star-forming galaxies (SFGs), from the present back to when the Universe was ten percent of its current age. I focus on the population of massive SFGs with a total stellar mass that is one to ten times that of the Milky Way. I investigate possible differences in physical processes that regulate star formation throughout cosmic history, to address why typical massive galaxies in the early Universe formed stars an order of magnitude more intensely than today.

I analyze observations at sub-millimeter-to-radio wavelengths of a large sample of 3184 massive SFGs in the COSMOS field. I inspect the spatial distribution of star formation (traced by radio continuum emission) in galaxies of the sample, and investigate how their molecular gas content (traced by carbon monoxide line emission) affected the star formation activity. I find that over the past 10 Gyr (redshift < 2) star formation in typical massive SFGs occurred out to large radii, strengthening the (previously) proposed scenario whereby typical massive SFGs are rotating disks with widespread star formation activity. On the other hand, I find that massive SFGs with enhanced star formation rates show more compact activity, which is consistent with expectations that star formation here is triggered by galaxy mergers that induce nuclear starbursts. I find that over the past 10 Gyr, the star formation rate per unit area in massive SFGs has declined at a rate that is related to the molecular gas content. In the early Universe, typical massive SFGs converted molecular gas into stars more efficiently than present-day galaxies do.

I present detailed studies of two massive SFGs in the very early Universe (12.5 Gyr ago, redshift $= 4.5$) that show extended, gas-rich disks with very high star formation rates and elevated star formation efficiencies, similar to that observed in present-day, merger-driven starbursts. Apparently, at these early epochs, strong gas accretion from the intergalactic medium fed unstable, gas-rich disks that broke into giant clumps that formed stars at high rates. I also show that in the very early Universe, the high star formation rate of satellite galaxies around massive SFGs drove large-scale outflows, which prevented further gas accretion and thus might have suppressed star formation in such companion galaxies.

I conclude that throughout most of cosmic history, star formation in typical massive SFGs was primarily regulated by the smooth accretion of cold gas from the intergalactic medium, which sustained steady star formation activity in extended, rotating disks. The more intense star formation in early galaxies resulted from their larger gas reservoirs, which were distributed across fragmenting, gravitationally unstable disks. In this respect, the stellar birthrate and star formation efficiency of typical massive SFGs in the early Universe were similar to those observed in local, merger-driven (maximal) starbursts.

List of publications

In this Ph.D. thesis, I document observational evidence regarding the physical mechanisms that regulate star formation in galaxies throughout cosmic history. The analysis and interpretation of my observations are divided in three Chapters. In Chapter 2, I explore the conditions for star formation in 3184 galaxies over the last ~10 Gyr of cosmic history (i.e., $0.35 < z < 2.25$), while in Chapters 3 and 4, I probe the properties of three star-forming galaxies (SFGs) at the epoch when the Universe was only ~1.5 Gyr old (i.e., $z \sim 4.5$). These research projects led to two peer-reviewed research publications and one more in preparation for submission:

- **[Chapter 2] Jiménez-Andrade, E. F.**, Magnelli, B., Karim, A., Zamorani, G., Bondi, M., Schinnerer, E., Sargent, M., Novak, M., Lang, P., Bertoldi, F., Vardoulaki, E., Romano-Díaz, E., Toft, S., Smolčić, V., Harrington, K., Leslie, S., Delhaize, J., Liu, D., Karoumpis, C., Kartaltepe, J., Koekemoer, A.M. (2019). Radio continuum size evolution of star-forming galaxies over $0.35 < z < 2.25$. *Astronomy & Astrophysics*, 625, A114. *Authors Contributions:* E.F.J.A. performed the source extraction, Monte Carlo simulations and subsequent scientific analysis under the supervision of B.M, A.K. and F.B. E.F.J.A. wrote the manuscript with the aid of B.M. The other co-authors conceived and planned the observations, contributed with the interpretation of the results and commented on the manuscript.

- **[Chapter 3] Jiménez-Andrade, E. F.**, Magnelli, B., Karim, A., Jones, G. C., Carilli, C. L., Romano-Díaz, E., Gómez-Guijarro, C., Toft, S., Bertoldi, F., Riechers, D. A., Schinnerer, E., Sargent, M., Michałowski, M. J., Fraternali, F., Staguhn, J. G., Smolčić, V., Aravena, M., Harrington, K. C., Sheth, K., Capak, P. L., Koekemoer, A. M., van Kampen, E., Swinbank, M., Zirm, A., Magdis, G. E., Navarrete, F. (2018). Molecular gas in AzTEC/C159: a star-forming disk galaxy 1.3 Gyr after the Big Bang. *Astronomy & Astrophysics*, 615, A25. *Authors Contributions:* E.F.J.A. reduced the NOEMA data, conducted the spectroscopic analysis and derived the properties of the molecular gas of AzTEC/C159. G.J. reduced the VLA data, while B.M. analyzed the far-infrared spectral energy distribution. E.F.J.A. wrote the manuscript with the aid of B.M and E.R.D. The other co-authors conceived and planned the observations, contributed with the interpretation of the results and commented on the manuscript.

- **[Chapter 3] Jiménez-Andrade, E. F.**, Zavala, J., Magnelli, B., Casey, C., Liu, D., Romano-Díaz, E., Karim, A., Bertoldi, F. (2019). The redshift and star formation mode of AzTEC2: a pair of disk galaxies at $z = 4.63$?. To be submitted by August 2019. *Authors Contributions:* E.F.J.A. reduced the NOEMA data, conducted the spectroscopic analysis, derived the properties of the molecular gas and structure of AzTEC2. J.Z. reduced the ALMA data. E.F.J.A. wrote the manuscript with input from all the co-authors, who also helped to plan the observations and contributed with the interpretation of the results.

The conclusions presented in this work are complementary to results from related collaborative research projects, to which the author of this dissertation has contributed. The publications derived from these projects are listed below.

- Fudamoto, Y., Oesch, P., Magnelli, B., Schinnerer, E., Liu, D., Lang, P., **Jiménez-Andrade, E. F.**, Groves, B., Leslie, S. and Sargent, M. T. "A^{3}COSMOS III: The Dust Attenuation of Star-Forming Galaxies at $z = 2.5 - 4.0$ from the COSMOS-ALMA Archive". Submitted to *Monthly Notices of the Royal Astronomical Society*. *Author Contributions:* E.F.J.A. assisted with the sample selection (source extraction) and contributed to the final version of the manuscript.

- Liu, D., Lang, P., Magnelli., B., Schinnerer, E., Leslie, S., Fudamoto, Y., Bondi, M., Groves, B., **Jiménez-Andrade, E. F.**, Harrington, K., Karim, A., Oesch, P., Sargent, M., Vardoulaki, E. et al. (2019). Auto-mining the ALMA Archive in the COSMOS Field (A^{3}COSMOS): I. Robust ALMA Continuum Photometry Catalogs and Stellar Mass and Star Formation Properties for 700+ Galaxies at Redshift 0.5-6. Submitted to *The Astrophysical Journal*. *Author Contributions:* E.F.J.A. assisted with the sample selection (source extraction), discussed the results with the leading author and contributed to the writing of the manuscript.

- Harrington, K., Vishwas, A., Weiss, A., Magnelli, B., Stacey, G., Yun, M.S., Leung, T.K.D., Grassitelli, L., Zajaček, M., **Jiménez-Andrade, E. F.**, Frayer, D.T., Riechers, D., Bertoldi, F. (2019). Ionised nitrogen and molecular gas in the $z \sim 2.55$ strongly lensed, active galactic nuclei/starburst, "The Red Radio Ring". *Monthly Notices of the Royal Astronomical Society*, in press. *Author Contributions:* E.F.J.A. assisted with the data analysis, contributed to the interpretation of the results and to the writing of the manuscript.

- Lang, P., Schinnerer, E., Smail, I., Swinbank, A.M., Liu, D., Leslie, S.K., Almaini, O., Xia An, F., Bertoldi, F., Blain, A.W., Chapman, S.C., Chen, C.C., Conselice, C., Cooke, E.A., Coppin, K.E.K., Dudzeviciute, U., Dunlop, J.S., Farrah, D., Fudamoto, Y., Geach, J.E., Gullberg, B., Harrington, K.C., Hodge, J.A., Ivison, R.J., **Jiménez-Andrade, E. F.**, Magnelli, B., Michałowski, M. J., Oesch, P., Sargent, M.T., Scott, D., Simpson, J.M., Smolčić, V., Stach, S.M., Thomson, A.P., Vardoulaki, E., Wardlow, J.L., Weiss, A., van der Werf, P. (2019). Revealing the stellar mass and dust distributions of submillimeter galaxies at $z \sim 2$. *The Astrophysical Journal*, in press. arXiv:1905.06960. *Author Contributions:* E.F.J.A. assisted with the sample selection (source extraction), discussed the results with the leading author and contributed to the writing of the manuscript.

- Magnelli, B., Karim, A., Staguhn, J., Kovács, A., **Jiménez-Andrade, E. F.**, Casey, C.M., Zavala, J.A., Schinnerer, E., Sargent, M., Aravena, M., Bertoldi, F., Capak, P.L., Riechers, D.A. (2019). The IRAM/GISMO two-millimeter survey in the COSMOS field. *The Astrophysical Journal*, 877, 45. *Author Contributions:* E.F.J.A. assisted with the counterpart association and produced the overlay images presented in the manuscript. He also contributed to the final version of the manuscript.

- Bondi, M., Zamorani, G., Ciliegi, P., Smolčić, V., Schinnerer, E., Delvecchio, I., **Jiménez-Andrade, E. F.**, Liu, D., Lang, P., Magnelli, B., Murphy, E. J., Vardoulaki, E. (2018). Linear radio size evolution of μJy populations. *Astronomy & Astrophysics*, 618, L8. *Author*

Contributions: E.F.J.A. discussed the results with the leading author, contributed to the interpretation of the results and to the writing of the manuscript.

- Gómez-Guijarro, C., Toft, S., Karim, A., Magnelli, B., Magdis, G. E., **Jiménez-Andrade, E. F.**, Capak, P. L., Fraternali, F., Fujimoto, S., Riechers, D. A., Schinnerer, E., Smolčić, V., Aravena, M., Bertoldi, F., Cortzen, I., Hasinger, G., Hu, E. M., Jones, G. C., Koekemoer, A. M., Lee, N., McCracken, H. J., Michałowski, M. J., Navarrete, F., Pović, M., Puglisi, A., Romano-Díaz, E., Sheth, K., Silverman, J. D., Staguhn, J., Steinhardt, C. L., Stockmann, M., Tanaka, M., Valentino, F., van Kampen, E., Zirm, A. (2018). Starburst to Quiescent from HST/ALMA: Stars and Dust Unveil Minor Mergers in Submillimeter Galaxies at $z \sim 4.5$. *The Astrophysical Journal*, 856, 121. *Author Contributions:* E.F.J.A. provided constraints on the molecular gas reservoirs of galaxies in the sample, which helped to define their evolutionary path. He also contributed to the writing of the manuscript.

- Harrington, K. C., Yun, M. S., Magnelli, B., Frayer, D. T., Karim, A., Weiß, A., Riechers, D., **Jiménez-Andrade, E. F.**, Berman, D., Lowenthal, J., Bertoldi, F. (2018). Total molecular gas masses of Planck - Herschel selected strongly lensed hyper luminous infrared galaxies. *Monthly Notices of the Royal Astronomical Society*, 474, 3866. *Author Contributions:* E.F.J.A. assisted with the data analysis, contributed to the interpretation of the results and to the writing of the manuscript.

In addition, the author has investigated the impact of Active Galactic Nuclei (AGN)-driven jets on the evolution of galaxies, leading to the publications listed below. One of them is a first-authored manuscript based on the results of previous Master thesis work, which was drafted and published during the first year of the Ph.D. program. AGN-related manuscripts are not presented and/or discussed further in this dissertation, as the AGN phenomena deviate from the main scientific goal of this Ph.D. thesis.

- Hernández-García, L., Panessa, F., Bassani, L., Bruni, G., Ursini, F., Chavushyan, V., González-Martín, O., Cazzoli, S., **Jiménez-Andrade, E. F.**, Arévalo, P., Díaz, Y. (2019). Multiwavelength analysis of the nucleus in Mark 1498. Submitted to *Monthly Notices of the Royal Astronomical Society*. *Author Contributions:* E.F.J.A. modeled the optical spectrum of Mark 1498 to infer the star formation history, velocity dispersion of stars in the bulge, and mass of the super-massive black hole. He also contributed to the interpretation of the results and to the writing of the manuscript.

- Vardoulaki, E., **Jiménez-Andrade, E. F.**, Karim, A., Novak, M., Leslie, S.K., Tisanic, K., Smolčić, V.,Schinnerer, E., Sargent, M., Bondi, M., Zamorani, G., Magnelli, B., Bertoldi, F., Herrera-Ruiz, N., Mooley, K. P., Delhaize, J., Myers, S.T., Marchesi, S., Koekemoer, A. M., Gozaliasl, G., Finoguenov, A., Middleberg, E., Ciliegi, P. (2019). A closer look at the deep radio sky: Multi-component radio sources at 3-GHz VLA-COSMOS. *Astronomy & Astrophysics*, in press. arXiv:1901.10168. *Author Contributions:* E.F.J.A. assisted with the sample selection, measured/characterized the properties of objects in the sample, and produced the overlay images presented in the manuscript. E.F.J.A. also contributed to the interpretation of the results and to the writing of the manuscript.

- Hernández-García, L., Vietri, G., Panessa, F., Piconcelli, E., Chavushyan, V., **Jiménez-Andrade, E. F.**, Bassani, L., Bazzano, A., Cazzoli, S., Malizia, A., Masetti, N., Monaco, L., Pović, M., Saviane, I., Ubertini, P. (2018). Variable broad lines and outflow in the weak blazar PBC J2333.9-2343. Monthly Notices of the Royal Astronomical Society, 478, 4634. *Author Contributions:* E.F.J.A. modeled the optical spectrum of PBC J2333.9-2343 to infer the velocity dispersion of stars in the bulge and the mass of the super-massive black hole. E.F.J.A. also contributed to the interpretation of the results and to the writing of the manuscript.

- **Jiménez-Andrade, E. F.**, Chavushyan, V., León-Tavares, J., Patiño-Álvarez, V. M., Olguín-Iglesias, A., Kotilainen, J., Falomo, R., Hyvönen, T. (2017). Detection of helicoidal motion in the optical jet of PKS 0521-365. *Monthly Notices of the Royal Astronomical Society: Letters*, 470, L107. *Author Contributions:* E.F.J.A. reduced the optical spectra and performed the scientific analysis under the supervision of V.C. and J.L.T. E.F.J.A. wrote the manuscript with input from all authors.

In summary, the overall scientific production consists of fourteen peer-reviewed articles, including three first-authored and one second-authored manuscript. They are cited accordingly in this dissertation and are marked with a dagger, for example: (Jiménez-Andrade[†] et al., 2019).

Contents

CHAPTER 1

Galaxy Formation and Evolution: an overview

Throughout history, humankind has been intrigued by the nature of the cosmos and our place in it. This curiosity has been driven by particular questions such as: how and when did the Universe start? what is its composition? how do galaxies, stars and planets form? Astronomy –the oldest of the natural sciences– has become our instrument to address such fundamental questions, enabling us to unveil a vast number of galaxies close to the Milky Way and beyond. It was only until recently, however, that powerful telescopes were able to explore farther back into the history of the Universe. These deep observations now allow us to explore the conditions for galaxy formation and the mechanism that drive the evolution of galaxies throughout cosmic time – the key goal of this Ph.D. thesis work.

This chapter is devoted to introducing the observational evidence and theoretical models that laid the foundation of our modern view of galaxy formation and evolution. To this end, in Sect. 1.1, we first summarize the history of cosmic structure formation, starting from the primordial fluctuations of the Universe until the re-ionization era during which the first galaxies emerged. Then, in Sect. 1.2, we describe the selection techniques used to identify distant galaxies, as well as the methods employed to determine their fundamental properties such as star formation rate and stellar mass. All those elements are integrated into Sect. 1.3, where we describe the current picture on how star formation, and thus galactic stellar mass growth, is regulated in galaxies throughout cosmic time. Lastly, the aims and structure of this Ph.D. thesis are given in Sect. 1.4.

1.1 From the Big Bang to the birth of galaxies

From a cosmological perspective, galaxies are considered as the cosmic building blocks of the Universe. Consequently, the research of galaxy formation and evolution has acquired special relevance to disclose the composition and timeline of the Universe. This section provides a brief review on those observational and theoretical studies that have explored the conditions for structure formation in the Universe, as well as the mechanisms that govern the evolution of the primeval galaxies. These elements provide a basis to revise, in the sections that follow, the contemporary paradigm of galaxy evolution, which has been partially formulated through observational studies of distant galaxies.

1.1.1 How did it all begin?

The evolution of the Universe is being described within the framework of the so-called ΛCDM (or "concordance") cosmological model (see Bull et al., 2016, for a review). Apart from ordinary (baryonic) matter, the ΛCDM model predicts two more components of the Universe: dark energy (Λ) and Cold Dark Matter (CDM). While the former is thought to be the responsible for the accelerating expansion of the Universe, the latter is an hypothetical form of matter that only interact through gravity (i.e., it remains dark) and aids the formation of structure in the Universe. According to this modern picture of cosmology, the Universe started ∼13.7 billion years ago with the Big Bang (e.g., Gorbunov & Rubakov, 2011) as a hot and dense singularity where the dominant form of energy was radiation. Within a fraction of a second the Universe underwent a period of accelerated expansion called "inflation", which transformed quantum fluctuations in the field driving inflation into macroscopic density fluctuations (e.g., Guth, 1981; Liddle & Lyth, 2000). After the inflationary period, the Universe continued to expand – albeit at a much lower rate – and cool. Once the temperature dropped below $T \sim 3000$ K (at redshift[1] ~ 1100), the Universe entered the "recombination" epoch during which electrons and protons were able to recombine into neutral hydrogen atoms (HI), while photons traveled in space without being absorbed or diffused by matter (i.e., the mean free path of photons increased dramatically). Density fluctuations in the primordial plasma, produced at the end of inflation, grew under the effect of gravity and led to the production of "dark matter" halos; settling the sites where star formation and subsequent galaxy formation took place (see Springel et al., 2006; Mo et al., 2010; Schneider, 2015, for a review).

Although the idea of a hot Big Bang is mainly based on theoretical considerations, there is robust observational evidence that support this model. The earliest indication of the Big Bang came from the correlation between distance and radial velocity of nearby galaxies (Hubble, 1929), which was subsequently interpreted as evidence of an expanding Universe. In addition, the "Big Bang nucleosynthesis theory" (e.g., Mathews et al., 2018) successfully reproduces the observed abundances of the lightest elements in the Universe – like hydrogen, deuterium, helium and lithium (e.g., Burles et al., 1999; Cyburt et al., 2016). The Big Bang model is mainly sustained by the detection of the Cosmic Microwave Background (CMB) radiation (e.g., Penzias & Wilson, 1965; Gawiser & Silk, 2000; Hu & Dodelson, 2002), which is composed of photons that last interacted with

[1] The electromagnetic spectrum of distant celestial objects is shifted towards longer wavelengths as the radiation travel across an expanding the Universe. Thus, the redshift, z, is a measure of the distance to a galaxy and/or of the lapse of time between the instant of emission and that of observation.

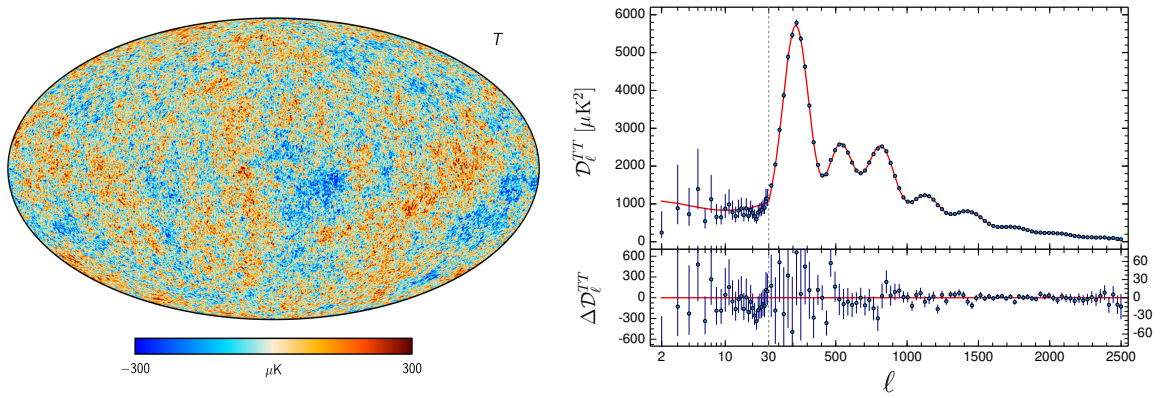

Figure 1.1: *Left panel:* CMB temperature map (5 arcmin resolution) derived from *Planck* observations. *Right panel:* CMB angular power spectrum, expressed in terms of $D_\ell = \ell(\ell+1)C_\ell/2\pi$. The error bars correspond to the $\pm 1\sigma$ uncertainties. The red line shows the best-fit base ΛCDM theoretical spectrum, while the residuals are presented in the bottom panel (Planck Collaboration et al., 2016).

the matter at the epoch of recombination. As the Universe expanded and cooled, this background of thermal radiation has reached a temperature of ~ 2.73 K at the present time (Fig. 1.1). With the development of sensitive space-born instruments such as COBE (Bennett et al., 1996), WMAP (Komatsu et al., 2011), *Planck* (Planck Collaboration I, 2014) and many other ground based telescopes, it has been possible to detect fluctuations in the CMB temperature of the order of $\Delta T/T \sim 10^{-5}$. Since those temperature anisotropies trace primordial density inhomogeneities of the Universe, characterizing the CMB in detail has become essential to unveil the initial conditions of structure formation.

The CMB anisotropy distribution defined as $\Theta(\hat{n}) \equiv \Delta T/T(\hat{n})$, where $\hat{n} = (\theta, \phi)$ is a particular direction on the sky, can be expressed as a series of spherical harmonics (Y_{lm}):

$$\Theta(\hat{n}) = \sum_{\ell,m} a_{\ell m} Y_{\ell m}(\hat{n}), \tag{1.1}$$

where the $a_{\ell m}$ are the expansion coefficients of the temperature anisotropy. The CMB angular power spectrum is then given by $C_\ell = \langle |a_{\ell m}|^2 \rangle$ (Fig. 1.1). Essentially, this spectrum characterizes the amplitudes of the CMB temperature fluctuations as a function of their angular size on the sky, and contains information on the geometry, structure, and matter composition of the Universe (e.g., Gawiser & Silk, 2000; Hu & Dodelson, 2002; Mo et al., 2010, and references therein). For instance, in the case of an open/hyperbolic (or closed/spherical) Universe, a given angular size on the sky would correspond to a larger (smaller) spatial scale with respect to a "flat" Euclidean Universe. Consequently, the location of the peaks of the CMB spectrum becomes highly sensitive to the spatial curvature of the Universe. The relative heights of the peaks, on the other hand, provides information on the baryon and dark matter content that gave rise to (and shaped) overdense regions in the Universe before/during the recombination epoch.

Thanks to the characterization of the CMB, and other large-scale structure datasets like galaxy redshift (z) surveys, it has been possible to determine key cosmological parameters that provide a

global description of the Universe. The density parameter (Ω_0), in particular, quantifies the average density of baryonic (Ω_b) and dark matter (Ω_c) in the Universe, whereas Ω_Λ represent the dark energy density. The *Hubble* constant (H_0) describes the present rate of the expansion of the Universe. Current estimates give a flat Universe with $\Omega_b = 0.0493 \pm 0.0010$, $\Omega_c = 0.264 \pm 0.011$, $\Omega_\Lambda = 0.685 \pm 0.007$, $H_0 = 67.4 \pm 0.5$ and age of the Universe of 13.797 ± 0.023 gigayear (Gyr; Planck Collaboration et al., 2018).

1.1.2 Structure formation in the Universe: dark matter halos

After the recombination epoch (i.e. $z \lesssim 1100$), the Universe was filled with neutral hydrogen gas and there were no radiation sources apart from the CMB. During this "dark epoch" of the Universe, primordial density fluctuations collapsed and formed gravitationally bounded halos. The growth of those fluctuations can be understood in the framework of perturbation theory for a fluid in a gravitational field (see Peebles & Harrison, 1994; Mo et al., 2010). In this approach, a perturbation in space and time grows against an average background of matter density $\bar{\rho}$. In the case of small perturbations, i.e., when the density contrast ($\delta = (\rho - \bar{\rho})/\bar{\rho}$) is less than 1, it is possible to linearize (and simplify) the equations that govern the motion of fluids in a gravitational field. This linear regime is valid, for example, at the epoch of recombination when the fluctuations were of the order of 10^{-5}. To explain the large inhomogeneities we observe in the Universe, where $\delta >> 1$, a full solution for the non-linear equations is required.

Using a spherically symmetric density perturbation, Press & Schechter (1974) presented an analytical description of the non-linear growth of cosmic structure. They proposed to smooth a field of linear density perturbations and identify overdense regions (i.e., peaks) above a certain density threshold ($\delta_c \sim 1.69$), which subsequently collapse and form dark matter halos. This formalism allows us to estimate the Halo Mass Function (HMF), that is, the number density of halos between mass M_h and $M_h + dM_h$ at redshift z:

$$n(M_h, z)dM_h = \sqrt{\frac{2}{\pi}} \frac{\bar{\rho}}{M_h^2} \nu e^{-\nu^2/2} \left| \frac{d\ln(\nu)}{d\ln(M_h)} \right| dM_h, \tag{1.2}$$

where $\nu = \delta_c/\sigma$ and σ is the rms density fluctuation. Qualitatively, the HMF predicts a large number of small halos that far exceeds the abundance of massive ones. Numerical simulations have shown that the Press & Schechter HMF is reasonably accurate at $z = 0$ (e.g., Cuesta et al., 2008), although it tends to under- (over)-predict the abundance of massive (low mass) haloes as the redshift increases (Springel et al., 2005). More robust HMF have been obtained, for example, using an ellipsoidal halo collapse model (Sheth et al., 2001) and empirical fits by Sheth & Tormen (1999); Jenkins et al. (2001); Reed et al. (2003); Tinker et al. (2008), which have been extensively tested over a wide range of stellar mass and redshift (see Fig. 1.2). The HMF, predicting the abundance of dark matter haloes, has been fundamental to evaluate the hierarchical nature of the ΛCDM model, in which small-scale bounded halos formed first and then merged into more massive ones (see the redshift evolution in Fig. 1.2). Certainly, observations suggest that high-redshift galaxies are preferentially low-mass systems (e.g., Grazian et al., 2015), while massive clusters of galaxies, that reside in the largest gravitationally bound halos, are mainly found in the local Universe (e.g., Kochanek et al., 2003).

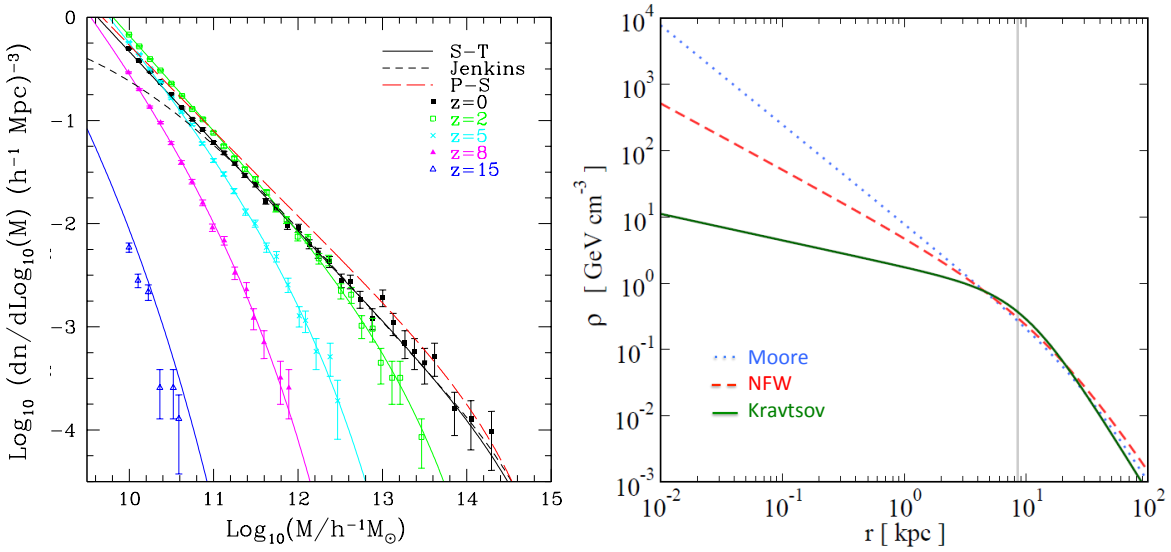

Figure 1.2: *Left panel:* The halo mass function derived from high-resolution ΛCDM numerical simulations at $z = 0$, 2, 5, 8, & 15 (Reed et al., 2003). Solid curves show the Sheth & Tormen HMF at different redshifts, while short and long dashed curves correspond to the Jenkins and Press & Schechter HMF at $z = 0$, respectively. *Right panel:* Dark matter density as a function of the distance to the Galactic Center inferred from a Moore, NFW and Kravtsov profile. The vertical line shows the orbital radius of the solar system (IceCube Collaboration et al., 2011).

If the internal structure of dark matter halos is considered as collapsing concentric shells of different densities, the mass distribution can be described by its density profile $\rho(r)$. Using numerical simulations, Navarro et al. (1997) found that dark matter halos of different mass have a near-universal shape, the so-called Navarro-Frenk-White (NFW) profile:

$$\rho(r) = \frac{\rho_{\rm crit}\delta_{\rm char}}{(r/r_{\rm s})(1 + r/r_{\rm s})^2}, \tag{1.3}$$

where $\delta_{\rm char}$ is the characteristic over-density, $\rho_{\rm crit}$ the critical density of the Universe, and $r_{\rm s}$ the characteristic radius. Alternative dark matter profiles have been proposed (e.g., Merritt et al., 2005, and references therein), some of them, for example, are preferred to better describe the inner-most regions of low-mass halos (e.g., Burkert, 1995). Furthermore, since the inferred distribution of dark matter appears to deviate from the standard NFW profile in some systems (e.g., Read et al., 2019), it is believed that, in the inner region of the halo, the density of dark matter is highly linked to the processes regulating the growth of galaxies – like mergers, high star formation activity and supernova feedback (e.g., Zhao et al., 2009; Chan et al., 2015).

1.1.3 The origin and growth of galaxies

It is expected that $3 - 4\sigma$ peaks in the gaussian random field of primordial density perturbations lead to halos with $M_h \simeq 10^6 M_\odot$ (where $M_\odot$ is the mass of the Sun) at $z \sim 20 - 30$ (e.g., Tegmark et al., 1997; Bromm et al., 2009). The primordial gas in these "minihalos" condensed to form the first

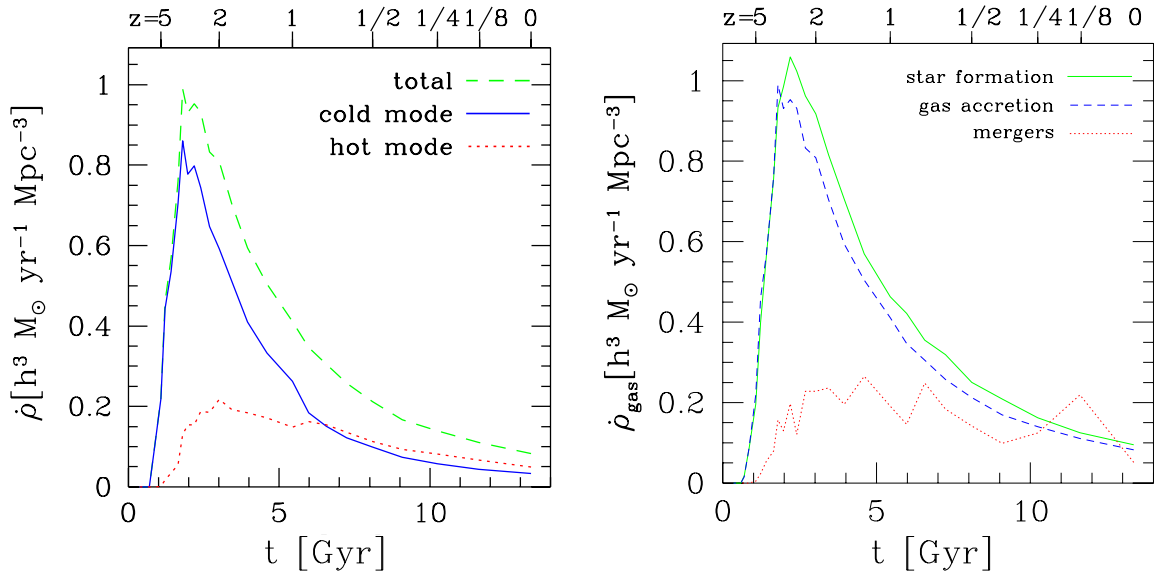

Figure 1.3: *Left panel:* Gas accretion rate as a function of redshift – inferred with numerical simulations by Kereš et al. (2005). The total smooth accretion is given by the dashed green line, while the blue solid (dotted red) line shows the contribution from the cold (hot) mode of gas accretion. *Right panel:* Star formation rate per unit comoving volume (solid green line) as a function of redshift (Kereš et al., 2005). The smooth gas accretion and merger accretion rates are shown by the dashed blue and dotted red lines, respectively. The merger accretion rate includes the total mass gain, i.e. gas and stars.

generation of stars (the so-called "Population III"; Bromm & Larson, 2004), i.e., those that initially contained no elements heavier than helium. Given the shallow potential well of $M_h \simeq 10^6 M_\odot$ halos, stellar winds and supernovae explosions were able to disrupt the gas reservoir and suppress further star formation (e.g., Alvarez et al., 2006; Greif et al., 2007). In contrast, $M_h \simeq 10^8 M_\odot$ halos collapsing by $z \simeq 10$ could retain their gas and sustain self-regulated star formation in a multiphase medium, leading to the formation of the first galaxies (e.g., Wise & Abel, 2008; Greif et al., 2010; Bromm & Yoshida, 2011). Their environment is expected to be already metal-enriched by supernovae explosions of the first stars, which enhanced the gas cooling rate (e.g., Choi & Nagamine, 2009). In addition, accretion-driven turbulence induced the collapse and fragmentation of star-forming gas clouds (e.g., Wise & Abel, 2007; Greif et al., 2008), leading to the formation of the first stellar clusters (Clark et al., 2008). With the emergence of the first radiating sources, bubbles of ionized gas around them percolated through the intergalactic medium (IGM), marking the end of the so-called reionization epoch around $z \sim 6$ (see Zaroubi, 2013, for a review).

Proto-galaxies evolved into more massive –and mature– systems through the accretion of matter into their halos. The accretion of gas, in particular, proceed in two modes (Fig. 1.3; e.g., Kereš et al., 2005, 2009). The first one, the so-called "hot mode", involves quasi-spherical accretion of gas that is shock heated to approximately the halo virial temperature. This hot and virialised gas cools, while losing its pressure support, and settles into a centrifugally supported disk (e.g., Rees & Ostriker, 1977; White & Rees, 1978; Fall & Efstathiou, 1980). The "cold mode", on the other hand, occurs when galaxies acquire cold gas directly from dense cosmological filaments that penetrate deep into

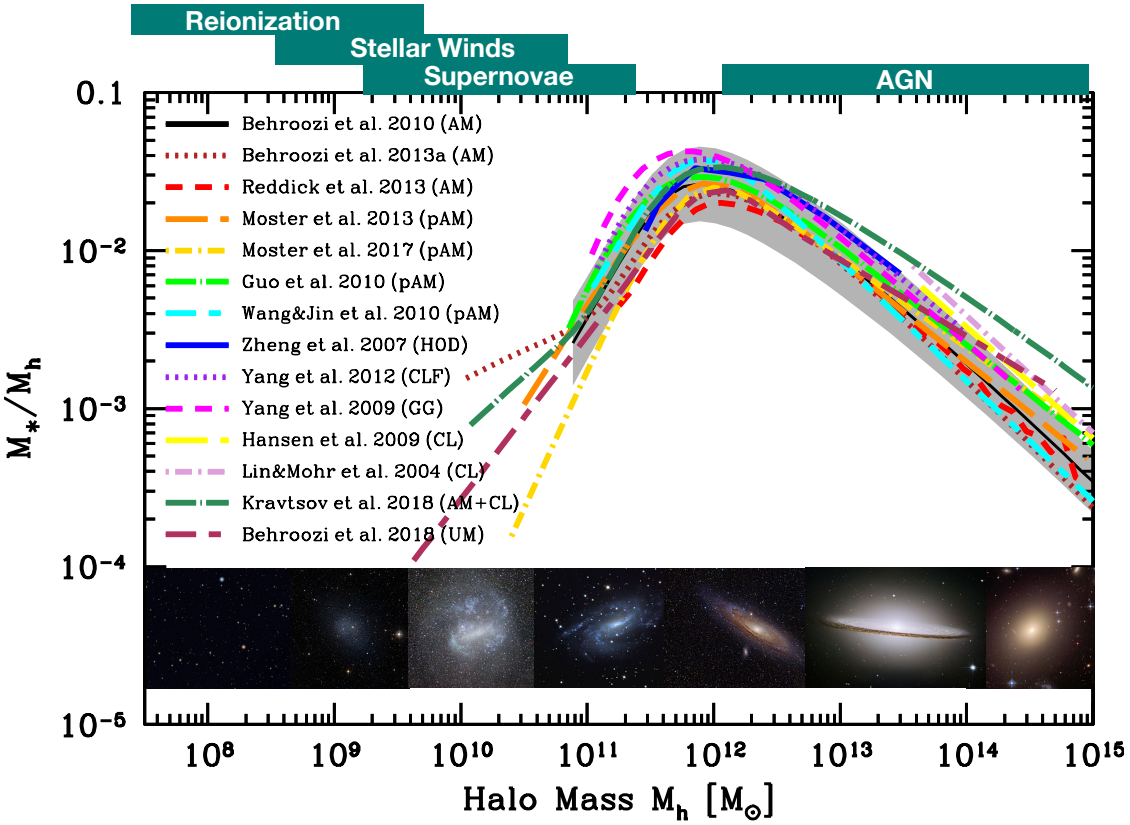

Figure 1.4: The galaxy stellar mass-to-halo mass ratio of central galaxies at $z = 0$, which has been empirically derived and reported by different research groups. The *upper panel* indicates the dominant physical mechanism – at a given halo mass scale – regulating the production of stars by ejecting and/or heating the gas. The *bottom panel* shows example galaxies residing in halos within the specified mass range. Figure adapted from Behroozi et al. (2018) and taken from Wechsler & Tinker (2018).

the halo, favoring the formation and growth of a disk (e.g., Shlosman, 2013, and references therein). While low mass halos with $M_h \lesssim 10^{11.4} M_\odot$ tend to accrete gas via the "cold mode", more massive systems are fed through the "hot mode" of gas accretion. As a corollary, the gas accretion rate in the hot mode becomes significant only $z \lesssim 1$ (see Fig. 1.3), rendering cold gas flows the dominant accretion mechanism in high-redshift galaxies ($z > 1$; e.g., Kereš et al., 2005).

The gas accretion processes, and the subsequent growth of galaxies, are influenced by stellar feedback and/or AGN (see Fabian, 2011; Erb, 2015, for a review). In massive halos ($M_h \gtrsim 10^{12}\, M_\odot$), AGN feedback could prevent radiative cooling –and hence gas accretion– by heating the surrounding medium (e.g., Croton et al., 2006). In low mass galaxies, stellar-driven winds and supernovae explosions eject and might prevent further accretion of star forming gas (e.g., Hopkins et al., 2012). While these two feedback mechanisms preferentially limit the production of stars in galaxies at the low- and high-mass ends, at $z \sim 0$ the maximum star formation efficiency (SFE) occurs in galaxies with $M_h \sim 10^{12} M_\odot$ halos (see Fig. 1.4; e.g., Behroozi et al., 2018; Wechsler & Tinker, 2018).

In addition to smooth gas accretion, galaxies can grow trough mergers. Yet, the fraction of mass assembled by this mechanism is relatively small (e.g., Kereš et al., 2005; L´Huillier et al., 2012; Romano-Díaz et al., 2014). Galaxy mergers do play a major role on the structure and star formation activity of galaxies. The origin and growth of bulges, for example, might be linked to the disruption and violent relaxation of the stellar component during galaxy mergers, as well as merger–induced star formation in the center of galaxies (e.g., Cox et al., 2008; Zavala et al., 2012; Brooks & Christensen, 2016, and references therein).

In summary, mainly from numerical simulations, and observations in the local Universe, it appears that smooth gas accretion, mergers, and feedback are the dominant processes regulating the production of stars and growth of galaxies over cosmic time. Numerical simulations, in particular, suggest that the occurrence and impact of these mechanisms seem to be a strong function of the galaxy mass and redshift. To verify these predictions, we still require observational probes of representative samples of galaxies at intermediate and high redshifts. Collecting and interpreting such empirical evidence is the focus of this Ph.D. dissertation, allowing us to better trace the physical mechanisms that regulate the production of stars in distant galaxies and, therefore, to constrain the formation path of our galaxy and other systems in the local Universe.

1.2 Detection and characterization of distant galaxies

In this section, we describe how large multi-wavelength surveys enable the identification of extensive samples of galaxies at intermediate (out to $z \sim 3$) and high redshifts ($z \gtrsim 3$), as well as the observational techniques employed to infer their fundamental properties from this multi-wavelength dataset. We then describe how such samples of galaxies can be used to build a coherent picture on galaxy evolution across cosmic time.

1.2.1 Deep extragalactic surveys: assembling large samples of galaxies

By mapping large regions of the sky, extragalactic surveys provide a homogeneous census of galaxies across representative volumes of the Universe at different cosmic epochs (see Napolitano et al., 2016, for a review). Deep sky surveys can lead to large and representative samples of galaxies suitable for robust statistical analysis, allowing systematic studies of –for example– the large scale structure in the Universe, the evolution and growth of super-massive black holes (SMBHs), and the formation and evolution of galaxies over cosmic time (e.g., Lutz, 2014). The mapped area and depth of the survey strongly depend on the scientific research goal; there is a compromise in which, for a given observing time, the achieved depth is inversely proportional to the surveyed region of the sky. For instance, while ‘all-sky” surveys are appropriate to reveal large samples of galaxies mostly at low redshift (like the Sloan Digital Sky Survey (SDSS); e.g., Blanton et al., 2017), the deepest extragalactic surveys enable the study of the highest-redshift galaxies within limited areas of the sky (as the Hubble Ultra Deep Field (HUDF) with an area of $2.4 \times 2.4\,\mathrm{arcmin}^2$; Beckwith et al., 2006).

The need for extragalactic surveys that map sufficiently large areas of the sky while probing a wide redshift range has motivated the Cosmic Evolution Survey (COSMOS). This has produced

some of the deepest observations ever taken over a 2 square degree region, enabling the study of the coupled evolution of large-scale structure, galaxies, star formation, and AGNs out to $z \sim 6$ (Scoville et al., 2007). The preferential equatorial location of the COSMOS field ensures visibility by all astronomical facilities, facilitating extensive ground- and space-based observations that span the "entire" electromagnetic spectrum (see Fig. 1.5): X-ray (Civano et al., 2016), ultraviolet (Zamojski et al., 2007), optical/near-infrared (e.g., Capak et al., 2007; McCracken et al., 2012), mid-infrared (e.g., Steinhardt et al., 2014), far-infrared (Lutz et al., 2011; Oliver et al., 2012), millimeter(mm)/sub-millimeter(sub-mm) (e.g., Aretxaga et al., 2011; Miettinen et al., 2015; Magnelli[†] et al., 2019), and radio (e.g., Smolčić et al., 2017a). This multi-wavelength approach, combined with the large co-moving volume traced by COSMOS, has uncovered the Spectral Energy Distribution (SED) of more than half a million galaxies over $0 \lesssim z < 5$ (Laigle et al., 2016). As demonstrated in this Ph.D. dissertation, such an extensive dataset is paramount to investigate the complex star formation processes that leave observational signatures across the whole SED of galaxies (see Fig. 1.5 for an overview). COSMOS is, therefore, adequate to systematically explore the mechanism driving star formation in galaxies throughout cosmic time – the key goal of this Ph.D. thesis.

1.2.2 Determining the properties of distant galaxies

The plethora of multi-wavelength information from surveys like COSMOS is essential to infer and characterize the properties of galaxies over a wide redshift range. Here, we describe the methods used to derive some of the most important ones: redshift, stellar mass, star formation rate (SFR), and size.

Redshift and stellar mass

Measuring the distance of galaxies is the first step to determine their intrinsic properties. Robust redshift estimates can be derived through spectroscopic observations that target bright emission lines (e.g., Lilly et al., 2007; van der Wel et al., 2016; Casey et al., 2017). Unfortunately, this approach is excessively time-consuming when determining the redshift of large samples of galaxies – as that unveiled by the deep extragalactic COSMOS survey. In this case, broadband photometric measurements that sparsely sample the SED of galaxies (Fig. 1.5) are preferred. The underlying idea is to fit the observed SED with spectral templates of galaxies, and different dust extinction curves, while leaving the redshift as a free parameter. Then, the best "photometric redshift" solution is inferred via a maximum-likelihood analysis (e.g., Ilbert et al., 2013; Laigle et al., 2016).

Once the redshift of a galaxy is constrained, the stellar mass can be measured via broadband photometry (or spectroscopy) in the ultraviolet (UV)/optical/near-infrared (IR) regimes (e.g., Shapley et al., 2005; Borch et al., 2006; Banerji et al., 2013). To this end, a model galaxy spectrum is constructed by combining synthetic stellar spectra weighted by an assumed initial mass function (IMF) and star formation history (SFH). A model for dust attenuation and emission as well as a range of metallicity values are considered. Then, the parameters that best fit the observed SED are associated with the galaxy of interest. For a fixed IMF, the SED-derived stellar mass is found to be –in general– accurate at the ~0.3 dex level (Conroy, 2013, and references therein).

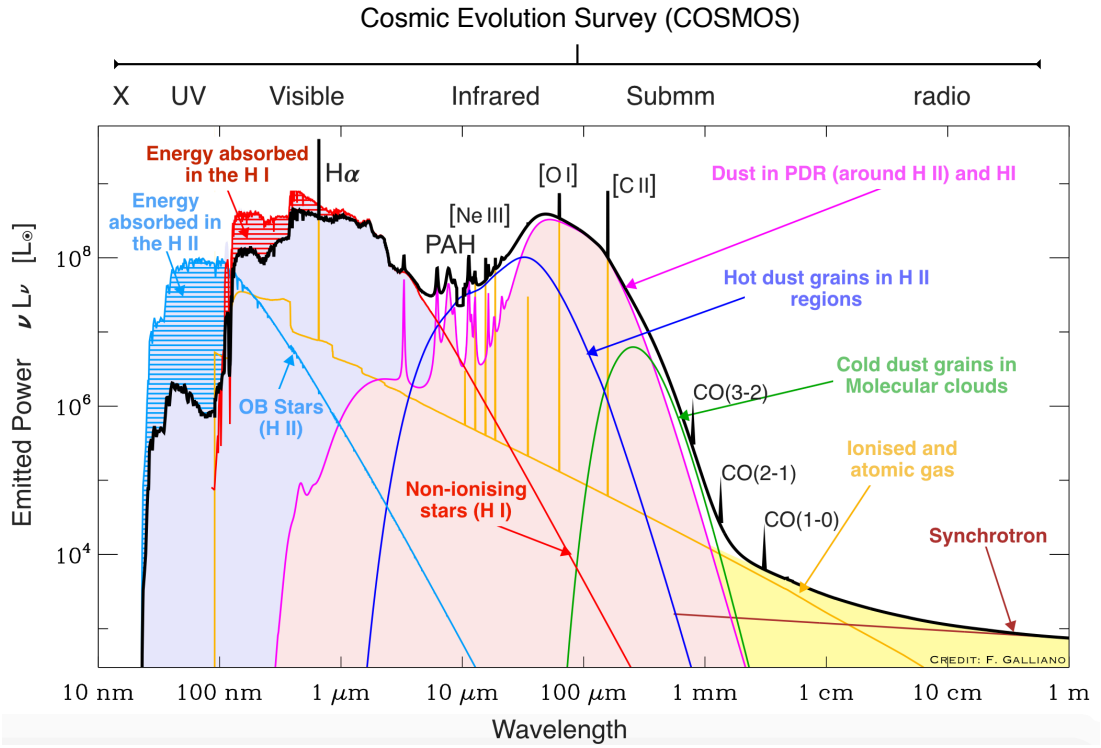

Figure 1.5: Spectral energy distribution of a typical starburst galaxy. The extensive multi-wavelength coverage of COSMOS enables the characterization of the complex star formation processes in galaxies. Observations in the sub-mm/mm regime can trace the cold phase of the interstellar medium where new stars are formed, including those massive/short-lived OB stars emitting strong ultraviolet radiation. Such stars thus ionize the surrounding gas and create an HII region, which emits, for instance, Hα line and free-free radio emission. Dust grains in the HII region, and farther away in the photodissociation region (PDR), can be heated by ultraviolet photons; subsequently, dust grains cool via radiation in the infrared regime. Ultimately, supernovae explosions from those massive and young OB stars lead to synchrotron emission at radio frequencies. Figure adapted from Galliano et al. (2008).

Star formation rate

A key property to probe the evolution and growth of galaxies is their SFR. This can be inferred, for example, from UV light that trace continuum emission of short-lived massive stars, and thermal infrared emission arising from dust grains heated by such young stars (Fig. 1.5; e.g., Kennicutt, 1998a; Kennicutt & Evans, 2011; Fudamoto† et al., 2019). Stellar evolutionary synthesis models, like `Starburst99` (Leitherer et al., 1999), have been used to calibrate the UV and IR luminosities as SFR indicators. This is done by convolving synthetic UV spectra with transmission curves of UV photometric filters typically centered at ~1500Å (far-UV) and ~2300Å (near-UV). The conversion from the IR luminosity (integrated over 8-1000 μm) to SFR relies on the assumption that the Balmer continuum (i.e. 912 Å $< \lambda <$ 3646 Å) is absorbed and re-radiated by dust (e.g., Murphy et al., 2011). In this approximation, the total IR luminosity would correspond to the bolometric luminosity of a completely dust-enshrouded stellar population. Since dust grains might not absorb all the stellar

emission, IR-based SFR estimates should be combined with those derived from the UV and vice-versa[2]. For instance, energy-balance SED fitting codes, like `Magphys` (Da Cunha et al., 2008) and `CIGALE` (Boquien et al., 2019), combine UV/optical and IR emission templates to account for the conservation of energy between the stellar light absorbed by dust and its re-distribution in the IR regime. Hence, by simultaneously fitting the UV-to-IR SED (see Fig. 1.5) it is possible to derive an integrated measure of the SFR, which trace both dust obscured (UV/optical) and unobscured (IR) star formation.

In addition to UV and IR emission, thermal and non-thermal radio continuum flux of galaxies traces star formation (see Fig. 1.5; e.g., Condon, 1992). Supernovae remnants, arising from young stellar populations, accelerate cosmic ray electrons and hence produce non-thermal synchrotron emission (e.g., Garn et al., 2009; Schober et al., 2017). Free-free (thermal Bremsstrahlung) emission originates from ionized gas surrounding young stars (e.g., Murphy et al., 2012). Both types of emission are characterized by a power law spectrum $S_\nu \propto \nu^\alpha$ (Fig. 1.5), where S_ν is the flux density at frequency ν and α is the spectral index with $\alpha \simeq -0.8$ and -0.1 for synchrotron and free-free emission, respectively. The radio SED of SFGs is, therefore, composed by the superposition of two power laws, where that for synchrotron emission dominates over $1 \lesssim \nu \lesssim 30$ (see Fig. 1.5).

A calibration of the radio continuum emission as a SFR indicator has been done through the tight correlation between non-thermal radio flux (at 1.4 GHz) and far-infrared (FIR) emission of galaxies (e.g., Helou et al., 1985; Magnelli et al., 2015; Delhaize et al., 2017), which allows one to infer the infrared luminosity (and hence dust-obscured SFR) from monochromatic radio luminosities (e.g., Karim et al., 2011). This has motivated the development of deep, large scale radio surveys at ~GHz frequencies in COSMOS, such as the Very Large Array (VLA)-COSMOS Large Project at 3 GHz that uncovered more than 10,000 galaxies over the redshift range $0 \lesssim z \lesssim 6$ (Smolčić et al., 2017a,b).

Size

Another fundamental property of galaxies is their size, as it encodes key information on the growth of galaxies over cosmic time (e.g., Furlong et al., 2017). Measuring and contrasting the structure of galaxies at different wavelengths can also provide insights into the co-evolution of the distinct galaxy's components (e.g., gas, stars, and dust; Bekki, 2013). The size of galaxies is usually parametrized with the so-called effective radius, R_e, defined as the radius enclosing half of the light within the galaxy. To derive R_e the surface brightness distribution $\Sigma(R)$ is modeled with Sérsic (1963) profiles;

$$\Sigma(R) = \Sigma(R_\mathrm{e})\ \exp\left(-b\, R/R_\mathrm{e}^{1/n} - 1\right), \tag{1.4}$$

where $\Sigma(R_\mathrm{e})$ is the central intensity, b a constant determined such that R_e contains half of the total intensity and n the Sersic index that quantifies the concentration of light. The stellar light distribution of galaxies, and their evolution with redshift, is relatively well characterized (e.g., van der Wel et al., 2014; Shibuya et al., 2015; Allen et al., 2017); with $n = 4$ (de Vaucouleurs profile) for elliptical and starburst galaxies, and $n = 1$ (exponential profile) for star-forming disks (e.g., Wuyts et al., 2011). Nevertheless, the star-forming extend of galaxies remains unconstrained. This open question is one of the main subjects of this Ph.D. thesis.

[2] We refer the reader to Table 1 in Kennicutt & Evans (2011) that presents relations to estimate the SFR from UV and IR emission, as well as other indicators of star formation.

1.2.3 The quest for the most distant ($z \gtrsim 3$) galaxies in the Universe

As the redshift of galaxies increases, their optical light emission –essential to derive photometric redshifts– is systematically diminished and redshifted to the near-IR regime, hindering the redshift determination of galaxies at early cosmic epochs ($z \gtrsim 3$). Therefore, dedicated methods are needed to better identify the most distant galaxies within the extensive multi-wavelength dataset provided by the COSMOS survey, or even deeper surveys like HUDF. One of the main techniques relies on the identification of the strong drop at $\lambda_{\rm rest} = 912$Å ("Lyman break") in the ultraviolet spectrum of young SFGs, known as Lyman break galaxies (LBGs). The Lyman break is a result of the hydrogen ionization edge in stellar photospheres and the photoelectric absorption by the abundant nuclear (HI) interstellar medium (see Fig. 1.5; e.g., Giavalisco, 2002, and references therein). For $z \gtrsim 3$ galaxies, the intervening neutral hydrogen in the IGM further dims the UV continuum between 912Å and 1216Å (e.g., Madau, 1995), providing a distinctive signature to identify high-redshift galaxies through observations in the optical/near-IR regime (e.g., Finkelstein, 2016). Nevertheless, the LBGs selection method overlooks dust-obscured galaxies that exhibit faint UV emission.

Retrieving the population of dust-obscured SFGs at high redshifts can be done through observations in the sub-mm and FIR regime (Fig. 1.5), which trace thermal emission from interstellar dust grains heated by UV radiation from young massive stars (see Blain et al., 2002; Casey et al., 2014; Fudamoto† et al., 2019, for a review). In particular, since observations at the sub-mm/mm wavelengths probe the frequency range around the peak of the FIR SED of distant galaxies (see Fig. 1.6), the observed flux density remains nearly constant over $1 < z < 10$. This effect (known as the negative K-correction) favors the identification of galaxies over a wide range of lookback time (e.g., Staguhn et al., 2014; Magnelli† et al., 2019). Dedicated observations towards sub-millimeter selected galaxies (SMGs) have revealed that these are massive systems ($M_\star \gtrsim 10^{10} M_\odot$) producing stars at an extremely high rate (SFR $\simeq 10^3 M_\odot\,{\rm yr}^{-1}$; e.g., Casey et al., 2014; Lang† et al., 2019; Gómez-Guijarro† et al., 2018a). The mechanisms that trigger star formation in such extreme galaxy population are still debated. A merger-driven scenario was initially preferred (e.g., Tacconi et al., 2006, 2008; Engel et al., 2010; Narayanan et al., 2010), yet accumulating evidence indicates that SMGs could also be non-interacting massive galaxies (e.g., Hodge et al., 2012; Hayward et al., 2018). Therefore, exploring in detail the properties of non-merging SMGs is a fundamental topic of this Ph.D. dissertation.

Although the SMGs selection technique provide a wealth of $z \gtrsim 3$ galaxy *candidates* (e.g., Magnelli† et al., 2019), dedicated spectroscopic follow-ups –like those presented in this Ph.D. thesis– are needed to confirm their high-redshift nature. Lyman α (Lyα) emission at 1216Å, for example, has become a remarkable tool address this issue (e.g., Leclercq et al., 2017; Wisotzki et al., 2018; Crighton et al., 2019). Bright and broad Lyα line emission could be a result of several mechanisms (e.g., Dijkstra, 2014; Cantalupo, 2017), including the scattering of Lyα photons produced in star-forming HII regions (e.g., Mas-Ribas et al., 2017), photo-ionization by AGN (e.g., Geach et al., 2009), and gravitational cooling radiation[3] (e.g., Fardal et al., 2001). Strong Lyα line emission of $3 \lesssim z \lesssim 7$ galaxies can be observed in the optical regime with ground-based 8-10 m class telescopes like Keck, Subaru and Very Large Telescope (VLT).

[3] Radiation originated from the compression and shock heating of the gas as this is condensed in the center of dark matter potential wells.

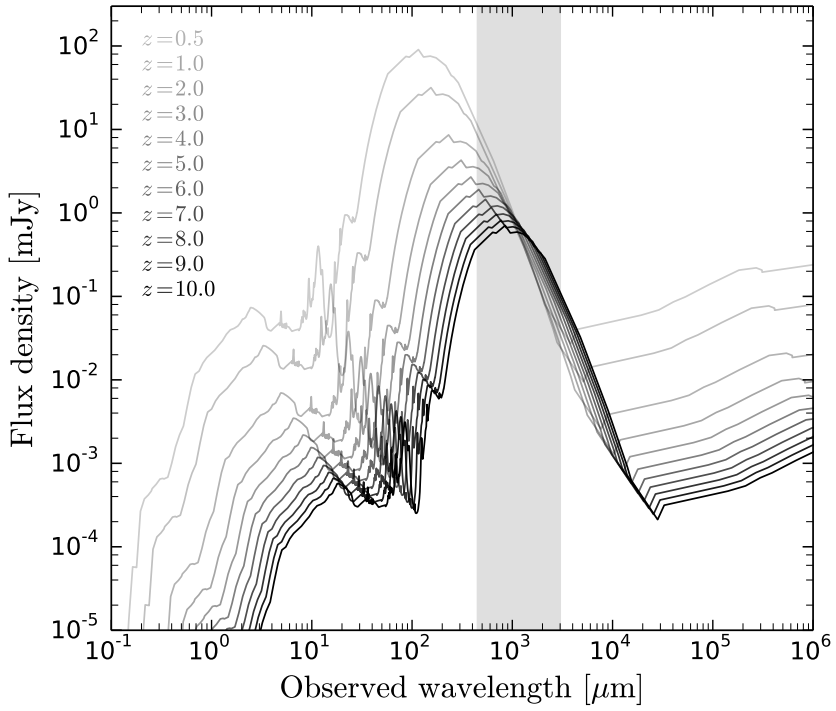

Figure 1.6: The SED of the prototypical starburst galaxy Arp 220 redshifted at z = 0.5, 1.0, 2.0 ... 10.0. Opposite to the optical, IR and radio regime, the observed flux density at sub-mm/mm wavelengths remains nearly constant for $z \gtrsim 1$. The gray shaded region shows the wavelength range (0.45 – 3.0 mm) probed by most sub-mm/mm galaxy surveys.

Alternately, the redshift of distant galaxies can be determined through observations of their molecular gas reservoir, which is substantial in high-redshift systems (e.g., Schinnerer et al., 2016; Jiménez-Andrade† et al., 2018). Carbon monoxide, ^{12}CO, is the second most abundant molecule in galaxies after H_2 (see Carilli & Walter, 2013, for a review). Since ^{12}CO has low excitation requirements (only $\sim$ 5K for the first state), it became the primary tracer of molecular gas. Due to ambient radiation and collisions, this asymmetric molecule is excited and experiences rotational transitions. The emitted photons have a frequency given by $\nu = \hbar J/2\pi I$; where J is the angular momentum quantum number (corresponding to the upper energy level) and I the moment of inertia of the ^{12}CO molecule. The first excited state ($J = 1 \rightarrow 0$) is observed at $\nu_{1\rightarrow0}$ = 115.27 GHz, while the frequency of photons emitted during higher-J transitions are multiples of $\nu_{1\rightarrow0}$ (see Fig. 1.5).

Atomic fine structure lines (FSLs) from the cool interstellar gas can also be detected at FIR/mm wavelengths. The brightest of them is singly ionized carbon, [CII] at 158 μm (Fig. 1.5; e.g., Croxall et al., 2017; Jones et al., 2017), which can be excited by collisions with hydrogen molecules, atoms, and free electrons (e.g., Lagache et al., 2018). Since carbon has an ionization potential (11.3 eV) below the 13.6 eV for hydrogen, [CII] ions can be present in neutral atomic clouds (e.g., Mamon et al., 1997). Consequently, [CII] line emission traces both ionized and neutral gas. Even faint FSLs (like [CI] and [NII]) have been detected in high-redshift galaxies (Carilli & Walter, 2013; Harrington†

et al., 2018, 2019); which is partially due to the advent of large sub-mm/mm interferometer telescopes like the NOrthern Extended Millimeter Array (NOEMA) and the Atacama Large Millimeter Array (ALMA). In this Ph.D. dissertation, in particular, we have used ^{12}CO and [CII] line observations from such observing facilities to derive spectroscopic redshift estimates and probe the conditions for star formation in three $z \sim 4.6$ galaxies, which were initially identified via the SMGs selection technique.

1.3 Towards a consistent picture of galaxy evolution

Thanks to the wealth of observations provided by large scale surveys like COSMOS, and predictions from cosmological simulations, we can quantitatively assess the evolution of galaxies throughout cosmic time. This section is devoted to introducing fundamental galaxy scaling relations on which the modern view on galaxy evolution has been built. In brief, the emerging consensus establishes that the star formation history of the Universe is coupled, to first order, to the cosmic density of cold gas through a "universal", redshift-independent star formation law. As a corollary, galaxies steadily form stars and grow as they accrete gas from the cosmic web until their gas reservoir is depleted and/or occasional mergers drastically enhance their SFE and SFR. AGN- and/or star formation-driven outflows can subsequently suppress the production of stars, leading to the formation of quenched "dead" galaxies.

1.3.1 The cosmic star formation history of the Universe

A fundamental step to characterize the main drivers of galaxy evolution consists in tracing the stellar birthrate of the Universe over cosmic time, which is known as the cosmic SFH. Specifically, this is parametrized through the redshift evolution of the cosmic star formation rate density (SFRD), i.e. SFR per comoving volume. The cosmic SFH can be inferred by determining the luminosity function, $\phi(L, z)$, that describes the number density (per volume) of galaxies of a specific luminosity, L, and redshift. Integrating the luminosity function over the whole range of luminosities leads to the luminosity density, $\rho(z)$. Since the UV and/or FIR luminosity densities account for the energy released during the production of stars, they can be converted into SFRD, $\psi(z)$, using suitable calibrations (Sect. 1.2.2; see Madau & Dickinson, 2014, for a review). Deep surveys have revealed a consistent trend of $\psi(z)$ (e.g., Magnelli et al., 2009, 2011; Cucciati et al., 2012; Gruppioni et al., 2013; Magnelli et al., 2013). A rising phase over $2 \lesssim z \lesssim 8$, likely driven by the increasing number density of halos that are able to host SFGs, followed by a gradual decline to the present day (see Fig. 1.7) that can be explained by a decreasing gas accretion rate onto dark matter halos (e.g., Tacchella et al., 2013). According to Madau & Dickinson (2014, and references therein), the cosmic SFH can be parametrized as:

$$\psi(z) = 0.015 \frac{(1+z)^{2.7}}{1+[(1+z)/2.9]^{5.6}} \; M_{\odot}\,\mathrm{yr}^{-1}\mathrm{Mpc}^{-3}. \tag{1.5}$$

By integrating $\psi(z)$ over redshift we can predict the stellar mass density (SMD) of the Universe at a given redshift ($\rho_{\star}(z)$, see Fig. 1.7). The latter can be independently constrained from observations of the galaxy stellar mass function (Grazian et al., 2015; Davidzon et al., 2017), which provides an alternative approach to explore the cosmic SFH (e.g., Behroozi et al., 2013). The comparison between the observed SFRD and that inferred from the SMD is highly debated (e.g., Yu & Wang, 2016), yet

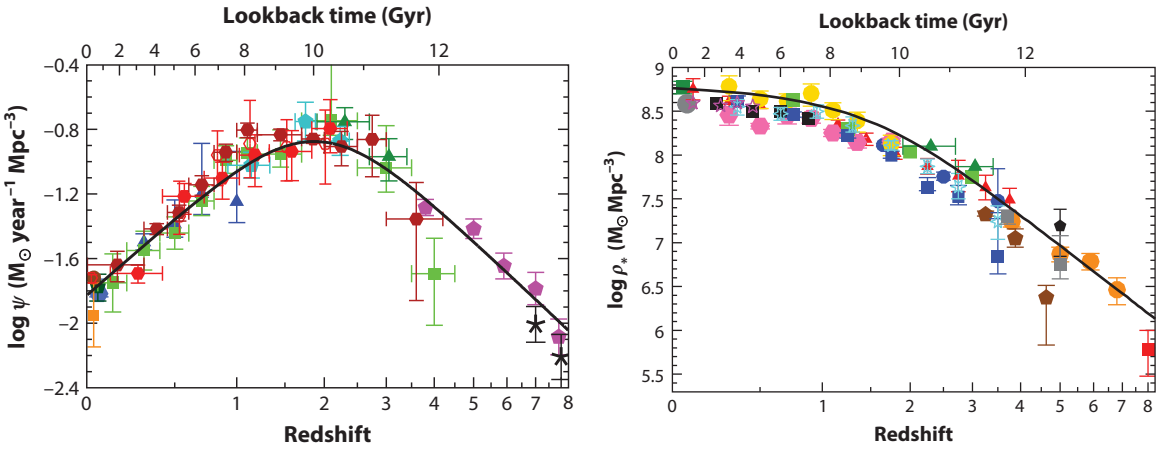

Figure 1.7: *Left panel:* Redshift evolution of the cosmic SFRD inferred from UV (black, magenta, blue and green symbols) and FIR (red and orange symbols) rest-frame measurements (Madau & Dickinson, 2014, and references therein). The solid black curve shows the best-fit SFRD given by Equation 1.5. *Right panel:* Redshift evolution of the stellar mass density (SMD; Madau & Dickinson, 2014). The solid black line shows the SMD obtained by integrating the best-fit SFRD (Equation 1.5).

there seems to be a consensus wherein most (75%) of the stellar mass observed today was built after the SFRD peak at $z \sim 2$ (see Fig. 1.7).

Interestingly, the redshift evolution of the SFRD resembles the accretion history of SMBHs (e.g., Shankar et al., 2009; Delvecchio et al., 2014, see Fig. 1.8). This has been constrained from the luminosity function of AGN (from infrared, optical, and/or X-ray observations) by assuming that the accretion rate onto a SMBH is directly proportional to the bolometric luminosity of the AGN (e.g., Hopkins et al., 2007). This finding strengthens the idea of a coeval growth of SMBHs and their host galaxies (see Kormendy & Ho, 2013, for a review), as also inferred from the correlation between the velocity dispersion of stars in the bulge and the mass of the SMBH (e.g., Gültekin et al., 2009).

Since cold gas constitutes the fuel for star formation (e.g., Carilli & Walter, 2013), determining the redshift evolution of the cosmic gas density, $\rho(H_2)$, is paramount to investigate how the gas reservoir of galaxies regulates the cosmic SFRD. To this end, recent efforts have been made to constrain the ^{12}CO luminosity density (per unit volume) out to $z \sim 7$ (Decarli et al., 2016; Riechers et al., 2019), which is converted into molecular gas mass density via the ^{12}CO→H_2 conversion factor (α_{CO}; e.g., Papadopoulos et al., 2012b). Alternatively, the redshift evolution of the cold gas density has been inferred from dust-based interstellar medium (ISM) mass estimates (Scoville et al., 2017, Magnelli et al. in prep.), ^{12}CO line intensity mapping (Keating et al., 2016), and predictions from semi-analytical (Obreschkow et al., 2009; Lagos et al., 2011; Popping et al., 2014) and empirical (Sargent et al., 2014) models. Despite the large uncertainties of current estimates, they all suggest that $\rho(H_2)$ peaks at $z \sim 2-3$ and decreases at lower/higher redshifts (see Fig. 1.8), following the overall shape of the cosmic SFRD (and accretion history of SMBHs). At all epochs, star formation (and black hole) activity thus appears to be regulated by the availability of molecular gas reservoirs in galaxies.

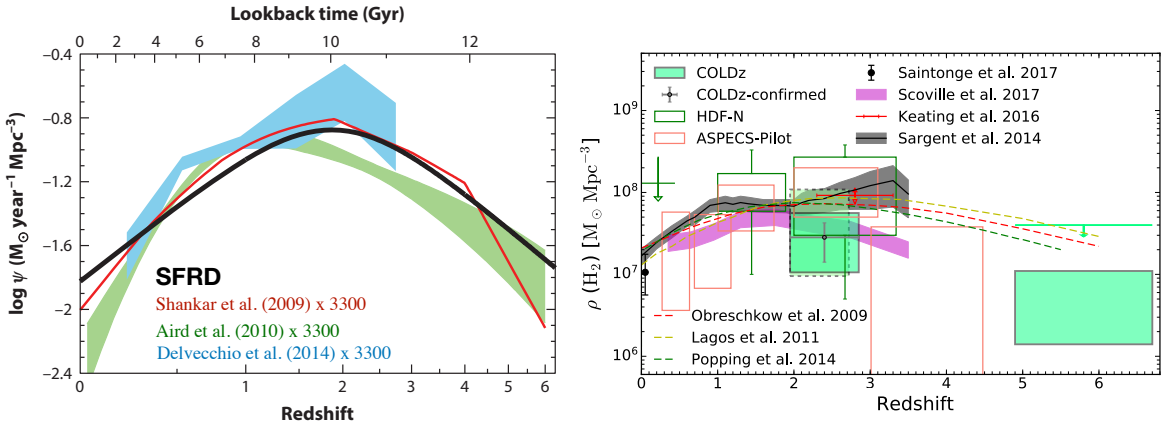

Figure 1.8: *Left panel:* SFRD in comparison with the accretion history of SMBHs (scaled up by a factor of 3300) from X-ray (Shankar et al., 2009; Aird et al., 2010) and infrared (Delvecchio et al., 2014) data. Image adapted from Madau & Dickinson (2014). *Right panel:* Co-moving cosmic mass density of cold molecular gas as a function of redshift derived from ^{12}CO line observations (green/red boxes, Decarli et al., 2016; Riechers et al., 2019), dust continuum (magenta region Scoville et al., 2017), intensity mapping of ^{12}CO line emission (red solid line, Keating et al., 2016), expectations from the $M_{\rm gas}-$SFR relation (grey region, Sargent et al., 2014) and predictions from semi-analytical models (Obreschkow et al., 2009; Lagos et al., 2011; Popping et al., 2014). Image adapted from Riechers et al. (2019).

1.3.2 The global "star formation law" of galaxies

The apparent co-evolution between the $\rho(\mathrm{H_2})$ and SFRD suggests a relatively redshift-independent star formation efficiency of galaxies, which is parametrized by the ratio between their stellar birthrate and gas content. Specifically, since the production of stars is the result of gravitational collapse of molecular gas clouds, it is expected that the SFR volume density, $\rho_{\rm SFR}$, relates to the volume density of cold gas, $\rho_{\rm gas}$, (Schmidt, 1959): $\rho_{\rm SFR} = A\rho_{\rm gas}^{N}$, where N is the power index and A is assumed to be constant. Determining SFR and gas volume densities is not practical for extragalactic systems, consequently, one has to assume a constant disk scale height and measure surface densities. By using this approximation, Kennicutt (1998b) concluded that nearby spiral and starburst galaxies satisfy the relation $\Sigma_{\rm SFR} \propto \Sigma_{\rm gas}^{1.4\pm0.2}$, which is usually referred as the Kennicutt-Schmidt (KS) relation (see Fig. 1.9). This empirical scaling relation appears to be valid out to $z \sim 3$ (e.g., Daddi et al., 2010; Genzel et al., 2010; Freundlich et al., 2013; Sargent et al., 2014; Schinnerer et al., 2016). Above $\Sigma_{\rm gas} \sim 10^2\ M_\odot \mathrm{pc}^{-2}$, star-forming disks and starburst galaxies seem to occupy two distinct regimes of the KS relation (see Fig. 1.9): while the former follows the classical KS relation, the latter forms stars at a rate that is one order of magnitude higher than expected from their gas surface density (e.g., Daddi et al., 2010; Genzel et al., 2010). It thus appears that there are two different regimes of star formation (Sargent et al., 2014). First, a long-lasting mode in which the production of stars in galaxies is mainly regulated by smooth gas accretion from the IGM (e.g., Dekel et al., 2009a; Kereš & Hernquist, 2009). Second, a more efficient mode of star formation driving short-lived starburst episodes as observed in merger-driven Ultra-Luminous Infrared Galaxies (ULIRGs; e.g., Genzel et al., 2001) and most SMGs at $z \sim 2$ (e.g., Engel et al., 2010). The exact physical mechanisms driving the apparent dichotomy of the KS relation, e.g., gas dynamics and fraction of dense gas, are still largely debated (e.g., Bouché et al., 2007; Krumholz & Thompson, 2007; Genzel et al., 2010; Narayanan

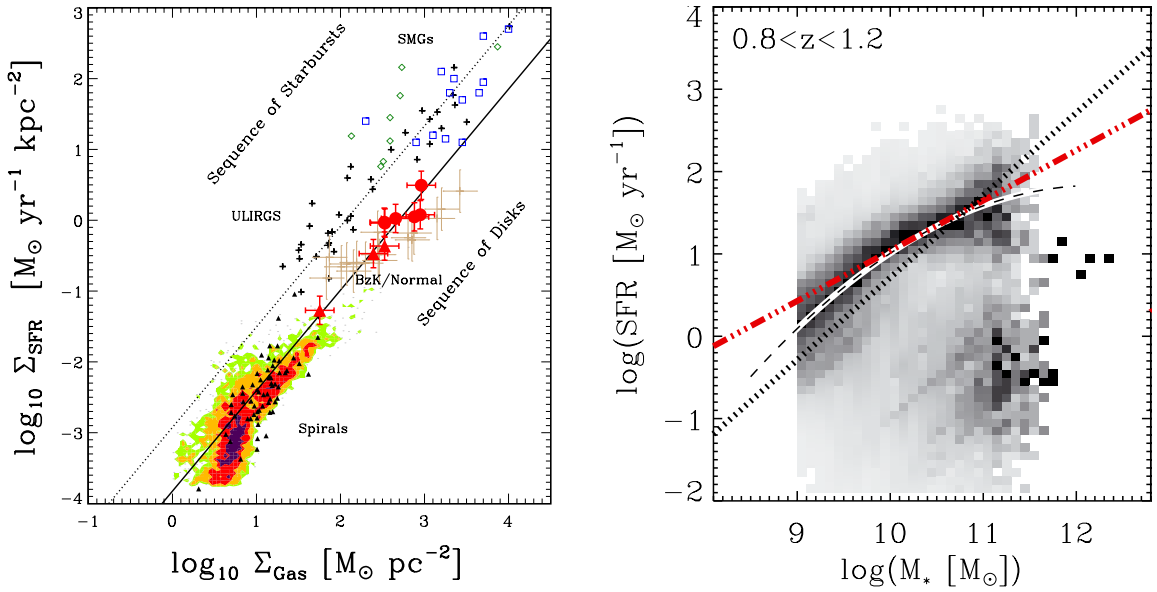

Figure 1.9: *Left panel:* The Kennicutt-Schmidt relation inferred from $z \sim 1.5$ disk galaxies (red/brown symbols), SMGs (empty blue/green squares), local Ultra-Luminous Infrared Galaxies (ULIRGs) (black crosses) and spiral galaxies (black triangles). The colored contours corresponds to local spirals from Bigiel et al. (2008). While the solid line is a fit to local spirals and $z \sim 1.5$ disk galaxies (with $N = 1.42$), the dashed line illustrate the same relation but shifted up by 0.9 dex to fit local ULIRGs and $z \sim 2$ SMGs. Image adapted from Daddi et al. (2010). *Right panel:* Distribution of SFGs, over the redshift range $0.8 < z < 1.2$, in the SFR-$M_\star$ plane Magnelli et al. (2015). The darkest colour indicates the highest number density of sources per stellar mass bin. The lines show the Main Sequence (MS) of SFGs reported by Magnelli et al. (2014, dashed line), Elbaz et al. (2011, dotted line) and Rodighiero et al. (2010, red line).

et al., 2012). It is also unclear whether this dichotomy remains out to the epoch of massive galaxy assembly ($z > 3$). Determining the mechanisms at the origin of this dichotomy, and whether this remains out to the highest redshifts, is thus one fundamental topic addressed in this Ph.D. thesis.

1.3.3 The Main Sequence of SFGs

From a cosmological perspective, the synchronous redshift evolution of $\rho(H_2)$ and SFRD (Sect. 1.3.1) already indicates that the secular mode of star formation, and not the starbursting one, dominates the cosmic stellar birthrate of the Universe. This appears to be verified by the fact that most SFGs, of a given stellar mass and redshift, form stars at a rate that varies within only a factor 2. Such SFGs define a tight correlation in the SFR–$M_\star$ plane known as the MS of SFGs (see Fig. 1.9; e.g., Speagle et al., 2014), whose normalization[4] approximately follows the redshift evolution of the gas fraction ($\mu_{gas} = M_{gas}/M_\star$) in galaxies (see Fig. 1.10; e.g., Schinnerer et al., 2016; Tacconi et al., 2018). Therefore, during the MS phase, the stellar birthrate seems to be coupled to the cosmological gas accretion through an apparent redshift-independent KS relation of normal SFGs (e.g., Sargent et al., 2014; Speagle et al., 2014), as opposed to the starburst KS law mentioned in the previous section.

[4] Equivalent to the specific star formation rate (SSFR) of galaxies on the MS ($SSFR_{MS} \equiv SFR_{MS}/M_\star$)

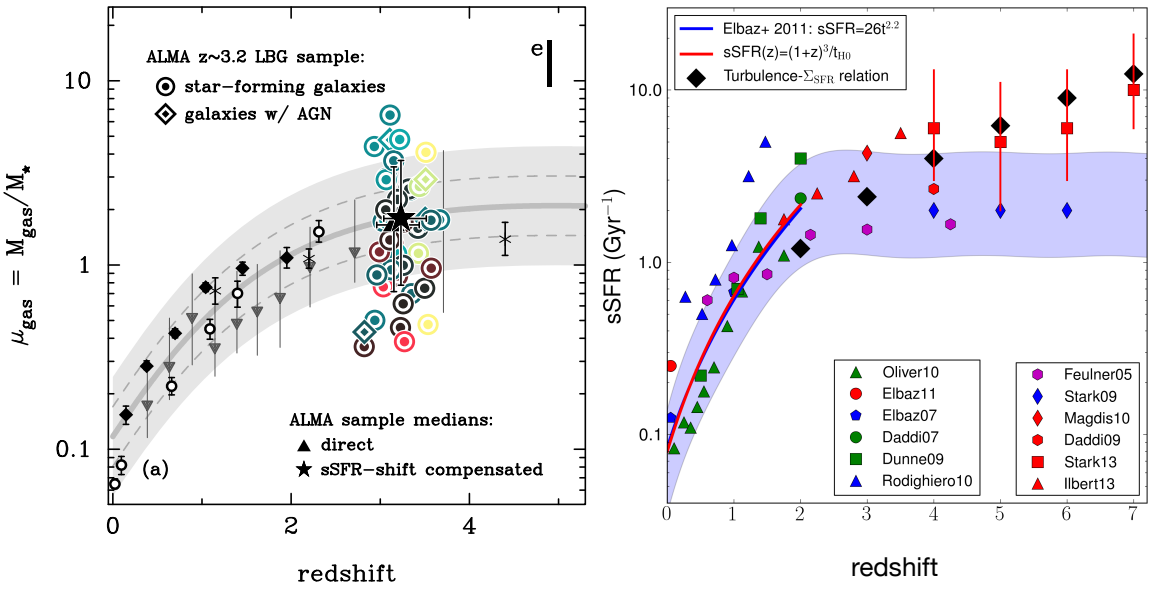

Figure 1.10: *Left panel:* Redshift evolution of the gas fraction of SFGs (Schinnerer et al., 2016). The solid gray line shows the prediction from a redshift-independent star formation law (calibrated for $z < 2.5$ MS galaxies) relating SFR and $M_{\rm gas}$ (Sargent et al., 2014). The dashed gray lines (shaded region) illustrates the gas fraction of galaxies lying 1σ (2σ) above or below the MS. The data points represents measurements of gas fraction derived from ^{12}CO line and dust continuum measurements. The large symbols correspond to $z \sim 3$ LBGs, where the redder (greener) colors indicate objects below (above) the MS. *Right panel:* SSFR of galaxies with $\log(M_\star/M_\odot) \sim 10$ as a function of redshift (Lehnert et al., 2015). The blue shaded region shows the scatter (± 0.3 dex) of SSFR measurements collected from the literature. The blue solid line is the best-fit observed relation from (Elbaz et al., 2011) over $0 < z < 2$, while the blue line and black diamonds are theoretical expectations.

As cosmic time increases, the cosmological gas accretion rate declines (Fig. 1.3) and hence the gas reservoirs of MS galaxies are no sufficiently replenished (e.g., Tacchella et al., 2015). Consequently, the SFR gradually decreases over several Gyr as SFGs slowly exhaust their remaining gas (e.g., Schawinski et al., 2014) – consistent with the drop of the SFRD below $z \sim 2$ (Fig. 1.7).

The well constrained parametrization of the MS, out to $z \sim 4-5$ (e.g., Schreiber et al., 2015; Pearson et al., 2018), provides a remarkable framework to identify the population of "normal" SFGs at different cosmic epochs. Since MS galaxies constitute the majority of the SFGs population, and hence dominate the cosmic SFRD, probing their properties has become essential to unveil the primary mechanisms regulating the stellar mass assembly and growth of galaxies across cosmic time. The MS paradigm can also be used to identify galaxies undergoing a more rapid/passive evolution than "normal" SFGs. There is a small fraction ($< 10\%$) of SFGs that exhibit high SSFR and, consequently, lie above the MS (see Fig. 1.9, e.g., Schreiber et al., 2015). Their properties are –in general– consistent with the starburst mode of star formation and seems to follow the second and more active branch of the KS relation (e.g., Daddi et al., 2010; Genzel et al., 2010; Sargent et al., 2014). Despite their enhanced star formation activity, SFGs above the MS modestly contribute to the cosmic SFRD (Rodighiero et al., 2011; Sargent et al., 2012), which is partially due to the short-lived nature of starburst that exhaust their large gas

reservoirs within megayear (Myr) time-scales (e.g., Tacconi et al., 2018). The physical mechanisms driving starbursts , e.g., mergers and/or shocks due to high gas flow rates (e.g., Hayward et al., 2011; Wang et al., 2018), are still debated. Addressing this open question is another subject of this Ph.D. thesis.

Beyond the population of galaxies on and above the MS, there are galaxies harboring low/negligible star formation activity that lie significantly below the MS of SFGs (Fig. 1.9). They are known as red sequence galaxies and have been identified at even $z \sim 4$ (Kubo et al., 2019). A formation scenario, yet to be validated, involves vigorous starburst episodes triggered by gas-rich mergers that are followed by a rapid quenching of star formation (e.g., Toft et al., 2014; Gómez-Guijarro[†] et al., 2018a), possibly via AGN and/or stellar feedback (e.g., McGee et al., 2014; Spilker et al., 2018). Obtaining observational evidence of quenching at high redshift is also part of this Ph.D. thesis work.

1.4 Aims and structure of this thesis

A MS of SFGs and has been widely reported over recent years (e.g., Speagle et al., 2014; Pearson et al., 2018, Sect. 1.3.3). The origin of this correlation, and its evolution with cosmic time, is likely coupled to the accretion history of cold gas onto galaxies through the apparent redshift-independent KS relation (at least up to $z \sim 3$; e.g., Sargent et al., 2014; Schinnerer et al., 2016, Sect. 1.3.2) – which relates the production of stars with the gas content of galaxies (Schmidt, 1959; Kennicutt, 1998b). This paradigm of galaxy evolution still lacks a comprehensive understanding of the mechanisms driving the transition of distant galaxies from the MS to a starburst and/or quenched phase (Fig. 1.11). Therefore, in the present Ph.D. dissertation we focus on two aspects of such an open issue. First, we probe the overall extent of star formation activity in SFGs to identify signatures of the cold gas accretion and merger mode of star formation. We verify if the structure of galaxies on the MS meets expectations for the cold gas accretion mode of star formation; correspondingly, we also explore if the properties of starbursts (i.e., SFGs above the MS) are consistent with a merger-driven scenario. By probing a wide redshift range ($0.35 < z < 2.25$, Chapter 2), we investigate how this dichotomy evolves with cosmic time. We examine, in particular, if this dichotomy remains out to the epoch of massive galaxy assembly ($z \sim 4.5$, Chapter 3) where the existence of a MS of SFGs is tentatively confirmed. Second, we characterize the signatures of large scale galactic outflows at $z \sim 4.5$ and evaluate their impact in quenching bursts of star formation, allowing us to better constrain the evolutionary link between $z \gtrsim 4$ starbursts and quenched galaxies on the red sequence at $z \sim 2$ (Chapter 4). All these relevant aspects of galaxy evolution are addressed through the following experiments (see Fig. 1.11).

- In **Chapter 2**, we use observations from the *Karl G. Jansky* Very Large Array (JVLA) to carry out the first systematic study of the radio continuum size evolution of 3184 SFGs over the redshift range $0.35 < z < 2.25$. We contrast the size distribution of galaxies on and above the MS to trace the signatures of the cold gas accretion and merger mode of star formation. By comparing the size of the stellar (optical/UV) and star-forming (radio continuum) component in galaxies, we also get insights into where star formation preferentially occurs in galaxies over cosmic time – since the peak and the subsequent decline of the cosmic SFRD (Fig. 1.11).
- In **Chapter 3**, we use deep ^{12}CO and [CII] line observations from the JVLA, NOEMA, and ALMA telescopes to investigate the structure and gas content of AzTEC/C159 and AzTEC2: two star-forming disk galaxies at $z \sim 4.6$. This is one of the first observational studies that

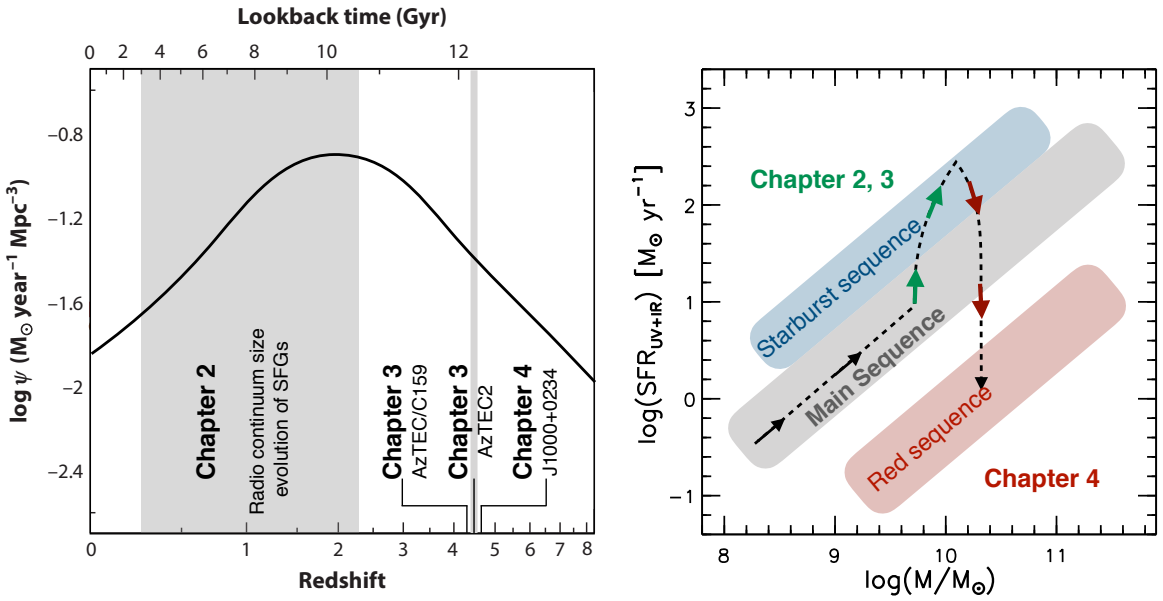

Figure 1.11: *Left panel:* The cosmic epochs of the Universe explored in this PhD thesis. In Chapter 2, we explore the star formation processes of SFGs on and above the MS over the redshift range $0.35 < z < 2.25$, which encompasses the peak and decline of the cosmic SFRD. In Chapters 3 and 4, we study the conditions for galaxy assembly at $z \sim 4.5$. *Right panel:* Evolutionary phases of galaxies probed in this work. In Chapter 2 and 3, we investigate the physical mechanisms that trigger starburst episodes, while in Chapter 4 we study signatures of negative feedback that might quench star formation.

explore the mechanisms of gas fueling and consumption in disk galaxies prior the peak of the cosmic SFRD (i.e., $z > 2$). We discuss the implications of our findings within the context of the cold gas accretion and merger mode of star formation. Specifically, we examine whether the dichotomy between the properties of secular disks (on/close to the MS) and merger-driven starbursts remains during the relatively unexplored $z > 4$ regime.

- In **Chapter 4**, we employ Subaru and Keck optical data to characterize the extended, likely expanding, Lyα halo surrounding J1000+0234−S: a satellite SFG neighboring a massive, dust-enshrouded SMG at $z = 4.5$, J1000+0234−N. We investigate the ability of star formation-driven winds in suppressing the production of stars in low-mass galaxies in the early Universe. We then evaluate the scenario in which "dry merges" at $z > 2$, between massive galaxies and their minor companions like J1000+0234−S, lead to the red sequence of massive quenched galaxies at $z \sim 2$ (Fig. 1.11).

By integrating the results derived from these research projects, in **Chapter 5**, we draw a more coherent and deeper understanding on the processes that regulate star formation –and thus growth of galaxies– throughout cosmic time. In Chapter 5, we also identify future research directions to complement and extend the evolutionary scenario for massive galaxies proposed in this Ph.D. thesis.

CHAPTER 2

Radio continuum size evolution of SFGs over $0.35 < z < 2.25$

To better constrain the physical mechanisms driving star formation, we present the first systematic study of the radio continuum size evolution of star-forming galaxies (SFGs) over the redshift range $0.35 < z < 2.25$. We use the VLA COSMOS 3GHz map (noise rms = $2.3\,\mu$Jy beam^{-1}, $\theta_{\rm beam} = 0.75$ arcsec) to construct a mass-complete sample of 3184 radio-selected SFGs that reside on and above the main sequence (MS) of SFGs. We constrain the overall extent of star formation activity in galaxies by applying a 2D Gaussian model to their radio continuum emission. Extensive Monte Carlo simulations are used to validate the robustness of our measurements and characterize the selection function. We find no clear dependence between the radio size and stellar mass, $M_\star$, of SFGs with $10.5 \lesssim \log(M_\star/M_\odot) \lesssim 11.5$. Our analysis suggests that MS galaxies are preferentially extended, while SFGs above the MS are always compact. The median effective radius of SFGs on (above) the MS of $R_{\rm eff} = 1.5 \pm 0.2$ (1.0 ± 0.2) kpc remains nearly constant with cosmic time; a parametrization of the form $R_{\rm eff} \propto (1+z)^\alpha$ yields a shallow slope of only $\alpha = -0.26 \pm 0.08$ (0.12 ± 0.14) for SFGs on (above) the MS. The size of the stellar component of galaxies is larger than the extent of the radio continuum emission by a factor ~2 (1.3) at $z = 0.5$ (2), indicating star formation is enhanced at small radii. The galactic-averaged star formation rate surface density ($\Sigma_{\rm SFR}$) scales with the distance to the MS, except for a fraction of MS galaxies ($\lesssim 10\%$) that harbor starburst-like $\Sigma_{\rm SFR}$. These "hidden" starbursts might have experienced a compaction phase due to disk instability and/or a merger-driven burst of star formation, which may or may not significantly offset a galaxy from the MS. We thus propose to use $\Sigma_{\rm SFR}$ and distance to the MS in conjunction to better identify the galaxy population undergoing a starbursting phase.

This chapter is a reproduction of the article of the same title that was published in Astronomy & Astrophysics under the reference:

Jiménez-Andrade, E. F., Magnelli, B., Karim, A., et al., 2019, A&A, 625, A114.

2.1 Introduction

Most galaxies follow a tight correlation in the star formation rate (SFR) – stellar mass ($M_\star$) plane known as the main sequence (MS) of star-forming galaxies (SFGs; e.g., Brinchmann et al., 2004; Noeske et al., 2007; Elbaz et al., 2007; Salim et al., 2007; Daddi et al., 2007; Pannella et al., 2009; Magdis et al., 2010; Peng et al., 2010; González et al., 2010; Rodighiero et al., 2011; Karim et al., 2011; Wuyts et al., 2011; Bouwens et al., 2012; Whitaker et al., 2012, 2014; Rodighiero et al., 2014; Pannella et al., 2015; Renzini & Peng, 2015; Schreiber et al., 2015, 2017). This relation holds over $\sim$ 90% of the cosmic history of the Universe (e.g., Stark et al., 2013; González et al., 2014; Steinhardt et al., 2014; Salmon et al., 2015) and has a slope and normalization that increase with redshift, while its dispersion of only 0.3 dex remains nearly constant throughout cosmic time (see Speagle et al., 2014; Pearson et al., 2018, and references therein).

Although most galaxies have an implied SFR that scatters within a factor two around the MS, some do show a significantly higher SFR. Those objects also exhibit a higher gas content, shorter gas depletion times (e.g., Genzel et al., 2015; Schinnerer et al., 2016; Tacconi et al., 2013, 2018), and higher dust temperatures (e.g., Magnelli et al., 2014). Likewise, the stellar-light radial distribution is different in these two galaxy populations; while MS galaxies are closely approximated by exponential disks (e.g., Bremer et al., 2018), those above (and below) it exhibit a higher central mass concentration (e.g., Wuyts et al., 2011). Based on this dichotomy and the parametrization of the MS over cosmic time, a scenario has been proposed to explain the evolutionary path of galaxies along the MS. Since the normalization of the MS, the gas fraction of galaxies, and cosmic molecular gas density decrease from $z \sim 2.5$ to 0 at a similar pace (e.g., Speagle et al., 2014; Decarli et al., 2016; Tacconi et al., 2018), it is thought that MS galaxies evolved through a steady mode of star formation, possibly regulated by the accretion of cool gas from the intergalactic medium (e.g., Dekel et al., 2009a; Kereš et al., 2009; Davé et al., 2010; Hodge et al., 2012; Romano-Díaz et al., 2014, 2017; Feng et al., 2015; Anglés-Alcázar et al., 2017). From theoretical predictions, the scatter of the MS could thus be explained as the result of a fluctuating gas inflow rate that is different in each galaxy (e.g., Tacchella et al., 2016; Mitra et al., 2017). In this context, a galaxy enhances its SFR and moves towards the upper envelope of the MS due to gas compaction. As the gas is depleted, the SFR decreases and the galaxy falls below the MS. As long as a SFG is replenished with fresh gas within a timescale shorter than its depletion time, it will be confined within the MS (Tacchella et al., 2016). On the other hand, the enhanced star formation efficiency of galaxies above the MS has been linked to mergers (e.g., Walter et al., 2009; Narayanan et al., 2010; Hayward et al., 2011; Alaghband-Zadeh et al., 2012; Riechers et al., 2013, 2014) and instability episodes in gas-rich disks (particularly at high redshift; e.g., Davé et al., 2010; Hodge et al., 2012; Wang et al., 2018).

A crucial parameter for verifying these scenarios is the size of a galaxy. Recent studies have explored the structural properties of SFGs by mapping their stellar component (e.g., van der Wel et al., 2014; Shibuya et al., 2015; Mowla et al., 2018). However, the size of the overall star-forming component has been poorly explored. This is partially due to observationally expensive high-resolution infrared (IR)/radio observations, which have been limited to relatively small samples of SFGs (e.g., Rujopakarn et al., 2016; Miettinen et al., 2017a; Murphy et al., 2017; Elbaz et al., 2018). While large and representative samples of SFGs can be obtained from ultraviolet (UV)/optical observations, they are affected by dust extinction, rendering size measurement difficult (e.g., Elbaz et al., 2011;

Nelson et al., 2016a). To better understand the mechanisms that regulate star formation in galaxies we need a statistically significant, mass-complete sample of radio-selected SFGs over cosmic time, and a dust-unbiased measure of the size of the star formation activity in galaxies.

The centimeter wavelength radio emission has been established as a proxy for the massive SFR in galaxies, both locally and at high redshift (e.g., Bell, 2003; Garn et al., 2009). Empirically, this is evidenced by a strong correlation between the radio flux density and the far-infrared (FIR) flux (e.g., Helou et al., 1985; Yun et al., 2001; Murphy et al., 2006a,b; Murphy, 2009; Murphy et al., 2012; Sargent et al., 2010; Magnelli et al., 2015; Delhaize et al., 2017). This can be understood in that the stellar UV radiation is mostly absorbed by dust that re-emits this energy in the FIR. On the other hand, supernova explosions of the same massive stars give rise to relativistic electrons emitting radio synchrotron radiation (Helou & Bicay, 1993). This radio emission is not affected by extinction, and with radio interferometers it can be imaged over wide fields at a resolution much better than is currently possible at FIR or submillimeter wavelengths.

The reliability of synchrotron emission as a star formation tracer has motivated the VLA COSMOS 3GHz imaging survey (Smolčić et al., 2017a). This has reached an unprecedented resolution and sensitivity ($\theta_{\rm beam} = 0.75$ arcsec, noise rms $= 2.3\,\mu$Jy beam^{-1}) over the two square degrees of the COSMOS field, enabling size measurements for a large number of radio sources in the μJy regime (Bondi[†] et al., 2018). Over the redshift range explored here, this survey allows us to sample the rest-frame frequency range $4 \lesssim \nu \lesssim 10$ GHz, which is dominated by the steep-spectrum of synchrotron radiation of SFGs (e.g., Murphy, 2009). In combination with reliable photometric redshifts and stellar mass content measurements accumulated in the COSMOS 2015 catalog (Laigle et al., 2016), we are able to study the radio size evolution over $0.35 < z < 2.25$ of a mass-complete sample of radio-selected SFGs.

Here, we report how the radio continuum size of a SFG relates to its stellar mass, size of its stellar component, and distance to the MS

$$\Delta \log(\mathrm{SSFR})_{\rm MS} = \log[\mathrm{SSFR}_{\rm galaxy}/\mathrm{SSFR}_{\rm MS}(M_\star, z)], \tag{2.1}$$

where SSFR=SFR$/M_\star$ is the specific SFR of a galaxy. In particular, by exploring the relation between the galactic-averaged star formation surface density ($\Sigma_{\rm SFR}$) and $\Delta \log(\mathrm{SSFR})_{\rm MS}$, our aim is to verify whether galaxies harboring intense star formation activity experience a compaction phase, as predicted by cosmological simulations (e.g., Tacchella et al., 2016) and observed in small samples of SFGs (e.g., Rujopakarn et al., 2016; Elbaz et al., 2018).

This paper is structured as follows. In Sect. 2.2 we present the VLA COSMOS 3GHz map and the COSMOS2015 catalog, both used to identify the SFGs studied in this work. The sample selection and the methodology to test the robustness of our measurements are given in Sect. 2.3. In Sect. 2.4, we present the relations of radio size−stellar mass, radio size−$\Delta \log(\mathrm{SSFR})_{\rm MS}$, and $\Sigma_{\rm SFR} - \Delta \log(\mathrm{SSFR})_{\rm MS}$, as well as the redshift evolution of the radio continuum size of SFGs with $10.5 \lesssim \log(M_\star/M_\odot) \lesssim 11.5$. The results are discussed in Sect. 2.5, while a summary is given in Sect. 2.6. Throughout, we assume a cosmology of $h_0 = 0.7$, $\Omega_M = 0.3$, and $\Omega_\Lambda = 0.7$.

2.2 Data

2.2.1 VLA COSMOS 3GHz Large Project

The VLA COSMOS 3 GHz survey (Smolčić et al., 2017a) consists of 384 hr of observations (A array – 324 h, C array – 60h) with the *Karl G. Jansky* Very Large Array. A total of 192 individual pointings (half-power beamwidth=15 arcmin) were performed to achieve a uniform rms over the two square degrees COSMOS field. Data calibration was performed with AIPSLite (Bourke et al., 2014). The imaging was done via the multiscale multifrequency synthesis (MSMF) algorithm in CASA, using a robust parameter of 0.5 to obtain the best possible combination between resolution and sensitivity. Given the large data volume of the observations, joint deconvolution of the 192 pointings was not practical. Therefore, each pointing was imaged individually using a circular restored beam with a full width at half maximum (FWHM) of 0.75 arcsec. The final mosaic was produced using a noise-weighted mean of all the individually imaged pointings, reaching a median rms of 2.3 μJy beam^{-1}.

2.2.2 COSMOS2015 catalog

The COSMOS2015 catalog includes photometric redshifts and stellar masses for more than half a million galaxies over the two square degrees of the COSMOS field (Laigle et al., 2016). This near-IR-selected catalog combines extensive deep photometric information from the YJHKs images of the UltraVISTA (McCracken et al., 2012) DR2 survey, Y-band images from Subaru/Hyper-Suprime-Cam (Miyazaki et al., 2012), and infrared data from the Spitzer Large Area Survey (SPLASH) within the Hyper-Suprime-Cam Spitzer legacy program.

Photometric redshifts were derived with LePhare (Arnouts et al., 2002; Ilbert, O. et al., 2006) using a set of 31 templates of spiral and elliptical galaxies from Polletta et al. (2007), and 12 templates of young blue SFGs using the Bruzual & Charlot (2003) models. Through a comparison with spectroscopic redshift samples in the COSMOS field, Laigle et al. (2016) derived a photometric redshift precision of $\sigma_{\Delta_z}/(1+z_s) = 0.007$ and a small catastrophic failure fraction of $\eta = 0.5\%$ for $z_s < 3$.

Stellar masses were also derived with LePhare using a library of synthetic spectra from the Stellar Population Synthesis model of Bruzual & Charlot (2003). A Chabrier (2003) initial mass function, an exponentially declining and delayed star formation history (SFH) and solar/half-solar metallicities were considered. The stellar masses used here correspond to the median of the inferred probability distribution function. A 90% completeness limit of $10^{8.5}$ (10^{10}) $M_\odot$ was achieved up to $z = 0.35$ (2.25).

2.3 Data analysis

We measure the size and flux density of radio sources directly from the VLA COSMOS 3GHz mosaic, i.e., in the image plane, and further revise those estimates using extensive Monte Carlo simulations. While these sizes and fluxes could also be estimated in the uv-plane, this is impractical due to the large data volume of the VLA COSMOS 3 GHz survey.

2.3.1 Source extraction

The advent of large radio astronomical surveys has stimulated the development of robust source extraction algorithms such as `blobcat` (Hales et al., 2012) and `PyBDSF` (Mohan & Rafferty, 2015). Here, we use `PyBDSF` as it provides parametric information of the source morphology such as the deconvolved major axis FWHM ($\theta_{\rm M}$), that is,

$$\theta_{\rm M} = \left(\left(\theta_{\rm M}^{\rm obs} \right)^2 - \left(\theta_{\rm beam} \right)^2 \right)^{\frac{1}{2}}, \tag{2.2}$$

where $\theta_{\rm beam}$ is the FWHM of the synthesized beam of the VLA COSMOS 3GHz map (0.75 arcsec) and $\theta_{\rm M}^{\rm obs}$ the observed/convolved major axis FWHM.

The `PyBDSF` algorithm characterizes the radio source properties as follows. First, it identifies peaks of emission above a given threshold (`thresh_pix`) that are surrounded by contiguous pixels, i.e., islands, with emission greater than a minimum value (`thresh_isl`). Second, it fits multiple Gaussians to each island depending on the number of the peaks identified within it. Finally, Gaussians are grouped into sources if (a) their centers are separated by a distance less than half of the sum of their FWHMs and (b) all the pixels on the line joining their centers have a value greater than `thresh_isl`. The total flux of the sources is estimated by adding those from the individual Gaussians, while the central position and source size are determined via moment analysis. The error of each fitted parameter is computed using the formulae in Condon (1997).

We run `PyBDSF` over the VLA COSMOS 3 GHz mosaic adopting `thresh_pix`=5σ, `thresh_isl`=3σ, and a minimum number of pixels in an island (`minpix_isl`) of 9 pixels (as in Smolčić et al. (2017a)). By selecting sources within the inner two square degrees of the COSMOS field, where the rms remains homogeneous, we find 10078 sources. Within the same area, there are 10689 sources in the catalog presented by Smolčić et al. (2017a), of which 9223 are also retrieved by `PyBDSF`. In the subsequent analysis, we use these matched sources to enhance the pureness of our radio source catalog.

2.3.2 AGN rejection

To identify galaxies in which the radio continuum emission is associated with an active galactic nucleus (AGN), and not star formation, we rely on the results from Smolčić et al. (2017b). They characterized the host galaxy of radio sources in the VLA COSMOS 3 GHz map by identifying their optical/near-IR/mid-IR counterparts from the i-band selected catalog (optical; Capak et al., 2007), the COSMOS2015 catalog (near-IR; Laigle et al., 2016), and the Spitzer COSMOS (S-COSMOS) Infrared Array Camera (3.6 μm-selected, IRAC ; Sanders et al., 2007). Based on this multiwavelength counterpart association, a sample of AGN and SFGs was assembled.

AGN host galaxies were identified as such, and excluded from our sample, if the following criteria were met:

- the intrinsic [0.5–8] keV X-ray luminosity is greater than $L_X = 10^{42}$ergs^{-1} (e.g., Szokoly et al., 2004);

- the flux throughout the four IRAC bands (3.6, 4.5, 5.8, and 8) displays a monotonic rise and follows the criterion proposed by Donley et al. (2012);
- an AGN component significantly improves the fitting of their optical to millimeter spectral energy distribution (SED, as in Da Cunha et al., 2008; Berta et al., 2013; Delvecchio et al., 2014; Delvecchio et al., 2017);
- $M_{NUV} - M_r$, i.e., rest-frame near-ultraviolet (NUV) minus $r+$ band, is greater than 3.5 (Ilbert et al., 2010);
- the observed radio emission $L_{1.4\,\mathrm{GHz}}$ exceeds that expected from the host galaxy $\mathrm{SFR_{IR}}$ (estimated via IR SED fitting, Delvecchio et al., 2017).

Excluding AGN hosts through all these criteria yields a highly clean sample of SFGs. Within the redshift range probed in this work ($0.35 < z < 2.25$), we find that 4216 galaxies match with our catalog of 9223 radio sources and have available stellar mass estimates in the COSMOS2015 catalog. While most of them (3248, i.e., 77%) are classified as SFGs, 968 galaxies (23%) exhibit one or more of the above-mentioned signatures of AGN activity. Since comparing the radio size evolution of AGN and SFGs is beyond the scope of this work, we refer the reader to Bondi[†] et al. (2018) who presented a similar analysis using the VLA COSMOS 3GHz map and following the same AGN-SFGs classification scheme used here.

We note that out of the 3248 radio-selected SFGs, 64 (2%) of them are fitted with multiple Gaussians by `PyBDSF`, suggesting a more complex and/or extended morphology. Since modeling such systems in our Monte Carlo simulations (Sect. 2.3.3) is challenging, we exclude them from the analysis. We verified, however, that none of the relations/results reported thereafter are affected, within the uncertainty, by the inclusion of these multicomponent sources. Our final sample, therefore, comprises 3184 radio-selected SFGs over the redshift range $0.35 < z < 2.25$, in which a mass-complete sample of $\log(M_\star/M_\odot) \gtrsim 10.5$ SFGs can be assembled (Sect. 2.3.5).

2.3.3 Accuracies and limitations of our size and flux density measurements

In this section, we describe the Monte Carlo (MC) simulations used to characterize the biases associated with size and flux determination of SFGs in the sample. This approach is based on the injection of mock sources, following a realistic flux and size distribution, into noise maps that accurately represent the original dataset (e.g., Casey et al., 2014, Sect. 3.2). After retrieving these sources from the maps with `PyBDSF`, we compare the input and output properties and hence address these particular questions: (a) what are the minimum/maximum source sizes we can detect in the VLA COSMOS 3GHz mosaic at a given flux density? and (b) how reliable are our measurements for a given intrinsic flux density and FWHM?

These MC simulations require a mock sample that follows the intrinsic, yet unknown, flux density (S_{int}) and angular size (θ_{M}) distributions of SFGs. For this purpose, we use previous constraints on the μJy radio source population as presented in Smolčić et al. (2017a). First, we approximate the observed flux density distribution of this mock sample with a single power-law model ($N \propto S_{\mathrm{int}}^{-0.8}$). Second, we assume that their angular size is linked to their total flux density (Windhorst et al., 1990; Richards, 2000) as $\theta_{\mathrm{median}}\,[\mathrm{arcsec}] = 1.8 S_{\mathrm{int}}^{0.6}\,[\mathrm{mJy}]$ (Bondi et al., 2003; Smolčić et al., 2017a).

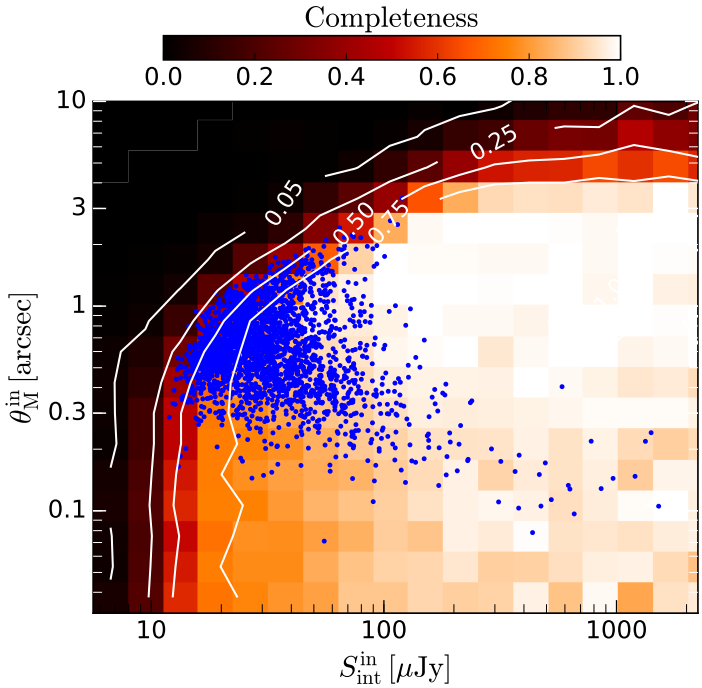

Figure 2.1: Completeness in the $\theta_{\rm M}^{\rm in}$ vs $S_{\rm int}^{\rm in}$ plane as inferred from extensive MC simulations. The completeness given by the color scale represents the fraction of sources recovered by PyBDSF (resolved and unresolved) over the original number of mock sources. The blue points show the position of resolved SFGs in the VLA COSMOS 3GHz map studied in this work. White contours represent a completeness levels of 5, 25, 50 and 75%.

The input sample comprises $\sim 7 \times 10^5$ sources modeled with a single Gaussian component. We explore the parameter space where $\theta_{\rm M}^{\rm in}$ ranges from $0.03-12$ arcsec (with ellipticity $e = 0.25, 0.5, 0.75, 1$ and random position angle) and 10^{-5} Jy $< S_{\rm int} < 10^{-1.5}$ Jy, which is the observed range of retrieved VLA-COSMOS 3GHz galaxies (see Fig. 2.1). These mock galaxies were convolved with the synthesized beam and randomly injected into the mosaic in purely noise dominated regions, i.e., those areas where no original source is found within 36×36 arcsec^2. They were subsequently retrieved with PyBDSF using the same parameters described in Sect. 2.3.1 and cross-matched with the input mock catalog (within a circle of 1 arcsec radius). The ratio of the number of successfully retrieved mock sources to the original mock sources injected in the map, in each [$S_{\rm int}^{\rm in}$, $\theta_{\rm M}^{\rm in}$] bin, represents the completeness (see Fig. 2.1)

Selection function, maximum recovered size

To constrain the maximum detectable size of a galaxy as a function of redshift, stellar mass, and $\Delta \log(\mathrm{SSFR})_{\rm MS}$, we explore the angular size of mock sources that were resolved by PyBDSF. The completeness levels in the $\theta_{\rm M}^{\rm in}$ versus $S_{\rm int}^{\rm in}$ plane (Fig. 2.1) reveal that the maximum recovered deconvolved FWHM ($\theta_{\rm M}^{\rm max}$), for sources within 10^{-5} Jy $< S_{\rm int}^{\rm in} < 10^{-3}$ Jy, strongly depends on $S_{\rm int}^{\rm in}$; i.e., a higher flux density increases the possibility of detecting extended sources[1]. Thus, at a given redshift,

[1] Not all bins at the bright/compact end exhibit a 100% completeness. We attribute this result to the minimum number of pixels in an island (`minpix_isl=9`) used to retrieve the radio sources with PyBDSF. Negative noise fluctuations might

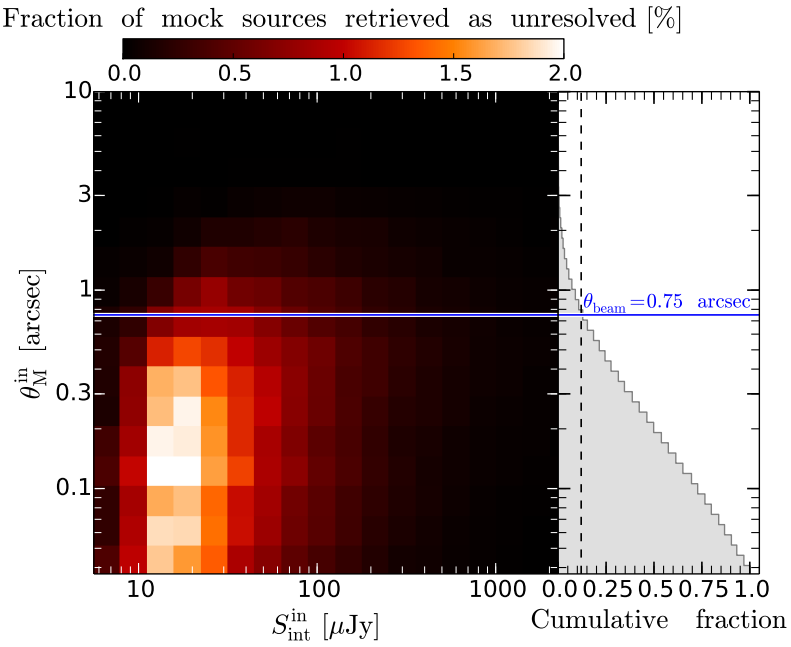

Figure 2.2: *Left panel:* Fraction of mock sources retrieved by PyBDSF as unresolved in the $\theta_M^{in} - S_{int}^{in}$ plane showing the ratio of the number of unresolved sources per bin to the total number of unresolved sources in the entire parameter space. *Right panel:* Cumulative size distribution of mock sources retrieved as unresolved, which represent 29% of the total number of sources injected in our MC simulations. Around 90% of them lie below $\theta_{beam} = 0.75$ arcsec (blue line), hence we use this value as the upper limit for the size of unresolved SFGs in the VLA COSMOS 3GHz map.

faint galaxies are preferentially detected if they are compact, while bright starbursting systems are detected even if they are extended. This selection function (i.e., completeness level of 10%) is further discussed in Sects. 2.4.1 and 2.4.2.

Upper limit for the size of unresolved sources

A total of 665 SFGs (21%) from our sample are unresolved ($\theta_M^{out} = 0$ arcsec) by PyBDSF. In order to assign an upper limit to their intrinsic angular size ($\theta_M^{in} < \theta_{lim}$), we explore the input size of mock sources retrieved as unresolved in the MC simulations. In Fig. 2.2, we plot their distribution in the $\theta_M^{in} - S_{int}^{in}$ plane. Most of the sources retrieved as unresolved by PyBDSF are, as expected, at the faint and compact end of the parameter space tested here. Based on their angular size distribution (Fig. 2.2, right panel), we find that around 90% of them satisfy the condition: $\theta_M^{in} \leq \theta_{beam}$ (blue line). We thus define $\theta_{beam} = 0.75$ arcsec as the upper limit for the size of the 665 unresolved SFGs in our sample.

hinder the detection of islands of emission above this threshold. Certainly, we verified that using `minpix_isl=6` yields a higher completeness at the bright/compact end. Even so, we adopted `minpix_isl=9` to be consistent with the original VLA COSMOS 3GHz catalog (Smolčić et al., 2017a).

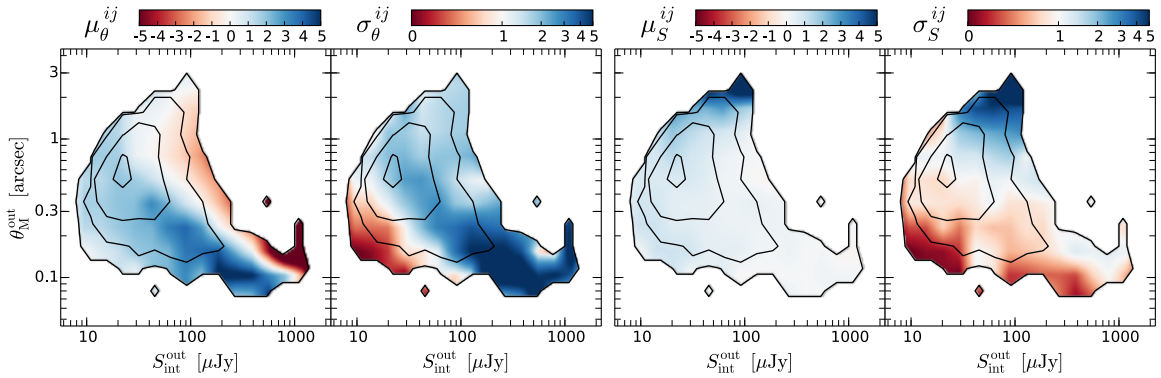

Figure 2.3: Systematic errors and uncertainties for the FWHM (*left two panels*) and flux density (*right two panels*) of mock sources in the $\theta_M^{out} - S_{int}^{out}$ plane covered by 2519 resolved SFGs studied in this work. Contour levels showing the distribution of these sources are at 1, 5, 50, 250 sources per bin. Positive (negative) values of μ_θ^{ij} and μ_S^{ij} indicate that the measured quantity is overestimated (underestimated). Values of σ_θ^{ij} and/or σ_S^{ij} higher (lower) than 1 suggest that the uncertainty of the measured parameter is being underestimated (overestimated).

How reliable are the retrieved FWHM and flux density?

It is well known that noise fluctuations boost the flux of faint sources detected in sensitivity-limited astronomical surveys (e.g., Hogg & Turner, 1998; Coppin et al., 2005; Casey et al., 2014). It is expected that a similar effect takes place when determining the size of faint and compact sources. Therefore, in a pioneering effort, we use the MC simulations to correct both the FWHM and flux density (and associated uncertainties) provided by `PyBDSF`. We proceeded as follows:

1. We create a catalog containing all mock sources retrieved by `PyBDSF`. Hence, it contains information about the input (S_{int}^{in}, θ_M^{in}) and output parameters (S_{int}^{out}, θ_M^{out}).

2. All the sources in the catalog are binned in the $S_{int}^{out} - \theta_M^{out}$ plane (as shown in Fig. 2.1). For all objects in each bin, we estimate $r_\theta \equiv (\theta_M^{out} - \theta_M^{in})/\sigma_\theta$ and/or $r_S \equiv (S_M^{out} - S_M^{in})/\sigma_S$, where σ_θ and σ_S are the uncertainties provided by `PyBDSF`.

3. We derive the mean (μ) and standard deviation (σ) of the r_θ and r_S distributions (Fig. 2.3). While the value of μ quantifies systematic biases (e.g., "flux boosting"), σ evaluates whether the uncertainties given by `PyBDSF` are under- or overestimated.

   In the ideal case where the measured properties and uncertainties are an appropriate description of the input mock sources, the mean (μ) and standard deviation (σ) of the distribution should be 0 and 1, respectively. Nevertheless, for both FWHM and flux density, μ is generally greater than zero (Fig. 2.3), meaning that `PyBDSF` tends to overestimate the size and flux density of mock sources. The value of σ is also heterogeneous across the $\theta_M^{out} - S_{int}^{out}$ plane (Fig. 2.3); σ_θ^{ij} and/or σ_S^{ij} higher (lower) than 1 suggests that the uncertainty provided by `PyPDSF` is being underestimated (overestimated).

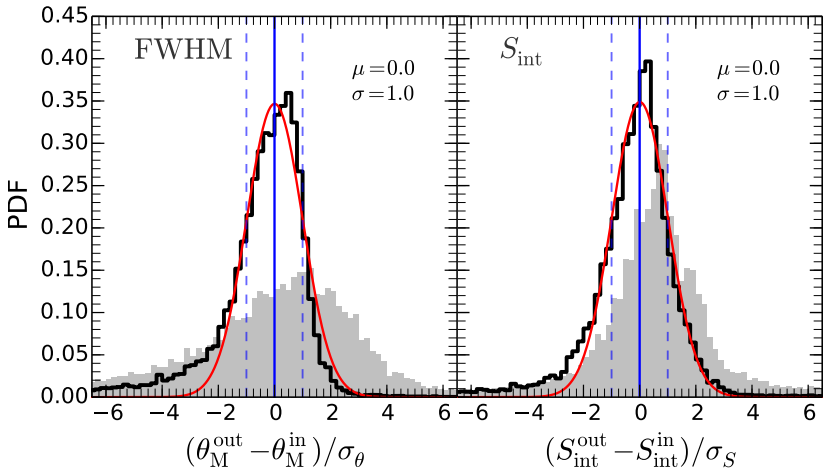

Figure 2.4: Distribution of sigma deviations for the FWHM (*left panel*) and integrated flux density (*right panel*) of all mock sources. The distribution that is produced from the corrected quantities is shown in black, while in gray that obtained from the measured quantities given by `PyBDSF`. A single-component Gaussian fit is shown in red. For both corrected distributions, we find the best fitting parameters of $\mu = 0$ and $\sigma = 1$ (blue solid and dashed lines), which indicates that the corrected flux density and FWHM (and associated uncertainties) are a proper description of the mock sources. Blue solid (dashed) lines illustrate the locus of $\mu = 0$ ($\sigma = 1$).

4. Under the condition that all r_θ and r_S distributions should have a mean of zero and dispersion of 1, the corrected source properties ($\theta_{\rm M}^{\rm ,out}$, $S_{\rm int}^{\rm ,out}$) and associated uncertainties (σ'_θ, σ'_S) are given by

$$\left.\begin{aligned} \theta_{\rm M}^{\rm ,out} &= \theta_{\rm M}^{\rm out} - \mu_\theta^{ij} \times \sigma_\theta, \\ S_{\rm int}^{\rm ,out} &= S_{\rm int}^{\rm out} - \mu_S^{ij} \times \sigma_S, \end{aligned}\right\} \tag{2.3}$$

and

$$\left.\begin{aligned} \sigma'_\theta &= \sigma_\theta^{ij} \times \sigma_\theta, \\ \sigma'_S &= \sigma_S^{ij} \times \sigma_S, \end{aligned}\right\}, \tag{2.4}$$

where μ_θ^{ij}, μ_S^{ij}, σ_θ^{ij}, and σ_S^{ij} are the mean and standard deviations of the r_θ and r_S distributions in each bin; here $i = 1...m$ and $j = 1...n$, with m and n the numbers of columns and rows used to grid the $\theta_{\rm M}^{\rm out} - S_{\rm int}^{\rm out}$ plane.

5. After applying our corrections to all mock resolved sources, we retrieve the distribution of r_θ and r_S. By fitting a single-Gaussian component, we find $\mu = 0.0$ and $\sigma = 1.0$ for both distributions (Fig. 2.4). This assures that the corrected flux densities and FWHM, as well as their associated uncertainties, are a good description of the input mock sources.

   It should be noted that for a small fraction of mock sources, our corrected FWHM is still being underestimated; this gives rise to a wing in the r_θ distribution (Fig. 2.4). We verified that these outliers are mainly located at the extended and bright end of the $\theta_{\rm M}^{\rm out} - S_{\rm int}^{\rm out}$ plane ($\theta_{\rm M}^{\rm out} > 0.75$ arcsec and $S_{\rm int}^{\rm out} > 0.1$mJy) where less than 1% of SFGs in our final sample reside (see Fig. 2.1).

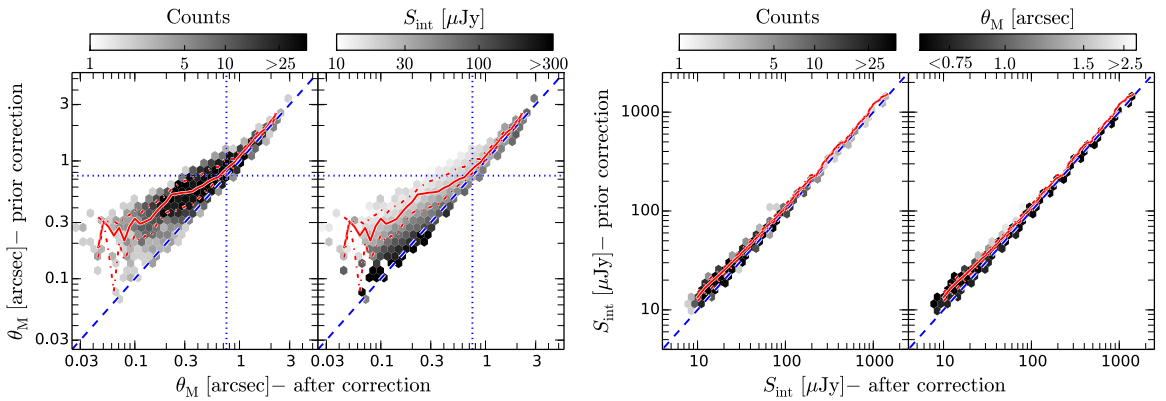

Figure 2.5: Comparison between observed and corrected source parameters of SFGs in the sample. *Left panels:* FWHM of 2519 resolved sources before and after correction, color-coded by number counts and median flux density. The red solid (dashed) lines show the 50th (16th, 84th) percentile of the FWHM values prior correction, using a 0.05 dex bin width along the x-axis. The dotted blue lines illustrate the FWHM of the synthesized beam (0.75 arcsec), while the 1:1 relation is shown by the blue dashed line. *Right panels:* Flux density of 3184 SFGs (resolved and unresolved) before and after correction, color-coded by number counts and median FWHM. The red solid (dashed) lines show the 50th (16th, 84th) percentile of the flux density values prior correction, using a 0.1 dex bin width along the x-axis. The 1:1 relation is shown by the blue dashed line.

6. To correct the measured flux density of unresolved sources, we compare the input and output flux density of mock sources retrieved as unresolved by `PyBDSF` (see Fig. 2.14). We then derive flux boosting factors as a function of S/N; at S/N = 5 the flux density is overestimated by 17%, while at S/N> 7 the effect of flux boosting is negligible.

7. We verified that the corrections and the completeness do not strongly depend on the input angular size and flux density distribution used in the MC simulations. A uniform distribution (equal number of sources per bin in the $\theta_{\rm M}^{\rm in} - S_{\rm int}^{\rm in}$ plane) yields correction factors that are consistent with those obtained from a realistic input distribution.

After validating our method, we then derived the corrected flux density and size of SFGs in our sample. In Fig. 2.5, we compare the flux and FWHM before and after revision in order to illustrate the effect of our corrections. Both flux and size measurements appear to be overestimated for faint radio sources. This result is expected as positive noise fluctuations enhance the flux density on a pixel-by-pixel basis and, consequently, the amplitude and variance of a 2D Gaussian model are magnified. This phenomenon translates into a flux boosting factor of $\sim$ 20% at the faint end (see right panel of Fig. 2.5), which is comparable with the uncertainty on the flux density of a 5σ radio source detection. On the other hand, "size boosting" seems to be ubiquitous for faint and compact sources that have a deconvolved FWHM smaller than the size of the synthesized beam (see left panel of Fig. 2.5). This can be attributed to the large uncertainties associated with the deconvolution process of slightly resolved and faint radio sources.

As a consistency test, we compare our corrected flux density measurements with those reported by Smolčić et al. (2017b), which were derived following a non-parametric approach with `blobcat`. By considering both resolved and unresolved sources (see Fig. 2.15), we found that the two quantities are, on average, consistent.

2.3.4 From flux and size measurements to SFR and effective size estimates

We estimate the total SFR by adding the estimates from the infrared ($\mathrm{SFR_{IR}}$) and uncorrected UV emission ($\mathrm{SFR_{UV}}$), allowing us to account for the dust obscured and unobscured star formation activity. We use the Kennicutt (1998a) calibration and the infrared-radio correlation (e.g., Magnelli et al., 2015; Delhaize et al., 2017) to derive $\mathrm{SFR_{IR}}$ as

$$\mathrm{SFR_{IR}}\,[M_\odot\,\mathrm{yr}^{-1}] = f_{\mathrm{IMF}} 10^{-24} 10^{q_{\mathrm{IR}}} L_{1.4\,\mathrm{GHz}}\,[\mathrm{W\,Hz}^{-1}], \tag{2.5}$$

where $f_{\mathrm{IMF}} = 1.72$ for a Salpeter initial mass function (IMF) and q_{IR} is parametrized as a function of redshift (for SFGs only) as $q_{\mathrm{IR}} = (2.83 \pm 0.02) \times (1+z)^{-0.15\pm0.01}$ (Delhaize et al., 2017). The value of $L_{1.4\,\mathrm{GHz}}$, on the other hand, can be derived from the observer-frame 3 GHz fluxes ($S_{\nu_{3\,\mathrm{GHz}}}$ [$\mathrm{W\,Hz^{-1}\,m^{-2}}$]) through

$$L_{1.4\,\mathrm{GHz}} = \frac{4\pi D_L(z)^2}{(1+z)^{1-\alpha}} \left(\frac{1.4}{3}\right)^{-\alpha} S_{3\,\mathrm{GHz}}, \tag{2.6}$$

where D_{L} is the luminosity distance in meters and α is the spectral index of the synchrotron power law ($S_\nu \propto \nu^{-\alpha}$) of 0.8 (Condon, 1992).

We also use the near-UV (NUV) emission of galaxies from the COSMOS2015 catalog (Laigle et al., 2016) to estimate $\mathrm{SFR_{UV}}$ as follows (Kennicutt & Evans, 2011):

$$\mathrm{SFR_{UV}} = 10^{-43.17} L_{\mathrm{NUV}}\,[\mathrm{erg\,s}^{-1}]. \tag{2.7}$$

Finally, to compare our radio continuum size estimates with those derived from the optical/UV, we convert our θ_M measurements into effective radius (R_{eff}), i.e., the radius enclosing half of the total flux density. To this end, we assume that most of our galaxies are star-forming disks with an exponentially declining surface brightness distribution. This is consistent with the average Sérsic index of $n \sim 1$ for MS galaxies (e.g., Nelson et al., 2016b) and luminous sub-mm selected galaxies (SMGs; Hodge et al., 2016), preferentially located above the MS. Under this assumption, Murphy et al. (2017) have analytically proven that for slightly resolved radio sources (with $R_{\mathrm{eff}} \lesssim \theta_{\mathrm{beam}}$) θ_M and R_{eff} can be related by

$$\theta_M \approx 2.430 R_{\mathrm{eff}}. \tag{2.8}$$

2.3.5 Final sample

We distributed the 3184 SFGs in our sample in five redshift bins following those presented by Laigle et al. (2016): (0.35, 0.65], (0.65, 0.9], (0.9, 1.35], (1.35, 1.7], and (1.75, 2.25]. This allows us to directly use the stellar mass completeness limits (per redshift bin) of the COSMOS2015 catalog, and hence assemble a mass-complete sample of radio-selected SFGs in the COSMOS field. The number of SFGs per redshift bin is nearly homogeneous (with a median of $\sim$ 650 sources). Given the small

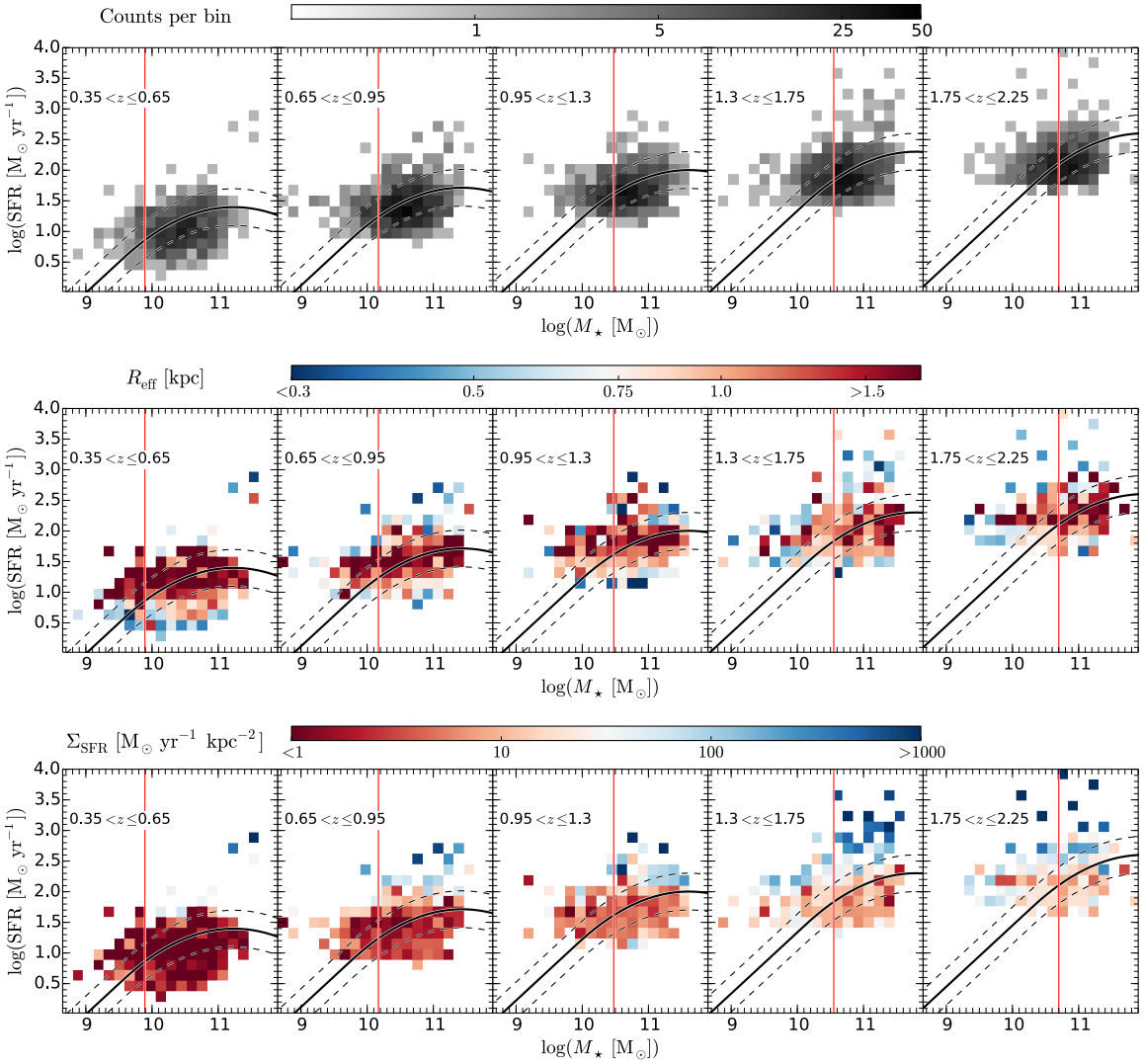

Figure 2.6: *Upper panels:* Sample of 3184 SFGs in the SFR $-$ $M_\star$ $-$ z plane, color-coded for the number of sources per bin. Shown are the positions of the MS of SFGs (black lines) and the associated dispersion (dashed black lines) given by Schreiber et al. (2015). Vertical red lines show the mass limit above which we consistently probe SFGs on and above the MS. *Middle and lower panels:* Median size and star formation surface density, respectively, of the 3184 SFGs in the sample. We use 1000 MC realizations to include the values for unresolved sources, which are drawn from the distributions described in Sects. 2.4.2 and 2.4.4.

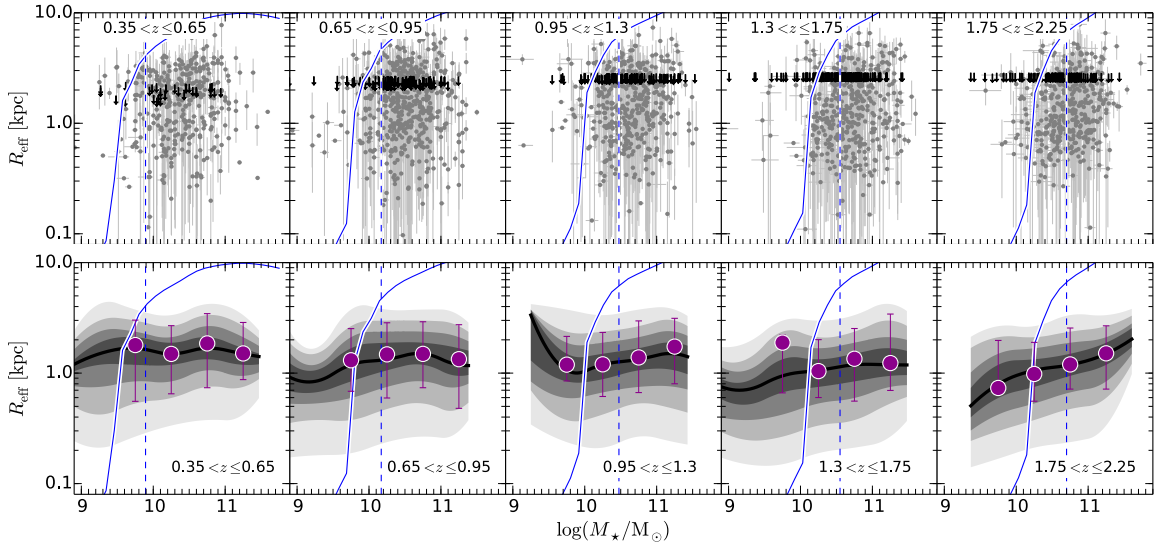

Figure 2.7: *Upper panels:* Sample of 3184 SFGs in the $R_{\rm eff} - M_\star - z$ plane. The blue solid line shows the maximum size, corresponding to the 10% completeness level, that can be observed for a galaxy with $\Delta\log({\rm SSFR}) = 0$ evaluated at the central redshift value per bin. Blue dashed lines show the mass limit above which we consistently probe SFGs on and above the MS. Black arrows show the upper limits for the size of unresolved sources. *Lower panels*: Density distribution per stellar mass bin (0.5 dex width) of SFGs in the $R_{\rm eff} - M_\star - z$ plane. Contour levels are at the 10, 20, 30, 40, 50, 60, 70, 80, and 90th percentiles. The median size derived via the Kaplan–Meier (KM) estimator is shown by the dark magenta circles, the error bars correspond to the 16th and 86th percentiles of the distribution.

comoving volume probed by COSMOS at low redshift and the selection function that restricts our parameter space to compact starburst galaxies, we are not able to explore the size evolution of SFGs in the redshift regime below $z = 0.35$.

In Fig. 2.6, we present the sample of 3184 SFGs in the SFR$-M_\star - z$ plane. The bulk of the radio-selected SFGs is consistent with the position and dispersion of the MS of SFGs, as given by Schreiber et al. (2015). At the low-mass end, however, our radio detection limit biases our sample towards the starburst population. Since we aim to statistically analyze the size distribution of SFGs on and above the MS, we need to focus on the high-mass end. For this purpose, we define a mass-limit ($M_\star^{\rm lim}$) for each redshift bin, above which we are able to consistently probe both SFGs on ($-0.3 \leq \Delta\log({\rm SSFR})_{\rm MS} \leq 0.3$) and above the MS ($\Delta\log({\rm SSFR})_{\rm MS} > 0.3$). By considering systems with $M_\star > M_\star^{\rm lim}$ we are also able to assemble a mass-complete sample of radio-selected SFGs, given that in all redshift bins $M_\star^{\rm lim}$ is higher than the stellar mass completeness limit of the COSMOS2015 catalog.

2.4 Results

In this section, we explore the dependence of the radio continuum size ($R_{\rm eff}$) on the stellar mass, distance to the MS and redshift. We carefully address these relations while keeping in mind the

completeness and size biases mentioned in Sec. 2.3.3 and that our analysis is restricted to $M_\star > M_\star^{\rm lim}$, i.e., the part of the parameter space where the sample of SFGs on and above the MS is complete. We also verified that the trends presented below remain even if we use uncorrected measurements (see Appendix 2.7.2).

2.4.1 Radio continuum size versus stellar mass

The stellar mass-size relation in galaxies (e.g., Furlong et al., 2017; Allen et al., 2017) is thought to be linked to the physical processes that regulate galaxy assembly, such as galaxy minor and major mergers and gas accretion (e.g., Khochfar & Silk, 2006, 2009; Dekel et al., 2009a; Oser et al., 2010; Gómez-Guijarro[†] et al., 2018a). Thus, it is a fundamental ingredient to understand galaxy evolution.

Here, we attempt to characterize the stellar mass-radio size relation up to $z = 2.25$. We thus explore the scatter of SFGs in the $R_{\rm eff} - M_\star$ plane by deriving their density distribution per stellar mass bin (0.5 dex width; Fig. 2.7). We use 10,000 Monte Carlo trial model runs to take into account the dispersion introduced by the uncertainties and upper limits of $R_{\rm eff}$ for resolved and unresolved sources, respectively. Based on our MC simulations (Fig. 2.2), the size of unresolved sources can be drawn from a uniform distribution in log space within the range $[0.1, R_{\rm eff}^{\rm lim}]$ kpc, where $R_{\rm eff}^{\rm lim}$ is the upper limit for the source size. We also derived the median size of SFGs through the KM estimator (Kaplan & Meier, 1958), which allows us to take into account the upper limits for the size of unresolved sources. We find that the two methods, MC realizations and KM estimator, yield consistent results (Fig. 2.7). In all redshift bins, the size distribution of SFGs remains constant over the range of stellar mass probed here, where the median size differs by less than 25% (see Table 2.1). Qualitatively, this result is consistent with the shallow slope ($\alpha_{\rm opt/UV}$) of the stellar mass and optical/UV size relation of SFGs ($\alpha_{\rm opt/UV} \sim 0.2$; e.g., van der Wel et al., 2014; Mowla et al., 2018). Finally, we checked that this relation remains if we use two separate samples of SFGs: one composed of galaxies on the MS ($-0.3 \leq \Delta\log({\rm SSFR})_{\rm MS} \leq 0.3$) and another above it ($\Delta\log({\rm SSFR})_{\rm MS} > 0.3$).

We still have to consider that the last result might be affected by our selection function. As mentioned in Sect. 2.3.3, galaxies are preferentially detected if they are compact, especially at the faint end. This could yield a misleading stellar mass–radio size relation, as low-mass SFGs are fainter than their massive counterparts (due to the MS slope, Fig. 2.6). To quantify this possible bias, we use the output of our MC simulation to estimate the maximum recoverable size as a function of stellar mass as follows. At a given redshift bin and for each mass, we infer the SFR of a galaxy with $\Delta\log({\rm SSFR})_{\rm MS} = 0$. Then we convert this SFR into flux density using the central redshift of the bin. Finally, this flux is associated with a maximum recoverable size using our 10% completeness limit in the $\theta_{\rm M}^{\rm in} - S_{\rm int}^{\rm in}$ plane (Sect. 2.3.3). As observed in Fig. 2.7, this selection function hinders the detection of extended SFGs with stellar mass below and near $M_\star^{\rm lim}$; however, it does not affect the parameter space above $\log(M_\star/M_\odot) = 10.5$. Hence, the negligible dependence of the stellar mass on the radio size of SFGs with $\log(M_\star/M_\odot) > 10.5$ remains unaffected by our selection.

2.4.2 Radio continuum size of SFGs on and above the main sequence

Since both the size and $\Delta\log({\rm SSFR})_{\rm MS}$ of SFGs can be discussed within the context of gas accretion and merger-driven star formation (e.g., Elbaz et al., 2011, 2018; Lang[†] et al., 2019), it is essential to

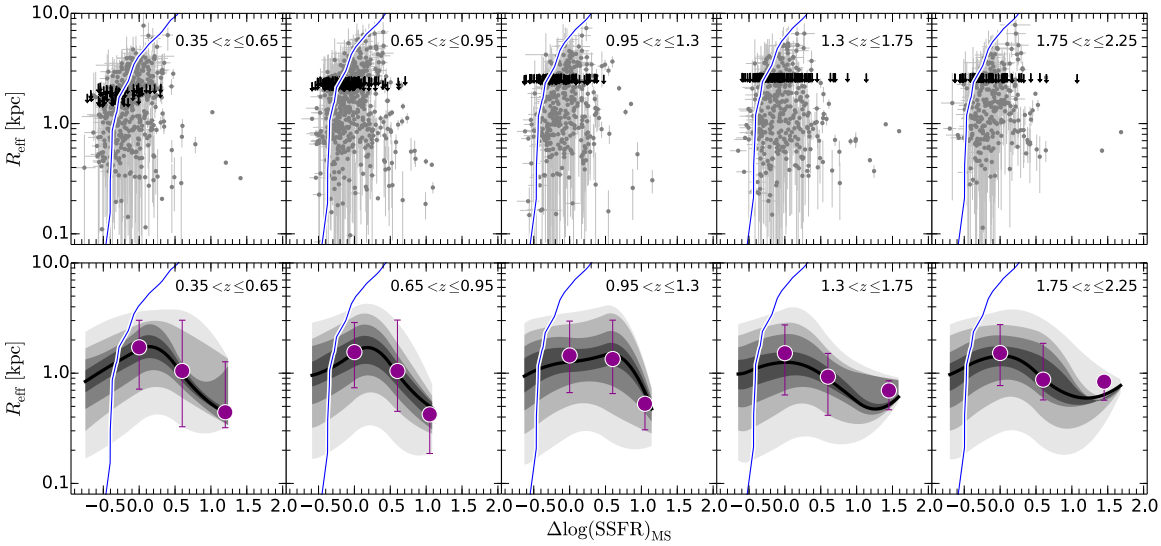

Figure 2.8: *Upper panels:* Star-forming galaxies with $M_\star > M_\star^{\rm lim}$ in the size−$\Delta\log(\mathrm{SSFR}) - z$ plane. The blue solid line shows the maximum size, corresponding to the 10% completeness level, that can be observed for a galaxy with $M_\star = M_\star^{\rm lim}$ evaluated at the central redshift value per bin. Black arrows show the upper limits for the size of unresolved sources. *Lower panels:* Density distribution per $\Delta\log(\mathrm{SSFR})$ bin (0.5 dex width) of SFGs in the size−$\Delta\log(\mathrm{SSFR}) - z$ plane. Contour levels are at the 10, 20, 30, 40, 50, 60, 70, 80, and 90th percentiles. The median size derived via the KM estimator is shown by the dark magenta circles, the error bars correspond to the 16th and 86th percentiles of the distribution.

characterize their interplay in detail. We therefore take advantage of our mass-complete sample of radio-selected SFGs to systematically explore their size distribution as a function of $\Delta\log(\mathrm{SSFR})_{\rm MS}$ and cosmic time (Fig. 2.8). We recall that we consider SFGs with $M_\star > M_\star^{\rm lim}$, which is the region of the parameter space where we can consistently probe galaxies on and above the MS.

Similarly to the previous section, we derive the median size of SFGs per $\Delta\log(\mathrm{SSFR})_{\rm MS}$ bin following a MC approach and using the KM estimator. As observed in Fig. 2.8, the two methods agree well and reveal a trend where SFGs with higher $\Delta\log(\mathrm{SSFR})_{\rm MS}$ values are compact, in particular at lower redshifts where this tendency is more pronounced. The median size of $z \sim 0.5$ ($z \sim 2$) MS galaxies is 4 (2) times larger than those with $\Delta\log(\mathrm{SSFR})_{\rm MS} > 0.9$ (see Table 2.2). We note that although SFGs on the MS are preferentially extended (median $R_{\rm eff} \sim 1.5 \pm 0.2$ kpc), some can be as compact as galaxies with elevated $\Delta\log(\mathrm{SSFR})_{\rm MS}$.

To verify that our selection function does not bias these trends, we estimate the maximum recoverable size as a function of $\Delta\log(\mathrm{SSFR})_{\rm MS}$. At a given redshift bin and for each $\Delta\log(\mathrm{SSFR})_{\rm MS}$, we infer the SFR of a galaxy with $M_\star = M_\star^{\rm lim}$ evaluated at the central redshift of the bin. We then convert this SFR into flux density and associate it to a maximum recoverable size using our completeness in the $\theta_{\rm M}^{\rm in} - S_{\rm int}^{\rm in}$ plane (Sect. 2.3.3). As inferred from Fig. 2.8, while the selection function does not affect the size distribution of SFGs above the MS, it does hamper the detection of extended SFGs on and below the MS. We note that retrieving these missing systems would only strengthen the anti-correlation between the median size of SFGs and $\Delta\log(\mathrm{SSFR})_{\rm MS}$.

The size dichotomy of SFGs on and above the MS is consistent with the results of Elbaz et al. (2011) and Rujopakarn et al. (2016). They did not report, however, that compact galaxies can be "hidden" within the MS (Fig. 2.8), which is in agreement with recent high-resolution observations of $z \sim 2$ SFGs (e.g., Elbaz et al., 2018; Lang[†] et al., 2019). This effect is related to the stacking approach followed by Elbaz et al. (2011), which can only provide median quantities, and the small sample of Rujopakarn et al. (2016), which might be affected by incompleteness.

In general, these findings support the emerging consensus where the global star-forming region of SFGs on the MS is preferentially but not exclusively extended, while SFGs above the MS are always more compact systems.

2.4.3 Size of SFGs in different wavelengths and its evolution with redshift

We now explore the radio continuum size evolution of SFGs over the redshift range $0.35 < z < 2.25$ to better constrain the processes regulating the growth of galaxies. In addition, through the comparison of the size-redshift relation as traced by stellar light, dust, and supernova remnants, we investigate where and how new stars are formed in galaxies. To this end, we select galaxies from our final sample (Sect. 2.3.5) with $\log(M_\star/M_\odot) > 10.5$, which is the only mass bin consistently probed across the redshift range explored here. For all the redshift bins, we then derive the median $R_{\rm eff}$ (via the KM estimator) of SFGs on and above the MS, i.e., $-0.3 \leq \Delta\log(\mathrm{SSFR})_{\rm MS} \leq 0.3$), and ($\Delta\log(\mathrm{SSFR})_{\rm MS} > 0.3$), respectively. As illustrated in Fig. 2.9, the radio continuum size of both SFG populations remains nearly constant across cosmic time. By using a parametrization of the form $R_{\rm eff} \propto (1+z)^{\alpha}$, we find a slope of only -0.26 ± 0.08 (0.12 ± 0.14) for SFGs on (above) the MS. As expected from the results in Sect. 2.4.2, the median size of SFGs on the MS ($R_{\rm eff} = 1.5 \pm 0.2$ kpc) is significantly larger than for those above it ($R_{\rm eff} = 1.0 \pm 0.2$ kpc).

The size evolution presented here is still influenced by two factors that cannot be characterized with the available data:

- First, our radio continuum size estimates trace different rest-frame frequencies, from 4 GHz at $z = 0.35$ to 9.7 GHz at $z = 2.25$. Since higher energy electrons lose energy more rapidly, their propagation throughout the galaxy is more limited than their low-energy counterparts (e.g., Kobayashi et al., 2004); 3 GHz emitting electrons, in particular, are expected to diffuse $\sim 25\%$ farther into the ISM than those at 10 GHz (Murphy et al., 2017). Thus, the observed radio continuum synchrotron emission would tend to be more concentrated as the redshift increases. This phenomenon does not significantly affect the trends presented above as a 25% larger radio size at $z = 2.25$ would lead to $\alpha \sim -0.10$ (~ 0.25) for SFGs on (above) the MS.
- Second, given the limited number of resolution elements across the SFGs in the sample, we cannot assess their radio continuum surface brightness distribution and determine $R_{\rm eff}$. Therefore, we converted the deconvolved FWHM to $R_{\rm eff}$ (following Murphy et al., 2017) assuming that most of our SFGs follow an exponentially declining surface brightness distribution (with Sérsic index $n = 1$). Naturally, such a conversion might deviate from the true $R_{\rm eff}$ on a galaxy-by-galaxy basis, especially for SFGs above the MS that tend to have cuspier light profiles (e.g., Wuyts et al., 2011). For slightly resolved sources, like the ones presented here, we do not

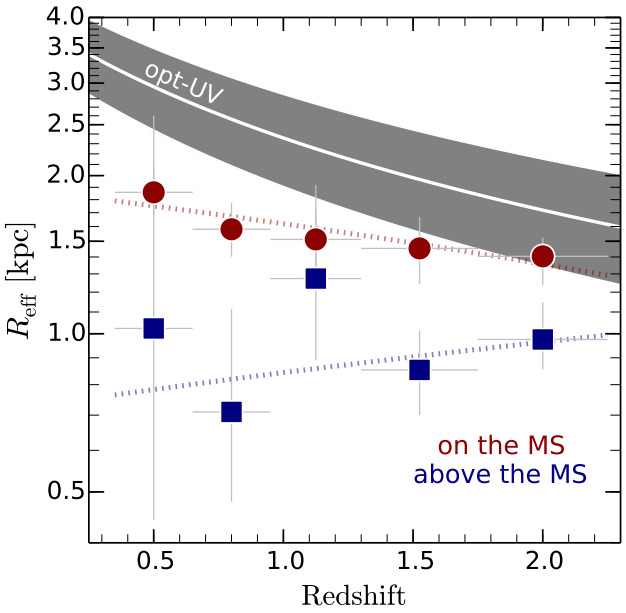

Figure 2.9: Radio continuum size (in terms of half-light radius, $R_{\rm eff}$) of galaxies on and above the MS as a function of redshift. Only SFGs with $\log(M_\star/M_\odot) > 10.5$ are included. Filled data points (squares and circles) show the median size for SFGs (above and on the MS) in the different redshift bins probed in this work. Vertical bars show the 95% interval confidence of the median, while horizontal bars represent the redshift bin width. Gray shaded region illustrates the growth curve derived in the UV-optical for UV-luminous SFGs given by $R_{\rm eff}/{\rm kpc} = (4.78 \pm 0.68)(1+z)^{(-0.84\pm0.11)}$ (Shibuya et al., 2015). Red and blue dotted lines show the linear fit to parametrize the redshift evolution of the median radio continuum size as $R_{\rm eff}/{\rm kpc} = (2.1 \pm 0.2)(1+z)^{(-0.26\pm0.08)}$ and $R_{\rm eff}/{\rm kpc} = (0.6 \pm 0.4)(1+z)^{(0.12\pm0.14)}$ for SFGs on and above the MS, respectively.

expect major changes in $R_{\rm eff}$ if the Sérsic index is larger than 1. For example, even for 0.2 arcsec resolution dust-continuum observations, Elbaz et al. (2018) report that $R_{1/2} \equiv 0.5 \times {\rm FWHM}$ and $R_{\rm eff}$ are both equally good proxies for the half-light radius, either leaving the index free or fixed to 1.

Comparison with other radio continuum size estimates

Bondi† et al. (2018) have independently derived the $R_{\rm eff}$ of radio sources detected in the VLA COSMOS 3GHz map (Smolčić et al., 2017a), including AGN and SFGs up to $z \sim 3$. They assembled a sample of SFGs that is complete in $L_{3\,{\rm GHz}}$ over $0.8 < z < 3$ with median $\log(M_\star/M_\odot) = 10.6$; no distinction was made between on and off MS galaxies. For this sample, the size of SFGs marginally increases with cosmic time, from median ~ 1.4 kpc at $z = 2.1$ to $R_{\rm eff} \sim 1.6$ kpc at $z = 0.8$. This is in agreement with the shallow size evolution of MS galaxies in our sample (which corresponds to $\sim 90\%$ of all SFGs) with median $R_{\rm eff} = 1.5 \pm 0.1$ kpc, within the same redshift range and comparable stellar mass. We note that despite the independent methodologies used to measure radio sizes in the μJy regime, and different selection criteria, our median sizes are consistent. Bondi† et al. (2018) used, in particular, the original and convolved images (up to a resolution of 2.2 arcsec) of the VLA COSMOS 3GHz mosaic

and took the flux density provided by `blobcat` as a prior in their 2D Gaussian fitting procedure. This flux prior limits the effect of size boosting, leading to comparable size measurement between our two studies. On the other hand, by using the VLA COSMOS 3GHz map, Miettinen et al. (2017a) reported a median $R_{\rm eff} \sim 1.9$ kpc for 152 SMGs over the redshift range of $1 \lesssim z \lesssim 6$. The discrepancy of $\sim 35\%$ between the Miettinen et al. value of $R_{\rm eff}$ and that reported here at $z = 2.25$ and in Bondi[†] et al. (2018) is likely driven by the different selection criteria.

The angular size of the μJy radio sources has also been recently explored in different extragalactic deep fields. At the same frequency, 3 GHz, it was found that $z \sim 1$ SFGs in the Lockman-Hole have a median effective radius of ~ 1.0 kpc (Cotton et al., 2018), which agrees with the median size of SFGs above the MS derived here (see Fig. 2.9). Murphy et al. (2017) have reported that $z \sim 1.2$ GOODS-N SFGs have a median $R_{\rm eff}$ of only ~ 0.5 kpc at 10 GHz. This small size could be associated with selection effects as the high-resolution 10 GHz observations (0.22 arcsec) are sensitive to smaller angular scales. Additionally, as stated by Murphy et al. (2017), the discrepancy between 3 GHz and 10 GHz radio sizes is driven by the frequency-dependent cosmic ray diffusion. This physical phenomenon could partially explain the large median $R_{\rm eff}$ of 2.3 ± 0.6 kpc at 1.4 GHz of $z \sim 1.5$ SFGs (in the Hubble Deep Field; Lindroos et al., 2018), which is ~ 1.5 times larger than the median size at 3 GHz of galaxies in our sample. On the contrary, the larger energy loss rate at higher frequencies cannot explain the large median $R_{\rm eff}$ of ~ 2.7 kpc (FWHM ~ 0.8 arcsec) at 5.5 GHz reported for SFGs at similar redshift (in GOODS-N; Guidetti et al., 2017). Finally, we note that (apart from the frequency and resolution of the observations) a more general issue about size determination is related to the surface brightness limit of each survey. As inferred from Fig. 2.1, a lower r.m.s. sensitivity hampers the maximum detectable angular size, biasing the sample towards more compact radio sources.

Comparison with FIR, optical, and Hα sizes

It has been reported that the FIR size of $z \sim 2$ SFGs is, on average, ~ 1.5 kpc (e.g., Rujopakarn et al., 2016; Elbaz et al., 2018; Lang[†] et al., 2019), which is consistent with the median radio size of SFGs reported here. Extinction-corrected Hα radial profiles tracing the global star-forming region of $z \sim 1.4$ SFGs yield a median effective radius of < 1 kpc (with $9.8 < \log(M_\star/M_\odot) < 11$; Nelson et al., 2016a), comparable with the radio continuum sizes of SFGs above the MS. In contrast, the median effective radius derived from uncorrected Hα emission is 4.2 ± 0.1 kpc for SFGs at $z \sim 1$ and similar stellar mass (Nelson et al., 2012). This disparity is related to the high dust content in massive galaxies; if star formation is highly obscured at small radii, Hα emission would appear less centrally concentrated, and the inferred effective radius will thus be larger (e.g., Möllenhoff et al., 2006; Nelson et al., 2016a,b).

In Fig. 2.9, we also present a comparison of the size of SFGs as observed from radio continuum and optical to UV throughout cosmic time. We use the size evolution derived by Shibuya et al. (2015) via broadband optical imaging with the *Hubble Space Telescope* (*HST*). In this case, we adopt the median fit obtained for the UV bright galaxies ($-24 < M_{UV} < -21$) corresponding to the stellar mass range of $10 < \log(M_\star/M_\odot) < 11$, which is consistent with the mass range of SFGs used in this work. Given that Shibuya et al. (2015) masked star-forming clumps, their size estimates can be used as a proxy for the stellar mass distribution of galaxies. As revealed by Fig. 2.9, the overall star-forming region of SFGs (on and above the MS) is more compact than their stellar component. In particular, at $z = 0.5$ (2) the optical to UV emission is $\sim$2 (1.3)

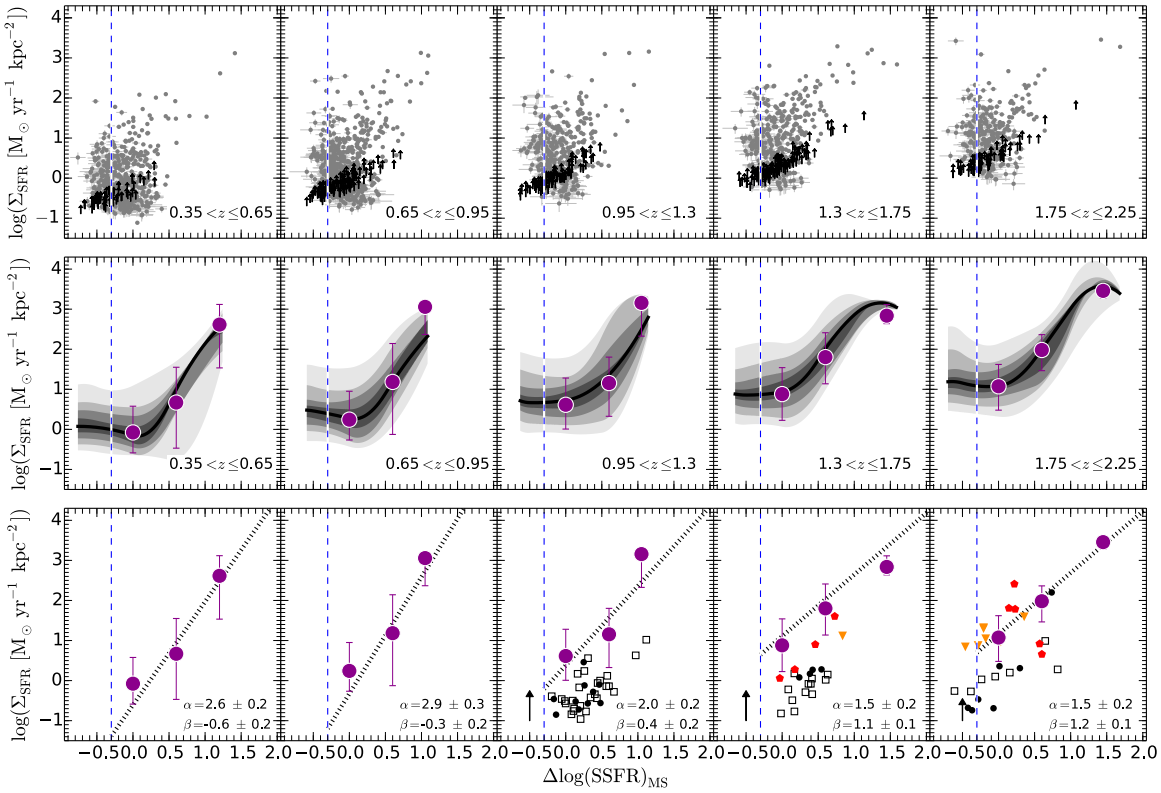

Figure 2.10: *Upper panels:* Star-forming galaxies with $M_\star > M_\star^{\rm lim}$ in the $\Sigma_{\rm SFR} - \Delta\log({\rm SSFR}) - z$ plane. Dashed blue lines show the $\Delta\log({\rm SSFR})$ limit of -0.3 above which our sample of SFGs is complete in terms of distance to the MS. Black arrows show the upper limits for the size of unresolved sources. *Middle panels:* Density distribution per $\Delta\log({\rm SSFR})$ bin (0.4 dex width) of SFGs in the $\Sigma_{\rm SFR} - \Delta\log({\rm SSFR}) - z$ plane. Contour levels are at the 10, 20, 30, 40, 50, 60, 70, 80, and 90th percentiles. The median size derived via the KM estimator is shown by the dark magenta circles; the error bars correspond to the 16th and 86th percentiles of the distribution. *Lower panels:* Power law describing the $\Sigma_{\rm SFR} - \Delta\log({\rm SSFR})$ relation (dotted black line). The slope and normalization are given in the lower right corner. The median size derived via the KM estimator is also shown by the dark magenta circles. For comparison, we present the compilation of SFGs from Genzel et al. (2010, black filled circles), Tacconi et al. (2013, black empty squares), Elbaz et al. (2018, red pentagons), and Lang[†] et al. (2019, orange triangles). The black arrow illustrates the factor to be considered when comparing $\Sigma_{\rm SFR}$ of galaxies in our sample with that reported by Genzel et al. (2010) and Tacconi et al. (2013) (see text for details).

times more extended than the radio continuum. Since these *HST*-based estimates are not corrected for extinction, it is likely that (similar to what has been shown for Hα sizes) the optical to UV effective radius is overestimated. Given that dust extinction becomes substantial in high-redshift galaxies (e.g., Leslie et al., 2018), we would expect that their optical to UV size is overestimated by a larger fraction than those galaxies at lower redshifts. Correcting for this effect could alleviate the discrepancy between the extent of the stellar and star-forming component of galaxies at high redshift.

In summary, radio continuum, FIR, and extinction-corrected Hα emission suggest that star formation occurs in smaller regions relative to the total stellar component (e.g., Simpson et al., 2015; Rujopakarn et al., 2016; Fujimoto et al., 2017; Elbaz et al., 2018, Karoumpis et al. in prep.). Here, in particular, we find that while the radio continuum size remains nearly constant, that inferred from optical to UV emission increases with cosmic time. In Sect. 2.5.2, we discuss this finding further within the context of bulge growth.

2.4.4 Cosmic evolution of $\Sigma_{\rm SFR}$

From numerical simulations, SFGs are expected to experience a compaction phase while the SFR increases and they move towards the upper end of the MS (e.g., Tacchella et al., 2016). This scenario can now be tested through our radio continuum size estimates. We thus derive the galactic-average SFR surface density, $\Sigma_{\rm SFR} = {\rm SFR}/2\pi R_{\rm eff}^2$, and use it to evaluate how concentrated the star formation activity in galaxies is as they evolve across the MS (see Fig. 2.6, 2.10). In calculating $\Sigma_{\rm SFR}$ we assume that the total SFR (${\rm SFR_{IR}}$ + ${\rm SFR_{UV}}$) is confined within the radio continuum-based $R_{\rm eff}$. This simplification is valid as the UV-based SFR is considerably low for massive, high-redshift SFGs (e.g., Buat et al., 2012); therefore, the star formation activity is mainly traced by the radio continuum (unobscured) emission.

As in Sects. 2.4.1 and 2.4.2, we follow a MC approach to derive the distribution of $\Sigma_{\rm SFR}$ per $\Delta\log({\rm SSFR})_{\rm MS}$ bin (Fig. 2.10); again, only galaxies with $M_\star > M_\star^{\rm lim}$ are included in the analysis. In this case, the $\Sigma_{\rm SFR}$ for unresolved sources is drawn from a uniform logarithmic distribution within the range $[\Sigma_{\rm SFR}(R_{\rm lim}), \Sigma_{\rm SFR}(0.1\,{\rm kpc})]$. We verify the reliability of this approach by using the KM estimator (Table 2.3). At all redshifts and for both methods, there is a positive relation between $\Sigma_{\rm SFR}$ and $\Delta\log({\rm SSFR})_{\rm MS}$ that can be described with a power law,

$$\log(\Sigma_{\rm SFR}) = \alpha \times \Delta\log({\rm SSFR})_{\rm MS} + \beta, \tag{2.9}$$

where α and β are the slope and normalization, respectively. We use a least-squares (Levenberg-Marquardt) algorithm to fit a linear function to $\Delta\log({\rm SSFR})_{\rm MS}$ and derive the best-fitting values for α and β. This procedure is done for each MC realization, while restricting our parameter space to $\Delta\log({\rm SSFR})_{\rm MS} > -0.3$ where our sample is complete. The final values for α and β, shown in Fig. 2.10, correspond to the median (and 16th and 84th percentiles) after executing 1000 MC trial model runs. While the normalization of the $\log(\Sigma_{\rm SFR}) - \Delta\log({\rm SSFR})_{\rm MS}$ relation decreases with redshift, the value of α reveals that this trend becomes shallower at higher redshift. At $z \sim 2$, the difference between $\Sigma_{\rm SFR}$ of galaxies on and above the MS is smaller than in the local Universe.

Spatially resolved studies of local SFGs have also reported more centrally peaked radial profiles of $\Sigma_{\rm SFR}$ as the distance to the MS increases (Ellison et al., 2018). It has been found that the FIR surface density evolves across the MS with a logarithmic slope of 2.6 (Lutz et al., 2016), which is consistent with the value we derived at $z \sim 0.5$ ($\alpha = 2.6$) using the radio continuum emission. Likewise, from Hα resolved maps it has been shown that $z \sim 1$ SFGs follow this relation with $\alpha \sim 1.1$ (Magdis et al., 2016), which is ~50% lower than that reported in this work. This tendency can also be inferred from the $\Sigma_{\rm SFR}$, $M_\star$, and SFR of $1 \lesssim z \lesssim 3$ SFGs reported by Genzel et al. (2010) and Tacconi et al. (2013). As presented in Fig. 2.10, these SFGs also exhibit higher $\Sigma_{\rm SFR}$ as the distance to the MS increases, yet their $\Sigma_{\rm SFR}$ values appear systematically lower than those reported here. This could be a consequence of the optical-/UV-/Hα-/CO-based size estimates used by the authors, which are larger than those obtained from radio continuum emission (Sect. 2.4.3). If we scale their $\Sigma_{\rm SFR}$ values by using our $R_{\rm opt}/R_{\rm radio}$ ratios, they increase by a factor of ~ 0.7 (0.4) dex at redshift 1.5 (2), which would alleviate this observed discrepancy. Finally, in Fig. 2.10 we present the sample of SFGs from Elbaz et al. (2018) and (Lang[†] et al., 2019). Although $z \sim 1.5$ SFGs also follow a positive relation between $\log(\Sigma_{\rm SFR})$ and $\Delta\log({\rm SSFR})_{\rm MS}$, those at $z \sim 2$ are widely scattered. As reported by Elbaz et al. (2018), $z \sim 2$ SFGs with starburst-like $\Sigma_{\rm SFR}$ are also found close to or within the MS. According to our results, there is a fraction of MS galaxies for which $\Sigma_{\rm SFR}$ is significantly higher than expected from the $\log(\Sigma_{\rm SFR}) - \Delta\log({\rm SSFR})_{\rm MS}$ relation. These high-$\Sigma_{\rm SFR}$ MS galaxies are present at all redshifts and comprise less than 10% of the MS galaxy population (see contour levels of Fig. 2.10).

2.5 Discussion

2.5.1 Cold gas accretion versus merger mode of star formation

We revealed that most SFGs ($\log(M_\star/M_\odot) > 10.5$) follow a linear relation in the $\log(\Sigma_{\rm SFR}) - \Delta\log({\rm SSFR})_{\rm MS}$ plane over the redshift range $0.35 < z < 2.25$. To the first order, these results can be discussed within the context of the Kennicutt-Schmidt (KS) relation ($\Sigma_{\rm SFR} - \Sigma_{\rm gas}$; Kennicutt, 1998a). We therefore use the scaling relations of Genzel et al. (2015) to derive the typical molecular gas mass of galaxies at three different $\Delta\log({\rm SSFR})_{\rm MS}$ bins, namely [−0.3,0.3], [0.3,0.6], and [0.9, 2.0] (see Fig. 2.10). Then we assume that our radio size estimates (Table 2.2) also trace the extent of the molecular gas reservoir; these estimates are subsequently used to approximate the galactic averaged molecular gas density ($\Sigma_{\rm mol\,gas} = M_{\rm mol\,gas}/2\pi R_{\rm eff}$). This information is combined with the $\Sigma_{\rm SFR}$ values presented in Table 2.3, allowing us to approximate the shape of the KS relation (see Fig. 2.11). It is reassuring that our data points, which cover a wide range in redshift and $\Delta\log({\rm SSFR})_{\rm MS}$, agree within the uncertainties with the KS relation presented by Genzel et al. (2010). Moreover, our data points are consistent with the scenario wherein low- and high-redshift SFGs follow a similar molecular gas–star formation relation (Bouché et al., 2007; Genzel et al., 2010). By considering SFGs with $-0.3 \lesssim \Delta\log({\rm SSFR})_{\rm MS} \lesssim 0.9$, we derive a super-linear slope of 1.3 ± 0.1. If SFGs with $\Delta\log({\rm SSFR})_{\rm MS} > 0.9$ are included, the slope becomes steeper (1.5 ± 0.1), which indicates that SFGs evolve towards a more efficient regime of star formation as $\Delta\log({\rm SSFR})_{\rm MS}$ increases. This is consistent with the small size, and hence higher $\Sigma_{\rm SFR}$, of galaxies above the MS (Fig. 2.8), which could be the result of gas-rich mergers (e.g., Moreno et al., 2015; Wellons et al., 2015) and/or violent disk instability (VDI; e.g., Dekel & Burkert, 2014; Tacchella et al., 2016; Wang et al., 2018).

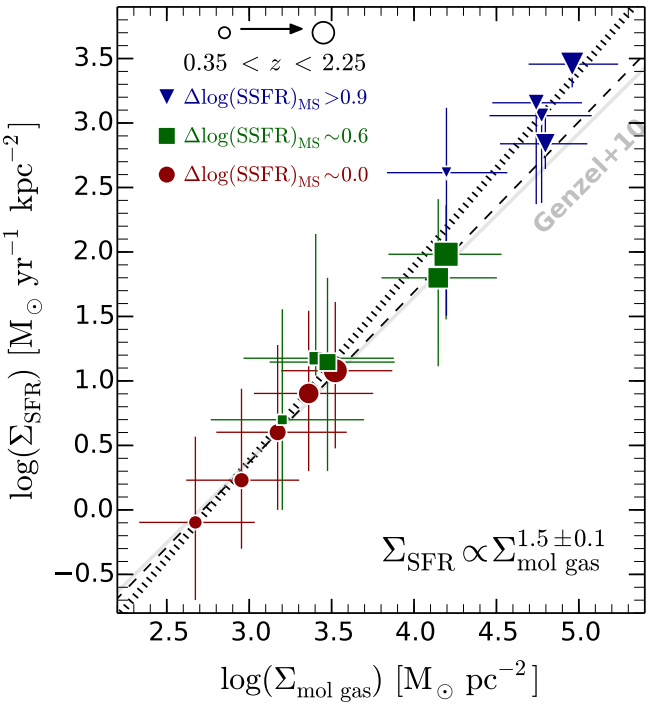

Figure 2.11: Star formation rate surface density ($\Sigma_{\rm SFR}$) as a function of the molecular gas surface density ($\Sigma_{\rm mol\,gas}$). The data points show the locus of the median $\Sigma_{\rm SFR}$ and $\Sigma_{\rm mol\,gas}$ of galaxies binned in $\Delta\log({\rm SSFR})_{\rm MS}$ and redshift (see Fig. 2.10). The symbol size increases with redshift, while the color indicates the median $\Delta\log({\rm SSFR})_{\rm MS}$. The solid gray line shows the KS relation reported by Genzel et al. (2010), adapted for a Salpeter IMF. The dotted black line illustrates the best linear fit to all the data points; the dashed thin line shows the best linear fit when we exclude SFGs with $\Delta\log({\rm SSFR})_{\rm MS} > 0.9$. Error bars represent the 16th and 84th percentiles of the inferred $\Sigma_{\rm SFR}$ and $\Sigma_{\rm mol\,gas}$ distributions. The molecular gas mass has been approximated by using the prescription of Genzel et al. (2015, see Table 4), where $M_{\rm mol\,gas} = M_{\rm mol\,gas}(z, {\rm SSFR}, M_\star = 10^{10.5\pm0.5}\,M_\odot)$.

Beyond the broad picture of galaxy evolution discussed above, we also reported the discovery of MS galaxies harboring starburst-like $\Sigma_{\rm SFR}$ conditions (Fig. 2.10). This result echoes, in particular, that of Elbaz et al. (2018), who reported the presence of hidden starbursts within the MS at $z \sim 2$. Then the fundamental question arises: what is the physical mechanism responsible for high-$\Sigma_{\rm SFR}$ MS galaxies? First, these systems could be a result of large cold gas reservoirs distributed over small disk radii (Wang et al., 2018) that, due to disk instability episodes (e.g., Dekel & Burkert, 2014), yield high $\Sigma_{\rm SFR}$. If the gas replenishment occurs when a galaxy lies at the lower envelope of the MS (i.e., $\Delta\log({\rm SSFR})_{\rm MS} \sim -0.3$), the SFR enhancement might not suffice to bring the galaxy above the MS. Second, high-$\Sigma_{\rm SFR}$ MS galaxies could be explained in the context of merger-driven bursts of star formation where, depending on the gas content, mergers could not significantly increase the SFR and offset the galaxy from the MS. (e.g., Fensch et al., 2017; Wang et al., 2018). This is in agreement with the observational evidence of merging activity in galaxies on and above the MS (e.g., Kartaltepe et al., 2012; Ellison et al., 2018; Calabrò et al., 2018; Wang et al., 2018; Cibinel et al., 2018, Karteltepe priv. communication).

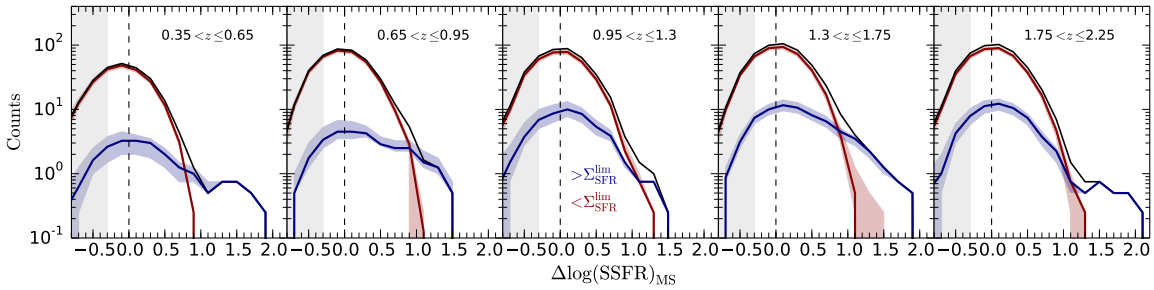

Figure 2.12: Distribution of SFGs along $\Delta\log(\rm SSFR)_{\rm MS}$ (black solid line). In this illustrative case, we separate the main sequence (red line) and starburst (blue) contribution using $\Sigma_{\rm SFR}^{\rm lim} \equiv Mdn[\Sigma_{\rm SFR}(\Delta\log(\rm SSFR)_{\rm MS} = 0.7)]$ for SFGs with $\log(M_\star/M_\odot) > 10.5$. The red and blue shaded regions show the scatter (16th and 84th percentiles) introduced by the uncertainties and upper limits of our measurements. The gray region indicates the parameter space where our sample is not complete.

In light of these findings, $\Sigma_{\rm SFR}$ arises as a remarkable proxy for identifying starburst galaxies, where star formation is triggered by either mergers or VDI that lead to high $\Sigma_{\rm SFR}$. As an illustrative case, here we evaluate $\Sigma_{\rm SFR}^{\rm lim} \equiv Mdn[\Sigma_{\rm SFR}(\Delta\log(\rm SSFR)_{\rm MS} = 0.7)]$[2] at each redshift bin (Sect. 2.4.4), and adopt it as a threshold to identify starbursting systems. Under this definition, it is possible to decompose the bimodal distribution of SFGs along $\Delta\log(\rm SSFR)_{\rm MS}$ (e.g., Sargent et al., 2012) into main sequence ($< \Sigma_{\rm SFR}^{\rm lim}$) and starburst ($> \Sigma_{\rm SFR}^{\rm lim}$) contribution (see Fig. 2.12). The first, and more dominant, distribution is centered at $\Delta\log(\rm SSFR)_{\rm MS} = 0$ and represents the population of galaxies forming stars through a secular mode of star formation (e.g., Dekel et al., 2009a; Sellwood, 2014). The distribution of non-merger-induced and merger-induced starbursts exhibits an enhanced tail at high $\Delta\log(\rm SSFR)_{\rm MS}$ and, consequently, its median lies at $\Delta\log(\rm SSFR)_{\rm MS} > 0$. We note that this $\Sigma_{\rm SFR}^{\rm lim}$-based scheme brings the galaxy-pair and merger rate in better agreement with the fraction of high-redshift starbursts (see Fig. 2.13), given that a $\Delta\log(\rm SSFR)_{\rm MS}$-based definition misses the merger-induced starbursts hidden within the MS (Elbaz et al., 2018; Cibinel et al., 2018).

2.5.2 Is the centrally concentrated star formation in galaxies evidence of bulge growth?

The finding of compact radio continuum emission of SFGs on and above the MS further support the evidence of star formation enhancement at small radii (e.g., Simpson et al., 2015; Rujopakarn et al., 2016; Nelson et al., 2016a; Fujimoto et al., 2017; Elbaz et al., 2018). Interestingly, while the extent of the stellar component increases with cosmic time, the overall region where most stars are formed remains nearly constant (see Fig. 2.9). This might indicate that fresh star-forming gas is constantly fueled towards the center of galaxies, either due to VDI, minor or major mergers, and/or tidal interactions (e.g., Larson, 2003; Rupke et al., 2010; Sillero et al., 2017; Ellison et al., 2018; Muñoz-Elgueta et al., 2018). Regardless of the dominant mechanism driving the formation of stars in galaxies (on and above the MS), violent and secular galaxy evolutionary channels lead to the

[2] We use this threshold as the number of $z \sim 0.35$ starbursts, which is consistent with that derived from the standard $\Delta\log(\rm SSFR)_{\rm MS}$-based definition (see Fig. 2.13). A different threshold in $\Sigma_{\rm SFR}$ also yields a larger starburst fraction at high redshift.

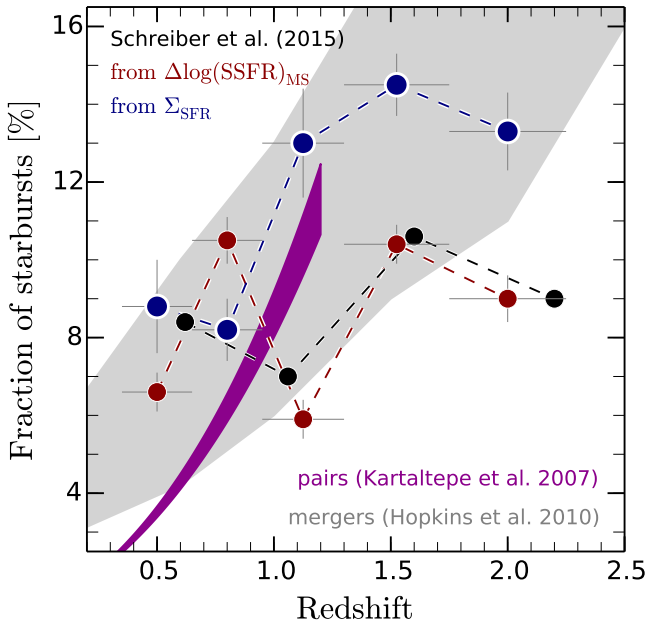

Figure 2.13: Redshift evolution of the starburst fraction from the mass-complete sample of radio-selected SFGs used in this work. We adopt two definitions of a starburst galaxy, a) systems with $\Delta\log(\mathrm{SSFR}) > 0.39$ and b) $\Sigma_{\mathrm{SFR}} > \Sigma_{\mathrm{SFR}}^{\mathrm{lim}}$ (see Sect. 2.5.1), in both cases $\log(M_\star/M_\odot) > 10.5$. For comparison, we present the starburst fraction for $\log(M_\star/M_\odot) > 10.5$ and $\Delta\log(\mathrm{SSFR}) > 0.39$ UV-/FIR-selected SFGs from Schreiber et al. (2015). The redshift evolution of the observed galaxy pair fraction is shown by the magenta shaded region (Kartaltepe et al., 2007). The gray region shows the major merger fraction predicted by Hopkins et al. (2010).

formation of a bulge (e.g., Kormendy & Kennicutt, 2004; Fisher, 2006; Hopkins et al., 2009; Brooks & Christensen, 2016; Tonini et al., 2016). Ultimately, the presence of a dominant bulge could stabilize the gas disk against gravitational instabilities, and thus prevent the formation of stars (e.g., Lang et al., 2014, and references therein).

In this context, we hypothesize that the centrally concentrated star formation activity of most SFGs in the sample might reflect the growth of the bulge, which might precede the quenching of the galaxy from the inside out (e.g., Ellison et al., 2018). At this late evolutionary stage the bulge of massive galaxies is fully quenched, while star formation activity still takes place at large radii (e.g., Tacchella et al., 2015; Rowlands et al., 2018). Spatially resolved studies of low- and high-mass SFGs at high redshift are needed to verify such a scenario, and will allow us to understand how star formation, and hence stellar mass, is distributed in galaxies across cosmic time.

2.6 Summary

We presented the first systematic study of the radio continuum size evolution of SFGs over $0.35 < z < 2.25$. We used a mass-complete sample of 3184 radio-selected SFGs, detected in the VLA COSMOS 3GHz map (Smolčić et al., 2017a), and performed extensive Monte Carlo simulations to characterize

our selection function and validate the robustness of our measurements. We found the following:

- The radio continuum size shows no clear dependence on the stellar mass of SFGs with $10.5 \lesssim \log(M_\star/M_\odot) \lesssim 11.5$, which is the mass range where our sample is not affected by our selection function;

- MS galaxies are preferentially (but not exclusively) extended, while SFGs above the MS are more compact systems; the median size of SFGs on (above) the MS is $R_{\rm eff} = 1.5 \pm 0.2\,(1.0 \pm 0.2)$ kpc. Using the parametrization of the form $R_{\rm eff} \propto (1+z)^{\alpha}$, we found that the median size remains nearly constant with cosmic time, with $\alpha = -0.26 \pm 0.08\,(0.12 \pm 0.14)$ for SFGs on (above) the MS;

- The median radio size of SFGs is smaller (by a factor $1.3 - 2$) than that inferred from optical to UV emission that traces their stellar component (Shibuya et al., 2015). Overall, these results are consistent with compact radio continuum, FIR, and extinction-corrected Hα emission ($\lesssim 1.5$ kpc; e.g., Nelson et al., 2016a; Rujopakarn et al., 2016; Murphy et al., 2017; Cotton et al., 2018; Elbaz et al., 2018; Lindroos et al., 2018);

- Most SFGs follow a linear relation in the $\log(\Sigma_{\rm SFR}) - \Delta\log({\rm SSFR})_{\rm MS}$ plane, consistent with previous studies of SFGs in the local Universe (Lutz et al., 2016) and at $z \sim 1$ (Magdis et al., 2016). While its normalization increases with redshift, its slope becomes steeper at lower redshifts (from $\alpha = 1.5$ at $z \sim 2$ to 2.6 at $z \sim 0.5$);

- There is a fraction ($\lesssim 10\%$) of MS galaxies harboring starburst-like $\Sigma_{\rm SFR}$, consistent with recent evidence of hidden starbursts within the MS at $z \sim 2$ (Elbaz et al., 2018).

Overall, our results suggest that SFGs with enhanced star formation undergo a compaction phase. These systems could be explained in the context of disk instability and/or merger-driven burst of star formation that, depending on the gas content, offset the galaxy from the MS in different proportions (e.g., Fensch et al., 2017; Wang et al., 2018). Since using $\Delta\log({\rm SSFR})$ alone prevents us from identifying those starburst galaxies hidden within the MS, we recommend using $\Sigma_{\rm SFR}$ as well to better identify starbursting systems. Having constraints on $\Sigma_{\rm SFR}$ is the first step towards the characterization of the KS relation at high redshift. Exploring in detail the gas content and optical morphology of SFGs in our sample is the subject of an upcoming manuscript.

2.7 Appendix

2.7.1 Flux boosting

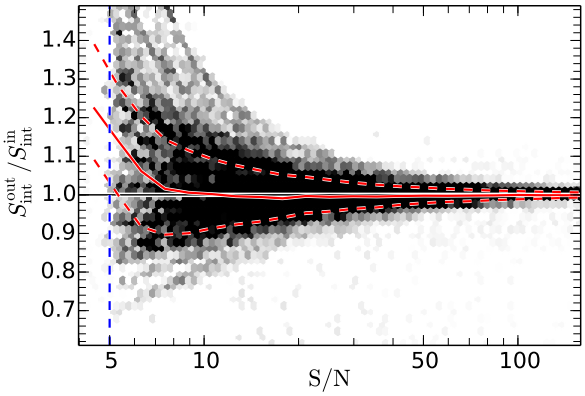

Figure 2.14: Flux boosting for unresolved sources as a function of S/N estimated from MC simulations. The solid and dashed red lines show the 50th percentile, and the 14th and 84th percentiles of the distribution as a function of S/N. The vertical blue dashed line indicates our detection threshold (S/N=5).

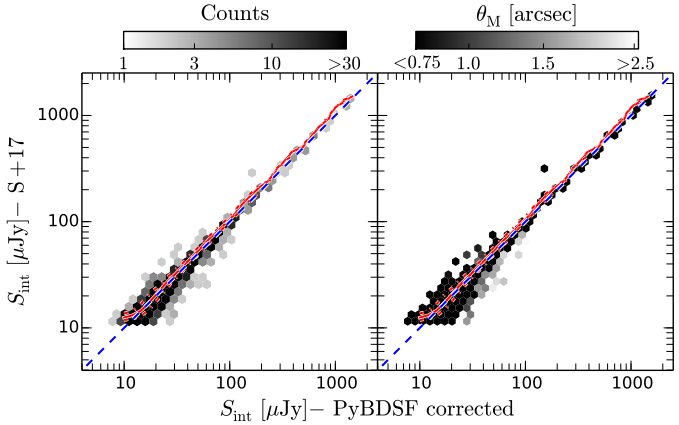

Figure 2.15: Comparison between the flux density of 3184 SFGs in the sample (resolved and unresolved) derived from PyBDSF (corrected) and those reported by Smolčić et al. (2017a). The solid and dashed red lines show the 50th percentile, and 14th and 84th percentiles of the distribution as a function of the flux density reported in this study.

2.7.2 Size evolution of SFGs using uncorrected FWHM and flux density

The extensive Monte Carlo simulations performed in this work indicate that the FWHM and flux density are being overestimated for most of the radio sources in the sample (see Fig. 2.5). Using these values, however, does not systematically affect the trends and relations presented in this work, as initially inferred from Fig. 2.16. First, this approach also leads to a flat relation between the

median radio size and stellar mass of SFGs (Fig. 2.17). Second, we find a similar radio size and $\Sigma_{\rm SFR}$ dichotomy between SFGs on and above the MS (Figs. 2.16 and 2.18). Using uncorrected measurements leads to a smaller fraction of MS galaxies with starburst-like $\Sigma_{\rm SFR}$ (Fig. 2.19), given that the size of faint MS galaxies is overestimated and, consequently, $\Sigma_{\rm SFR}$ becomes smaller. We note that regardless of the use of corrected or uncorrected values, the fraction of starburst-like $\Sigma_{\rm SFR}$ systems remains unclear, due to the presence of MS galaxies that are unresolved in the VLA COSMOS 3GHz map.

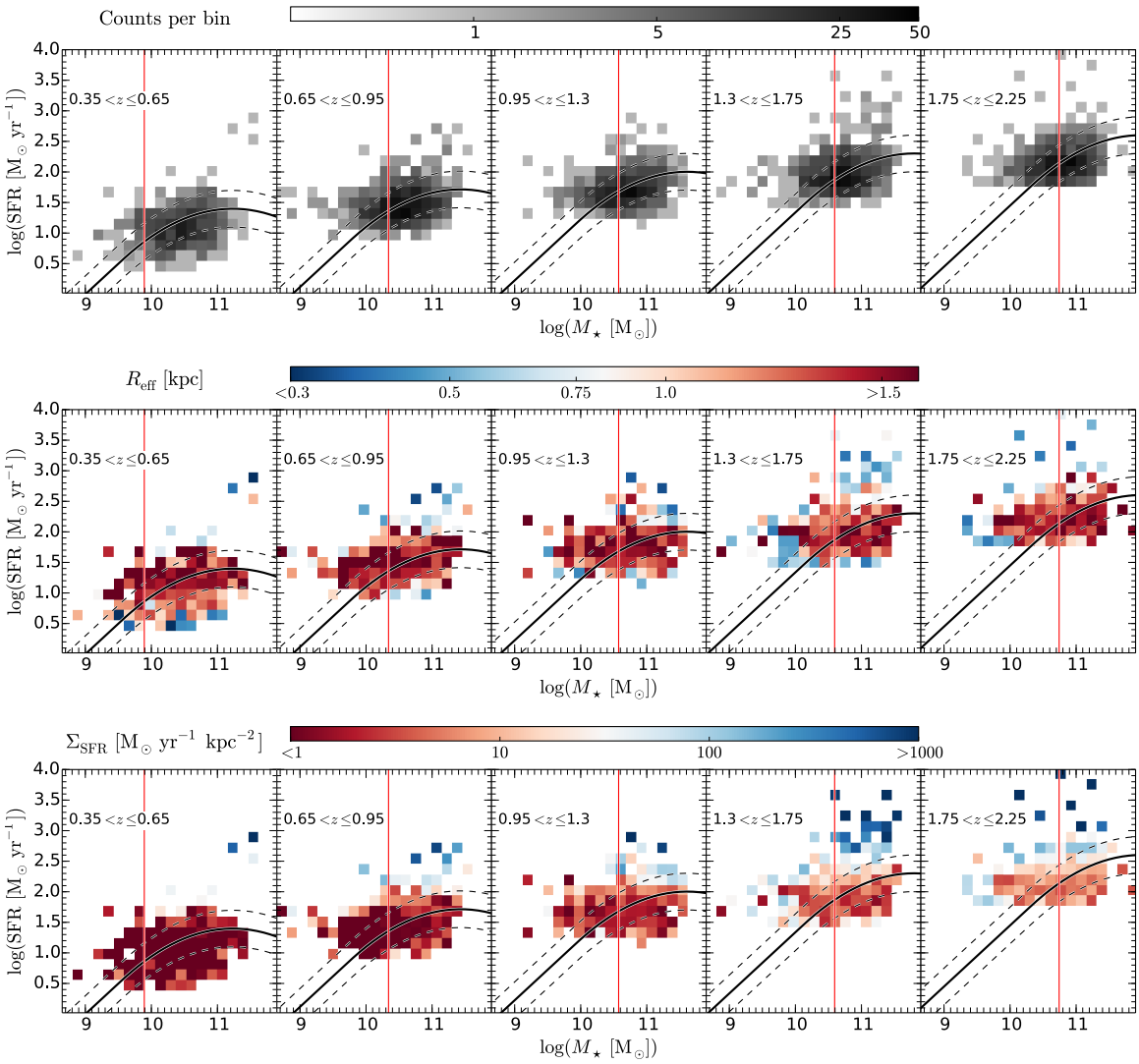

Figure 2.16: *Upper panels:* Sample of 3184 SFGs in the SFR $- M_\star - z$ plane color-coded for the number of sources per bin. Solid and dashed black lines show the position of the MS of SFGs and the associated dispersion given by Schreiber et al. (2015). Vertical red solid lines show the mass-limit above which we consistently probe SFGs on and above the MS. *Middle and lower panels:* Median size and star formation surface density, respectively, of the 3184 SFGs in the sample. We use 1000 MC realizations to include the values for unresolved sources, which are drawn from the distributions described in Sects. 2.4.2 and 2.4.4.

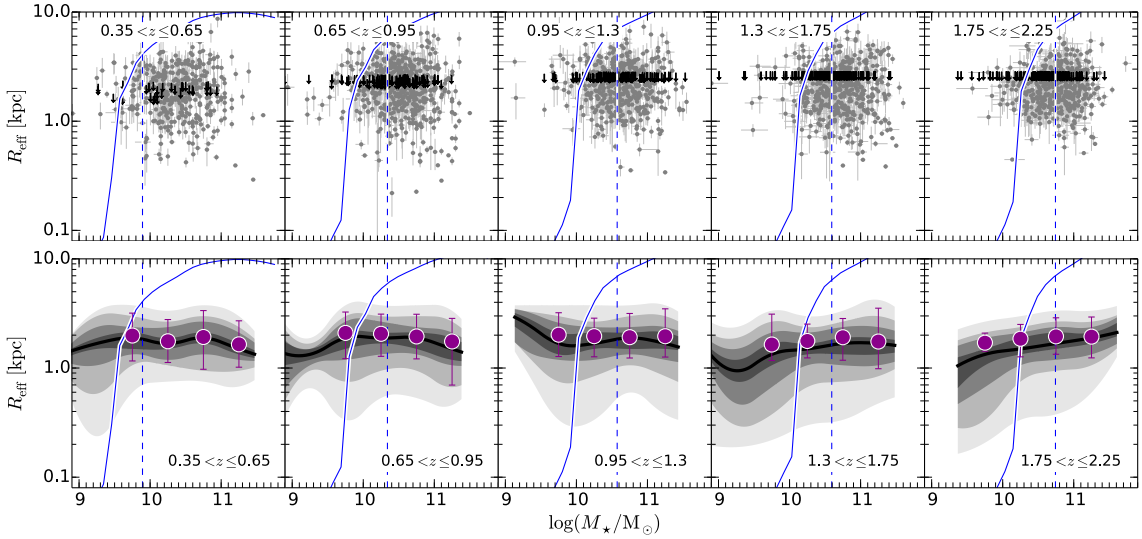

Figure 2.17: Sample of 3184 SFGs in the $R_{\rm eff} - M_\star - z$ plane. The blue solid line shows the maximum size, corresponding to the 10% completeness level, that can be observed for a galaxy with $\Delta\log(\mathrm{SSFR}) = 0$ evaluated at the central redshift value per bin. Blue dashed lines show the mass-limit above which we consistently probe SFGs on and above the MS. Black arrows show the upper limits for the size of unresolved sources. *Lower panels*: Density distribution per stellar mass bin (0.5 dex width) of SFGs in the $R_{\rm eff} - M_\star - z$ plane. Contour levels are at the 10, 20, 30, 40, 50, 60, 70, 80, and 90th percentiles. The median size derived via the KM estimator is shown by the dark magenta circles; the error bars correspond to the 16th and 86th percentiles of the distribution.

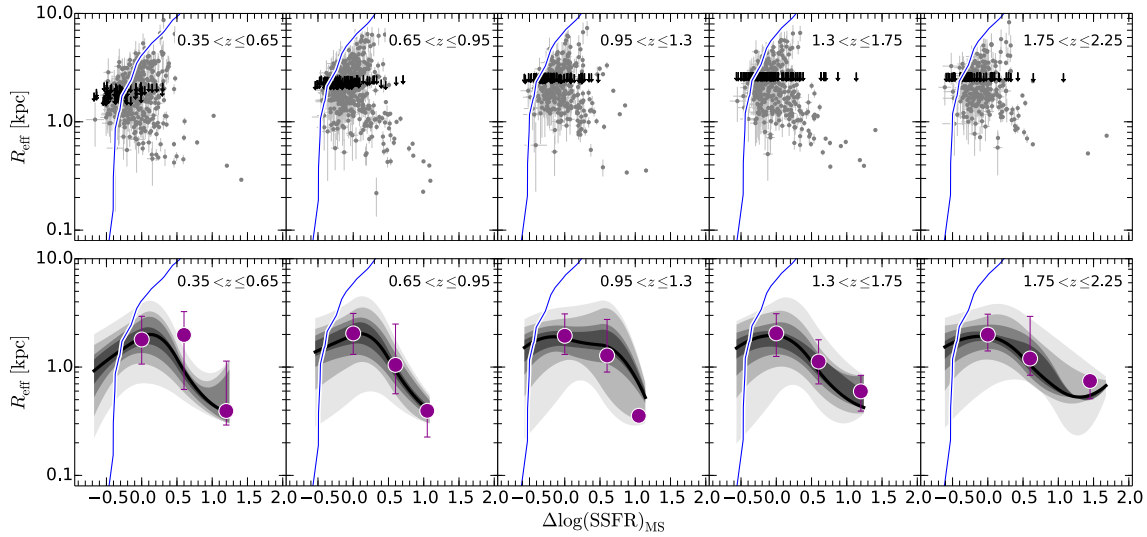

Figure 2.18: *Upper panels:* Star-forming galaxies with $M_\star > M_\star^{\rm lim}$ in the size$-\Delta\log(\mathrm{SSFR}) - z$ plane. The blue solid line shows the maximum size, corresponding to the 10% completeness level, that can be observed for a galaxy with $M_\star = M_\star^{\rm lim}$ evaluated at the central redshift value per bin. Black arrows show the upper limits for the size of unresolved sources. *Lower panels:* Density distribution per $\Delta\log(\mathrm{SSFR})$ bin (0.5 dex width) of SFGs in the size$-\Delta\log(\mathrm{SSFR}) - z$ plane. Contour levels are at the 10, 20, 30, 40, 50, 60, 70, 80, and 90th percentiles. The median size derived via the KM estimator is shown by the dark magenta circles; the error bars correspond to the 16th and 86th percentiles of the distribution.

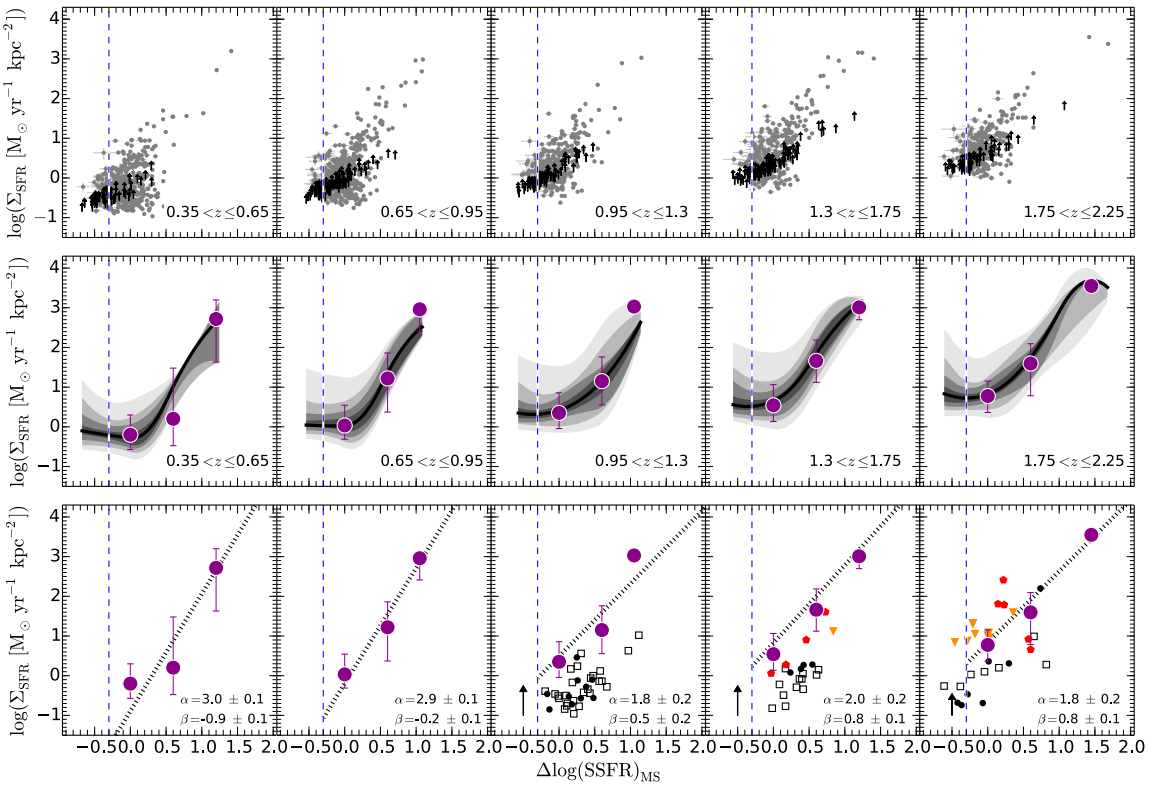

Figure 2.19: *Upper panels:* Star-forming galaxies with $M_\star > M_\star^{\rm lim}$ in the $\Sigma_{\rm SFR} - \Delta\log({\rm SSFR}) - z$ plane. Dashed blue lines show the $\Delta\log({\rm SSFR})$ limit of -0.3 above which our sample of SFGs is complete in terms of distance to the MS. Black arrows show the lower limits for the size of unresolved sources. *Middle panels:* Density distribution per $\Delta\log({\rm SSFR})$ bin (0.4 dex width) of SFGs in the $\Sigma_{\rm SFR} - \Delta\log({\rm SSFR}) - z$ plane. Contour levels are at the 10, 20, 30, 40, 50, 60, 70, 80, and 90th percentiles. The median size derived via the KM estimator is shown by the dark magenta circles; the error bars correspond to the 16th and 86th percentiles of the distribution. *Lower panels:* Power law describing the $\Sigma_{\rm SFR} - \Delta\log({\rm SSFR})$ relation (dotted black line). The slope and normalization are given in the lower right corner. The median size derived via the KM estimator is also shown by the dark magenta circles. For comparison, we present the compilation of SFGs from Genzel et al. (2010, black filled circles), Tacconi et al. (2013, black empty squares), Elbaz et al. (2018, red pentagons), and Lang[†] et al. (2019, orange triangles). Black arrow illustrates the factor to be considered when comparing $\Sigma_{\rm SFR}$ of galaxies in our sample with that reported by Genzel et al. (2010) and Tacconi et al. (2013).

2.7.3 Tables

Table 2.1: Radio continuum size as a function of the stellar mass of SFGs

$\log(M_\star/M_\odot)$ [dex]	$0.35 < z < 0.65$	$0.65 < z < 0.95$	$0.95 < z < 1.30$	$1.30 < z < 1.75$	$1.75 < z < 2.25$
$[10.0, 10.5]$	$1.5^{+1.2}_{-0.8}$	$1.5^{+1.4}_{-0.9}$	...[a]	...	...
$[10.5, 11.0]$	$1.8^{+1.6}_{-1.1}$	$1.5^{+1.4}_{-0.7}$	$1.4^{+1.6}_{-0.7}$	$1.3^{+1.2}_{-0.8}$	$1.2^{+1.4}_{-0.5}$
$[11.0, 11.5]$	$1.5^{+1.4}_{-0.6}$	$1.3^{+1.4}_{-0.8}$	$1.7^{+1.4}_{-0.9}$	$1.2^{+2.2}_{-0.5}$	$1.5^{+1.2}_{-0.8}$

The effective radius is given in kpc. The uncertainties correspond to the 16th and 84th percentiles of the size distribution per stellar mass bin. [a]No values are given for the mass bins that are strongly affected by incompleteness.

Table 2.2: Radio continuum size as a function of distance to the MS of SFGs

$\Delta\log(\mathrm{SSFR})_{\mathrm{MS}}$ [dex]	$0.35 < z < 0.65$	$0.65 < z < 0.95$	$0.95 < z < 1.30$	$1.30 < z < 1.75$	$1.75 < z < 2.25$
$[-0.3, 0.3]$	$1.7^{+1.3}_{-1.0}$	$1.5^{+1.3}_{-0.8}$	$1.4^{+1.5}_{-0.8}$	$1.5^{+1.2}_{-0.9}$	$1.5^{+1.2}_{-0.7}$
$[0.3, 0.9]$	$1.0^{+2.0}_{-0.7}$	$1.0^{+2.0}_{-0.6}$	$1.3^{+1.7}_{-0.7}$	$0.9^{+0.6}_{-0.5}$	$0.9^{+1.0}_{-0.3}$
> 0.9[a]	$0.4^{+0.8}_{-0.1}$	$0.4^{+0.1}_{-0.2}$	$0.5^{+0.1}_{-0.2}$	$0.7^{+0.2}_{-0.2}$	$0.8^{+0.1}_{-0.3}$

The effective radius is given in kpc. The uncertainties correspond to the 16th and 84th percentiles of the size distribution per $\Delta\log(\mathrm{SSFR})_{\mathrm{MS}}$ bin. The minimum stellar mass probed throughout the different redshift bins is $\log(M_\star^{\mathrm{lim}}/M_\odot) = 9.9, 10.2, 10.5, 10.5$, and 10.7. [a]The highest $\Delta\log(\mathrm{SSFR})_{\mathrm{MS}}$ bin is centered at $\Delta\log(\mathrm{SSFR})_{\mathrm{MS}} = 1.2, 1.05, 1.05, 1.45, 1.45$.

Table 2.3: Star formation surface density (Σ_{SFR}) as a function of distance to the MS of SFGs

$\Delta\log(\mathrm{SSFR})_{\mathrm{MS}}$ [dex]	$0.35 < z < 0.65$	$0.65 < z < 0.95$	$0.95 < z < 1.30$	$1.30 < z < 1.75$	$1.75 < z < 2.25$
$[-0.3, 0.3]$	$0.8^{+2.9}_{-0.6}$	$1.7^{+7.0}_{-1.2}$	4^{+15}_{-3}	8^{+27}_{-6}	12^{+29}_{-9}
$[0.3, 0.9]$	5^{+31}_{-4}	15^{+123}_{-14}	14^{+49}_{-12}	63^{+194}_{-50}	96^{+135}_{-66}
> 0.9[a]	412^{+900}_{-380}	1140^{+190}_{-900}	1435^{+100}_{-1200}	690^{+610}_{-250}	2860^{+100}_{-970}

Σ_{SFR} is given in $M_\odot\,\mathrm{yr}^{-1}\,\mathrm{kpc}^{-2}$. The uncertainties correspond to the 16th and 84th percentiles of the Σ_{SFR} distribution per $\Delta\log(\mathrm{SSFR})_{\mathrm{MS}}$ bin. The minimum stellar mass probed throughout the different redshift bins is $\log(M_\star^{\mathrm{lim}}/M_\odot) = 10.0, 10.2, 10.5, 10.5$, and 10.7. [a]The highest $\Delta\log(\mathrm{SSFR})_{\mathrm{MS}}$ bin is centered at $\Delta\log(\mathrm{SSFR})_{\mathrm{MS}} = 1.2, 1.05, 1.05, 1.45, 1.45$.

CHAPTER 3

The conditions for star formation in massive disk galaxies 1.3 Gyr after the Bing Bang

We combine ^{12}CO(2→1), ^{12}CO(5→4), and [CII] line observations from the NOEMA, ALMA, and VLA telescopes to unveil the conditions for star formation in AzTEC/C159 and AzTEC2-A: two SMGs at $z \sim 4.6$ that exhibit vigorous star formation activities. Based on their IR luminosity, we infer a SFR of the order of 1500 $M_\odot$ yr^{-1} for AzTEC2-A, and half of it for AzTEC/C159. Similarly, ^{12}CO line measurements indicate that AzTEC2-A harbors a molecular gas reservoir ($M_{\rm H_2} \sim 3 \times 10^{11}\,M_\odot$) that is two times that of AzTEC/C159. These properties suggest that the enhanced stellar birthrate of these galaxies is explained by the combination of a vast gas reservoir and –to some extent– enhanced star formation efficiency ($\equiv$ SFR$/M_{\rm H_2}$), similarly to those observed in merger-driven starbursts and SMGs at $z \sim 2$. Nevertheless, the CO→H_2 conversion factor, star formation surface density and/or gas depletion time scale suggest that AzTEC/C159 and AzTEC2-A are forming stars through a secular mode of star formation, as observed in star-forming disks at lower redshifts. Certainly, high-resolution [CII] line observations have uncovered a rotating [CII] disk in AzTEC/C159 (previously reported in the literature) and AzTEC2-A (this work). The implications of these findings are multi-fold. First, this study demonstrates that the SMG population at $z \gtrsim 3$ is rather heterogeneous, including gas-rich mergers and secular disk galaxies. Second, consistent with numerical simulations, our results indicate that the enhanced gas supply from cosmological filaments at high redshift can build and maintain an unstable gas-rich disk, which breaks into giant clumps that form stars nearly as efficiently as in merger-driven systems. Third, our analysis strengthens the emerging scenario whereby merging activity mildly enhance the –already intense– production of stars in early galaxies. Thus, at $z \gtrsim 4$, there is only a subtle difference between the integrated/global properties of star formation in massive, secular disk galaxies and merger-driven starbursts.

Section 3.2 is a reproduction from the article "Molecular gas in AzTEC/C159: a star-forming disk galaxy 1.3 Gyr after the Big Bang", which was published in Astronomy & Astrophysics under the reference:

Jiménez-Andrade, E. F., Magnelli, B., Karim, A., et al., 2018, A&A, 615, A25.

Section 3.3 is part of a forthcoming manuscript, which is being prepared in collaboration with J. Zavala, B. Magnelli, C. Casey, D. Liu, E. Romano-Díaz, A. Karim, and F. Bertoldi.

3.1 Introduction

As discussed in Chapter 1, and demonstrated in Chapter 2, the stellar mass assembly of galaxies can proceed in two modes: the cold gas accretion and merger mode (e.g., L´Huillier et al., 2012; Hayward et al., 2012). Observations of local/low-redshift galaxies initially suggested that these processes lead to two distinctive regimes of star formation (e.g., Kennicutt, 1998a). Dissipative mergers of gas-rich galaxies lead to short-lived and compact starbursts – as observed in local ULIRGs (Armus et al., 1987; Sanders & Mirabel, 1996; Ellison et al., 2013); whereas steady accretion of cool gas (from the intergalactic medium) drives widespread star formation in disk galaxies (e.g., Dekel et al., 2009b; Bouché et al., 2013), which remain confined within the MS of SFGs over Gyr-timescales (e.g., Tacchella et al., 2016). Observational studies at high redshift suggest that the contrast between merger-driven starbursts and secular star-forming disks remains out to $z \sim 2$ (e.g., Genzel et al., 2010; Daddi et al., 2010) – although some exceptions apply (e.g., non-merger starbursts and/or mergers that weakly enhance star formation; e.g., Elbaz et al., 2018; Jiménez-Andrade[†] et al., 2019). Whether the same dichotomy in the star formation processes holds at even higher redshifts, i.e. $z \gtrsim 2$, remains to be confirmed.

Sub-mm selected galaxies (SMGs; see Casey et al., 2014, for a review) have acquired particular relevance to probe the merger and cold gas accretion mode in the yet unexplored $z > 3$ regime (e.g., Carilli et al., 2010; Hayward et al., 2012). Although the "canonical" formation scenario of these massive starbursts (SFR= $10^{2-3}\,M_{\odot}\mathrm{yr}^{-1}$) involves major gas-rich mergers (e.g., Tacconi et al., 2006, 2008; Engel et al., 2010; Narayanan et al., 2010), recent observational (and theoretical) evidence indicates that highly active star-forming disks can also lead to SMG-like luminosities (e.g., Davé et al., 2010; Hodge et al., 2012, 2016; Narayanan et al., 2015; Hayward et al., 2018; Tadaki et al., 2018). A heterogeneous SMG population, i.e., secular disks and major mergers, could also explain the diversity of quiescent massive galaxies at $z \sim 2-3$ (e.g., Gobat et al., 2012; Toft et al., 2012, 2017). Indeed, whereas the structure and dynamics of most of those quiescent systems seem to be a result of compact, merger-driven SMGs at $z > 3$ (Toft et al., 2014; Ikarashi et al., 2015; Fudamoto et al., 2017; Gómez-Guijarro[†] et al., 2018a), the progenitors of quiescent disk galaxies at $z \sim 2$ (Newman et al., 2012; Toft et al., 2017) might have hosted enhanced star formation distributed across a massive rotating disk.

Despite the evident needs to characterize the properties of $z > 3$ massive star-forming disks, only limited/small samples of such galaxies exist (e.g., Hodge et al., 2012; De Breuck et al., 2014; Jones et al., 2017; Shao et al., 2017). Over the two square degrees of the COSMOS field, for instance, only AzTEC1 ($z = 4.341$), AzTEC/C159 ($z = 4.569$), J1000+0234 ($z = 4.542$), and Vd−17871 ($z = 4.622$) exhibit robust evidence of a gas-dominated rotating disks (Jones et al., 2017; Tadaki et al., 2018, Karim et al. in prep., hereafter K19). Consequently, these systems emerge as key laboratories to investigate the role of cold gas accretion in driving extreme levels of star formation in the early Universe. This has motivated the present research project, in which we explore the physical conditions of the star-forming gas in two rotation-dominated SMGs at $z \sim 4.6$: AzTEC/C159 and AzTEC2.

This chapter is organized as follows. In Sect. 3.2, we use deep observations from the VLA and NOEMA telescope to detect the ^{12}CO(2→1) and ^{12}CO(5→4) emission lines towards AzTEC/C159. We use the low−J ^{12}CO emission line to constrain the mass and extent of the molecular gas reservoir; in combination with the high−J ^{12}CO line detection, we infer the overall excitation conditions of the molecular gas in this high-redshift rotating disk. In Sect. 3.3, we employ [CII] and ^{12}CO(5→4) line observations, from the ALMA and NOEMA telescope, respectively, to constrain the redshift, gas content, and dynamics in AzTEC2: a pair of galaxies at $z \sim 4.6$ in which the major component shows indications of a rotation-dominated disk. The broader implications of this research project on the cold gas accretion and merger mode of star formation are given in Sect. 3.4, while in Sect. 3.5 we summarize our results. As in the previous chapter, we adopt a flat ΛCDM cosmology with $h_0 = 0.7$, $\Omega_M = 0.3$, and $\Omega_\Lambda = 0.7$.

3.2 AzTEC/C159

AzTEC/C159 was originally detected at the 3.7σ level in the ASTE/AzTEC-COSMOS 1.1 mm survey of the inner COSMOS 1 deg^2 (Aretxaga et al., 2011). Long-slit spectroscopy with DEIMOS/Keck has revealed a narrow Lyα line, which places AzTEC/C159 at a redshift $z = 4.569$ (Smolčić et al., 2015). The broadband spectral energy distribution (SED) from the optical through the FIR is consistent with a dusty star-forming galaxy, with an SFR of $\sim 700\,M_\odot\,\mathrm{yr}^{-1}$, a stellar mass of $(4.5 \pm 0.4) \times 10^{10}\,M_\odot$, and a dust mass of $2.0^{+3.0}_{-1.2} \times 10^9\,M_\odot$ (Smolčić et al., 2015; Gómez-Guijarro† et al., 2018a, hereafter GG18). High-resolution [CII] 158 μm line observations (FWHM = 0.36 arcsec) with the Atacama Large Millimeter/submillimeter Array (ALMA; project 2012.1.00978.S, PI: A. Karim) have revealed a double-horn profile, while the [CII] 158μm first moment and channel maps are well described by the classic pattern for rotating disks (Jones et al., 2017). AzTEC/C159 complements the sample of galaxies at $z > 4$ exhibiting regular gas rotation on kiloparsec scales (i.e., disks): GN20 ($z = 4.05$), ALESS73.1 ($z = 4.755$), J1000+0234 ($z = 4.542$), Vd−17871 ($z = 4.622$), and J1319+0950 ($z = 6.127$, Hodge et al., 2012; De Breuck et al., 2014; Jones et al., 2017; Shao et al., 2017, K19). The kinematic signatures of rotation revealed by ALMA (Jones et al., 2017), including evidence of a flat rotation curve at large radius, render AzTEC/C159 one of the best examples to date for an apparently rotating disk galaxy in the early Universe. We note, however, that given the achieved ~ 2.3 kpc resolution ALMA observations, we cannot completely rule out a merging scenario from the [C II] line dynamical analysis alone. In this context, studies that probe the physical properties of the interstellar medium (ISM), for example, molecular gas, are also key to indirectly probe the dominant mode of star formation in this system.

3.2.1 Karl G. Jansky VLA and NOEMA observations

^{12}CO(2→1) line observations were carried out in January 2016 with the *Karl G. Jansky* Very Large Array (VLA) of the NRAO in the D– and DnC–configurations (project 15B-280, PI: A. Karim). Five observing sessions of 3.5 hr each resulted in a total of 17.5 hr, with 9.0 hr on target. We used the quasar 3C286 for bandpass, delay, and flux calibration, and J1038+0512 for complex gain calibration. We made use of the *Q*-band receivers and the pair of 8-bit samplers on each VLA antenna, resulting in a pair of 1.024 GHz bands in right and left circular polarization. These bands were overlapped by 128 MHz to correct for the loss of signal at their edges, so that the total bandwidth was 1.92 GHz (from 40.963 to 42.883 GHz), which covers the redshifted ^{12}CO(2→1) line at 41.41 GHz, according to the prior redshift estimation of $z = 4.567 \pm 0.002$ based on the [CII] 158μm line detection with ALMA (Jones et al., 2017). Data were calibrated using the Common Astronomy Software Applications (CASA). Images were created with the CASA task `clean` and using a range of robust parameters. Ultimately, we used the image computed with robust=1 as it provides the best balance between spatial resolution and rms noise. This results in a data cube with a synthesized beam size of 1.70×1.24 arcsec resolution (PA = 77.5°) with an rms of 0.05 mJy beam^{-1} for 27 MHz (~ 200 km s^{-1}) wide channels.

The ^{12}CO(5→4) line was observed with the NOrthern Extended Millimeter Array (NOEMA) interferometer on December 8, 2015, and January 19, 2016, over two tracks (project 15CX001, PI: A. Karim) in D- and C-configuration. We used the WideX correlator, which covers a frequency range of 3.6 GHz. The tuning frequency of 103.51 GHz was chosen to encompass the redshifted ^{12}CO(5→4) line, considering $z = 4.567 \pm 0.002$. We used the quasars 3C84 and B0906+015 as flux and phase or amplitude calibrators, respectively. The data calibration and mapping were performed with the IRAM GILDAS software packages `clean` and `mapping`. The final cube corresponds to 9.4 hr on source out of ~19 hr of total observing time, with a synthesized beam size of 5.0×2.6 arcsec and PA= 23.5° (using natural weighting). We reach a sensitivity of 0.13 mJy beam^{-1} per 200 km s^{-1} wide channel.

3.2.2 Analysis and results

CO lines

The ^{12}CO(2→1) and ^{12}CO(5→4) integrated lines are detected at the 5.5 and 8.1σ level, respectively. Fig. 3.1 shows the intensity maps integrated over ~1500 km s^{-1} where significant line emission was detected. The peak position of the ^{12}CO lines spatially coincides with that of the [CII] 158 μm line (Jones et al., 2017) within the positional uncertainties of ~0.2 and 0.5 arcsec, respectively. The ^{12}CO(2→1) line spectrum was extracted within an ellipse of 2.1×1.7 arcsec (PA = 90 deg). This aperture contains the total extent of the [CII] 158 μm line emission (~7 kpc; Jones et al., 2017) and ensures that no flux is missed. We fit Gaussians to the ^{12}CO line spectra within ±850 km s^{-1} of the centroid (see Fig. 3.1) and measured an FWHM of 750 km s^{-1} for both lines. The line emission of ^{12}CO(2→1) is centered at 41.425 ± 0.02 GHz, giving $z = 4.565 \pm 0.003$; and the ^{12}CO(5→4) centroid at 103.550 ± 0.05 GHz yields $z = 4.565 \pm 0.003$. These values are in agreement with the redshift derived from the [CII] 158 μm line of 4.567 ± 0.002 (K19). Finally, we measured an integrated flux of 105 ± 19 mJy km s^{-1} for the ^{12}CO(2→1) line and 417 ± 51 mJy km s^{-1} for ^{12}CO(5→4). We verified that the latter values differ by less than 6% from those derived by adding individual flux densities per channel within the velocity range used in the Gaussian fit.

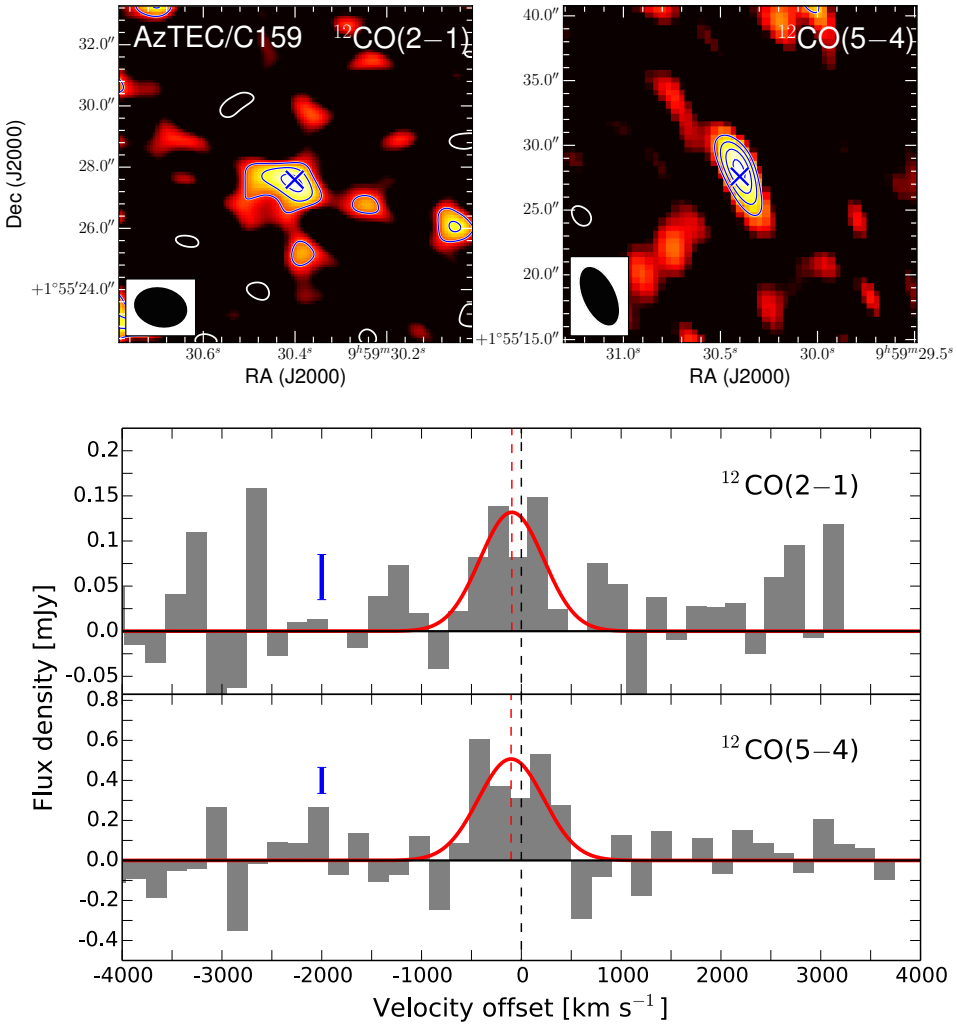

Figure 3.1: *Upper panels:* Velocity-integrated intensity maps of the ^{12}CO(2→1) and ^{12}CO(5→4) line. We integrated emission within the velocity range of ±750 km s^{-1}, i.e. about 8 channels, where significant line emission was detected. The contour levels of the ^{12}CO(2→1) line emission map are at [-2, 2, 3, 4] × 1σ, with σ = 0.05 mJy beam^{-1} per 200 km s^{-1} wide channel. Negative contours are shown in white and positive contours in blue. The beam size of 1.70 × 1.24 arcsec is plotted in the bottom left corner. The blue cross denotes the peak position of the [CII] 158 μm emission line. In the right panel we show the velocity-integrated intensity map of the ^{12}CO(5→4) line emission. Contour levels are at [-3, 3, 4, 5, 6] × 1σ, with σ = 0.13 mJy beam^{-1} per 200 km s^{-1} wide channel. The beam size of 5.0 × 2.6 arcsec is also plotted in the bottom left corner. *Lower panels:* ^{12}CO(2→1) and ^{12}CO(5→4) line spectra binned to 200 km s^{-1} channels. The red solid lines are Gaussian fits to the line spectra, the central position is shown by the red dashed lines. The blue error bar denotes the typical 1σ rms value.

The measured ^{12}CO integrated line flux of high-redshift galaxies is influenced by cosmic microwave background (CMB) emission. While the higher temperature of the CMB at $z = 4.5$ enhances the line excitation, the background against which the ^{12}CO lines are measured also increases (e.g., da Cunha et al., 2013). For example, in a dense ISM ($n_{\rm H_2} = 10^{4.2}{\rm cm}^{-3}$), with a gas kinetic temperature of $T_{\rm kin} = 40$ K, we can measure 70% and 80% of the intrinsic value of the ^{12}CO(2→1) and ^{12}CO(5→4) line, respectively. In low-density environments ($n_{\rm H_2} = 10^{3.2}{\rm cm}^{-3}$) with $T_{\rm kin} = 18$ K, only 20% of the intrinsic value of the ^{12}CO(2→1) line is detected, and less than that for ^{12}CO(5→4) (da Cunha et al., 2013). Unfortunately, we lack estimates for the gas density and kinetic temperature in AzTEC/C159. It is known, however, that high SFR is likely to be associated with high temperatures of gas and dust as well as gas density (e.g., Narayanan & Krumholz, 2014). Under the assumption of thermodynamic equilibrium between the gas and dust, we would have $T_{\rm kin} \simeq T_{\rm dust} = 37$ K (from our mid-infrared (MIR)−millimeter spectral energy distribution (SED) fitting presented in Sect. 3.2.2). Therefore, we favor the scenario with dense gas and $T_{\rm kin} = 40$ K that yields an increase in $S_{\rm CO(2\rightarrow1)}$ and $S_{\rm CO(5\rightarrow4)}$ by a factor [1/0.7] and [1/0.8], respectively (da Cunha et al., 2013). Consequently, we derive $S^{\rm intrinsic}_{\rm CO(2\rightarrow1)} = 150 \pm 27$ mJy km s^{-1} and $S^{\rm intrinsic}_{\rm CO(5\rightarrow4)} = 521 \pm 64$ mJy km s^{-1}.

In Fig. 3.2 we compare the ^{12}CO and [CII] 158 μm line profiles. We find that the ^{12}CO lines are as broad as the [CII] 158 μm line (Jones et al., 2017), all with an FWHM $\sim$ 750 km s^{-1}. There is also marginal evidence of double-horn profiles in the two ^{12}CO lines, where two peaks are close to or above the 3σ level. To constrain the size of the ^{12}CO(2 → 1) line emitting region, we fit a single Gaussian model to the uv data and find evidence for a point-like structure. Based on the synthesized beam size and signal-to-noise ratio (S/N) of the line detection, we used the results from Martí-Vidal et al. (2012, Eq. (7)) to estimate an upper limit of ∼1 arcsec for the source size, which corresponds to an intrinsic size of $\sim$ 6.5 kpc at the redshift of AzTEC/C159. An extended and possibly rotating molecular gas reservoir would be consistent with the [CII] 158 μm gas extent (∼7 kpc) and dynamics of AzTEC/C159 (Jones et al., 2017). However, we advise caution when interpreting our results on the ^{12}CO size and dynamics of AzTEC/C159 because of the current limitation of our ^{12}CO line observations.

FIR properties

Continuum emission from AzTEC/C159 was detected at 3 mm from our NOEMA observations. By averaging line-free channel maps, around the ^{12}CO(5→4) centroid at 103.550 GHz, we derived a value of 220 ± 40 μJy. No continuum emission was detected in our VLA observations at $\sim$ 7 mm; based on the noise level of the continuum image, we derive a 3σ upper limit of 20 μJy. These new millimeter data points mitigate the uncertainties in determining the FIR properties of AzTEC/C159.

We derived the infrared luminosity ($L_{\rm IR}$; in the range 8 − 1000 μm), SFR, and dust mass ($M_{\rm dust}$) of AzTEC/C159 via MIR−millimeter SED fitting using the Draine & Li (2007) dust model. We refer to Smolčić et al. (2015) for a detailed description of the fitting process. As shown in Fig. 3.3, in addition to our millimeter SED constraints, the 1.1 mm data point from the JCMT/AzTEC 1.1 mm survey (Scott et al., 2008), and the ALMA 870 μm continuum data point (GG18), we used observations from the *Herschel* Space Observatory (Pilbratt et al., 2010) toward the COSMOS field: those from the Photodetector Array Camera and Spectrometer (PACS at 100 and 160 μm; Lutz et al., 2011) as well as from the

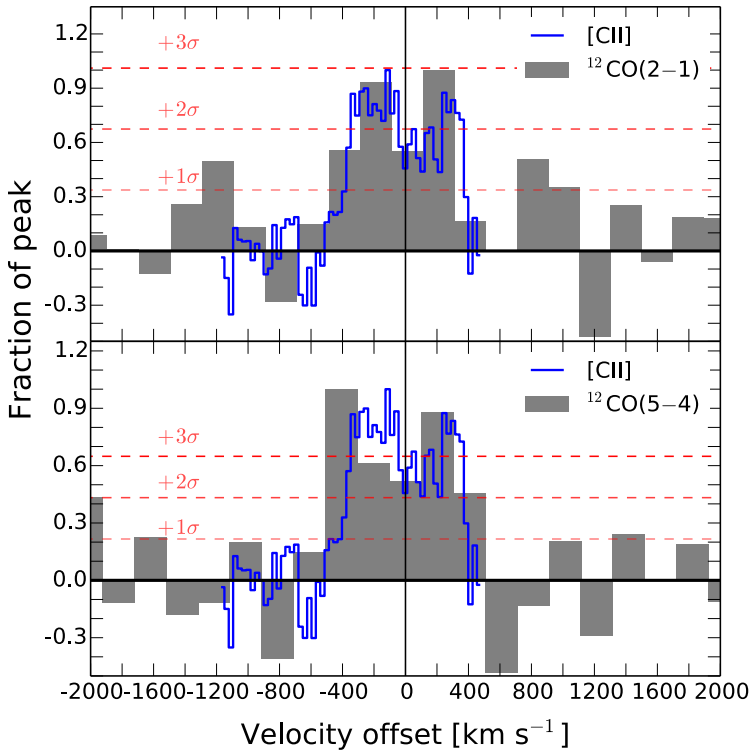

Figure 3.2: [CII] 158 μm line spectrum of AzTEC/C159 (blue line; Jones et al., 2017) together with the ^{12}CO (2→1) and ^{12}CO (5→4) detections from VLA and NOEMA, respectively. Each line is renormalized by its peak intensity. Red dashed lines show the typical noise level per channel.

Spectral and Photometric Imaging Receiver (SPIRE at 250, 350, and 500 μm; Oliver et al., 2012). We find $L_{\rm IR} = 7.4^{+2.1}_{-1.7}\times10^{12}\ L_\odot$, $T_{\rm dust} = 37\pm3$ K, $M_{\rm dust} = 2.5^{+0.6}_{-0.5}\times10^{9}\ M_\odot$. By assuming a Chabrier initial mass function (IMF) and the relation SFR $[M_\odot {\rm yr}^{-1}]=10^{-10}L_{\rm IR}[L_\odot]$ (Kennicutt, 1998a), we estimate an SFR=$740^{+210}_{-170}\ M_\odot {\rm yr}^{-1}$. The derived $L_{\rm IR}$ and $T_{\rm dust}$ are 0.3 dex and 5 K higher, respectively, than the characteristic values for the full ALESS SMG sample with a median redshift of ~2.5 (Swinbank et al., 2014). Similar to the $z > 4$ SMGs presented by Smolčić et al. (2015), AzTEC/C159 lies at the high end of the $L_{\rm IR} - T_{\rm dust}$ correlation (e.g., Chapman et al., 2005; Magnelli et al., 2012), consistent with an extrapolation of the trend for *Herschel*-selected $0.1 < z < 2$ infrared galaxies (Symeonidis et al., 2013).

Molecular gas mass and star formation efficiency

The molecular gas mass can be estimated from the relation

$$M_{\rm H_2} = \alpha_{\rm CO} L'_{\rm CO}\ , \tag{3.1}$$

where $\alpha_{\rm CO}$ is the conversion factor of CO luminosity to H_2 mass, and $L'_{\rm CO}$ is the ^{12}CO(1→0) line luminosity. The latter can be derived from our ^{12}CO(2→1) line assuming that $L'_{\rm CO} = 1.18 L'_{\rm CO(2\to1)}$

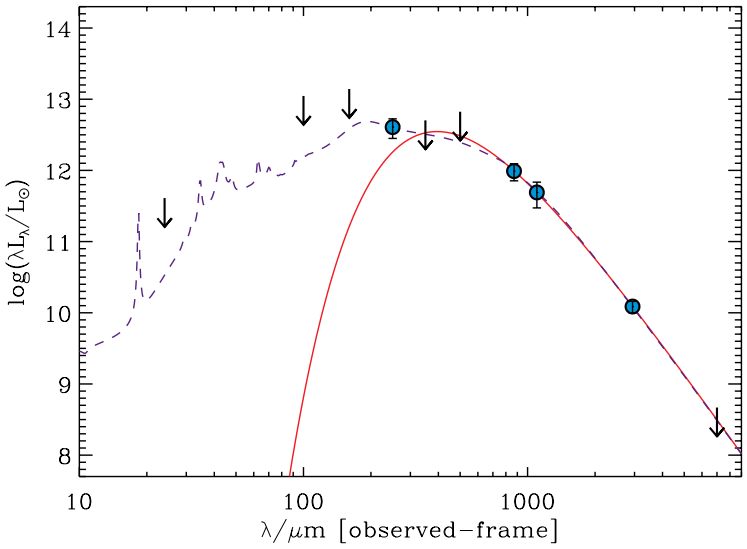

Figure 3.3: Broadband SED of AzTEC/C159. The best-fit Draine & Li (2007) model is shown with the blue dashed line. A modified blackbody (red line) is used to fit the FIR-to-millimeter data points. The monochromatic flux densities from *Herschel* PACS/SPIRE and JCMT/AzTEC observations used in the fit are listed as follows: $S_{100\mu m} < 6.8$ mJy, $S_{160\mu m} < 13.6$ mJy, $S_{250\mu m} = 6.2 \pm 1.9$ mJy, $S_{350\mu m} < 10.8$ mJy, $S_{500\mu m} < 20.4$ mJy, and $S_{1.1mm} = 3.3 \pm 1.3$ mJy (Smolčić et al., 2015). We add three more submillimeter/millimeter data points from our observations: $S_{870\mu m} = 6.9 \pm 0.2$ mJy (GG18), $S_{3mm} = 220 \pm 40\,\mu$Jy, and $S_{7mm} < 20\,\mu$Jy. The downward-pointing arrows denote upper limits to the corresponding flux densities.

for typical SMG excitation conditions (consistent with the results in Sect. 3.2.2) and using the relation (Carilli & Walter, 2013)

$$L'_{CO(2\rightarrow1)} = 3.25 \times 10^7 S_{CO(2\rightarrow1)} \nu^{-2}_{CO(2\rightarrow1)} D^2_L (1+z)^{-1}, \tag{3.2}$$

where $S_{CO(2\rightarrow1)}$ is the integrated line flux in Jy km s^{-1}, $\nu_{CO(2\rightarrow1)}$ is the rest-frame frequency of the ^{12}CO(2→1) line in GHz, and D_L is the luminosity distance in Mpc. Based on $S^{intrinsic}_{CO(2\rightarrow1)}$ (i.e., the corrected value from the CMB) and Eq. (3.2), we derive $L'_{CO} = (3.4 \pm 0.6) \times 10^{10}$ K km s^{-1} pc^2.

The value for α_{CO} depends on local ISM conditions and may consequently vary across different galaxy types (Daddi et al., 2010; Papadopoulos et al., 2012a; Magnelli et al., 2012; Bolatto et al., 2013). According to Papadopoulos et al. (2012a), the main driver of the α_{CO} value is the average dynamical state of the molecular gas. As a result, while low values for α_{CO} could be related to highly turbulent molecular gas, which is likely associated with merging systems, as observed in local ultra-luminous infrared galaxies (ULIRGs) with $\alpha_{CO} = 0.8\,M_\odot$ K^{-1} km^{-1} s pc^{-2} (e.g., Downes & Solomon, 1998), self-gravitating gas yields high α_{CO} values (e.g., Papadopoulos et al., 2012b) as in star-forming spiral disks like the Milky Way with $\alpha_{CO} = 4.3\,M_\odot$ K^{-1} km^{-1} s pc^{-2} (e.g., Abdo et al., 2010). Spatially resolved observations of nearby SFGs have also probed that α_{CO} might vary within the galaxy itself, where central values could be significantly lower than the galaxy average (Sandstrom et al., 2013). For high-redshift unresolved sources, on the other hand, we have to rely

Table 3.1: Properties of AzTEC/C159

Properties	**Units**	**Values**	
		^{12}CO(2→1)	^{12}CO(5→4)
FWHM	km s^{-1}	750 ± 200	770 ± 360
Peak flux	mJy	0.13 ± 0.05	0.50 ± 0.13
Integrated flux	mJy km s^{-1}	105 ± 19[a]	417 ± 51[a]
Peak frequencies	GHz	41.425 ± 0.020	103.550 ± 0.050
z[b]	...	4.567±0.002	
RA, Dec[b]	...	09:59:30.401 +01:55:27.59	
$L_{\rm IR}$	$L_\odot$	$7.4^{+2.1}_{-1.7} \times 10^{12}$	
SFR	$M_\odot$ yr^{-1}	740^{+210}_{-170}	
$M_\star$[c]	$M_\odot$	$(4.5 \pm 0.4) \times 10^{10}$	
$M_{\rm dust}$	$M_\odot$	$2.5^{+0.6}_{-0.5} \times 10^{9}$	
$M_{\rm dyn}$[d]	$M_\odot$	$2.8^{+1.1}_{-0.6} \times 10^{11}$	
$S_{103\rm GHz}$	μJy	220±40	
$S_{41\rm GHz}$	μJy	< 20	
$L'_{\rm CO}$[e]	K km s^{-1} pc^2	$(3.4 \pm 0.6) \times 10^{10}$	
$M_{\rm H_2}(\alpha_{\rm CO}/4.3)$[e]	$M_\odot$	$(1.5 \pm 0.3) \times 10^{11}$	
$\tau_{\rm gas} \times (\alpha_{\rm CO}/4.3)$[e]	Myr	200 ± 100	
$\mu_{\rm gas} \times (\alpha_{\rm CO}/4.3)$[e]	...	3.3 ± 0.7	
$L_{\rm IR}/L'_{\rm CO}$	$L_\odot$(K km s^{-1} pc^2)$^{-1}$	216 ± 80	

[a] After considering the CMB effect, the integrated flux density of ^{12}CO(2→1) and ^{12}CO(5→4) will increase by a factor [1/0.7] and [1/0.8], respectively (see Sect. 3.2.2). We use the corrected value, i.e., $S^{\rm intrinsic}_{\rm CO(2\rightarrow1)} = 150 \pm 27$ mJy km s^{-1} and $S^{\rm intrinsic}_{\rm CO(5\rightarrow4)} = 521 \pm 64$ mJy km s^{-1}.
[b] Karim et al. (in prep.). [c] Gómez-Guijarro† et al. (2018a).
[d] Jones et al. (2017); within a radius of 2.9 kpc. [e] Values corrected for the CMB.

on an average $\alpha_{\rm CO}$ that reflects the overall physical conditions of the molecular gas. Since (Jones et al., 2017) have revealed a rotationally supported gas disk in AzTEC/C159, it is likely that the bulk of the molecular gas is in self-gravitating clouds, pointing toward a Milky Way-like $\alpha_{\rm CO}$ value. We discuss the nature of $\alpha_{\rm CO}$ in this source in more detail and validate this assumption in Sect. 4.5. By adopting $\alpha_{\rm CO} = 4.3\,M_\odot\,{\rm K}^{-1}\,{\rm km}^{-1}\,{\rm s\,pc}^{-2}$, we find $M_{\rm H_2} = (1.5 \pm 0.3) \times 10^{11}\,M_\odot$. Together with the stellar mass of AzTEC/C159 of $M_\star = (4.5 \pm 0.4) \times 10^{10} M_\odot$ (GG18), we estimate a gas fraction of $\mu_{\rm gas} \equiv M_{\rm H_2}/M_\star = 3.3 \pm 0.7$ that is five times greater than the median for main-sequence (MS) galaxies at $z \sim 3$ (Schinnerer et al., 2016). It should be noted that even when assuming a ULIRG-like

α_{CO} prescription (and a CMB uncorrected $S_{CO(2\rightarrow1)}$ flux), the gas fraction would be high, that is, 0.43 ± 0.10. The massive molecular gas reservoir of AzTEC/C159 is consistent with the general picture that large cool-ISM reservoirs fuel intense star formation activity at high redshift (e.g., Carilli & Walter, 2013).

We used the empirical ratio L_{IR}/L'_{CO} as a proxy of the SFE of AzTEC/C159, allowing a more direct comparison with the average SFE of different galaxy populations. Based on the information in Table 3.1, we derive $L_{IR}/L'_{CO} = (216 \pm 80)\, L_{\odot}(\mathrm{K\,km\,s^{-1}\,pc^2})^{-1}$, which places it within the upper scatter of the L_{IR}/L'_{CO} correlation as presented by Carilli & Walter (2013). This ratio is much higher than that observed in normal star-forming disk galaxies such as nearby spirals and $z \sim (0.4-2)$ MS galaxies (between 20 and 100 $L_{\odot}(\mathrm{K\,km\,s^{-1}\,pc^2})^{-1}$; Daddi et al., 2010; Magnelli et al., 2012), but comparable to merger-driven starbursts such as local ULIRGs and SMGs (e.g., Genzel et al., 2010; Bothwell et al., 2013; Aravena et al., 2016, and references therein). The SFE of AzTEC/C159 is, however, similar to those of the very high-redshift starburst disk galaxies GN20 ($\sim$180 $L_{\odot}(\mathrm{K\,km\,s^{-1}\,pc^2})^{-1}$; Carilli et al., 2010; Hodge et al., 2012) and J1000+0234 ($\sim$140 $L_{\odot}(\mathrm{K\,km\,s^{-1}\,pc^2})^{-1}$; Schinnerer et al., 2008; Smolčić et al., 2015). Thus, while the extreme SFE of AzTEC/C159 seems unusual for a star-forming disk galaxy at $z < 2$, at $z > 4$, disk galaxies harboring vigorous SFE (such as AzTEC/C159, GN20, and J1000+0234) might be common.

Gas excitation

We combined our ^{12}CO(2→1) and ^{12}CO(5→4) line detections to obtain insights into the molecular gas excitation in AzTEC/C159. As mentioned before, at $z \sim 4.5$, the CMB emission affects the observed ^{12}CO line flux density in both lines (da Cunha et al., 2013). This could modify the ^{12}CO(5→4)/CO(2→1) line brightness temperature ratio (r_{52}) and in consequence, our interpretation. We first considered the observed line flux densities in AzTEC/C159 and compared its ^{12}CO spectral line energy distribution (SLED) with those of some SMGs at $z > 4$, where the effect of the CMB might be considerable but no corrections have been applied yet. In Fig. 3.4 we plot the ^{12}CO SLED of J1000+0234 (Schinnerer et al., 2008) and GN20 (Carilli et al., 2010), both star-forming disk galaxies with extreme SFE. We also show the ^{12}CO SLED of AzTEC-3, a massive starburst galaxy possibly triggered by a major merger and associated with a protocluster at $z = 5.3$ (Riechers et al., 2010). All these ^{12}CO SLEDs are consistent with high gas excitation, where $r_{52} = 0.63 \pm 0.16$ for AzTEC/C159.

The effect of the CMB on the ^{12}CO SLED shape below $z = 2.5$ is negligible (da Cunha et al., 2013). In consequence, no corrections need to be made to the observed median ^{12}CO SLED of SMGs (median redshift of $z = 2.2$ as in Bothwell et al. (2013)) and disk galaxies at $z \sim 1.5$ (Daddi et al., 2010). We applied corrections to the observed flux densities of AzTEC/C159 to mitigate potential bias due to the CMB emission (see Sect. 3.2.2), and compared its "intrinsic" ^{12}CO SLED with those of the aforementioned galaxy populations. As observed in Fig. 3.4, with $r_{52} = 0.55 \pm 0.15$, the molecular gas excitation conditions of AzTEC/C159 are consistent with those observed in SMGs, and they significantly deviate from the expected trend for star-forming disk-like MS galaxies at $z \sim 1.5$ (Daddi et al., 2015) and the MW (Fixsen et al., 1999). The elevated ^{12}CO SLED of AzTEC/C159 might be a result of intrinsic processes, such as elevated gas density and kinetic temperature, which yield a higher collision rate between ^{12}CO and H_2 (e.g., Narayanan & Krumholz, 2014).

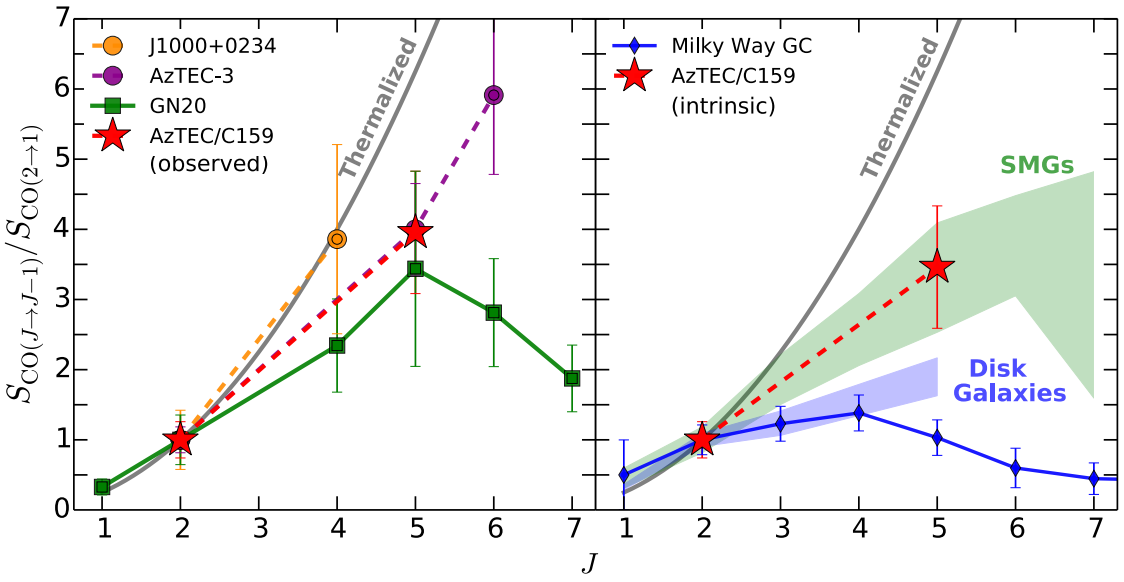

Figure 3.4: *Left panel*: Observed ^{12}CO SLED of AzTEC/C159 and other $z > 4$ SMGs for comparison: GN20 (Carilli et al., 2010), AzTEC-3 (Riechers et al., 2010), and J1000+0234 (Schinnerer et al., 2008). Gray lines show the expected trend for thermalization, i.e., LTE conditions. The dashed and solid color lines connect the data points to illustrate the shape of the different ^{12}CO SLED. The line fluxes have been normalized to the ^{12}CO(2→1) line. *Right panel:* Intrinsic ^{12}CO SLED of AzTEC/C159. The observed flux densities for ^{12}CO(2→1) and ^{12}CO(5→4) have been corrected up by 1/0.7 and 1/0.8, respectively, to take into account the CMB effect (see Sect. 3.2.2). We also present the ^{12}CO SLED of the Milky Way galactic center (Fixsen et al., 1999), MS disk-galaxies at $z \sim 1.5$ (Daddi et al., 2015), and a sample of SMGs (median of $z = 2.2$, Bothwell et al., 2013); similarly, we normalize all the line fluxes to the ^{12}CO(2 → 1) line. Shaded regions show the dispersion of the ^{12}CO SLED for different SMGs and disk galaxies samples.

CO→ H_2 conversion factor

By determining the α_{CO} value in AzTEC/C159, we can mitigate uncertainties on our gas mass estimates and at the same time infer the overall physical conditions of its molecular gas (e.g., Papadopoulos et al., 2012b,a). Here, we constrained α_{CO} from (a) the gas-to-dust ratio (δ_{GDR}) and (b) the balance between the baryonic and dark matter content with the dynamical mass.

Gas-to-dust method: By assuming that the molecular component dominates the ISM, that is, $M_{H_2} \gg M_{HI} + M_{HII}$, the molecular gas mass can be estimated from the relation (e.g., Magnelli et al., 2012; Aravena et al., 2016)

$$M_{gas} \simeq M_{H_2} = \delta_{GDR} M_{dust}, \tag{3.3}$$

where δ_{GDR} is the gas-to-dust ratio relation constrained locally by Leroy et al. (2011), which varies with metallicity as $\log(\delta_{GDR}) = 9.4 - 0.85 \times [12 + \log(O/H)]$. In the absence of direct metallicity estimates for AzTEC/C159 and a robust mass-metallicity relation at such high redshift, we assumed that AzTEC/C159 has solar metallicity. Then, by combining Eqs. 3.1 and 3.3,

$$\alpha_{\rm CO} = \frac{\delta_{\rm GDR} M_{\rm dust}}{L'_{\rm CO}}. \tag{3.4}$$

In Sect. 3.2.2 we favored a scenario with dense gas and $T_{\rm kin} = 40\,{\rm K}$ to correct the observed $L'_{\rm CO}$ for the CMB effect. Here, we also explore the possibility of cool ($T_{\rm kin} = 14\,{\rm K}$) and low-density molecular gas, that is, following da Cunha et al. (2013), we varied $L'_{\rm CO}$ within the range $[3.4 \pm 0.6, 12.0 \pm 2.2] \times 10^{10}\,{\rm K\,km\,s^{-1}\,pc^2}$. Based on $M_{\rm dust} = 2.5^{+0.6}_{-0.5} \times 10^9 M_\odot$ (derived in Sect. 3.2.2) and Eq. (3.4), we estimate $\alpha_{\rm CO} = 3.8^{+2.6}_{-1.4}\,M_\odot\,{\rm K^{-1}\,km^{-1}\,s\,pc^{-2}}$. Note that a lower value of $\delta_{\rm GDR}$ could lower the estimated $\alpha_{\rm CO}$, but it would require unlikely supra-solar metallicity. In contrast, sub-solar metallicities would yield even higher $\alpha_{\rm CO}$.

Dynamical mass method: Another approach to constrain $\alpha_{\rm CO}$ is based on the estimation of the mass content, which should match the baryonic and dark matter content, that is, $M_{\rm dyn} = M_{\rm ISM} + M_\star + M_{\rm DM}$. Since we assumed that the ISM is dominated by molecular gas, $M_{\rm ISM} \simeq M_{\rm H2}$. In combination with Eq. (3.1), this leads to

$$\alpha_{\rm CO} = \frac{M_{\rm dyn} - M_\star - M_{\rm DM}}{L'_{\rm CO}}. \tag{3.5}$$

The [CII] 158 μm gas dynamics of AzTEC/C159 has been characterized in detail by Jones et al. (2017). Via the tilted-ring fitting method, they find that at an intrinsic radius of 2.9 kpc $M_{\rm dyn} = (2.8^{+1.1}_{-0.6}) \times 10^{11} M_\odot$. This value agrees within the uncertainties with the value derived by K19 ($M_{\rm dyn} \sim 2.4 \times 10^{11} M_\odot$) using the software 3D-Barolo and assuming an inclination angle of $\sim$ 30 degs as in Jones et al. (2017). Within an aperture radius of 2.9 kpc, we find that $S^{\rm observed}_{\rm CO(2\rightarrow1)} = 91 \pm 16\,{\rm mJy}$, which is $\sim$ 13% lower than that derived from the aperture that contains the full emission line (see Sect. 3.2.2). Consequently, as in the gas-to-dust ratio method, we consider $L'_{\rm CO} \in [2.9 \pm 0.5, 10.5 \pm 1.9] \times 10^{10}\,{\rm K\,km\,s^{-1}\,pc^2}$.

GG18 have estimated the stellar mass of AzTEC/C159 ($[4.5 \pm 0.4] \times 10^{10} M_\odot$) using LePHARE (Arnouts et al., 1999; Ilbert, O. et al., 2006) and adopting the Bruzual & Charlot (2003) stellar population synthesis models, a Chabrier (2003) IMF, and a exponentially declining star formation history (SFH). For this purpose, a substantial optical/near-IR dataset was used by GG18: the *g*, r, i, z, and *y* bands from the Subaru Hyper Suprime-Cam imaging (HSC, Tanaka et al., 2017), near-IR J, H, and Ks bands from the UltraVISTA DR3 survey (McCracken et al., 2012), and the MIR Spitzer/IRAC 3.6 and 4.5μm bands from the Spitzer Large Area Survey with Hyper-Suprime-Cam (SPLASH, Capak et al. in prep.). As discussed in detail in GG18, this stellar mass estimate could be subject to a number of systematic uncertainties. For instance, if the stars formed in situ, it is possible that a fraction of the stellar light might be obscured by the dust and the stellar mass used here might therefore be underestimated[1]. GG18 have quantified the stellar mass fraction we might be missing by this effect using different prescriptions for the dust-to-stellar-mass ratio (DTS). By considering the ratio derived from simulations in (Popping et al., 2017) of $\log({\rm DTS}) = -1.8$, the stellar mass would increase by $\sim$ 0.4 dex; on the other hand, the median DTS ratio for local ULIRGs

[1] Observations with high spatial resolution rest-frame UV/optical/FIR are required to map the dust and stellar light distribution and better constrain the stellar mass of AzTEC/C159. This would also allow exploring multiple interacting components (and not a massive single component) that might fit into a merger-driven star formation scenario

log(DTS) = −2.83 (Calura et al., 2017) yields an increment of ∼ 1.1 dex. The original estimate for the stellar mass (combined with the SFR of $740^{+210}_{-170}\,M_\odot\,\mathrm{yr}^{-1}$) places AzTEC/C159 on the upper-end of the MS of SFGs at $z \sim 4.5$, as given by (Schreiber et al., 2015). An increase in stellar mass by ∼ 0.4 dex would instead place AzTEC/C159 right on the MS of SFGs, while an increase by ∼ 1.1 dex would lead to a very unlikely scenario in which AzTEC/C159 lies significantly below the MS. From this, we conclude that the stellar mass of AzTEC/C159 reported by GG18 might be underestimated by at most ∼0.4 dex. By applying Eq. (3.5) and considering the original estimate for the stellar mass ($[4.5 \pm 0.4] \times 10^{10} M_\odot$) from GG18, as well as a negligible dark matter component, we derive[2] $\alpha_{\rm CO} = 3.9^{+2.7}_{-1.3}\,M_\odot\,\mathrm{K}^{-1}\,\mathrm{km}^{-1}\,\mathrm{s}\,\mathrm{pc}^{-2}$. The addition of a 0.4 dex factor in the stellar mass (i.e., $[1.0 \pm 0.4] \times 10^{11} M_\odot$) still yields a relatively high $\alpha_{\rm CO}$ value of $2.7^{+2.1}_{-1.1}\,M_\odot\,\mathrm{K}^{-1}\,\mathrm{km}^{-1}\,\mathrm{s}\,\mathrm{pc}^{-2}$.

Our two independent methods point toward a high value of $\alpha_{\rm CO}$. This result agrees well with our previous assumption of $\alpha_{\rm CO} \sim 4.3\,M_\odot\,\mathrm{K}^{-1}\,\mathrm{km}^{-1}\,\mathrm{s}\,\mathrm{pc}^{-2}$. It is known that the most important influencing factor on $\alpha_{\rm CO}$ is the average dynamical state of the molecular gas. While low values are associated with unbound gas, as observed in local ULIRGs, high values are related with self-gravitating gas (e.g., Papadopoulos et al., 2012a); hence, the molecular gas dynamics in AzTEC/C159 might be more similar to that of local star-forming disks than those of disturbed major mergers.

3.3 AzTEC2

AzTEC2 was originally identified in the 1.1 mm surveys undertaken with AzTEC/JCMT (Scott et al., 2008) and AzTEC/ASTE (Aretxaga et al., 2011) as source AzTEC2 and AzTEC/C3 respectively, i.e. the second/third brightest 1.1mm source in the COSMOS field. AzTEC2 is also the second brightest SMG detected in the IRAM/GISMO 2 mm deep survey (Magnelli[†] et al., 2019). In addition, it was detected in the deep Herschel/HerMES survey (250-500μm maps) and SCUBA-2 at both 450μm and 850μm (Casey et al., 2013). Recent imaging with ALMA (Brisbin et al., 2017) reveals that AzTEC2 is composed of two components separated by 3 arcsec (see Fig. 3.10): namely component A and B, both with a signal-to-noise ratio (SNR) > 10 and with counterparts in the VLA 3GHz radio continuum imaging at 0.75 arcsec resolution (Miettinen et al., 2017a). A spectroscopic redshift solution of $z = 1.12$ has been adopted for AzTEC2 in past studies (e.g., Smolčić et al., 2012, 2017; Miettinen et al., 2015; Brisbin et al., 2017; Miettinen et al., 2017a). Nevertheless, by using recent optical/near-IR spectroscopy we have revealed that such redshift value corresponds to a foreground SFG at only 1.5 arcsec to the south of AzTEC2 (see Appendix 3.6.1). High-resolution observations with ALMA and NOEMA are, therefore, crucial to obtain a reliable counterpart association and redshift determination of the AzTEC2 complex; enabling us to probe its gas content, star formation efficiency, and gas dynamics within the context of cold gas accretion and merger-driven star formation in the early Universe.

[2] A highly conservative error bar for $M_{\rm dyn}$ of 1 dex has been suggested by Jones et al. (2017) to take into account systematic uncertainties of the method, that is, $M_{\rm dyn} = (2.8^{+6.1}_{-1.9}) \times 10^{11} M_\odot$. This wide range for $M_{\rm dyn}$ also affords a wider range of inclination angles. We derive $\alpha_{\rm CO} = 6.7^{+6.3}_{-4.4}\,M_\odot\,\mathrm{K}^{-1}\,\mathrm{km}^{-1}\,\mathrm{s}\,\mathrm{pc}^{-2}$. Thus, it remains true that $\alpha_{\rm CO}$ is still higher than the prescription for ULIRGs-like systems ($\alpha_{\rm CO} = 0.8\,M_\odot\,\mathrm{K}^{-1}\,\mathrm{km}^{-1}\,\mathrm{s}\,\mathrm{pc}^{-2}$).

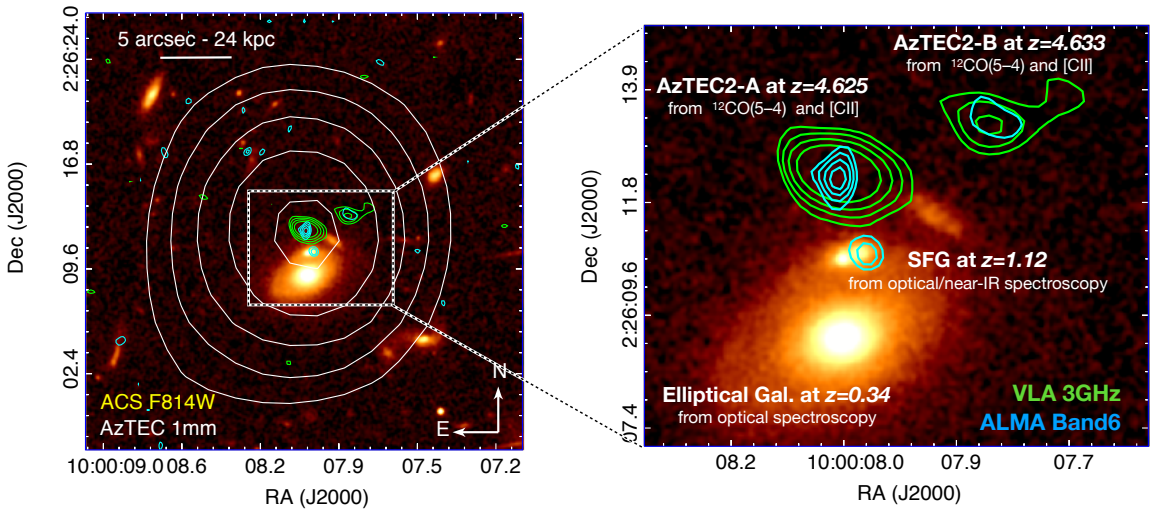

Figure 3.5: Multi-wavelength view towards the AzTEC2 source. *Left panel:* AzTEC/JCMT 1.1mm (white), ALMA (green) and VLA (blue) > 3σ contours overlaid on the *Hubble Space Telescope* (*HST*)/ACS F814W image. The zoomed image (*right panel*) shows two foreground galaxies: a massive elliptical at $z = 0.34$ and a SFG at $z = 1.12$ (Appendix 3.6.1). ALMA and VLA imaging at sub-arcsec resolution reveal two optically-undetected components at $z \sim 4.63$, labeled as AzTEC2-A and AzTEC2-B.

3.3.1 NOEMA and ALMA observations

A blind spectral scan was performed with NOEMA in Band 1 over two tracks on January 26th and 29th, 2019 (project W18EU, PI: E.F. Jiménez-Andrade) using 10 antennas in A-configuration, which account for a total observing time of 3.3 hours. We used the PolyFix correlator to cover the frequency range 84.9–92.7 GHz and 100.2–108.0GHz. The data reduction was performed with the software `GILDAS` using the NOEMA standard pipeline, while imaging was done with the package `mapping` using natural weighting. The achieved spatial resolution of 1.7×0.9 arcsec (PA=-163 degs) suffices to resolve the two components of AzTEC2 separated by ~3 arcsec (Fig. 3.10). The spectral data cube was smoothed to a ~34 MHz resolution, reaching a sensitivity of 0.13 mJy beam^{-1} per channel.

ALMA observations were conducted on April 23rd, 2016 in Band 7 (project 2015.1.00568.S, PI: C. Casey) to inspect the frequency ranges of 335.5-339.5 GHz and 347.5-351.5 GHz. Data reduction and imaging (adopting natural weighting) were performed with the standard pipeline/routines in `CASA`[3]. We achieve a sensitivity of 4.3 mJy beam^{-1} per 16 MHz wide channel (after ~ 10min of on-source integration time) and a spatial resolution of 0.30×0.27 arcsec (PA=121 degs), allowing us to pinpoint the emission from all the components in the crowded field around AzTEC2.

3.3.2 Data analysis and results

The NOEMA spectrum reveals emission at the position of AzTEC2-A and AzTEC2-B peaking at ~ 102.5 GHz. By collapsing the data cube within the frequency range 102.2–102.7 GHz, that encompass the full emission line, we derive the intensity map shown in the central-upper panel

[3] Data reduction and imaging was done by J. Zavala

of Fig. 3.6. A 2D Gaussian fit indicates that AzTEC2-A is resolved by our observations, with a deconvolved FWHM of (1.2 ± 0.4) arcsec along the major axis; hence, we use an aperture that is a factor 1.5 larger than the convolved FWHM of AzTEC2-A to retrieve most of the emission and extract the ^{12}CO(5 → 4) line spectrum. Since AzTEC2-B appears as a point-like (unresolved) source, we integrate emission across a region that equals the size of the synthesized beam to obtain the spectrum (right-lower panel of Fig. 3.6). We identify a broad (FWHM ∼ 900 km s^{-1}), double-peaked emission line centered at (102.429 ± 0.020) GHz associated with AzTEC2-A. Through a least-squares algorithm (Levenberg-Marquardt), we find that a model with two Gaussian components describes better the line profile than that using a single one – yielding a reduced χ^2 of 2.3 and 3.1, with 24 and 27 degrees of freedom, respectively). We thus adopt the former model and derive an integrated flux density of (1035 ± 90) μJy. We identify, in addition, a 8.2σ line detection at the locus of AzTEC2-B that is centered at (102.303 ± 0.020) GHz. A single Gaussian model (reduced χ^2 = 1.1 with 12 degrees of freedom) leads to an integrated flux density of (280 ± 35) μJy. By averaging line-free channel maps in the data cube, we also detect dust continuum emission from both components. These values and all the source properties derived in this work are given in Table 3.2.

Strong line emission is detected at ∼ 338 GHz towards both AzTEC2 components in the ALMA data cube (left-upper panel of Fig. 3.6). The velocity-integrated intensity map shows that these sources are well-resolved; AzTEC2-A, in particular, exhibits extended emission distributed across ∼ 10 spatial resolution elements. A 2D Gaussian fit indicates a deconvolved FWHM of (1.05 ± 0.08) arcsec along the major axis (Table 3.2). Consequently, to extract the line spectra we use an aperture that is a factor 1.5 larger than the measured FWHM, allowing us to recover most of the extended line emission. As illustrated in the left-central panel of Fig. 3.6, these ALMA line detections lie at the edges of the spectral windows used in our observations, preventing us from recovering/inspecting their total line profiles. There is tentative evidence, however, of a double-peaked line profile in AzTEC2-A, as that observed at ∼103 GHz with NOEMA. We use the relative amplitude and FWHM of the two peaks from the ∼103 GHz line detection as fixed priors to fit a two Gaussian profile to the line at ∼ 338 GHz (reduced χ^2 = 1.9 with 66 degrees of freedom), leading to a total integrated flux density of (26.2 ± 0.8) mJy km s^{-1} and central frequency of (337.8 ± 0.2) GHz. Similarly, we use the FWHM of our ∼103 GHz line detection as a prior to model the profile of that at ∼ 338 GHz in AzTEC2-B (reduced χ^2 = 1.3 with 78 degrees of freedom), which gives a total integrated flux density of (12.3 ± 0.8) mJy km s^{-1} and central frequency of (337.4 ± 0.2) GHz. Finally, we average line-free channel maps to derive dust continuum flux density at ∼ 338 GHz (observed frame) for both AzTEC2 sources, these photometric values are listed in Table 3.2. We also derive the deconvolved FWHM of the dust continuum emission via a 2D Gaussian model, leading to a value of (0.75 ± 0.04) arcsec for both components.

By combining the line detections towards AzTEC2-A at ∼102.5 GHz and 337.5 GHz, we are able to unambiguously associate them with ^{12}CO(5→4) and [CII], respectively, leading to a redshift solution of z = 4.626 ± 0.001. Similarly, for AzTEC2-B we estimate a redshift of z = 4.633 ± 0.001, implying a velocity offset of +375 ± 50 km s^{-1} with respect to AzTEC2-A. The small velocity offset combined with the projected separation of ∼20 kpc indicate that AzTEC2-A and AzTEC2-B are two physically associated galaxies. Furthermore, these robust line detections and counterpart association, rule out the preliminary redshift solution of 1.1235 for AzTEC2 adopted in past studies (e.g., Smolčić et al., 2012, 2017; Brisbin et al., 2017; Miettinen et al., 2017a, see Appendix 3.6.1).

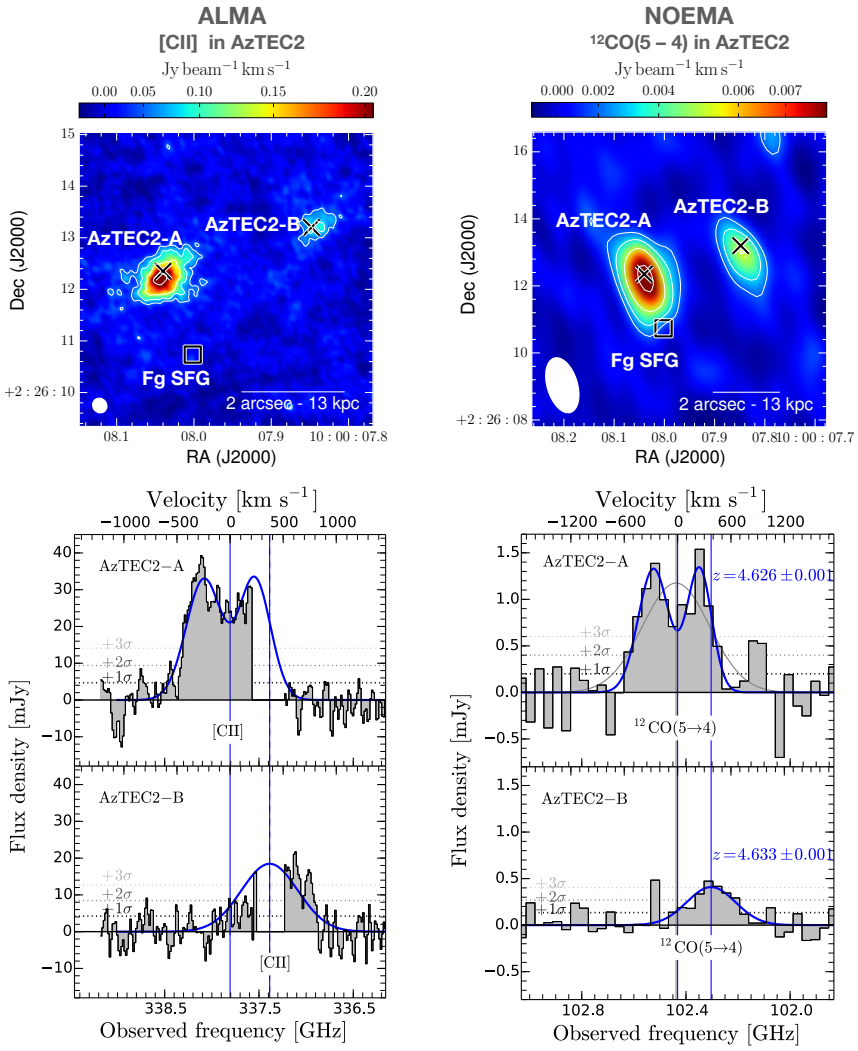

Figure 3.6: *Left panels:* Velocity-integrated intensity map ($[-600, +850]$ km s^{-1}) and spectra of the [CII] line emission in AzTEC2-A and AzTEC2-B detected with ALMA. The contour levels are at $[3\sigma, 5\sigma, 8\sigma, 13\sigma]$ with $\sigma = 16$ mJy beam^{-1} km s^{-1}. The velocities displayed in the spectra are relative to the central frequency of the [CII] line emission in AzTEC2-A. The black crosses signalize the position of AzTEC2-A and AzTEC2-B inferred from high-resolution FIR and radio continuum imaging with ALMA and the VLA (Brisbin et al., 2017; Smolčić et al., 2017a). The center of the foreground (Fg) SFG at $z = 1.1235$ (Appendix 3.6.1), is marked by the black square. The synthesized beam is shown in the lower-left corner. The blue solid line represents the model used to fit the line profile, while the vertical lines mark the central frequency. The horizontal gray lines show the noise level per channel. *Right panels:* Velocity-integrated intensity map and spectra of the ^{12}CO(5→4) line emission in AzTEC2-A and AzTEC2-B detected with NOEMA. We integrate emission within the velocity range $(-600, 1100)$ km s^{-1} where significant line emission is detected. The contour levels are at $[3\sigma, 5\sigma, 8\sigma, 13\sigma]$ with $\sigma = 0.6$ mJy beam^{-1} per 100 km s^{-1} wide channel. The blue solid line represents a model with one (two) Gaussian component(s) that reproduce the ^{12}CO(5→4) line profile in AzTEC2-B (AzTEC2-A). The gray line shows a Gaussian model to fit the ^{12}CO(5→4) line profile of AzTEC2-A. The vertical lines mark the central frequency of the line; in the case of AzTEC2-A, this is derived from a model with two (blue) and one (gray) Gaussian component(s). The velocities displayed in the spectra are relative to the central frequency of the ^{12}CO(5→4) line emission in AzTEC2-A.

Table 3.2: Properties of AzTEC2

Properties	**Units**	**AzTEC2-A**		**AzTEC2-B**	
		^{12}CO(5→4)	[CII]	^{12}CO(5→4)	[CII]
FWHM	km s^{-1}	890 ± 150	...	640 ± 150	...
Peak flux	mJy	1.2 ± 0.2	32 ± 1	0.4 ± 0.1	18 ± 2
Integrated flux	Jy km s^{-1}	1.035 ± 0.090[a]	26.2 ± 0.8	0.28 ± 0.04[a]	12.3 ± 1.5
Central frequency	GHz	102.429 ± 0.020	337.8 ± 0.2	102.303 ± 0.020	337.4 ± 0.2
z[b]	...	4.626 ± 0.001		4.633 ± 0.001	
RA, Dec	hh:mm:ss.sss, dd:mm:ss.ss	10:00:08.042 +02:26:12.19		10:00:07.842 +02:26:13.32	
$S_{3\mathrm{GHz}}$	μJy	35 ± 6		25 ± 6	
$S_{102.5\mathrm{GHz}}$	μJy	330 ± 50		95 ± 20	
$S_{338\mathrm{GHz}}$	mJy	34.2 ± 1.1		10.6 ± 0.7	
$\mathrm{FWHM}^{\text{major-axis}}_{\text{[CII]}}$	arcsec/kpc	1.05 ± 0.08/6.8 ± 0.5		0.95 ± 0.12/6.2 ± 0.8	
$\mathrm{FWHM}^{\text{major-axis}}_{\text{dust}}$	arcsec/kpc	0.76 ± 0.02/4.9 ± 0.1		0.74 ± 0.04/4.8 ± 0.2	
L_{IR}	$L_\odot$	$1.6^{+1.6}_{-0.8} \times 10^{13}$		$5.0^{+5.0}_{-2.5} \times 10^{12}$	
L'_{CO}	K km s^{-1} pc^2	$(12.5 \pm 2.6) \times 10^{10}$		$(3.3 \pm 0.7) \times 10^{10}$	
$L_{\mathrm{IR}}/L'_{\mathrm{CO}}$	$L_\odot$(K km s^{-1} pc^2)$^{-1}$	140 ± 60		170 ± 70	
SFR	$M_\odot$ yr^{-1}	1580^{+1580}_{-790}		490^{+490}_{-250}	
$M_{\mathrm{H_2}}(\alpha_{\mathrm{CO}} = 0.8, \alpha_{\mathrm{CO}} = 4.3)$	$M_\odot$	$(1.0 \pm 0.2, 5.4 \pm 1.1) \times 10^{11}$		$(0.3 \pm 0.1, 1.4 \pm 0.3) \times 10^{11}$	
$\tau_{\mathrm{gas}}(\alpha_{\mathrm{CO}} = 0.8, \alpha_{\mathrm{CO}} = 4.3)$	Myr	(60 ± 20, 300 ± 110)		(50 ± 20, 250 ± 90)	

[a] These observed flux densities will increase by a factor [1/0.8] when considering the effect of the CMB. We use the corrected value, i.e., $S^{\text{intrinsic}}_{\mathrm{CO(5\to4)}} = 1.30 \pm 0.10$ mJy km s^{-1} and 350 ± 40 μJy km s^{-1} for AzTEC2-A and AzTEC2-B, respectively.

[b] Redshift derived from ^{12}CO(5→4) line measurements.

Gas content and star formation rate of AzTEC2

We use the ^{12}CO(5→4) line detections to estimate the ^{12}CO(1→0) line luminosity, $L'_{\rm CO(1\rightarrow0)} \equiv L'_{\rm CO}$, and hence infer the molecular gas mass in the AzTEC2 complex. As previously discussed for AzTEC/C159 (Sect. 3.2.2), due to the higher temperature of the CMB at $z = 4.6$, the intrinsic value of the ^{12}CO(5→4) line, $S^{\rm intrinsic}_{\rm CO(5\rightarrow4)}$, is a factor [1/0.8] higher (da Cunha et al., 2013) than that measured from our observations. In using this factor, we assume that AzTEC2-A and AzTEC2-B harbor a dense ISM with elevated gas kinetic temperature ($T_{\rm kin} \sim 40$ K) – as the majority of SMG (e.g., Magnelli et al., 2012; Cañameras et al., 2018). Therefore, we find that $S^{\rm intrinsic}_{\rm CO(5\rightarrow4)}$ is 1.30 ± 0.10 mJy km s^{-1} (350 ± 40 μJy km s^{-1}) for AzTEC2-A (AzTEC2-B). The corresponding line luminosity is subsequently derived following Carilli & Walter (2013, Sect. 2.4). We adopt typical SMG-like gas excitation conditions to convert the ^{12}CO(5→4) line luminosity, $L'_{\rm CO(5\rightarrow4)}$, to $L'_{\rm CO}$: i.e., $L'_{\rm CO} = [1/0.32] \times L'_{\rm CO(5\rightarrow4)}$ (e.g., Bothwell et al., 2013; Carilli & Walter, 2013), which gives $(12.5 \pm 2.6) \times 10^{10}$ K km s^{-1} pc^{-2} and $(3.3 \pm 0.7) \times 10^{10}$ K km s^{-1} pc^{-2} for AzTEC2-A and AzTEC2-B, respectively (see Table 3.2). Finally, the molecular gas mas, $M_{\rm gas}$, can be inferred through the CO-to-H$_2$ ($\alpha_{\rm CO}$) conversion factor: $M_{\rm gas} = \alpha_{\rm CO} L'_{\rm CO}$. Depending on the physical and chemical conditions of the ISM, $\alpha_{\rm CO}$ ranges –in general– between 0.8 and 4.3 $M_\odot$ K^{-1} km s^{-1} pc^{-2} (see Sect. ; e.g., Papadopoulos et al., 2012a,b). Since we lack robust information on the chemical and dynamical state of AzTEC2, we use the aforementioned $\alpha_{\rm CO}$ values as boundaries to constrain the expected range for $M_{\rm gas}$ (see Table 3.2). Using a mean $\alpha_{\rm CO} = 2.5$ $M_\odot$ K^{-1} km s^{-1} pc^{-2}, in particular, we find a molecular gas mass in AzTEC2-A of $(3.1 \pm 0.5) \times 10^{11} M_\odot$, and a factor four lower in AzTEC2-B. Such mass budgets are consistent with the massive ($\log(M_\star/M_\odot) \gtrsim 11$) gas reservoirs found in other $z \sim 4-5$ SMGs, like AzTEC/C159 (Sect. 3.2.2), AzTEC1, AzTEC3, and J1000+0234 (Schinnerer et al., 2008; Riechers et al., 2010; Yun et al., 2015).

We use the $L_{\rm IR}$ of AzTEC2-A and AzTEC2-B derived through SED fitting (as in Magnelli† et al., 2019, see Table 3.2) to infer their SFR following the calibration from Kennicutt (1998a): SFR[$M_\odot$ yr^{-1}]= $10^{-10} L_{\rm IR}$ (assuming a Chabrier IMF). We find that AzTEC2-A produces stars at a rate of 1580^{+1580}_{-790} $M_\odot$ yr^{-1}, while AzTEC2-B does it at 490^{+490}_{-250} $M_\odot$ yr^{-1}. The estimate for AzTEC2-A, in particular, is a factor 1.5 larger than the average SFR of SMGs at similar redshift (e.g., Smolčić et al., 2015; Gómez-Guijarro† et al., 2018a; Jiménez-Andrade† et al., 2018; Magnelli† et al., 2019).

Mode of star formation in AzTEC2

The $L_{\rm FIR}/L'_{\rm CO}$ ratio[4] gives an indication on how efficient is the production of stars in galaxies for a given molecular gas reservoir. For AzTEC2-A and AzTEC2-B we derive 140 ± 60 and 170 ± 70 $L_\odot$(K km s^{-1}pc^{-2})$^{-1}$, respectively (Table 3.2). While these estimates are larger than those of nearby and $z \sim 2$ star-forming disks (20−100 $L_\odot$(K km s^{-1}pc^{-2})$^{-1}$; Daddi et al., 2010; Genzel et al., 2010), they are closer to the star formation efficiency of $z \sim 4.5$ star-forming disks like GN20 and AzTEC/C159 (180−220 $L_\odot$(K km s^{-1}pc^{-2})$^{-1}$; Hodge et al., 2012; Jiménez-Andrade† et al., 2018). Certainly, while most of the reported SMGs lie on/above the empirical $L_{\rm FIR} - L'_{\rm CO}$ relation for "starburst" galaxies, AzTEC2-A and AzTEC2-B are closer to that for normal, MS galaxies (see Fig. 3.7; e.g., Genzel et al., 2010).

[4] We convert the $L_{\rm IR}$ measurements into $L_{\rm FIR}$ by considering that $\langle \log(L_{\rm IR}) \rangle = 0.3 + \langle \log(L_{\rm FIR}) \rangle$ (e.g., Delhaize et al., 2017).

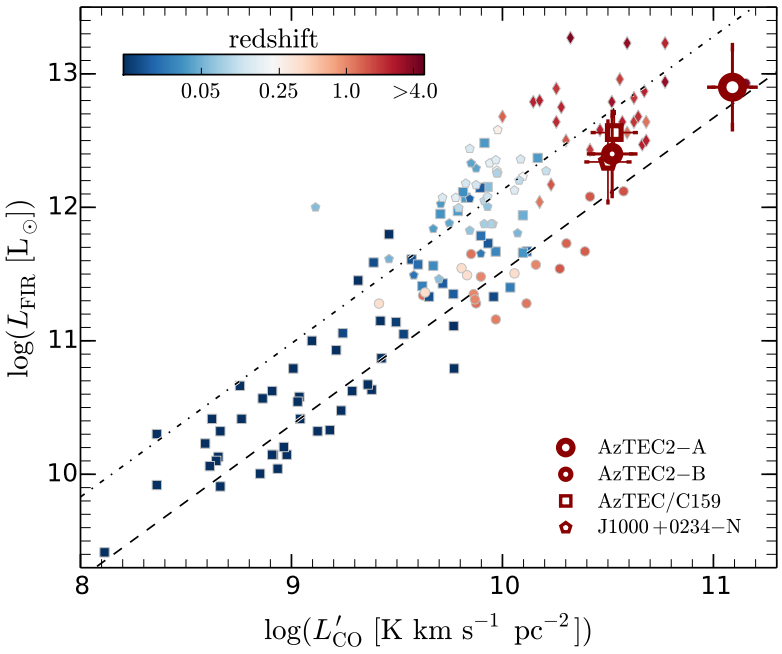

Figure 3.7: FIR luminosity as a function of ^{12}CO(1→0) line luminosity for local and high-redshift SFGs. The squares represent nearby normal and starburst galaxies reported by Gao & Solomon (2004), while pentagons correspond to low-redshift ULIRGs in the sample of Solomon et al. (1997). The circles show $z \sim 1.5$ star-forming disks presented in Daddi et al. (2010); Geach et al. (2011) and Magnelli et al. (2012). The diamonds represent the parameter space covered by the SMGs reported in Bothwell et al. (2013). Large symbols correspond to the SMGs studied in this work, including J1000+0234−N (Chapter 4). The dashed and dotted line show the best-fitting relation MS and starburst galaxies, respectively, reported by Genzel et al. (2010).

With the available gas reservoir of AzTEC2-A and AzTEC2-B, they will be able to sustain the current SFR during a period of 50-300 Myr – depending on which $\alpha_{\rm CO}$ is used to derive $M_{\rm gas}$ (Table 3.2). Despite the large uncertainties of the gas depletion time-scale ($\tau_{\rm gas}$), we note that these estimates are –in general– larger than the average for SMGs at similar redshift ($\tau_{\rm gas} \sim 45$ Myr; Aravena et al., 2016). Instead, constraints on the redshift evolution of $\tau_{\rm gas}$ (e.g., Tacconi et al., 2013; Genzel et al., 2015) suggest that expected gas depletion time for MS disk galaxies at $z \sim 4.5$ (120−270 Myr; Saintonge et al., 2013) is comparable within the proposed range of $\tau_{\rm gas}$ for both AzTEC2 sources.

Using the FWHM of the dust continuum emission from our ALMA observations (Table 3.2), we also infer the galaxy-averaged SFR surface density: $\Sigma_{\rm SFR} \equiv {\rm SFR}/(2\pi R_{\rm eff})$. The effective radius containing half of the total emission, $R_{\rm eff}$, is approximated as $R_{\rm eff} \sim {\rm FWHM}/2.430$ (Murphy et al., 2017), assuming an exponentially declining surface brightness distribution as observed in disk galaxies. We estimate $\Sigma_{\rm SFR} = (70 \pm 21)$ and $(23 \pm 8)\ M_\odot\ {\rm yr}^{-1}{\rm kpc}^{-2}$ for AzTEC2-A and AzTEC2-B, respectively, placing both systems at the middle-to-low end of the $\Sigma_{\rm SFR}$ distribution for SMGs (Miettinen et al., 2017b). According to the empirical relation between $\Sigma_{\rm SFR}$ and distance to the MS, reported by us in Jiménez-Andrade[†] et al. (2019, see Chapter 2), the properties of AzTEC2-A and AzTEC2-B are more consistent with those of extended galaxies close to the MS than compact starbursts with $\Sigma_{\rm SFR}$ up to $10^3\ M_\odot\ {\rm yr}^{-1}{\rm kpc}^{-2}$.

Overall, our results suggest that AzTEC2-A and AzTEC2-B deviate from the scenario of short-lived bursts of star formation occurring in a compact region as observed in the majority of bright SMGs (e.g., Schinnerer et al., 2008; Engel et al., 2010; Iono et al., 2016). These sources, therefore, seem to form stars through a smoother mode of star formation, as found in star-forming disk galaxies at lower redshifts (e.g., Daddi et al., 2010; Genzel et al., 2010).

A rapidly rotating, massive disk in AzTEC2-A

We use the high-resolution [CII] line observations to explore the kinematics of the brightest component of AzTEC2, for which the high SNR of the detection enable us to derive the velocity field and velocity dispersion of the gas (Fig. 3.8). As initially suggested from the double-peaked ^{12}CO(5→4) and [CII] line profiles (Fig. 3.6), AzTEC2-A exhibits a smooth velocity gradient that appears to be consistent with a rotating disk. To parameterize its motion, we derive the position-velocity (P/V) diagram (Fig. 3.8) along the major-axis FWHM of the [CII] line emission using a 0.3 arcsec width aperture. The rotation curve is then fitted with a simple model of the form $v(r) = (2/\pi)v_{\rm asym}\arctan(r/r_{\rm t})$ (e.g., Courteau, 1997; Swinbank et al., 2012), where $v_{\rm asym}$ is the asymptotic rotational velocity and $r_{\rm t}$ is the radius at which the rotation curve turns over. Our fit, limited by the lack of velocity channels above $+200\,{\rm km\,s^{-1}}$, suggests an asymptotic velocity of $(360 \pm 40)\,{\rm km\,s^{-1}}$ and $r_{\rm t} = (0.8 \pm 0.2)$ kpc. To derive the intrinsic (de-projected) rotational velocity, $v_{\rm rot}^{\rm int} = v_{\rm rot}/\sin(i)$, we infer the inclination of the disk (i) from the apparent ellipticity of the galaxy: i.e., $i = \arcsin({\rm FWHM_{minor}}/{\rm FWHM_{major}}) = (44 \pm 6)$ deg, where the respective FWHM values are derived from the surface brightness distribution of the [CII] line (Fig. 3.6). By taking $v_{\rm asym} = v_{\rm rot}$, we find that the intrinsic rotational velocity is $v_{\rm rot}^{\rm int} = (510 \pm 90)\,{\rm km\,s^{-1}}$.

To evaluate the rotational-to-dispersion support ($v_{\rm rot}/\sigma$) of the disk, we inspect the line-of-sight velocity dispersion (σ) map in Fig. 3.8. We anticipate that at the innermost region of the galaxy, the measured σ is highly enhanced by "beam smearing"[5] (e.g., Davies et al., 2011; Stott et al., 2016). Since such a contribution is expected to be modest at the outermost radii, we adopt $100\,{\rm km\,s^{-1}}$ (from the contour levels in the map, Fig. 3.8) as an upper limit for the intrinsic velocity dispersion of the gas in the disk. Then, we derive $v_{\rm rot}/\sigma \gtrsim 5$, indicating that AzTEC2-A is rather unperturbed, rotation-dominated disk that resembles the $v_{\rm rot}/\sigma$ ratio of more evolved disk galaxies at $z \sim 1$ (e.g., Di Teodoro et al., 2016, and references therein). This finding, therefore, provides more evidence of kinematically mature disks that can be found at even $z \sim 4.5$, such as GN20 (Hodge et al., 2012), ALESS 73.1 (De Breuck et al., 2014), AzTEC/C159, J1000+0234, (Jones et al., 2017) and AzTEC1 (Tadaki et al., 2018).

Finally, by assuming that the kinematics of the disk is mainly dominated by the gravitational potential of AzTEC2-A, its dynamical mass ($M_{\rm dyn}$) can be estimated through the relation: $M_{\rm dyn}\sin^2(i) = Rv(R)^2/G$, where $v(R)$ is the rotation velocity at radius R and G is the gravitational constant. Using $R = 0.8$ arcsec/5.2 kpc that encompass the full extent of the [CII] line emission, we find $M_{\rm dyn} = (2.5 \pm 1.0) \times 10^{11} M_{\odot}$. This mass budget is comparable with that expected for the molecular gas mass ($[1.0, 5.4] \times 10^{11}\,M_{\odot}$), indicating that AzTEC2-A is a massive gas-rich disk likely assembled through the accretion of gas from the cosmic web (e.g., Dekel et al., 2009a,b; Romano-Díaz et al., 2014).

[5] At the innermost region of galaxies, the measured line width is boosted by large-scale motions occurring within the region traced by a relatively coarse (finite) point spread function (PSF).

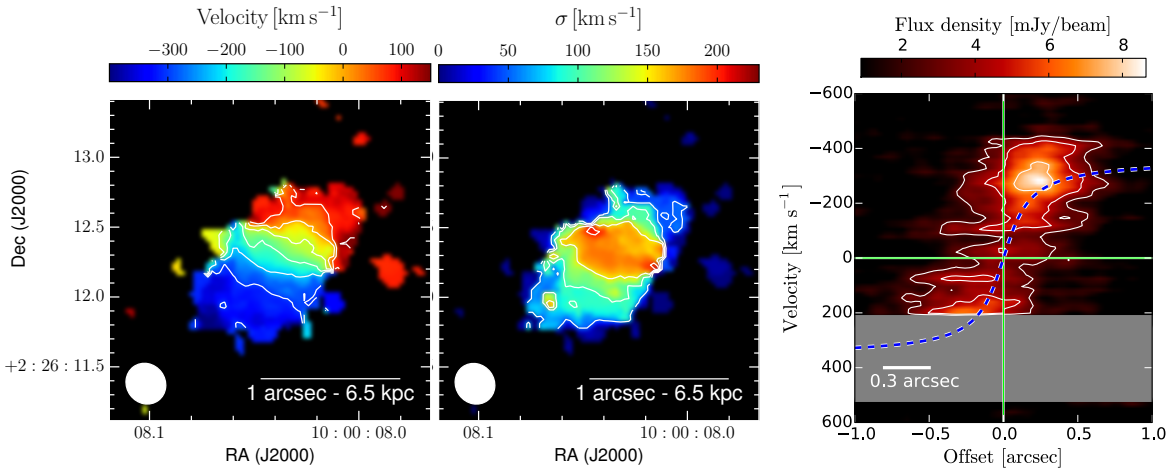

Figure 3.8: Velocity field (*left panel*) and velocity dispersion (*central panel*) of the gas in AzTEC2-A ($z = 4.626$), derived from [CII] line observations with ALMA. Note that the velocity channels above 200 km s^{-1} are not available in the data set. The contour levels are at $[-300, -200, -100, 0, 100]$ km s^{-1} and $[0, 50, 100, 150, 200]$ km s^{-1} for the velocity field and velocity dispersion maps, respectively. The synthesized beam is shown in the lower-left corner. The P/V diagram (*right panel*) has been extracted using a 0.3 arcsec width aperture along the galaxy's major-axis (PA= −40 deg). The blue-dashed line is a simple arctan model to describe the rotation curve of AzTEC2-A. The contour levels are at $[3\sigma, 5\sigma, 8\sigma]$, where σ is the rms noise level. The gray shaded region shows the velocity range that is not available in the current data set. The horizontal bar shows the major axis of the synthesized beam.

3.4 Implications for galaxy evolution at high redshift

The identification and subsequent dynamical characterization of AzTEC/C159 and AzTEC2 add new evidence on the existence of massive vigorously star-forming disks in the early Universe. By including these two sources, the sample of SMGs at $4 < z < 5$ with robust evidence of rotation has now increased to seven sources: AzTEC/C159, AzTEC2-A, ALESS 73.1, GN20, AzTEC1, Vd-17871, and J1000+0234 (see Fig. 3.9 Carilli et al., 2010; Hodge et al., 2012; De Breuck et al., 2014; Jones et al., 2017; Gómez-Guijarro et al., 2018b, K19). Here, we discuss the implications of these findings within the context of cold gas accretion and merger-driven star formation in massive, high-redshift galaxies.

3.4.1 A heterogeneous SMG population

The enhanced production of stars in SMGs has been largely attributed to gas-rich galaxy mergers (e.g., Tacconi et al., 2008; Younger et al., 2010; Engel et al., 2010; Riechers et al., 2011; Iono et al., 2016), which is compatible with the merger-driven starbursts in local ULIRGs (e.g., Sanders & Mirabel, 1996). AzTEC/C159 seems to deviate from this scenario, as there is no clear evidence for companions and/or interaction in the high-resolution [CII] line imaging presented by Jones et al. (2017). In the case of AzTEC2, its two components (namely AzTEC2-A and AzTEC2-B), are separated by a projected distance of ∼20 kpc with a relative velocity of 350 km s^{-1}. Since the morphology of AzTEC2-A and AzTEC2-B do not show clear signs of disturbance, these two components might undergo a pre-coalescence (first approach) phase (e.g., Calderón-Castillo et al., 2019). Consequently, the main

driver for the ongoing vigorous star formation activity in AzTEC2 (A and B) and AzTEC/C159 appears not to be ongoing merging activity. Instead, the dynamics, $\alpha_{\rm CO}$, and/or $\Sigma_{\rm SFR}$ value of AzTEC/C159 and AzTEC2 (A and B) point towards a smoother mode of star formation that drives a massive, star-forming disk (e.g., Dekel et al., 2009a,b; Carilli et al., 2010; Hodge et al., 2012). These results strengthen the scenario in which single-dish selected SMGs are a heterogeneous population (e.g., Hayward et al., 2011, 2013), including major mergers (e.g., AzTEC3; Riechers et al., 2014), pairs of (likely infalling) disk galaxies that are blended into a single sub-mm source –as observed in AzTEC2, and isolated disk galaxies like AzTEC/C159. This heterogeneity, in part, can be explained within the context of the MS alongside the SMGs selection function. Since sub-mm surveys lead to flux (≡SFR) limited samples of galaxies (e.g., Scott et al., 2008; Aretxaga et al., 2011), at high redshift ($z \gtrsim 3$), only SFGs harboring a SFR$\gtrsim 300\,M_{\odot}\,{\rm yr}^{-1}$ can be selected (e.g., Magnelli[†] et al., 2019). Therefore, this selection function tends to identify the extreme and massive-end of the SFGs population at high redshifts, including galaxies on and above the MS (see Fig. 3.9).

3.4.2 Star-forming disks at $z \sim 4.5$ and their connection to the main sequence

According to observations in the local/low-redshift Universe (e.g., Ellison et al., 2018), star-forming disk galaxies remain confined within the MS as their stellar mass grows steadily. Whether this evolutionary scenario for disk galaxies remains out to the epoch of massive galaxy assembly ($3 \lesssim z \lesssim 6$) has not been systematically explored yet. In a pioneering effort, we combine the SFR and stellar mass constraints of AzTEC/C159 and AzTEC2-A[6] with those of SMGs over $4 < z < 5$ exhibiting a rotating massive disk (Fig. 3.9) – that has been previously reported in the literature (Carilli et al., 2010; Hodge et al., 2012; De Breuck et al., 2014; Jones et al., 2017; Gómez-Guijarro et al., 2018b, K19). Classifying these galaxies into interacting and isolated disks, we find that the former (latter) are preferentially located at the low(high)-mass end. This is, again, partially driven by the SMGs selection function that biases the sample towards the starburst population at lower stellar masses. However, for $\log(M_{\star}/M_{\odot}) \gtrsim 10.5$ where this selection effect diminishes, we find that secular disks at $z \sim 4.5$ do not appear to be confined within the MS. Whereas both AzTEC2-A and AzTEC/C159 are approaching to the upper-end of the MS, some of them, e.g., AzTEC1 (Tadaki et al., 2018), are offset by $> 2\sigma$ with respect to the MS (where $\sigma = 0.3$ dex is the dispersion of the MS; e.g., Schreiber et al., 2015). Thus, using only the offset with respect to the MS to infer the dominant star formation mechanism (mergers and/or cold gas accretion) in high-redshift SMGs might be misleading.

3.4.3 The cold gas accretion versus merger mode of star formation at $z \sim 4.5$

The gas-dominated rotating disks at $z \sim 4.5$ with concomitant intense star formation activity seem to have no analog in the local/low-redshift Universe. Yet, numerical simulations do predict that the enhanced gas supply from cosmological filaments at high redshifts can build and maintain an unstable dense gas-rich disk (Romano-Díaz et al., 2014; Feng et al., 2015; Anglés-Alcázar et al., 2017), which breaks into clumps forming stars at a high rate (Dekel et al., 2009b). This intense level of star formation can be further enhanced via gravitational harassment (as advocated for GN20; Carilli et al., 2010), consistent, for example, with the presence of a companion galaxy in the vicinity of AzTEC2-A.

[6] We adopt the dynamical mass of AzTEC2-A ($2.5 \times 10^{11}\,M_{\odot}$) as an upper limit for its stellar mass. Oppositely, the molecular gas mass derived via an ULIRG-like $\alpha_{\rm CO}$ conversion factor, i.e., $10^{11}\,M_{\odot}$, might be considered as a lower limit.

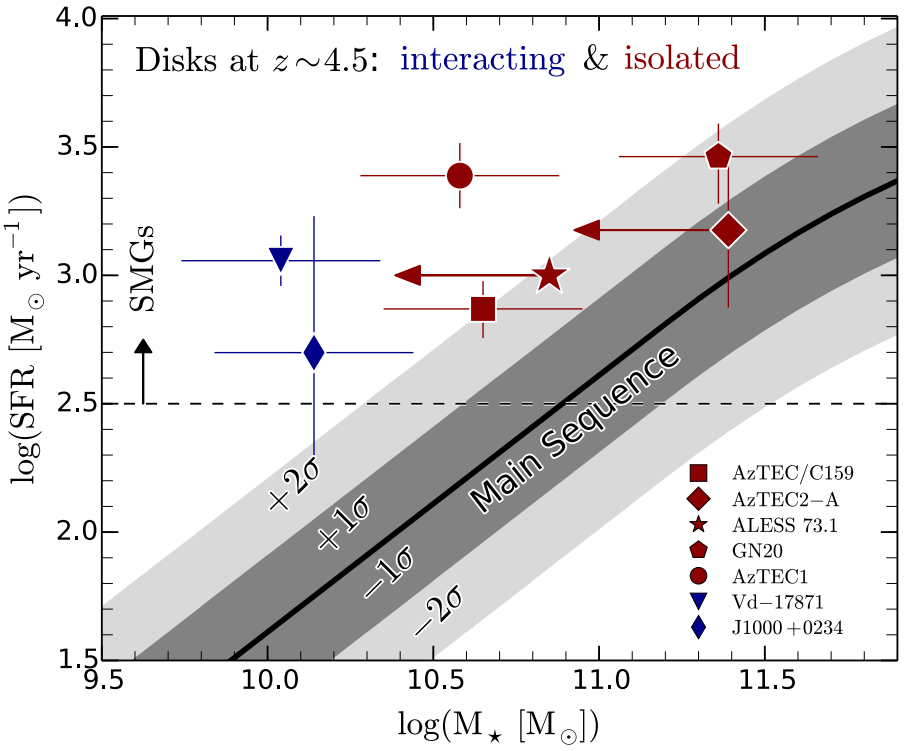

Figure 3.9: Star-forming disks at $z \sim 4.5$ in the SFR–$M_\star$ plane. This compilation only includes SMGs at $4.0 < z < 5.0$ for which robust evidence of rotation (stellar mass and SFR) have been reported in the literature (Carilli et al., 2010; Hodge et al., 2012; De Breuck et al., 2014; Jones et al., 2017; Gómez-Guijarro et al., 2018b, K19). The upper limits for the stellar mass of AzTEC2 and ALESS 73.1 are constrained from measurements of their dynamical mass. The MS of SFGs at $z = 4.5$ (Schreiber et al., 2015) is shown by the black solid line, while its associated dispersion (at 1σ and 2σ) is illustrated by the gray regions. The data points are color-coded according to the signatures of interaction in these SMGs. The horizontal dashed line shows the average IR flux (i.e., SFR) limit in sub-mm/mm surveys that uncovered these sources (e.g., Scott et al., 2008; Aretxaga et al., 2011; Magnelli[†] et al., 2019).

It is also expected that the extreme SFR of such disk-like systems could lead to high gas excitation conditions as a result of heating by turbulence and/or cosmic rays (Papadopoulos et al., 2012b). Since the mean radiation field intensity in $z \gtrsim 3$ MS galaxies becomes comparable to that of local ULIRGs (Daddi et al., 2015), the ^{12}CO SLEDs of $z \gtrsim 3$ star-forming disks and merger-driven starbursts may look similar. Certainly, we have found that the ^{12}CO SLED of AzTEC/C159 (see Fig. 3.4), and GN20 (Carilli et al., 2010; Hodge et al., 2012), is compatible with that of the merger-driven SMG AzTEC3 (Riechers et al., 2010, 2014) and J1000+0234 (Schinnerer et al., 2008). We recall that high excitation conditions could also be a result of AGN-driven mechanical and radiative feedback (Papadopoulos et al., 2008, 2010; Dasyra et al., 2014; Moser et al., 2016); however, there is no robust evidence of an AGN in AzTEC/C159 (Smolčić et al., 2015) indicating that its ^{12}CO SLED primely traces star formation activity.

To summarize, contrary to the clear dichotomy between the global properties of star formation (e.g., SFE and localization with respect to the MS) in low-redshift secular disks and merger-driven starbursts (e.g., Kennicutt, 1998a; Genzel et al., 2010), our results indicate that such a dichotomy diminishes

during the $z \gtrsim 4$ regime. At this early epoch, star-forming disks that harbor vast gas reservoirs (e.g., Sargent et al., 2014; Schinnerer et al., 2016; Tacconi et al., 2018) could form stars nearly as efficiently as merger-driven starbursts (e.g., Hayward et al., 2012; Narayanan et al., 2015; Hayward et al., 2018) located above the MS. Indeed, numerical simulations predict that whereas galaxy mergers with a low gas fraction (i.e., at low redshift) do trigger strong starbursts, the elevated gas fractions of merging systems in the early Universe weakly enhance the –already intense– production of stars (Fensch et al., 2017). Thus, at $z \gtrsim 4$, there is only a subtle difference between the integrated/global properties of star formation in massive secular disk galaxies and merger-driven starbursts.

3.5 Summary

We have used ^{12}CO(2−1), ^{12}CO(5−4) and [CII] line observations from the NOEMA, VLA, and ALMA telescopes to explore the conditions for star formation in AzTEC/C159 and AzTEC2 (A): two massive star-forming disks at $z \sim 4.6$.

We have inferred the following properties for AzTEC/C159:

- Its molecular gas mass of $M_{\rm H2}(\alpha_{\rm CO}/4.3) = (1.5 \pm 0.3) \times 10^{11}\,M_{\odot}$ implies a high gas fraction of $\mu_{\rm gas}(\alpha_{\rm CO}/4.3) \equiv M_{\rm H_2}/M_{\star} = 3.3 \pm 0.7$. Its $L_{\rm IR}/L'_{\rm CO}$ ratio of $(216 \pm 80)\,L_{\odot}\,({\rm K\,km\,s^{-1}\,pc^2})^{-1}$, tracing the star formation efficiency, is as high as of local ULIRGs and typical SMGs (e.g., Aravena et al., 2016, and references therein);

- The ^{12}CO(5−4)/CO(2−1) line brightness temperature ratio of $r_{52} = 0.55 \pm 0.15$ agrees with the high gas excitation of the star-forming disk galaxy GN20 at $z = 4.05$ (Carilli et al., 2010; Hodge et al., 2012). Surprisingly, such gas excitation conditions are comparable to those of the merger-driven SMGs J1000+0234 (Schinnerer et al., 2008, J17) and AzTEC3 (Riechers et al., 2010, 2014) at similar redshift;

- Its CO→ H_2 conversion factor ($\alpha_{\rm CO}$) is $3.9^{+2.7}_{-1.3}\,M_{\odot}\,{\rm K^{-1}\,km^{-1}\,s\,pc^{-2}}$ and $3.8^{+2.6}_{-1.4}\,M_{\odot}\,{\rm K^{-1}\,km^{-1}\,s\,pc^{-2}}$, as given by the dynamical and gas-to-dust method, respectively; indicating that the conditions of the ISM in AzTEC/C159 are more consistent with those of local star-forming disks.

Whereas for AzTEC2:

- We have detected ^{12}CO(5→4) and [CII] line emission in both components, leading to a redshift of 4.626 ± 0.001 and 4.633 ± 0.001 for AzTEC2-A and AzTEC2-B, respectively, ruling out a preliminary redshift solution for the AzTEC2 complex of $z = 1.12$;

- We have derived $L'_{\rm CO} = (12.5 \pm 2.6) \times 10^{10}\,{\rm K\,km\,s^{-1}\,pc^{-2}}$ for AzTEC2-A, implying a molecular gas mass of $(1.0 - 5.4) \times 10^{11}\,M_{\odot}$. Opposite to the merger-driven mode of star formation, its $L_{\rm IR}/L'_{\rm CO}$ ratio of $(140 \pm 60)\,L_{\odot}({\rm K\,km\,s^{-1}\,pc^{-2}})^{-1}$, $\tau_{\rm gas} = (60 - 300)\,{\rm Myr}$, and $\Sigma_{\rm SFR} = (70 \pm 21)\,M_{\odot}\,{\rm yr^{-1}\,kpc^{-2}}$ are more consistent with the expected properties of secular evolution in high-redshift disk galaxies (e.g., Hodge et al., 2012; Saintonge et al., 2013; Jiménez-Andrade[†] et al., 2019).

- Correspondingly, for ATEC2-B we have found that $L'_{\rm CO} = (3.3 \pm 0.7) \times 10^{10}\,{\rm K\,km\,s^{-1}\,pc^{-2}}$, $M_{\rm gas} = (0.3-1.4)\times10^{11}\,M_\odot$, $L_{\rm IR}/L'_{\rm CO} = (170\pm70)\,L_\odot({\rm K\,km\,s^{-1}\,pc^{-2}})^{-1}$, $\tau_{\rm gas} = (50-250)\,{\rm Myr}$ and $\Sigma_{\rm SFR} = (23 \pm 8)\,M_\odot\,{\rm yr^{-1}\,kpc^{-2}}$; which are compatible –to some extent– with a secular mode of star formation;
- We have revealed a rotation-dominated [CII] disk in AzTEC2-A, with an intrinsic (de-projected) rotational velocity of $v_{\rm rot} = (510 \pm 80)\,{\rm km\,s^{-1}}$, velocity dispersion of $\sigma \lesssim 100\,{\rm km\,s^{-1}}$ and dynamical mass of $M_{\rm dyn} = (2.5 \pm 1.0) \times 10^{11}\,M_\odot$.

With the increasing evidence of gas-rich disks vigorously forming stars at $z > 4$ (e.g., Carilli et al., 2010; Hodge et al., 2012; Tadaki et al., 2018), we are now departing from the conventional picture wherein SMGs are primely merging systems (Engel et al., 2010). Our results indicate that even secular disk galaxies, that harbor vast gas reservoirs (e.g., Sargent et al., 2014; Schinnerer et al., 2016; Tacconi et al., 2018), could sustain intense star formation activity that nearly resembles that of merger-driven SMGs (e.g., Hayward et al., 2012). As a result, the dichotomy between the integrated/global properties of star formation in massive secular disks and merger-driven starbursts diminishes at $z \gtrsim 4$. A more systematic study of high-redshift SMGs is required to verify this scenario, which will also help us to understand the mechanisms that suppress star formation in $z \gtrsim 4$ massive disks: the possible progenitors of quiescent disks at $z \sim 2$ (Toft et al., 2017). We partially address the latter topic, quenching, in the following chapter.

3.6 Appendix

3.6.1 The misleading redshift solution of $z = 1.12$ for AzTEC2

Since the discovery of AzTEC2 (Scott et al., 2008), extensive multi-wavelength campaigns have been undertaken to determine its redshift. A preliminary spectroscopic redshift of $z = 1.12$ has been adopted in past studies (e.g., Smolčić et al., 2012, 2017; Miettinen et al., 2015; Brisbin et al., 2017; Miettinen et al., 2017a). This value has been inferred from a tentative line detection at 108.436 GHz, obtained with the Combined Array for Research in Millimeter-wave Astronomy (CARMA), and an optical line emission at 7915Å detected with Keck/DEIMOS; which have been associated with ^{12}CO($2 \rightarrow 1$) and [OII], respectively (M. Baloković, priv. comm.). Using archival optical/near-IR spectroscopy from VLT/VIMOS and Keck/MOSFIRE, here we demonstrate that those line detections correspond to a foreground SFG at $z = 1.1235 \pm 0.0005$ that lies at 1.5 arcsec to the south of AzTEC2-A (see Fig. 3.10).

Optical/near-IR spectroscopy from VLT and Keck

We use long-slit optical spectra obtained with the VLT using VIMOS, as part of the Large Early Galaxy Astrophysics Census (LEGA-C) (van der Wel et al., 2016). Two spectra of 1200s integration time each were obtained on 2015/02/18 during good weather conditions (seeing=1.3 arcsec, airmass=1.25). The slit was centered on the brightest component of AzTEC2 and set with PA = 0° (see Fig. 3.10). The pipeline provided by the European Southern Observatory (ESO) was employed to produce wavelength-calibrated 2D spectra, while sky/object subtraction and flux calibration were performed with the custom pipeline described in van der Wel et al. (2016). The final/co-added spectrum covers the wavelength range from 6300Å to 8600Å and has a spectral resolution of ~ 5.5Å.

We also use near-IR spectra obtained with MOSFIRE (mounted in the Keck telescope) in K band on December 22nd, 2012 by Casey et al. (2017). An `ABBA` nod with 180s individual integrations was needed to secure a total time integration of 0.70 hrs. The slit orientation was set at a PA = −32.6° and centered on the bright optical source C (see Fig. 3.10). Data reduction was performed by using the `MOSKY` package, as described in detail in Casey et al. (2017). The final spectrum spans over $1.9 - 2.3\mu$m and has a spectral resolution of 2.9 Å.

[OII] and [SIII] line detection in source C: a foreground SFGs at $z = 1.12$

We benefit from the orientation of the slits used to obtain the VLT/VIMOS and Keck/MOSFIRE spectra (i.e. PA = 90° and PA = −32.6°, respectively; Fig. 3.10) to retrieve emission from all the sources around AzTEC2. To accurately retrieve 1D spectra of those components, we first identify the emission from the bright elliptical galaxy in the 2D spectrum (see insets in Fig. 3.11). Then, we use apertures of 1 arcsec width to integrate emission along the spatial axis of the 2D spectra at the expected locus of AzTEC2-A (or AzTEC2-B) and source C. In the left panel of Fig. 3.11, we present the 1D spectra of the foreground elliptical galaxy, source C and AzTEC2-A that are covered by the VLT/VIMOS long-slit spectroscopy. The spectrum of the elliptical galaxy reveals absorption features that we associate with Hβ 4862 Å, Mg 4862 Å and Na 4862 Å at $z = 0.3379 \pm 0.0001$. A bright line at 7915 Å displaying a doublet structure is observed in the spectrum of the complex C, and not in AzTEC2 as previously inferred from Keck/DEIMOS spectroscopy (M. Balaković priv. comm.). This

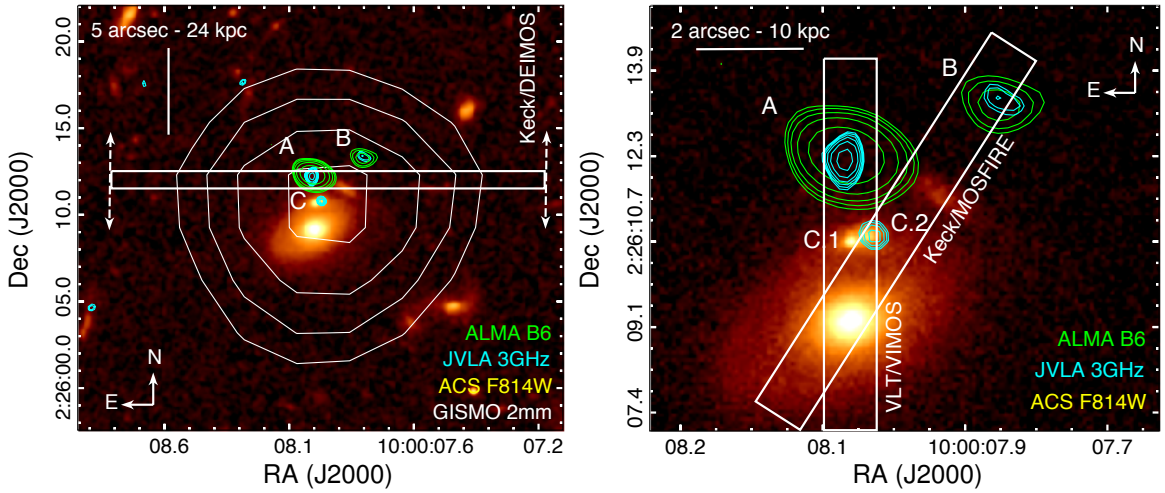

Figure 3.10: Long-slit setup used to obtain optical/near-IR spectra towards AzTEC2. *Left panel:* GISMO/IRAM 2mm (white), ALMA (green) and VLA (blue) > 3σ contours overlaid on the *HST*/ACS F814W image. The white rectangle shows the position of the slit (PA=90°) used to obtain an optical spectrum with Keck/DEIMOS (M. Baloković priv. comm.). Given the highly crowded optical field, it is likely that the slit was not properly centered on AzTEC2 (see text for details). *Right panel:* Long-slit setup used to obtain optical and near-IR spectroscopy with VLT/VIMOS and Keck/MOSFIRE, respectively. This zoomed image shows that the source C splits into two components (C.1 and C.2), both of them at $z \sim 1.12$. The white rectangles show the position of the VLT/VIMOS (PA=0°) and Keck/MOSFIRE (PA=−32.6°) slit.

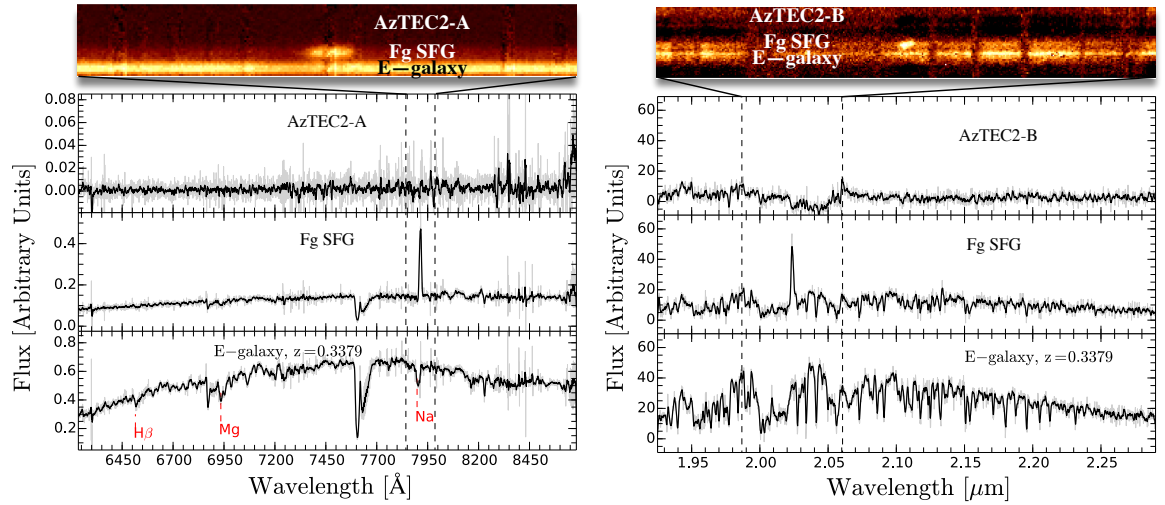

Figure 3.11: *Left panel:* VLT/VIMOS spectra of the nearby elliptical galaxy, the foreground SFG at $z = 1.1235$ (source C), and the main component of AzTEC2 (i.e. A). The inset image shown above displays the 2D spectrum around the line at 7915Å associated with source C. *Right panel:* Keck/MOSFIRE spectra of the nearby elliptical galaxy, the foreground SFG at $z = 1.1235$ (source C) and the component B of AzTEC2. The inset image presented above shows the 2D spectrum around the near-IR line at 2.024μm, which is also associated with the foreground SFG (source C).

indicates that the slit used to obtain the Keck/DEIMOS spectrum was not properly centered on the sub-millimeter source (see Fig. 3.10).

The position of the MOSFIRE slit, on the other hand, covers the source C and AzTEC2-B. While the spectrum of AzTEC-B features a faint continuum with no clear indications of emission lines, the spectrum of the C complex shows a strong emission line at 2.024 μm (see right panel of Fig. 3.11). By associating the lines at 7915 Å and 2.024μm with the nebular lines [OII] 3727 Å and [SIII] 9532 Å, respectively, we derive a redshift solution for the complex C of $z = 1.1235 \pm 0.0005$. Such emission lines, tracing HII regions around massive young stars (e.g., Kehrig et al., 2006; Kennicutt & Evans, 2011), indicate ongoing star formation in this foreground galaxy – albeit the contribution of an AGN to the observed line emission cannot be neglected.

Beyond the aforementioned nebular lines, it appears that the tentative line detection with CARMA (peak SNR∼3, M. Baloković, priv. comm.) is also associated with the source C. With an observed central frequency of 108.437 ± 0.010 GHz, this line might correspond to ^{12}CO(2→1) at $z = 1.126 \pm 0.001$. Deeper and high-resolution observations with NOEMA or ALMA are needed to confirm this line detection.

CHAPTER 4

A kpc-scale outflow in J1000+0234−S: a satellite galaxy at $z = 4.54$

We use archival Keck spectroscopy, and Subaru imaging, to characterize the extended Lyman α (Lyα) emission surrounding J1000+0234−S: a star-forming satellite galaxy neighboring a massive, dust-enshrouded sub-millimeter source at $z = 4.54$, J1000+0234−N. The Lyα emission exhibits a concentric, “ring-like” distribution (with a radius $R \sim 3$ kpc) that surrounds the rest-frame UV emission of J1000+0234−S. The optical Keck spectrum reveals a broad and asymmetric Lyα line profile, which resembles that proposed for an expanding shell model. Fitting this Lyα line profile using the radiative transfer code `LyaRT`, we find that the outflowing medium has a column density of $N_{\rm HI} \simeq 2 \times 10^{20}$ cm^{-2}, an expansion velocity of $V_{\rm exp} \simeq 230$ km s^{-1} and gas mass of $M_{\rm HI} \simeq 1.8 \times 10^{8}\, M_{\odot}$. Interestingly, the inferred dynamical lifetime of the shell (i.e., $V_{\rm exp}/R$) of 13 Myr is comparable with the age of the starburst. These findings suggest that a recent burst of star formation has driven a galactic-scale outflow, creating a "super-bubble" of hot gas that expands into the circum-galactic medium. By combining the previously reported star formation rate ($\sim 150\, M_{\odot}$ yr^{-1}) and cold gas content of J1000+0234−S, we speculate that the production of stars will be quenched within only ~ 20 Myr. We discuss these results in the context of “negative" feedback and its role in transforming $z \gtrsim 3$ starbursts into massive, spheroidal, early-type galaxies at $z \sim 2$.

This project has been carried out in collaboration with B. Magnelli, C. Gómez-Guijarro, E. Romano-Díaz, T. Bădescu, A. Karim, and F. Bertoldi.

4.1 Introduction

There is growing evidence of kpc-scale Lyman α (Lyα) halos at high redshift (e.g., Wisotzki et al., 2016; Leclercq et al., 2017; Childs & Stanway, 2018; Wisotzki et al., 2018; Crighton et al., 2019). Several physical mechanisms have been proposed to explain their origin (see review in Dijkstra, 2014; Cantalupo, 2017): resonant scattering of Lyα photons associated with star formation (e.g., Dijkstra & Loeb, 2009; Behrens & Braun, 2014; Faucher-Giguère et al., 2015; Lake et al., 2015; Momose et al., 2016; Mas-Ribas et al., 2017), gravitational cooling radiation (e.g., Fardal et al., 2001), Lyα fluorescence (e.g., Cantalupo et al., 2005, 2012, 2014), photo-ionization by active galactic nuclei (AGN; e.g., Geach et al., 2009) and shock-heated gas by galactic superwinds (e.g., Taniguchi & Shioya, 2000). Regardless of the nature of the emission, Lyα halos are adequate to explore the interaction between high-redshift galaxies and their circumgalactic medium (CGM).

Particular emphasis is given to $z \gtrsim 3$ Lyα halos surrounding dusty, highly star-forming galaxies (SMGs; e.g., Geach et al., 2005, 2016; Bridge et al., 2013). These are thought to undergo a short-lived, intense feedback phase that transforms high-redshift starbursts into mature/quenched systems (e.g., Bridge et al., 2013; Toft et al., 2014) – like $z \gtrsim 3$ massive, "dead" galaxies (e.g., Gobat et al., 2012; Glazebrook et al., 2017). In this context, Lyα halos around high-redshift starbursts could be explained by star formation-driven winds (e.g., Tenorio-Tagle et al., 1999; Taniguchi & Shioya, 2000), which expel gas into the CGM and, ultimately, suppress the production of stars (e.g., McGee et al., 2014; Somerville & Davé, 2015). A verification of such a scenario demands observational constraints of feedback in the epoch of galaxy assembly. However, such studies are mainly limited to extreme, massive galaxies (e.g., Spilker et al., 2018) that usually host an AGN (e.g., Swinbank et al., 2015); rendering the study of stellar feedback in high-redshift galaxies an open field of observational astronomy (see Gallerani et al., 2018).

Here, we aim at better characterizing the strong signatures of feedback in J1000+0234−S ($z \sim 4.54$, Carilli et al., 2008; Capak et al., 2008); a low-mass ($\log(M_\star/M_\odot) \sim 9$) SFG neighboring a massive, dust-enshrouded starburst (Gómez-Guijarro† et al., 2018a). We report that J1000+0234−S is surrounded by an extended, likely in expansion, Lyα halo driven a recent burst of star formation. Thus, this finding provides the first observational evidence of stellar feedback regulating the growth of low-mass galaxies at $z > 4$. This manuscript is organized as follows. The properties of J1000+0234−S and details of the observations are given in Sect. 4.2 and 4.3, respectively. The data analysis and results are presented in Sect. 4.4. Finally, we discuss the results in Sect. 4.5. Throughout, we assume a flat ΛCDM cosmology with $h_0 = 0.7$, $\Omega_M = 0.3$, and $\Omega_\Lambda = 0.7$.

4.2 J1000+0234

J1000+0234 was originally identified as a Lyman Break Galaxy (LBG) in the COSMOS field at $z = 4.547$ (Capak et al., 2008). ^{12}CO line observations unveiled a massive cold gas reservoir of $M_{\rm gas} \simeq 2.6 \times 10^{10} M_\odot$ (Schinnerer et al., 2008), which occupies an overdense environment (galaxy overdensity parameter of $\delta_{\rm g} \gtrsim 4$; Smolčić et al., 2017). *HST* WFC3 imaging, tracing the rest-frame UV emission, revealed that J1000+0234 is composed by two major (likely interacting) components separated by a projected distance of ~ 6 kpc (see Fig. 4.1; Gómez-Guijarro† et al., 2018a).

The northern and more massive component ($\log(M_\star/M_\odot) \sim 10.1$; J1000+0234−N) is embedded in a dusty environment with $\log(L_{\rm IR}/L_\odot) \sim 12.6$, where stars form at a rate of $\sim 500\, M_\odot\, {\rm yr}^{-1}$ (Gómez-Guijarro† et al., 2018a). A strong, double-peaked [C II] 158 μm emission line was detected with ALMA at the position of J1000+0234−N (at $z = 4.540$), indicating that this is a single, rapidly rotating disk with a dynamical mass of $\log(M_{\rm dyn}/M_\odot) \sim 11.6$ (Jones et al., 2017). The southern component, J1000+0234−S, is ∼10 times less massive than J1000+0234−N. Yet, it emits the bulk (∼ 75%) of the rest-frame UV emission observed with *HST*, consistent with the fact that no dust continuum (nor [CII] line) emission has been detected towards this component (Capak et al., 2008; Gómez-Guijarro† et al., 2018a). The UV emission suggests a star formation rate (SFR) of $148 \pm 8\, M_\odot\, {\rm yr}^{-1}$ and a UV slope (β) of −2, as expected for LBGs at similar redshift (Gómez-Guijarro† et al., 2018a, and references therein).

4.3 Keck spectroscopy and Subaru imaging

We use the optical spectra obtained by Capak et al. (2008) with the DEIMOS instrument mounted at the Keck II telescope. Eight spectra of 1800s exposure time each, i.e. 4hrs total integration, were obtained in January 2007 under good atmospheric conditions (seeing=0.4 − 0.6 arcsec, airmass=1.25). The slit of 1 arcsec width was centered at the position of the brightest UV component, corresponding to J1000+0234−S, and set at PA = -87° (see Fig. 4.1). Data reduction was performed with a modified version of the DEEP2 DEIMOS pipeline (Capak et al., 2008). Based on the skylines in the spectrum, a spectral resolution of ${\rm FWHM}_{\rm sky} = 3.3$ Å is measured; which translates into $\sim 145\, {\rm km\, s}^{-1}$ at the locus of the Lyα line.

We also employ optical imaging obtained with the Suprime-Cam mounted at the Subaru telescope as part of the "Subaru COSMOS 20 project" (Taniguchi et al., 2015). In particular, we use the intermediate-band filter IA679 centered at $\lambda_{\rm eff} = 6781.1$Å (FWHM= 335.9Å, PSF=1.58 arcsec), since it covers the Lyman-alpha line at the redshift of J1000+0234. Following the procedure of narrow-band surveys (e.g., Villar et al., 2008; Gómez-Guijarro et al., 2016), we subtract the adjacent continuum using the broad-band filter Subaru r+, isolating the line flux (see Fig. 4.1).

4.4 Data Analysis and Results

4.4.1 Surface brightness radial profile

In Fig. 4.1, we overlay the rest-frame UV continuum emission from the *HST*/Wide Field Camara 3 (WFC3) (Gómez-Guijarro† et al., 2018a, F125W) with the extended Lyα line emission revealed by the Subaru/Suprime-Cam imaging (IA679). A visual inspection reveals strong Lyα emission exhibiting a "ring-like" shape around the low-mass SFG J1000+0234−S. The Lyα emission does not spatially correlate with the massive, dust-enshrouded component, J1000+0234−N, that is offset by a projected distance of ∼ 6 kpc from the satellite galaxy. Faint UV emission is also detected towards a foreground system ($z = 1.41$; Capak et al., 2008); this is seen in projection at ∼ 1.5 arcsec east to J1000+0234−S where, as expected, Lyα emission is absorbed.

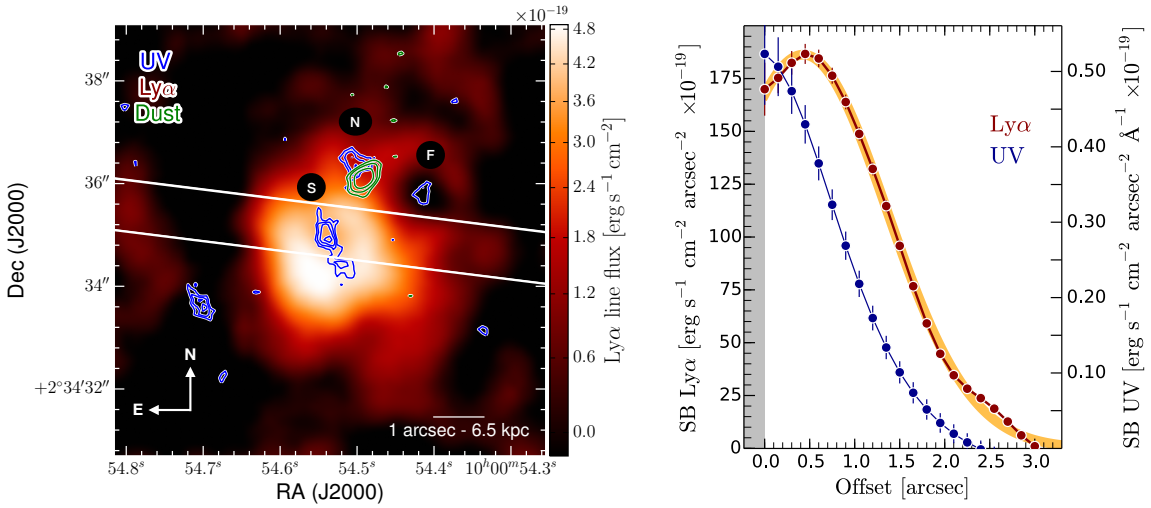

Figure 4.1: *Left panel:* extended Lyα emission around the low-mass SFG (S) neighboring the massive SMG J1000+0234 (N). The color scale shows the flux of Lyα emission as revealed by Subaru/Suprime-Cam imaging with the IA679 filter. Blue contours illustrate the rest-frame UV emission detected with the *HST*/WFC3 F125W filter, while green contours show the far-infrared (ALMA band 7) emission (see Gómez-Guijarro† et al., 2018a). Contour levels start at the 3σ level and increase logarithmically. The component "F" is a foreground galaxy at z = 1.41 (Capak et al., 2008) and hence absorbs Lyα emission from the J1000+0234 complex. The white rectangle shows the locus of the slit used to obtain optical spectroscopy with Keck/DEIMOS (Capak et al., 2008). *Right panel:* Azimuthally averaged Lyα surface brightness (red solid line) of J1000+0234−S. The UV continuum emission (blue dots) has been convolved with the PSF of the IA679 image and re-scaled to the Lyα emission profile to aid the visual comparison. The error bars illustrate the 1σ uncertainty of the integrated flux within the annulus. The thick orange curve shows the Gaussian component fit to the Lyα surface brightness radial profile. The gray region signalizes the negative offset of the radial profile.

To better compare the spatial extent and distribution of the UV and Lyα emission, we derive their azimuthally averaged surface brightness profiles (right panel of Fig. 4.1). We use concentric, one-pixel-wide annuli centered at the pixel containing the brightest rest-frame UV emission that we adopt as the center of J1000+0234−S. For visualization purposes only, we convolve (and re-scale) the UV surface brightness distribution to match the instrumental broadening (and normalization) of the Lyα radial profile. This analysis corroborates that the Lyα emission is more extended that the rest-frame UV, which is consistent with recent studies of extended Lyα halos around individual high-redshift SFGs (e.g., Wisotzki et al., 2016; Leclercq et al., 2017). We confirm in addition that the Lyα emission exhibits a concentric, “ring-like” structure around the low-mass satellite galaxy (J1000+0234−S); where the Lyα radial profile can be reproduced with a single Gaussian component that is offset by $\sim$ 0.45 arcsec, i.e. 3kpc, with respect to the UV peak emission. The Gaussian model also yields a FWHM of 2.15 arcsec; given the PSF width of 1.58 arcsec, we infer a deconvolved FWHM of 1.5 arcsec. This value does not necessarily represent the width of the "ring-like" structure, as the radial light profile is being broadened by diffuse Lyα emission lying in the inner region of the structure.

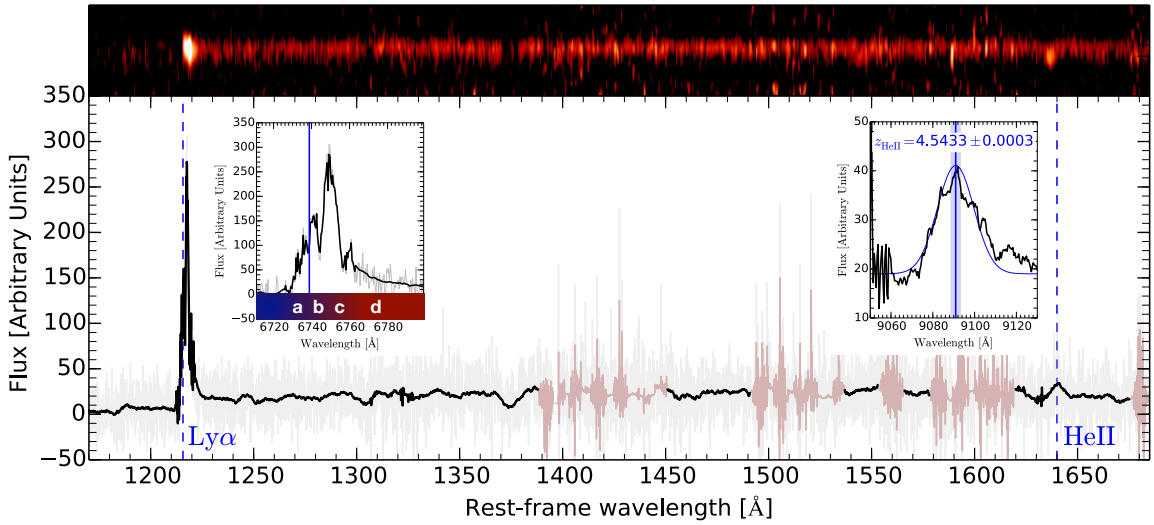

Figure 4.2: Keck/DEIMOS spectrum (upper panel:2D, lower panel:integrated/1D) obtained towards J1000+0234−S (Capak et al., 2008). The original 1D spectrum is shown by the gray solid line, while a noise-filtered version (using Weiner filtering) is illustrated by the solid black line. The wavelength range highly affected by the sky-lines is shown by the red solid lines. The vertical solid/dashed blue line show the observed/rest frame wavelength of the Lyα and HeII 1640 line. The right inset image shows the spectrum (observed frame) around the HeII 1640 line. We fit a Gaussian component (blue line) to retrieve the central observed wavelength and hence estimate the systematic redshift of 4.5433±0.0003. The left inset image contains the spectrum (observed frame) around the Lyα line. We point out the expected velocity components for an expanding thin shell around a central source (e.g., Verhamme et al., 2006; Orsi et al., 2012; Gurung-López et al., 2018): a small blue-shifted wing (a), one narrow emission peak nearly centered at the systemic velocity (b), two red-shifted peaks (c) and one extended red wing (d).

4.4.2 Lyα line profile

The integrated/1D optical spectrum of J1000+0234 (obtained within a 2 arcsec-width aperture along the 2D spectra's spatial axis) reveals a prominent, broad and asymmetric line around 6740Å associated with Lyα by Capak et al. (2008, see Fig. 4.2). This spectroscopic data also unveil a faint emission line at 9091Å that corresponds to HeII 1640Å . Given the non-resonant nature of the latter nebular line, we employ it to estimate the systemic redshift of J1000+0234−S, that is, $z = 4.5433 \pm 0.0003$. This redshift value allow us to set the Lyα line in the rest-frame and characterize its multiple components (see Fig. 4.2): one small blue-shifted wing (a), one narrow emission peak centered nearly at the systemic velocity (b), two red-shifted peaks (c) and one extended red wing (d).

Modelling the line profile with LyaRT

Wide and asymmetric Lyα line profiles have been interpreted as evidence of galactic-scale outflows driven by starburst galaxies (e.g., Taniguchi & Shioya, 2000; Dawson et al., 2002; Dijkstra & Loeb, 2009): while photons experiencing multiple backscatterings produce an extended and redshifted wing, the external and expanding neutral HI gas along the line of sight absorbs the blue velocity component. Interestingly, the velocity components of the Lyα line in J1000+0234−S (see inset in

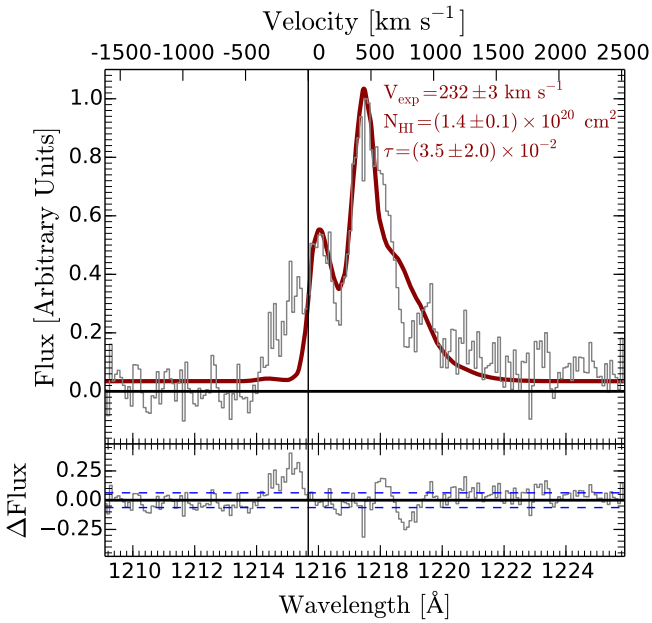

Figure 4.3: Lyα line spectrum of J1000+0234−S. The expanding shell model obtained with `LyaRT` (e.g., Gurung-López et al., 2018) is shown by the red solid line. Residuals are presented in the lower panel, where the $\pm 1\sigma$ noise level is shown by the dashed blue lines.

Fig. 4.2) resemble those predicted for an expanding thin shell (e.g., Verhamme et al., 2006; Orsi et al., 2012). To better constrain this scenario, we use the Lyα radiative transfer code `LyaRT`[1], based on the results of Orsi et al. (2012), which predicts the spectrum produced by resonant scattering of Lyα photons traveling in different outflow geometries, hydrogen column densities ($N_{\rm HI}$), expansion velocities ($V_{\rm exp}$) and dust absorption optical depths (τ). We thus adopt the expanding shell model (along with a flat-continuum level) and fit the observed Lyα line via the least-squares Levenberg-Marquardt algorithm. We use 1000 MC realizations to propagate the uncertainty of the input flux values into the fitting procedure[2]. We then derive the best-fitting parameters of $N_{\rm HI} = (1.4 \pm 0.1) \times 10^{20}$ cm^{-2}, $V_{\rm exp} = 232 \pm 3$ km s^{-1} and $\tau = (3.5 \pm 2.0) \times 10^{-2}$, consistent with the range of values reported for LBGs and Lyα emitters (e.g., Verhamme et al., 2008). We estimate, in addition, the HI mass ($M_{\rm HI}$) in the shell following Verhamme et al. (2008):

$$M_{\rm HI} \approx 10^7 \left(\frac{r}{1\,\rm kpc}\right)^2 \left(\frac{N_{\rm HI}}{10^{20}\,\rm cm^{-2}}\right) M_\odot, \tag{4.1}$$

where r is the radius of the shell, that is ∼3 kpc. By using the column density derived above, we find that $M_{\rm HI} \approx 1.8 \times 10^8\, M_\odot$.

[1] https://pypi.org/project/LyaRT-Grid/

[2] We note that the error bars for $V_{\rm exp}$, $N_{\rm HI}$ and τ do not contain the systematic uncertainties associated with the adopted `LyaRT`'s model.

As observed in Fig. 4.3, the expanding shell model succeed in reproducing (within the uncertainties) most of the observed components of the Lyα line profile in J1000+0234−S, strengthening the emerging picture wherein a large fraction of Lyα emitters are consistent with an outflowing shell geometry (e.g., Dawson et al., 2002; Tapken et al., 2007; Verhamme et al., 2008; Schaerer & Verhamme, 2008; Dessauges-Zavadsky et al., 2010; Schaerer et al., 2011; Chonis et al., 2013; Gronke & Dijkstra, 2014; Hashimoto et al., 2015; Patrício et al., 2016; Yang et al., 2016). This model, however, fails to reproduce the blue shifted narrow peak of J1000+0234−S (i.e. component "a" in Fig. 4.2). This discrepancy could be a result of additional physical processes, not included in conventional shell-models, that produce Lyα blue peaks (e.g., Fermi acceleration, Neufeld & McKee, 1988; Chung et al., 2016; Orlitová et al., 2018). Alternatively, beyond the central source considered in the model, another Lyα radiation sources might contribute to the observed spectrum, e.g., fluorescence, cosmological UV background (e.g., Cantalupo et al., 2005; Kollmeier et al., 2010; Trainor & Steidel, 2013; Dijkstra, 2014).

4.5 Implications for galaxy evolution

We have shown that prominent Lyα emission is concentrically distributed around J1000+0234−S; a low-mass SFG ($\log(M_\star/M_\odot) \sim 9$) neighboring a massive, dust-obscured starburst at $z = 4.54$ (namely J1000+0234−N; with $\log(M_\star/M_\odot) \sim 10.1$). This configuration suggests that the main physical mechanism behind the extended Lyα emission is the vigorous burst of star formation in J1000+0234−S (SFR$\sim 150\, M_\odot\, \mathrm{yr}^{-1}$); Ly$\alpha$ photons are produced in the HII regions surrounding young stars and subsequently scattered outwards in the circumgalactic neutral medium (e.g., Dijkstra, 2014). The apparent minimal contribution of J1000+0234−N, to the Lyα emission, might be a result of its elevated dust content that hinders the escape of Lyα photons. Hence, this finding is consistent with the major role of satellite galaxies in powering extended Lyα halos (e.g., Shimizu & Umemura, 2010; Lake et al., 2015; Momose et al., 2016), particularly around dusty and massive starburst galaxies like J1000+0234−N.

The presence of extended Lyα emission around high-redshift galaxies might also indicate ongoing AGN feedback (e.g., Swinbank et al., 2015). In the case of J1000+0234−S, the only tentative evidence of an obscured AGN is the HeII 1640Å line detection (Scarlata et al., 2009). Yet to firmly constrain the contribution of an AGN to the observed Lyα halo, additional emission line detections such as NV 1240Å and CIV 1549Å (e.g., Villar-Martín et al., 2007; Scarlata et al., 2009; Swinbank et al., 2015) are needed. Moreover, since AGN-dominated feedback occurs in $\log(M_\star/M_\odot) \gtrsim 10$ galaxies (e.g., Martín-Navarro & Mezcua, 2018, and references therein), it favors a star formation-driven feedback scenario in the low-mass galaxy J1000+0234−S.

We have also reported that the Lyα line profile resembles that proposed for an expanding shell model (Verhamme et al., 2008; Orsi et al., 2012), suggesting that intense bursts of star formation could drive "super-bubbles" of ionized gas around high-redshift galaxies (e.g., Appleton et al., 1987; Tenorio-Tagle et al., 1999; Silich et al., 2010). Assuming that $V_{\mathrm{exp}} \sim 230\,\mathrm{km\,s}^{-1}$ remains constant, across a radius of ~ 3 kpc (Sect. 4.4), we infer that the expanding shell should have originated ~ 13 Myr ago. It is reassuring that, despite the "simplicity" of the model, the latter value is of the same order of magnitude as the starburst age in J1000+0234−S (< 10 Myr; Capak et al., 2008); supporting, again, the star formation-driven winds scenario.

The remaining question is whether the outflowing activity is able to exhaust the cool gas reservoir and, consequently, suppress the star formation activity in J1000+0234−S. According with Schinnerer et al. (2008), the J1000+0234 complex harbors a cold gas reservoir of $M_{\rm gas} = 2.6 \times 10^{10}\,M_{\odot}$; given the relatively coarse resolution of the observations (~ 2 arcsec), it is not clear what is the contribution of J1000+0234−S to the inferred gas content. Since J1000+0234−S is ∼10 times less massive than J1000+0234−N, as suggested from their respective $M_{\star}$ values (Gómez-Guijarro† et al., 2018a), we would expect that J1000+0234−S hosts a cold gas mass of $\sim 3 \times 10^{9}\,M_{\odot}$. If cosmological gas accretion is halted, the available gas reservoir of J1000+0234−S will be able to sustain the current SFR ($\sim 150\,M_{\odot}{\rm yr}^{-1}$) during only ~ 20 Myr. Certainly, the evidence of an extended, likely expanding, Lyα halo indicates that fresh star-forming gas (from the galaxy's halo) might not be accreted within this time-scale. The radiative/kinetic energy from stellar winds and supernovae is expected to maintain an over-pressured, expanding bubble of hot gas that can propagate further into the intergalactic medium (e.g., Heckman et al., 1993; Heckman & Thompson, 2016). Therefore, star formation in J1000+0234−S will most likely be quenched once the gas reservoir is consumed – as predicted for high-redshift satellite galaxies (McGee et al., 2014).

This discovery of a satellite galaxy experimenting a rapid quenching is of utter importance to evaluate the proposed formation path of massive, compact early-type galaxies at $z \sim 2$ (e.g., Toft et al., 2012; Glazebrook et al., 2017). Such a scenario involves the abrupt cessation of star formation in $z > 3$ dusty starbursts (like J1000+0234−N; Jones et al., 2017; Gómez-Guijarro† et al., 2018a) that subsequently merge with quenched satellite galaxies (e.g., Davé et al., 2017); however, the quenching mechanisms in such massive galaxies and satellite systems have remained elusive. In this context, the expanding Lyα halo around J1000+0234−S arises as the first observational evidence of negative stellar feedback in $z \sim 4.5$ low-mass/satellite galaxies, which prevent further gas accretion and, hence, might be able to suppress star formation already by $z \sim 4$.

4.6 Summary

We have used archival Keck spectroscopy and Subaru imaging to investigate the extended Lyα halo surrounding J1000+0234−S: a low-mass galaxy neighboring the massive SMG J1000+0234−N at $z = 4.5$. We have found the following:

- The Lyα emission exhibits a concentric, "ring-like" distribution (with $R \sim 3$ kpc) that surrounds the rest-frame UV emission of J1000+0234−S;
- The broad and asymmetric Lyα line profile is well reproduced by the model of an expanding shell of ionized gas, with column density $N_{\rm NI} \simeq 2{\times}10^{20}\,{\rm cm}^{-2}$, expansion velocity of $V_{\rm exp} \simeq 230\,{\rm km\,s}^{-1}$ and gas mass of $M_{\rm HI} \simeq 1.8 \times 10^{8}\,M_{\odot}$;
- The dynamical lifetime of the shell ($V_{\rm exp}/R$) of ∼13 Myr is comparable with the previously reported age of the most recent starburst of J1000+0234−S ($\lesssim$10 Myr);
- With the current SFR of J1000+0234−S ($\sim 150\,M_{\odot}{\rm yr}^{-1}$), the available reservoir of cold gas ($\sim 3 \times 10^{9}\,M_{\odot}$) will be depleted within ~ 20 Myr.

The finding of an extended, likely expanding, Lyα halo around J1000+0234−S strengthens the role of vigorous stellar feedback in producing large-scale outflows that expel star-forming gas, prevent further gas accretion and thus might suppress star formation in the early Universe. Since this discovery, we have further explored the available optical spectroscopy/imaging towards the COSMOS field and found more signatures of extended Lyα emission around $z \gtrsim 3$ dusty starbursts. Thus, we hypothesize that intense "negative" feedback episodes in high-redshift galaxies might be more common than expected. With the advent of the Multi Unit Spectroscopic Explorer (MUSE) instrument at the VLT, a detailed tomography of such extended Lyα nebulae is now feasible, allowing us to disentangle the relative role of AGN and stellar feedback in the growth of high-redshift galaxies.

CHAPTER 5

Conclusions and outlook

This chapter presents a summary of the main results derived from this Ph.D. thesis work, along with a brief description of the broader implications of our findings in the current view of galaxy evolution. We provide a final assessment, in particular, on how the Main-Sequence (MS) of star-forming galaxies (SFGs) and the Kennicutt-Schmidt (KS) relation relate to the global star formation processes in massive SFGs across cosmic history. Finally, we evaluate future research paths to address some of the remaining open questions concerning our understanding of galaxy formation and evolution.

5.1 Summary

We have explored the physical mechanisms that regulate the production of stars and the growth of massive galaxies across cosmic history. To this end, we have used deep and high-resolution observations mainly obtained with the VLA, NOEMA, and ALMA telescopes, which have enabled us to investigate the structure and mass content of 3187 massive SFGs over the redshift range $0.35 < z \lesssim 4.5$. The main results derived in this Ph.D. thesis work are listed below.

- [**Chapter 2**] For 3184 SFGs with $\log(M_\star/M_\odot) \gtrsim 10.5$ over $0.35 < z \lesssim 2.25$:

  The overall extent of star formation activity tends to be more extended in "normal" MS galaxies than in those undergoing a starbursting phase (i.e., galaxies above the MS). As a result, the average stellar birthrate per unit area ($\equiv \Sigma_{\rm SFR}$) tends to be a factor $\sim 10^{2-3}$ higher in starbursts, suggesting that different mechanisms drive star formation in massive galaxies on and above the MS. The typical $\Sigma_{\rm SFR}$ of galaxies on the MS increases with redshift. By $z \simeq 2$, the $\Sigma_{\rm SFR}$ of massive MS galaxies is a factor ~ 15 higher than their counterparts at $z \simeq 0.5$.

  In comparison to the total extend of massive SFGs, star formation preferentially occurs at small galactic radii ($R_{\rm eff} \sim 1.5\,$kpc) . To sustain this centrally concentrated star formation activity, fresh star-forming gas might be constantly fueled towards the center of galaxies leading to the growth of a bulge.

- [**Chapter 3**] AzTEC/C159 ($z = 4.567$) and AzTEC2-A ($z = 4.626$) exhibit star formation efficiencies comparable with those of merger-driven starbursts, as observed in the majority of ULIRGs and SMG. Even so, the dynamics of AzTEC/C159 and AzTEC2-A reveal that they are gas-rich disk galaxies for which there is no clear indication of merging activity. In addition,

either their CO–H_2 conversion factor, stellar mass and/or Σ_{SFR} values are also more consistent with those observed in MS galaxies. It thus appears that, at higher redshifts, cold gas streams (from cosmological filaments) fuel gas-rich disk galaxies and drive vigorous star formation episodes nearly as efficiently as in merger-driven systems.

- [**Chapter 4**] The low-mass SFG J1000+0234−S ($z = 4.543$) exhibits indications of an expanding shell of ionized gas (radius of ∼3 kpc), whose dynamical lifetime matches the age of the most recent burst of star formation. Since cosmological gas accretion is likely to be suppressed by such large-scale galactic winds, the available gas reservoir will maintain star formation during only ∼20 Myr. This finding thus suggests that negative stellar feedback might be able to quench the production of stars in galaxies already by $z \sim 4$, strengthening the establishment of a "red sequence" of galaxies at even $z > 2$.

5.2 Modes of star formation in massive SFGs and their evolution throughout cosmic history

By characterizing the structural properties of massive SFGs throughout cosmic history – the primary goal of this Ph.D. dissertation, we have found that the enhanced production of stars in massive galaxies above the MS remains concentrated within their inner/central region, whereas MS galaxies tend to sustain star formation over a more extended region. This structural dichotomy agrees with the extended morphology of secular star-forming disks on the MS and the compact light distribution of starbursts (Wuyts et al., 2011; Bremer et al., 2018). Our results thus support the scenario whereby the steady accretion of cool gas from the IGM drives widespread star formation in disk galaxies as they remain confined within the MS (e.g., Tacchella et al., 2016) – albeit a small fraction of compact MS galaxies also exists (see Chapter 2). This secular mode of star formation is interrupted by occasional gas-rich mergers and/or violent disk instability episodes triggering short-lived and compact starbursts that lie above the MS (e.g., Dekel & Burkert, 2014; Moreno et al., 2015; Wellons et al., 2015; Wang et al., 2018).

To further investigate the global processes regulating the stellar birthrate in MS and starburst galaxies, and their evolution with cosmic history, we have used our measurements to infer the KS relation of massive SFGs over the redshift range $0.35 < z < 2.25$ (Fig. 2.11 and 5.1). Such a pilot analysis suggests that low- and high-redshift SFGs follow similar relations, as previously proposed in the literature (e.g., Bouché et al., 2007; Genzel et al., 2010). We have found that the typical Σ_{SFR} and Σ_{gas} of MS galaxies systematically increase with redshift (Fig. 5.1, Table 2.3). Qualitatively, this is in agreement with the elevated gas fractions (e.g., Schinnerer et al., 2016; Genzel et al., 2015; Tacconi et al., 2018) and enhanced specific SFR of high-redshift galaxies (e.g., Karim et al., 2011; Speagle et al., 2014; Schreiber et al., 2015; Lehnert et al., 2015).

We have also found that massive galaxies on the MS harbor a higher star formation efficiency (SFE $\equiv$ SFR$/M_{gas}$) as its redshift increases (Fig. 5.1), which is consistent with the systematically lower gas depletion time-scales ($\tau \equiv 1/\mathrm{SFE}$) of MS galaxies at higher redshifts (e.g., Saintonge et al., 2013; Tacconi et al., 2018). Such efficient regime of star formation could be explained by the turbulent ISM and rapid dynamical evolution that characterize high-redshift disks (e.g., Förster Schreiber et al., 2009; Bournaud et al., 2012; Swinbank et al., 2012). In this context, the enhanced Σ_{SFR} of early

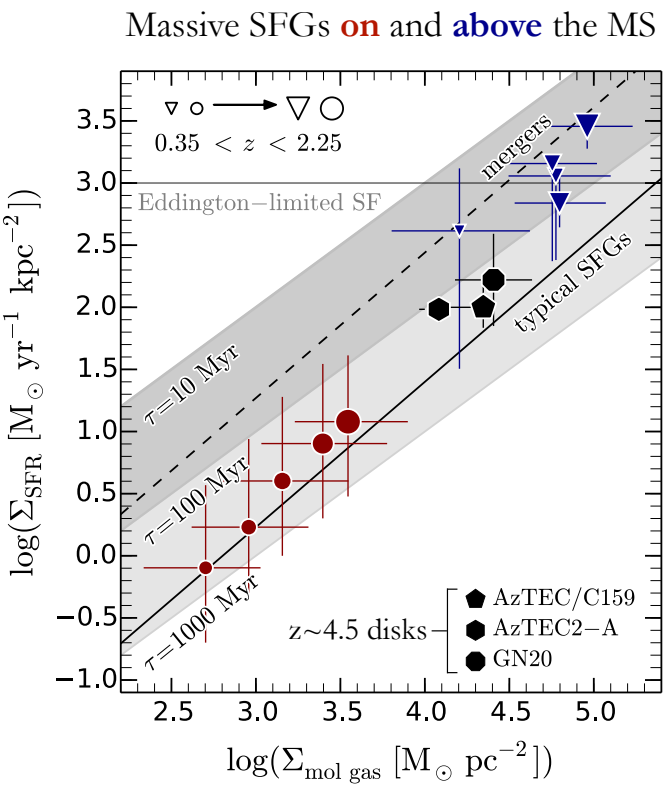

Figure 5.1: The Kennicutt-Schmidt relation for massive ($\log(M_\star/M_\odot) \gtrsim 10.5$) SFGs on (red) and above (blue) the MS at different redshifts. This is a reproduction of Fig. 2.11 (Chapter 2); here, we also present the locus of the $z \sim 4.5$ star-forming disks AzTEC/C159, AzTEC2 (Chapter 3), and –for comparison– GN20 (Carilli et al., 2010; Hodge et al., 2012). In estimating $\Sigma_{\rm gas}$ and $\Sigma_{\rm SFR}$ for these three galaxies, we use their $R_{\rm eff}$ from dust continuum emission and adopt the typical $\alpha_{\rm CO}$ conversion factor for star-forming disks like the Milky Way. The solid (dashed) black line illustrates the KS relation for typical SFGs (mergers) over the redshift range $1 \lesssim z \lesssim 3$ derived by Genzel et al. (2010). The gray diagonal lines show the $\Sigma_{\rm SFR}$ required to consume the available gas reservoirs within a gas depletion time-scale (τ) of 10 Myr (*upper*), 100 Myr (*middle*), and 1000 Myr (*lower*). The gray shaded regions illustrate the τ range for galaxies with (from top-to-bottom) high-to-low SFE. The horizontal gray line illustrates the upper limit for $\Sigma_{\rm SFR}$ imposed by Eddington-limited star formation (SF; e.g., Crocker et al., 2018).

star-forming disks is a result of their inherent large gas reservoirs and –to some extent– a higher SFE. This evolutionary scenario is in agreement with our findings on AzTEC2-A and AzTEC/C159 at $z \sim 4.5$; two massive, extended, gas-rich disks harboring intense star formation activity that does not seem to be driven by merging activity. Certainly, the locus of AzTEC2-A and AzTEC/C159 in the $\Sigma_{\rm SFR} - \Sigma_{\rm gas}$ plane (Fig. 5.1) suggests that these are scaled (more active) versions of star-forming disks at lower redshifts (Genzel et al., 2010); as a result, the high SFE of AzTEC2-A and AzTEC/C159 is approaching that of merger-driven starbursts. It thus appears that at $z \gtrsim 4$ the enhanced gas accretion from the cosmic web can maintain an unstable gas-rich disk, which breaks into giant clumps and forms stars at a high rate (e.g., Bouché et al., 2007; Hodge et al., 2012; Romano-Díaz et al., 2014, Chapter 3).

Finally, contrary to the evolving SFE of massive MS galaxies, the (elevated) SFE of starbursts weakly depends on the redshift (Fig. 5.1). At all epochs, starbursts remain concentrated at the upper end of the KS relation, close to the upper limit for $\Sigma_{\rm SFR}$ imposed by stellar radiation pressure in Eddington-limited starbursts ($\sim 10^3\ M_\odot\ {\rm yr}^{-1}\ {\rm kpc}^{-2}$; Thompson et al., 2005; Crocker et al., 2018). As a result, the contrast between the SFE of massive galaxies on and above the MS varies with redshift. While the low SFE of MS galaxies in the local/low-redshift Universe is abruptly enhanced by starburst episodes, at higher redshifts massive "normal" disk galaxies (on/close to the MS) can harbor high SFE that becomes closer to that of merger-driven starbursts. From an observational perspective, our results thus suggest that the dichotomy between the global/integrated properties of secular star-forming disks and merger-driven starbursts diminishes with increasing redshift.

5.3 Outlook

Despite the progress that we have made in this dissertation to understand the growth and structural evolution of massive galaxies, many open questions remain. We have identified, in particular, three future research projects that could lead to a more complete picture of galaxy formation and evolution. They are listed below.

- *An unbiased probe of the Kennicutt-Schmidt relation across cosmic history.* We have constrained the size of SFG up to $z = 2.25$, allowing us to approximate the redshift evolution of the KS ($\Sigma_{\rm SFR}$ - $\Sigma_{\rm gas}$) relation (Sect. 2.5.1). Nevertheless, in deriving $\Sigma_{\rm gas}$ we have used scaling relations to infer the gas content of galaxies. An independent and robust probe of the molecular gas, and its distribution in galaxies, could be obtained through high-resolution observations of low-J ^{12}CO line emission. Although powerful telescope arrays like ALMA, NOEMA and VLA are now capable of performing such an experiment, this would demand extensive integration times. An alternative approach consists in deriving the gas mass through prescriptions for the gas-to-dust ratio (e.g., Magdis et al., 2012) and dust mass estimates inferred via far-infrared SED fitting (e.g., Magnelli et al., 2012), using, for instance, archival observations from the *Herschel* and ALMA telescopes (e.g., Liu[†] et al., 2019).

  By directly deriving $\Sigma_{\rm gas}$ for galaxies in our sample, we would also be able to systematically probe the apparent bimodality of the KS relation (e.g., Daddi et al., 2010; Genzel et al., 2010, Sect. 2.5.1) up to $z = 2$. In particular, robust gas mass estimates will be essential to evaluate the nature of galaxies with starburst-like $\Sigma_{\rm SFR}$ that remain "hidden" within the MS (Sect. 2.4.4; Elbaz et al., 2018).

  Beyond the mass-complete sample of SFGs studied here (at $0.35 < z < 2.25$, Chapter 2), there is an increasing number of high-resolution IR/radio continuum observations towards spectroscopically confirmed $z > 3$ SFGs (Chapter 3, 4 and references therein). This will enable a systematic study of KS relation in the context of merger-driven and quiescent star formation during the epoch of massive galaxy assembly ($z \sim 4$).

- *Dynamical characterization of high-redshift galaxies in the context of the cold mode of star formation and dark matter content.* Rotation-dominated star-forming disks at $z \sim 4.5$, like AzTEC/C159 and AzTEC2-A (Chapter 3), have become key laboratories to validate models of galaxy formation. First, it is expected that, at high redshift, the enhanced gas accretion

from cosmological filaments and/or the vigorous star formation environments lead to large velocity dispersions of the gas in disk galaxies (Förster Schreiber et al., 2009; Green et al., 2010). Second, it has been proposed that the distribution of rapidly growing dark matter halos at early cosmic times, that have not yet reached virial equilibrium, deviate from the standard Navarro-Frenk-White profile (Genzel et al., 2017). As a result, the falling outer rotation curves of high-redshift galaxies could indicate that they are strongly baryon dominated within the disk scale. With the increased sensitivity of ALMA, it is now possible to perform detailed [CII] line observations to probe the velocity dispersion and the shape of the rotation curve of systems like AzTEC2-A and AzTEC/C159, allowing us to put the first constraints on the concentration of baryons and dark matter in the yet unexplored $z > 4$ regime. *Notice*: An ALMA observing proposal to obtain deeper [CII] line observations towards AzTEC/C159, and thus perform the analysis described above, has been accepted (proposal ID: 2018.1.01676.S; PI. Eric F. Jiménez-Andrade).

- *Exploring the impact of galactic outflows in suppressing star formation in high-redshift SFG.* The indications of an expanding shell of ionized gas in J1000+0234 arises as one of the first observational evidence of negative feedback at $z > 4$ (Chapter 4). Nevertheless, our analysis is still limited by the spectral/spatial coverage of the current data set, hindering the detection of the non-resonant lines [CIV] and HeII that are essential to constrain the ionization source (e.g., Villar-Martín et al., 2007). Furthermore, contrary to the Lyα line, non-resonant lines offer a model-independent probe of the gas kinematics. With the integral-field observations enabled by the MUSE instrument at the VLT, it is now possible to simultaneously map extended Lya nebulae –along [CIV] and HeII line emission– around $z > 3$ SMGs like J1000+0234. Such a systematic study would allow us to investigate the ability of AGN/star formation-driven winds to expel and heat the gas from the galaxy halo (e.g., Swinbank et al., 2015), leading to massive quenched galaxies at $z \sim 2$ that are believed to be the progenitors of massive elliptical galaxies in the local Universe (e.g., Toft et al., 2014). *Notice*: MUSE observations have been obtained towards J1000+0234 as part of a collaboration agreement between the MUSE consortium and members of the COSMOS team (lead author: Eric F. Jiménez-Andrade).

Finally, we foresee that the synergy between the most advanced optical/radio telescopes, e.g., ALMA, VLT, and *James Webb Space Telescope*, will enable the dynamical characterization of the gas and stars in the earliest galaxies ($z > 6$). Those observations combined with predictions from numerical simulations will improve our understanding of galaxy assembly, allowing us to better trace the evolutionary paths that lead to mature systems like our galaxy: the Milky Way. Looking far into the future we envision an exciting era of astronomy, where telescopes like the Next Generation Very Large Array (ngVLA) and Origins Space Telescope will bring us closer to the epoch of the Universe where it all started. The quest for our cosmic origins continues.

Bibliography

Abdo A. A., et al., 2010, ApJ, 710, 133

Aird J., et al., 2010, MNRAS, 401, 2531

Alaghband-Zadeh S., et al., 2012, MNRAS, 424, 2232

Allen R. J., et al., 2017, ApJL, 834, L11

Alvarez M. A., Bromm V., Shapiro P. R., 2006, ApJ, 639, 621

Anglés-Alcázar D., Faucher-Giguère C.-A., Kereš D., Hopkins P. F., Quataert E., Murray N., 2017, MNRAS, 470, 4698

Appleton P. N., Ghigo F. D., van Gorkom J. H., Schombert J. M., Struck-Marcell C., 1987, Nature, 330, 140

Aravena M., et al., 2016, MNRAS, 457, 4406

Aretxaga I., et al., 2011, MNRAS, 415, 3831

Armus L., Heckman T., Miley G., 1987, AJ, 94, 831

Arnouts S., Cristiani S., Moscardini L., Matarrese S., Lucchin F., Fontana A., Giallongo E., 1999, MNRAS, 310, 540

Arnouts S., et al., 2002, MNRAS, 329, 355

Banerji M., et al., 2013, MNRAS, 431, 2209

Beckwith S. V. W., et al., 2006, ApJ, 132, 1729

Behrens C., Braun H., 2014, A&A, 572, A74

Behroozi P. S., Wechsler R. H., Conroy C., 2013, ApJ, 770, 57

Behroozi P., Wechsler R., Hearin A., Conroy C., 2018, submitted to MNRAS, arXiv:1806.07893

Bekki K., 2013, MNRAS, 432, 2298

Bell E. F., 2003, ApJ, 586, 794

Bennett C. L., et al., 1996, ApJL, 464, L1

Berta S., et al., 2013, A&A, 551, A100

Bigiel F., Leroy A., Walter F., Brinks E., de Blok W. J. G., Madore B., Thornley M. D., 2008, AJ, 136, 2846

Blain A. W., Smail I., Ivison R. J., Kneib J.-P., Frayer D. T., 2002, Phys. Rep., 369, 111

Blanton M. R., Bershady M. A., Abolfathi B., Albareti F. D., Allende Prieto C., et al., 2017, ApJ, 154, 35

Bolatto A. D., Wolfire M., Leroy A. K., 2013, ARA&A, 51, 207

Bondi M., et al., 2003, A&A, 403, 857

Bondi[†] M., et al., 2018, A&A, 618, L8

Boquien M., Burgarella, D. Roehlly, Y. Buat, V. Ciesla, L. Corre, D. Inoue, A. K. Salas, H. 2019, A&A, 622, A103

Borch A., et al., 2006, A&A, 453, 869

Bothwell M. S., et al., 2013, MNRAS, 429, 3047

Bouché N., et al., 2007, ApJ, 671, 303

Bouché N., Murphy M. T., Kacprzak G. G., Péroux C., Contini T., Martin C. L., Dessauges-Zavadsky M., 2013, Science, 341, 50

Bourke S., Mooley K., Hallinan G., 2014, in Manset N., Forshay P., eds, Astronomical Data Analysis Software and Systems XXIII. No. 485 in Astronomical Society of the Pacific Conference Series. p. 367

Bournaud F., et al., 2012, ApJ, 757, 81

Bouwens R. J., et al., 2012, ApJ, 754, 83

Bremer M. N., et al., 2018, MNRAS, 476, 12

Bridge C. R., et al., 2013, ApJ, 769, 91

Brinchmann J., Charlot S., White S. D. M., Tremonti C., Kauffmann G., Heckman T., Brinkmann J., 2004, MNRAS, 351, 1151

Brisbin D., et al., 2017, A&A, 608, A15

Bromm V., Larson R. B., 2004, ARA&A, 42, 79

Bromm V., Yoshida N., 2011, ARA&A, 49, 373

Bromm V., Yoshida N., Hernquist L., McKee C. F., 2009, Nature, 459, 49

Brooks A., Christensen C., 2016, Galactic Bulges. Astrophysics and Space Science Library. Springer, Cham, pp 317–353, doi:https://doi.org/10.1007/978-3-319-19378-6_12

Bruzual G., Charlot S., 2003, MNRAS, 344, 1000

Buat V., et al., 2012, A&A, 545, A141

Bull P., et al., 2016, Physics of the Dark Universe, 12, 56

Burkert A., 1995, ApJL, 447, L25

Burles S., Nollett K. M., Truran J. W., Turner M. S., 1999, Phys. Rev. Lett., 82, 4176

Cañameras R., et al., 2018, A&A, 620, A61

Calabrò A., et al., 2018, ApJL, 862, L22

Calderón-Castillo P., Nagar N. M., Yi S., Orellana G., Chang Y.-Y., Leiton R., Hughes T. M., 2019, A&A, in press., arXiv:1904.09300

Calura F., et al., 2017, MNRAS, 465, 54

Cantalupo S., 2017, Gas Accretion onto Galaxies. Astrophysics and Space Science Library, Springer, pp 195–220, doi:10.1007/978-3-319-52512-9_9

Cantalupo S., Porciani C., Lilly S. J., Miniati F., 2005, ApJ, 628, 61

Cantalupo S., Lilly S. J., Haehnelt M. G., 2012, MNRAS, 425, 1992

Cantalupo S., Arrigoni-Battaia F., Prochaska J. X., Hennawi J. F., Madau P., 2014, Nature, 506, 63 EP

Capak P., et al., 2007, ApJSS, 172, 99

Capak P., et al., 2008, ApJL, 681, L53

Carilli C. L., Walter F., 2013, ARA&A, 51, 105

Carilli C. L., et al., 2008, ApJ, 689, 883

Carilli C. L., et al., 2010, ApJ, 714, 1407

Casey C. M., et al., 2013, MNRAS, 436, 1919

Casey C. M., Narayanan D., Cooray A., 2014, Phys. Rev, 541, 45

Casey C. M., et al., 2017, ApJ, 840, 101

Chabrier G., 2003, PASP, 115, 763

Chan T. K., Kereš D., Oñorbe J., Hopkins P. F., Muratov A. L., Faucher-Giguère C.-A., Quataert E., 2015, MNRAS, 454, 2981

Chapman S. C., Blain A. W., Smail I., Ivison R. J., 2005, ApJ, 622, 772

Childs H. J. T., Stanway E. R., 2018, MNRAS, 480, 1938

Choi J.-H., Nagamine K., 2009, MNRAS, 393, 1595

Chonis T. S., et al., 2013, ApJ, 775, 99

Chung A. S., Dijkstra M., Ciardi B., Gronke M., 2016, MNRAS, 455, 884

Cibinel A., Daddi E., Sargent M. T., Le Floc'h E., Liu D., Bournaud F., Oesch P. A., et al., 2018, MNRAS, 485, 5631

Civano F., et al., 2016, ApJ, 819, 62

Clark P. C., Glover S. C. O., Klessen R. S., 2008, ApJ, 672, 757

Condon J. J., 1992, ARA&A, 30, 575

Condon J. J., 1997, PASP, 109, 166

Conroy C., 2013, ARA&A, 51, 393

Coppin K., Halpern M., Scott D., Borys C., Chapman S., 2005, MNRAS, 357, 1022

Cotton W. D., et al., 2018, ApJ, 856, 67

Courteau S., 1997, AJ, 114, 2402

Cox T. J., Jonsson P., Somerville R. S., Primack J. R., Dekel A., 2008, MNRAS, 384, 386

Crighton N. H. M., Prochaska J. X., Murphy M. T., O'Meara J. M., Worseck G., Smith B. D., 2019, MNRAS, 482, 1456

Crocker R. M., Krumholz M. R., Thompson T. A., Clutterbuck J., 2018, MNRAS, 478, 81

Croton D. J., et al., 2006, MNRAS, 365, 11

Croxall K. V., et al., 2017, ApJ, 845, 96

Cucciati O., et al., 2012, A&A, 539, A31

Cuesta A. J., Prada F., Klypin A., Moles M., 2008, MNRAS, 389, 385

Cyburt R. H., Fields B. D., Olive K. A., Yeh T.-H., 2016, Rev. Mod. Phys., 88, 015004

Da Cunha E., Charlot S., Elbaz D., 2008, MNRAS, 388, 1595

Daddi E., et al., 2007, ApJ, 670, 156

Daddi E., et al., 2010, ApJ, 713, 686

Daddi E., et al., 2015, A&A, 577, A46

Dasyra K. M., Combes F., Novak G. S., Bremer M., Spinoglio L., Pereira Santaella M., Salomé P., Falgarone E., 2014, A&A, 565, A46

Davé R., Finlator K., Oppenheimer B. D., Fardal M., Katz N., Kereš D., Weinberg D. H., 2010, MNRAS, 404, 1355

Davé R., Rafieferantsoa M. H., Thompson R. J., 2017, MNRAS, 471, 1671

Davidzon I., et al., 2017, A&A, 605, A70

Davies R., et al., 2011, ApJ, 741, 69

Dawson S., Spinrad H., Stern D., Dey A., van Breugel W., de Vries W., Reuland M., 2002, ApJ, 570, 92

De Breuck C., et al., 2014, A&A, 565, A59

Decarli R., et al., 2016, ApJ, 833, 69

Dekel A., Burkert A., 2014, MNRAS, 438, 1870

Dekel A., et al., 2009a, Nature, 457, 451

Dekel A., Sari R., Ceverino D., 2009b, ApJ, 703, 785

Delhaize J., et al., 2017, A&A, 602, A4

Delvecchio I., et al., 2014, MNRAS, 439, 2736

Delvecchio I., et al., 2017, A&A, 602, A3

Dessauges-Zavadsky M., D'Odorico S., Schaerer D., Modigliani A., Tapken C., Vernet J., 2010, A&A, 510, A26

Di Teodoro E. M., Fraternali, F. Miller, S. H. 2016, A&A, 594, A77

Dijkstra M., 2014, Publications of the Astronomical Society of Australia, 31, e040

Dijkstra M., Loeb A., 2009, MNRAS, 396, 377

Donley J. L., et al., 2012, ApJ, 748, 142

Downes D., Solomon P. M., 1998, ApJ, 507, 615

Draine B. T., Li A., 2007, ApJ, 657, 810

Elbaz D., et al., 2007, A&A, 468, 33

Elbaz D., et al., 2011, A&A, 533, A119

Elbaz D., et al., 2018, A&A, 616, A110

Ellison S. L., Mendel J. T., Scudder J. M., Patton D. R., Palmer M. J. D., 2013, MNRAS, 430, 3128

Ellison S. L., Sánchez S. F., Ibarra-Medel H., Antonio B., Mendel J. T., Barrera-Ballesteros J., 2018, MNRAS, 474, 2039

Engel H., et al., 2010, ApJ, 724, 233

Erb D. K., 2015, Nature, 523, 169

Fabian A. C., 2011, ARA&A, 50, 455

Fall S. M., Efstathiou G., 1980, MNRAS, 193, 189

Fardal M. A., Katz N., Gardner J. P., Hernquist L., Weinberg D. H., Dave R., 2001, ApJ, 562, 605

Faucher-Giguère C.-A., Hopkins P. F., Kereš D., Muratov A. L., Quataert E., Murray N., 2015, MNRAS, 449, 987

Feng Y., Matteo T. D., Croft R., Tenneti A., Bird S., Battaglia N., Wilkins S., 2015, ApJL, 808, L17

Fensch J., et al., 2017, MNRAS, 465, 1934

Finkelstein S. L., 2016, Publications of the Astronomical Society of Australia, 33, e037

Fisher D. B., 2006, ApJL, 642, L17

Fixsen D. J., Bennett C. L., Mather J. C., 1999, ApJ, 526, 207

Förster Schreiber N. M., et al., 2009, ApJ, 706, 1364

Freundlich J., et al., 2013, A&A, 553, A130

Fudamoto Y., et al., 2017, MNRAS, 472, 2028

Fudamoto[†] Y., et al., 2019, submitted to MNRAS

Fujimoto S., Ouchi M., Shibuya T., Nagai H., 2017, ApJ, 850, 83

Furlong M., et al., 2017, MNRAS, 465, 722

Gallerani S., Pallottini A., Feruglio C., Ferrara A., Maiolino R., Vallini L., Riechers D. A., Pavesi R., 2018, MNRAS, 473, 1909

Galliano F., Dwek E., Chanial P., 2008, ApJ, 672, 214

Gao Y., Solomon P. M., 2004, ApJ, 606, 271

Garn T., Green D. A., Riley J. M., Alexander P., 2009, MNRAS, 397, 1101

Gawiser E., Silk J., 2000, Physics Reports, 333-334, 245

Geach J. E., et al., 2005, MNRAS, 363, 1398

Geach J. E., et al., 2009, ApJ, 700, 1

Geach J. E., Smail I., Moran S. M., MacArthur L. A., Lagos C. d. P., Edge A. C., 2011, ApJL, 730, L19

Geach J. E., et al., 2016, ApJ, 832, 37

Genzel R., Tacconi L. J., Rigopoulou D., Lutz D., Tecza M., 2001, ApJ, 563, 527

Genzel R., et al., 2010, MNRAS, 407, 2091

Genzel R., et al., 2015, ApJ, 800, 20

Genzel R., et al., 2017, Nature, 543, 397

Giavalisco M., 2002, ARA&A, 40, 579

Glazebrook K., et al., 2017, Nature, 544, 71

Gobat R., et al., 2012, ApJL, 759, L44

Gómez-Guijarro C., Gallego J., Villar, V. Rodríguez-Muñoz, L. Clément, B. Cuby, J.G. 2016, A&A, 591, A151

Gómez-Guijarro† C., et al., 2018a, ApJ, 856, 121

Gómez-Guijarro C., et al., 2018b, ApJ, 856, 121

González V., Labbé I., Bouwens R. J., Illingworth G., Franx M., Kriek M., Brammer G. B., 2010, ApJ, 713, 115

González V., Bouwens R., Illingworth G., Labbé I., Oesch P., Franx M., Magee D., 2014, ApJ, 781, 34

Gorbunov D. S., Rubakov V. A., 2011, Introduction to the Theory of the Early Universe. World Scientific Publishing Company, doi:doi:10.1142/7874, https://doi.org/10.1142/7874

Grazian A., et al., 2015, A&A, 575, A96

Green A. W., et al., 2010, Nature, 467, 684

Greif T. H., Johnson J. L., Bromm V., Klessen R. S., 2007, ApJ, 670, 1

Greif T., Johnson J., S. Klessen R., Bromm V., 2008, MNRAS, 387

Greif T. H., Glover S. C. O., Bromm V., Klessen R. S., 2010, ApJ, 716, 510

Gronke M., Dijkstra M., 2014, MNRAS, 444, 1095

Gruppioni C., et al., 2013, MNRAS, 432, 23

Guidetti D., et al., 2017, MNRAS, 471, 210

Gültekin K., et al., 2009, ApJ, 698, 198

Gurung-López S., Orsi A. A., Bonoli S., Baugh C. M., Lacey C. G., 2018, submitted to MNRAS, arXiv:1807.00006

Guth A. H., 1981, Physical Review D, 23, 347

Hales C. A., Murphy T., Curran J. R., Middelberg E., Gaensler B. M., Norris R. P., 2012, MNRAS, 425, 979

Harrington† K. C., et al., 2018, MNRAS, 474, 3866

Harrington† K. C., Vishwas A., Weiß A., Magnelli, B. et al., 2019, submitted to MNRAS

Hashimoto T., et al., 2015, ApJ, 812, 157

Hayward C. C., Kereš D., Jonsson P., Narayanan D., Cox T. J., Hernquist L., 2011, ApJ, 743, 159

Hayward C. C., Jonsson P., Kereš D., Magnelli B., Hernquist L., Cox T. J., 2012, MNRAS, 424, 951

Hayward C. C., Primack J. R., Moreno J., Behroozi P. S., Somerville R. S., Wechsler R. H., 2013, MNRAS, 434, 2572

Hayward C. C., et al., 2018, MNRAS, 476, 2278

Heckman T. M., Thompson T. A., 2016, Handbook of Supernovae. Springer, doi:10.1007/978-3-319-20794-0_23-1

Heckman T. M., Lehnert M. D., Armus L., 1993, Galactic superwinds. Astrophysics and Space Science Library, p. 455, doi:10.1007/978-94-011-1882-8_25

Helou G., Bicay M. D., 1993, ApJ, 415, 93

Helou G., Soifer B. T., Rowan-Robinson M., 1985, ApJL, 298, 7

Hodge J. A., Carilli C. L., Walter F., de Blok W. J. G., Riechers D., Daddi E., Lentati L., 2012, ApJ, 760, 11

Hodge J. A., et al., 2016, ApJ, 833, 103

Hogg D. W., Turner E. L., 1998, PASP, 110, 727

Hopkins P. F., Richards G. T., Hernquist L., 2007, ApJ, 654, 731

Hopkins P. F., Cox T. J., Younger J. D., Hernquist L., 2009, ApJ, 691, 1168

Hopkins P. F., et al., 2010, ApJ, 724, 915

Hopkins P. F., Quataert E., Murray N., 2012, MNRAS, 421, 3522

Hu W., Dodelson S., 2002, ARA&A, 40, 171

Hubble E., 1929, Proceedings of the National Academy of Sciences, 15, 168

IceCube Collaboration et al., 2011, Phys. Rev., 84, 022004

Ikarashi S., et al., 2015, ApJ, 810, 133

Ilbert, O. et al., 2006, A&A, 457, 841

Ilbert O., et al., 2010, ApJ, 709, 644

Ilbert O., et al., 2013, A&A, 556, A55

Iono D., et al., 2016, ApJL, 829, L10

Jenkins A., Frenk C. S., White S. D. M., Colberg J. M., Cole S., Evrard A. E., Couchman H. M. P., Yoshida N., 2001, MNRAS, 321, 372

Jiménez-Andrade† E. F., et al., 2019, A&A, 625, A114

Jiménez-Andrade† E. F., et al., 2018, A&A, 615, A25

Jones G. C., et al., 2017, ApJ, 850, 180

Kaplan E. L., Meier P., 1958, Journal of the American Statistical Association, 53, 457

Karim A., et al., 2011, ApJ, 730, 61

Kartaltepe J. S., et al., 2007, ApJSS, 172, 320

Kartaltepe J. S., et al., 2012, ApJ, 757, 23

Keating G. K., Marrone D. P., Bower G. C., Leitch E., Carlstrom J. E., DeBoer D. R., 2016, ApJ, 830, 34

Kehrig C., Vílchez, J. M. Telles, E. Cuisinier, F. Pérez-Montero, E. 2006, A&A, 457, 477

Kennicutt J. R. C., 1998a, ARA&A, 36, 189

Kennicutt J. R. C., 1998b, ApJ, 498, 541

Kennicutt R. C., Evans N. J., 2011, ARA&A, 50, 531

Kereš D., Katz N., Weinberg D. H., Davé R., 2005, MNRAS, 363, 2

Kereš D., Katz N., Fardal M., Davé R., Weinberg D. H., 2009, MNRAS, 395, 160

Kereš D., Hernquist L., 2009, ApJL, 700, L1

Khochfar S., Silk J., 2006, ApJL, 648, L21

Khochfar S., Silk J., 2009, MNRAS, 397, 506

Kobayashi T., Komori Y., Yoshida K., Nishimura J., 2004, ApJ, 601, 340

Kochanek C. S., White M., Huchra J., Macri L., Jarrett T. H., Schneider S. E., Mader J., 2003, ApJ, 585, 161

Kollmeier J. A., Zheng Z., Davé R., Gould A., Katz N., Miralda-Escudé J., Weinberg D. H., 2010, ApJ, 708, 1048

Komatsu E., et al., 2011, ApJSS, 192, 18

Kormendy J., Ho L. C., 2013, ARA&A, 51, 511

Kormendy J., Kennicutt R. C., 2004, ARA&A, 42, 603

Krumholz M. R., Thompson T. A., 2007, ApJ, 669, 289

Kubo M., Tanaka M., Yabe K., Toft S., Stockmann M., Gómez-Guijarro C., 2019, submitted to ApJ, arXiv:1810.00543

L´Huillier B., Combes, F. Semelin, B. 2012, A&A, 544, A68

Lagache G., Cousin, M. Chatzikos, M. 2018, A&A, 609, A130

Lagos C. d. P., Benson A. J., Baugh C. M., Lacey C. G., Power C., Kim H.-S., Lagos C. d. P., 2011, MNRAS, 418, 1649

Laigle C., et al., 2016, ApJSS, 224, 24

Lake E., Zheng Z., Cen R., Sadoun R., Momose R., Ouchi M., 2015, ApJ, 806, 46

Lang P., et al., 2014, ApJ, 788, 11

Lang† P., Schinnerer E., Smail I., Swinbank A., Liu D., et al., 2019, ApJ, in press., arXiv:1905.06960

Larson R., 2003, Mass-Transfer Induced Activity in Galaxies. Cambridge University Press, p. 524

Leclercq F., et al., 2017, A&A, 608, A8

Lehnert M. D., van Driel, W. Le Tiran, L. Di Matteo, P. Haywood, M. 2015, A&A, 577, A112

Leitherer C., et al., 1999, ApJSS, 123, 3

Leroy A. K., et al., 2011, ApJ, 737, 12

Leslie S., et al., 2018, A&A, 615, A7

Liddle A., Lyth D., 2000, Cosmological Inflation and Large-Scale Structure. Vol. -1, Cambridge University Press, doi:10.1017/CBO9781139175180

Lilly S. J., et al., 2007, ApJSS, 172, 70

Lindroos L., Knudsen K. K., Stanley F., Muxlow T. W. B., Beswick R. J., Conway J., Radcliffe J. F., Wrigley N., 2018, MNRAS, 476, 3544

Liu† D., Lang, P. Magnelli, B. Schinnerer, E. Leslie, S. et al., 2019, submitted to ApJ

Lutz D., 2014, ARA&A, 52, 373

Lutz D., et al., 2011, A&A, 532, A90

Lutz D., et al., 2016, A&A, 591, A136

Madau P., 1995, ApJ, 441, 18

Madau P., Dickinson M., 2014, ARA&A, 52, 415

Magdis G. E., Rigopoulou D., Huang J. S., Fazio G. G., 2010, MNRAS, 401, 1521

Magdis G. E., et al., 2012, ApJ, 760, 6

Magdis G. E., et al., 2016, MNRAS, 456, 4533

Magnelli B., Elbaz, D. Chary, R. R. Dickinson, M. Le Borgne, D. Frayer, D. T. Willmer, C. N. A. 2009, A&A, 496, 57

Magnelli B., et al., 2011, A&A, 528, A35

Magnelli B., et al., 2012, A&A, 548, A22

Magnelli B., et al., 2013, A&A, 553, A132

Magnelli B., et al., 2014, A&A, 561, A86

Magnelli B., et al., 2015, A&A, 573, A45

Magnelli† B., Karim A., Staguhn J. G., Kovacs A., Jiménez-Andrade E. F., et al., 2019, ApJ, 877, 45

Mamon G. A., Thuan T. X., Tran Thanh Van J., 1997, Extragalactic astronomy in the infrared. Editions Frontieres

Martí-Vidal I., Pérez-Torres, M. A. Lobanov, A. P. 2012, A&A, 541, A135

Martín-Navarro I., Mezcua M., 2018, ApJ, 855, L20

Mas-Ribas L., Dijkstra M., Hennawi J. F., Trenti M., Momose R., Ouchi M., 2017, ApJ, 841, 19

Mathews G., Kusakabe, Motohiko Gangopadhyay, Mayukh Kajino, Toshitaka Sasankan, Nishanth 2018, EPJ Web Conf., 184, 01011

McCracken H. J., et al., 2012, A&A, 544, A156

McGee S. L., Bower R. G., Balogh M. L., 2014, MNRAS, 442, L105

Merritt D., Graham A., Moore B., Diemand J., Terzić B., 2005, Empirical Models for Dark Matter Halos. I. Nonparametric Construction of Density Profiles and Comparison with Parametric Models. Vol. 132, doi:10.1086/508988,

Miettinen O., et al., 2015, A&A, 577, A29

Miettinen O., et al., 2017a, A&A, 597, A5

Miettinen O., Delvecchio, I. Smolci´c, V. Aravena, M. Brisbin, D. Karim, A. 2017b, A&A, 602, L9

Mitra S., Davé R., Simha V., Finlator K., 2017, MNRAS, 464, 2766

Miyazaki S., Komiyama Y., Nakaya H., et al., 2012, in Proc. SPIE. , doi:10.1117/12.926844

Mo H., van den Bosch F., White S., 2010, Galaxy Formation and Evolution. Cambridge University Press, Cambridge, doi:DOI: 10.1017/CBO9780511807244

Mohan N., Rafferty D., 2015, Astrophysics Source Code Library, 1502.007

Möllenhoff C., Popescu C. C., Tuffs R. J., 2006, A&A, 456, 941

Momose R., et al., 2016, MNRAS, 457, 2318

Moreno J., Torrey P., Ellison S. L., Patton D. R., Bluck A. F. L., Bansal G., Hernquist L., 2015, MNRAS, 448, 1107

Moser L., et al., 2016, A&A, 587, A137

Mowla L., van Dokkum P., Brammer G., Momcheva I., van der Wel A., et al., 2018, arXiv:1808.04379

Muñoz-Elgueta N., Torres-Flores S., Amram P., Hernandez-Jimenez J. A., Urrutia-Viscarra F., Mendes de Oliveira C., Gómez-López J. A., 2018, MNRAS, 480, 3257

Murphy E. J., 2009, ApJ, 706, 482

Murphy E. J., et al., 2006a, ApJ, 638, 157

Murphy E. J., et al., 2006b, ApJL, 651, L111

Murphy E. J., et al., 2011, ApJ, 737, 67

Murphy E. J., et al., 2012, ApJ, 761, 97

Murphy E. J., Momjian E., Condon J. J., Chary R.-R., Dickinson M., Inami H., Taylor A. R., Weiner B. J., 2017, ApJ, 839, 35

Napolitano N., Longo G., Marconi M., Paolillo M., Iodice E., 2016, The Universe of Digital Sky Surveys: A Meeting to Honour the 70th Birthday of Massimo Capaccioli. Astrophysics and Space Science Proceedings Vol. 42, Springer International Publishing, doi:10.1007/978-3-319-19330-4

Narayanan D., Krumholz M. R., 2014, MNRAS, 442, 1411

Narayanan D., Hayward C. C., Cox T. J., Hernquist L., Jonsson P., Younger J. D., Groves B., 2010, MNRAS, 401, 1613

Narayanan D., Krumholz M. R., Ostriker E. C., Hernquist L., 2012, MNRAS, 421, 3127

Narayanan D., et al., 2015, Nature, 525, 496

Navarro J. F., Frenk C. S., White S. D. M., 1997, ApJ, 490, 493

Nelson E. J., et al., 2012, ApJL, 747, L28

Nelson E. J., et al., 2016a, ApJL, 817, L9

Nelson E. J., et al., 2016b, ApJ, 828, 27

Neufeld D. A., McKee C. F., 1988, ApJL, 331, L87

Newman S. F., et al., 2012, ApJ, 761, 43

Noeske K. G., et al., 2007, ApJL, 660, L43

Obreschkow D., Heywood I., Klöckner H.-R., Rawlings S., 2009, ApJ, 702, 1321

Oliver S. J., et al., 2012, MNRAS, 424, 1614

Orlitová I., Verhamme, A. Henry, A. Scarlata, C. Jaskot, A. Oey, M. S. Schaerer, D. 2018, A&A, 616, A60

Orsi A., Lacey C. G., Baugh C. M., 2012, MNRAS, 425, 87

Oser L., Ostriker J. P., Naab T., Johansson P. H., Burkert A., 2010, ApJ, 725, 2312

Pannella M., et al., 2009, ApJL, 698, L116

Pannella M., et al., 2015, ApJ, 807, 141

Papadopoulos P. P., Kovacs A., Evans A. S., Barthel P., 2008, A&A, 491, 483

Papadopoulos P. P., van der Werf P., Isaak K., Xilouris E. M., 2010, ApJ, 715, 775

Papadopoulos P. P., van der Werf P. P., Xilouris E. M., Isaak K. G., Gao Y., Mühle S., 2012a, MNRAS, 426, 2601

Papadopoulos P. P., van der Werf P., Xilouris E., Isaak K. G., Gao Y., 2012b, ApJ, 751, 10

Patrício V., et al., 2016, MNRAS, 456, 4191

Pearson W. J., et al., 2018, A&A, 615, A146

Peebles P., Harrison E., 1994, The Principles of Physical Cosmology. Vol. 62, doi:10.1119/1.17585,

Peng Y.-j., et al., 2010, ApJ, 721, 193

Penzias A. A., Wilson R. W., 1965, ApJ, 142, 419

Pilbratt G. L., et al., 2010, A&A, 518, L1

Planck Collaboration I 2014, A&A, 571, A1

Planck Collaboration et al., 2016, A&A, 594, A1

Planck Collaboration et al., 2018, submitted to A&A, arXiv:1807.06209

Polletta M., et al., 2007, ApJ, 663, 81

Popping G., Spaans M., Trager S. C., Pérez-Beaupuits J. P., Somerville R. S., 2014, MNRAS, 444, 1301

Popping G., Somerville R. S., Galametz M., 2017, MNRAS, 471, 3152

Press W. H., Schechter P., 1974, ApJ, 187, 425

Read J. I., Walker M. G., Steger P., 2019, MNRAS, 484, 1401

Reed D., Gardner J., Quinn T., Stadel J., Fardal M., Lake G., Governato F., 2003, MNRAS, 346, 565

Rees M. J., Ostriker J. P., 1977, MNRAS, 179, 541

Renzini A., Peng Y.-j., 2015, ApJL, 801, L29

Richards E. A., 2000, ApJ, 533, 611

Riechers D. A., et al., 2010, ApJL, 720, L131

Riechers D. A., Hodge J., Walter F., Carilli C. L., Bertoldi F., 2011, ApJL, 739, L31

Riechers D. A., et al., 2013, Nature, 496, 329

Riechers D. A., et al., 2014, ApJ, 796, 84

Riechers D. A., et al., 2019, ApJ, 872, 7

Rodighiero G., et al., 2010, A&A, 518, L25

Rodighiero G., et al., 2011, ApJL, 739, L40

Rodighiero G., et al., 2014, MNRAS, 443, 19

Romano-Díaz E., Shlosman I., Choi J.-H., Sadoun R., 2014, ApJL, 790, L32

Romano-Díaz E., Garaldi E., Borzyszkowski M., Porciani C., 2017, MNRAS, 469, 1809

Rowlands K., et al., 2018, MNRAS, 480, 2544

Rujopakarn W., et al., 2016, ApJ, 833, 12

Rupke D. S. N., Kewley L. J., Barnes J. E., 2010, ApJL, 710, L156

Saintonge A., et al., 2013, ApJ, 778, 2

Salim S., et al., 2007, ApJSS, 173, 267

Salmon B., et al., 2015, ApJ, 799, 183

Sanders D. B., Mirabel I. F., 1996, ARA&A, 34, 749

Sanders D. B., et al., 2007, ApJSS, 172, 86

Sandstrom K. M., et al., 2013, ApJ, 777, 5

Sargent M. T., et al., 2010, ApJSS, 186, 341

Sargent M. T., Béthermin M., Daddi E., Elbaz D., 2012, ApJL, 747, L31

Sargent M. T., et al., 2014, ApJ, 793, 19

Scarlata C., et al., 2009, ApJ, 706, 1241

Schaerer D., Verhamme A., 2008, A&A, 480, 369

Schaerer D., Hayes M., Verhamme A., Teyssier R., 2011, A&A, 531, A12

Schawinski K., et al., 2014, MNRAS, 440, 889

Schinnerer E., et al., 2008, ApJL, 689, L5

Schinnerer E., et al., 2016, ApJ, 833, 112

Schmidt M., 1959, ApJ, 129, 243

Schneider P., 2015, Extragalactic Astronomy and Cosmology, second edn, doi:10.1007/978-3-642-54083-7.

Schober J., Schleicher D. R. G., Klessen R. S., 2017, MNRAS, 468, 946

Schreiber C., et al., 2015, A&A, 575, A74

Schreiber C., Pannella, M. Leiton, R. Elbaz, D. Wang, T. Okumura, K. Labbé, I. 2017, A&A, 599, A134

Scott K. S., et al., 2008, MNRAS, 385, 2225

Scoville N., et al., 2007, ApJSS, 172, 1

Scoville N., et al., 2017, ApJ, 837, 150

Sellwood J. A., 2014, Rev. Mod. Phys., 86, 1

Sérsic J. L., 1963, Boletin de la Asociacion Argentina de Astronomia, 6, 41

Shankar F., Weinberg D. H., Miralda-Escudé J., 2009, ApJ, 690, 20

Shao Y., et al., 2017, ApJ, 845, 138

Shapley A. E., Steidel C. C., Erb D. K., Reddy N. A., Adelberger K. L., Pettini M., Barmby P., Huang J., 2005, ApJ, 626, 698

Sheth R. K., Tormen G., 1999, MNRAS, 308, 119

Sheth R. K., Mo H. J., Tormen G., 2001, MNRAS, 323, 1

Shibuya T., Ouchi M., Harikane Y., 2015, ApJSS, 219, 15

Shimizu I., Umemura M., 2010, MNRAS, 406, 913

Shlosman I., 2013, Cosmological Evolution of Galaxies. Cambridge University Press, p. 555, doi:10.1017/CBO9781139547420.011

Silich S., Tenorio-Tagle G., Muñoz-Tuñón C., Hueyotl-Zahuantitla F., Wünsch R., Palouš J., 2010, ApJ, 711, 25

Sillero E., Tissera P. B., Lambas D. G., Michel-Dansac L., 2017, MNRAS, 472, 4404

Simpson J. M., et al., 2015, ApJ, 799, 81

Smolčić V., et al., 2017a, A&A, 602, A1

Smolčić V., et al., 2017b, A&A, 602, A2

Smolčić V., et al., 2012, A&A, 548, A4

Smolčić V., et al., 2015, A&A, 576, A127

Smolčić V., et al., 2017, A&A, 597, A4

Solomon P. M., Downes D., Radford S. J. E., Barrett J. W., 1997, ApJ, 478, 144

Somerville R. S., Davé R., 2015, ARA&A, 53, 51

Speagle J. S., Steinhardt C. L., Capak P. L., Silverman J. D., 2014, ApJSS, 214, 15

Spilker J. S., et al., 2018, Science, 361, 1016

Springel V., et al., 2005, Nature, 435, 629

Springel V., Frenk C. S., White S. D. M., 2006, Nature, 440, 1137

Staguhn J. G., et al., 2014, ApJ, 790, 77

Stark D. P., Schenker M. A., Ellis R., Robertson B., McLure R., Dunlop J., 2013, ApJ, 763, 129

Steinhardt C. L., et al., 2014, ApJL, 791, L25

Stott J. P., et al., 2016, MNRAS, 457, 1888

Swinbank A. M., Sobral D., Smail I., Geach J. E., Best P. N., McCarthy I. G., Crain R. A., Theuns T., 2012, MNRAS, 426, 935

Swinbank A. M., et al., 2014, MNRAS, 438, 1267

Swinbank A. M., et al., 2015, MNRAS, 449, 1298

Symeonidis M., et al., 2013, MNRAS, 431, 2317

Szokoly G. P., et al., 2004, ApJSS, 155, 271

Tacchella S., Trenti M., Carollo C. M., 2013, ApJ, 768, L37

Tacchella S., et al., 2015, Science, 348, 314

Tacchella S., Dekel A., Carollo C. M., Ceverino D., DeGraf C., Lapiner S., Mandelker N., Primack Joel R., 2016, MNRAS, 457, 2790

Tacconi L. J., et al., 2006, ApJ, 640, 228

Tacconi L. J., et al., 2008, ApJ, 680, 246

Tacconi L. J., et al., 2013, ApJ, 768, 74

Tacconi L. J., et al., 2018, ApJ, 853, 179

Tadaki K., et al., 2018, Nature, 560, 613

Tanaka M., Hasinger G., Silverman J. D. e. a., 2017, arXiv:1706.00566

Taniguchi Y., Shioya Y., 2000, ApJ, 532, L13

Taniguchi Y., et al., 2015, PASP, 67, 104

Tapken C., Appenzeller I., Noll S., Richling S., Heidt J., Meinköhn, E. Mehlert, D. 2007, A&A, 467, 63

Tegmark M., Silk J., Rees M. J., Blanchard A., Abel T., Palla F., 1997, ApJ, 474, 1

Tenorio-Tagle G., Silich S. A., Kunth D., Terlevich E., Terlevich R., 1999, MNRAS, 309, 332

Thompson T. A., Quataert E., Murray N., 2005, ApJ, 630, 167

Tinker J., Kravtsov A. V., Klypin A., Abazajian K., Warren M., Yepes G., Gottlöber S., Holz D. E., 2008, ApJ, 688, 709

Toft S., Gallazzi A., Zirm A., Wold M., Zibetti S., Grillo C., Man A., 2012, ApJ, 754, 3

Toft S., et al., 2014, ApJ, 782, 68

Toft S., et al., 2017, Nature, 546, 510

Tonini C., Mutch S. J., Croton D. J., Wyithe J. S. B., 2016, MNRAS, 459, 4109

Trainor R., Steidel C. C., 2013, ApJL, 775, L3

Verhamme A., Schaerer D., Maselli A., 2006, A&A, 460, 397

Verhamme A., Schaerer D., Atek H., Tapken C., 2008, A&A, 491, 89

Villar-Martín M., Sánchez S. F., Humphrey A., Dijkstra M., Di Serego Alighieri S., De Breuck C., González Delgado R., 2007, MNRAS, 378, 416

Villar V., Gallego J., Pérez-González P. G., Pascual S., Noeske K., Koo D. C., Barro G., Zamorano J., 2008, ApJ, 677, 169

Walter F., Riechers D., Cox P., Neri R., Carilli C., Bertoldi F., Weiss A., Maiolino R., 2009, Nature, 457, 699

Wang L., De Lucia G., Fontanot F., Hirschmann M., 2018, submitted to MNRAS, arXiv:1809.06026

Wechsler R. H., Tinker J. L., 2018, ARA&A, 56, 435

Wellons S., et al., 2015, MNRAS, 449, 361

Whitaker K. E., van Dokkum P. G., Brammer G., Franx M., 2012, ApJL, 754, L29

Whitaker K. E., et al., 2014, ApJ, 795, 104

White S. D. M., Rees M. J., 1978, MNRAS, 183, 341

Windhorst R. A., Mathis D., Neuschaefer L., 1990, in ASP Conf. Ser., Evolution of the universe of galaxies. p. 389

Wise J. H., Abel T., 2007, ApJ, 665, 899

Wise J. H., Abel T., 2008, ApJ, 685, 40

Wisotzki L., et al., 2016, A&A, 587, A98

Wisotzki L., et al., 2018, Nature, 562, 229

Wuyts S., et al., 2011, ApJ, 742, 96

Yang H., Malhotra S., Gronke M., Rhoads J. E., Dijkstra M., Jaskot A., Zheng Z., Wang J., 2016, ApJ, 820, 130

Younger J. D., et al., 2010, MNRAS, 407, 1268

Yu H., Wang F. Y., 2016, ApJ, 820, 114

Yun M. S., Reddy N. A., Condon J. J., 2001, ApJ, 554, 803

Yun M. S., et al., 2015, MNRAS, 454, 3485

Zamojski M. A., et al., 2007, ApJSS, 172, 468

Zaroubi S., 2013, The First Galaxies. Astrophysics and Space Science Library. Springer, Berlin, Heidelberg, pp 45–101, doi:https://doi.org/10.1007/978-3-642-32362-1_2

Zavala J., Avila-Reese V., Firmani C., Boylan-Kolchin M., 2012, MNRAS, 427, 1503

Zhao D. H., Jing Y. P., Mo H. J., Börner G., 2009, ApJ, 707, 354

da Cunha E., et al., 2013, ApJ, 766, 13

van der Wel A., et al., 2014, ApJ, 788, 28

van der Wel A., et al., 2016, ApJSS, 223, 29

List of Figures

List of Tables

Acronyms

HST *Hubble Space Telescope*. 11, 12, 39, 66, 79, 82–84

AGN Active Galactic Nuclei. ix, 6, 12, 14, 18, 25, 26, 38, 80, 82, 87, 89, 95

ALMA Atacama Large Millimeter Array. 13, 19, 53, 55, 56, 58, 65–68, 71, 73, 76, 79, 80, 83, 84, 91, 94, 95

CARMA Combined Array for Research in Millimeter-wave Astronomy. 78, 80

CASA Common Astronomy Software Applications. 56

CDM Cold Dark Matter. 2

CGM circumgalactic medium. 82

CMB Cosmic Microwave Background. 2–4, 58, 60–64, 69, 70, 117

COSMOS Cosmic Evolution Survey. 8, 10, 11, 13, 21, 23–28, 32, 34, 38, 39, 45, 48, 55, 58, 65, 82, 89

DTS dust-to-stellar-mass. 64

ESO European Southern Observatory. 78

FIR far-infrared. 9–11, 13–15, 23, 39, 41, 42, 45, 46, 55, 58, 60, 64, 68, 71, 117, 118

FSL fine structure line. 13

FWHM full width at half maximum. 24–27, 29–31, 37, 47, 56, 67, 69, 71, 72, 83, 84, 117

HMF Halo Mass Function. 4, 5, 117

HSC Hyper Suprime-Cam. 64

HUDF Hubble Ultra Deep Field. 8

IGM intergalactic medium. 6, 11, 15

IMF initial mass function. 9, 32, 59, 64, 70

IR infrared. 9, 11, 12, 22, 24–26, 53, 64, 65, 79, 94, 118

IRAC Infrared Array Camera. 25, 26, 64

ISM interstellar medium. 14, 55, 58, 60, 62–64, 70, 76

JVLA *Karl G. Jansky* Very Large Array. 19

KM Kaplan–Meier. 34–37, 40, 41, 49, 50

KS Kennicutt-Schmidt. 15–18, 42, 46, 91–94

LBG Lyman break galaxy. 11, 18, 82, 83, 86

MC Monte Carlo. 26–29, 31, 33, 35, 36, 41, 47, 48, 86, 117

MIR mid-infrared. 58, 64

MS Main Sequence. 16–23, 32–44, 46, 48–51, 54, 61–63, 65, 70, 71, 74, 75, 91–93, 117, 119

MSMF multiscale multifrequency synthesis. 24

MW Milky Way. 62

NFW Navarro-Frenk-White. 4, 5, 117

ngVLA Next Generation Very Large Array. 95

NOEMA NOrthern Extended Millimeter Array. 13, 19, 53, 55, 56, 58, 59, 65–68, 76, 80, 91, 94

NUV near-ultraviolet. 26, 32

PACS Photodetector Array Camera and Spectrometer. 58, 60

PSF point spread function. 72, 83, 84

SDSS Sloan Digital Sky Survey. 8

SED Spectral Energy Distribution. 8, 9, 11, 12, 26, 55, 58, 60, 70, 94, 118

SFE star formation efficiency. 62

SFG star-forming galaxies. vii, xi, xii, 9, 11, 14, 16–51, 54, 60, 65, 66, 68, 71, 74, 75, 78, 79, 82–84, 87, 91–95, 117–119

SFH star formation history. 9, 14, 24, 64

SFR star formation rate. 8–11, 13–18, 22, 23, 32, 35, 36, 41–43, 53–55, 58, 65, 70, 71, 74, 75, 83, 87, 88, 92, 93, 117

SFRD star formation rate density. 14–17, 19, 20

SLED spectral line energy distribution. 62, 63, 75, 118

SMBH super-massive black hole. 8, 14–16, 117

SMD stellar mass density. 14, 15

SMG sub-millimeter selected galaxy. 11, 16, 17, 20, 32, 39, 53–55, 59, 60, 62, 63, 65, 70–77, 82, 84, 88, 92, 93, 95, 118

SNR signal-to-noise ratio. 65, 72, 80

SPIRE Spectral and Photometric Imaging Receiver. 59, 60

SPLASH Spitzer Large Area Survey. 24, 64

SSFR specific star formation rate. 16–18

ULIRG Ultra-Luminous Infrared Galaxy. 16, 17, 54, 60–62, 64, 65, 71, 73–76, 92, 93

UV ultraviolet. 9, 11, 14, 15, 19, 22, 23, 32, 35, 38, 39, 41, 42, 45, 46, 64, 81–84, 87

VDI violent disk instability. 42, 44

VLA Very Large Array. 10, 21, 23–28, 38, 39, 45, 48, 53, 55, 56, 58, 59, 65, 66, 68, 76, 79, 91, 94

VLT Very Large Telescope. 12, 78, 79, 95

WFC3 Wide Field Camara 3. 11, 83, 84

Acknowledgements

The intellectual debt to my mentors is absolute. I am deeply grateful to Benjamin Magnelli, Alexander Karim and Emilio Romano-Díaz for their guidance and warm encouragement during my doctoral studies. Special thanks to my supervisor Frank Bertoldi for his generous support and constructive comments that have greatly improved my academic performance.

I thank the members of our research group for their assistance, cheerful comments and pleasant lunch breaks: Eleni, Miriam (my IMPRS buddy), Toma, Basilio, Aarti and –last but not least– Chris. My gratitude also goes to all my friends at the AIfA/MPIfR for making my life in Germany a delightful experience. I am especially grateful to Jens, Ana and Kevin (my officemates) who have been my second family during the past four years.

I gratefully acknowledge the unwavering support and uplifting feedback that I have received from Christina Stein-Schmitz. Thanks should also go to Simone Pott and Rainer Mauersberger for their assistance with the procedures related to the International Max Planck Research School (IMPRS).

This Ph.D. thesis would not have been materialized without the contribution and constructive criticism of members of COSMOS collaboration, including Eva Schinnerer, Chris Carilli, Vernessa Smolčić, Carlos Gómez-Guijarro, Gareth Jones, Sune Toft, Mladen Novak, Gianni Zamorani, and Marco Bondi. Finally, I very much appreciate the generous financial, practical and scientific support from the SFB 956, the IMPRS and the Bonn-Cologne Graduate School for Physics and Astronomy.